



**Politecnico
di Torino**

Politecnico di Torino
Master course in ICT for Smart Societies

Master Degree

Impact of GNSS antenna calibration model for attitude estimation in UAV platform

Student:

Alessio Ruberti s277489

Supervisor:
Marco Piras

Co-rapporteur:
Giuseppe Virone

Academic Year 2020/21

Acknowledgement

Thank you to my Supervisor, Professor Marco Piras, for your patience, guidance, and support. I have benefited greatly from your wealth of knowledge and. I am extremely grateful that you took me on as a student and continued to have faith in me over the past months.

Thank you to my Co-rapporteur, Prof. Giuseppe Virone, for your noble guidance and for assisting me through the data acquisition tests and helping me with the post-processing of a huge amount of data.

Thank you to CNR-IEIIT and DET Departments, especially Professor Riccardo Maggiora for the laboratories availability and joint activities without which I could never have achieved these results.

Thank you to Professor Paolo Dabove and Researcher Vincenzo di Pietra for your precious support through the test activities and a special thank to Horea Bendea for producing the baseline support.

Ed infine un grazie immenso ai miei genitori che mi hanno sempre accompagnato durante questa lunga avventura iniziata due anni fa, supportandomi e sopportandomi con ogni loro mezzo a disposizione. Grazie ai miei amici, nonchè colleghi, per aver condiviso ogni singolo giorno con me, vi voglio bene. Grazie ai miei nonni Giacomo e Annita per essersi sempre preoccupati se, tra una derivata parziale e un algoritmo di regressione, avessi provveduto a soddisfare il mio fabbisogno nutrizionale giornaliero. Grazie anche a te nonno Rocco, che da lassù mi hai sempre protetto e continuerai a farlo durante tutta la mia vita.

Contents

1	Introduction	1
2	Brief introduction of UAV system	3
2.1	Classification of UAV	3
2.1.1	Based on Aerodynamics	3
2.1.2	Based on landing, weight and range	5
2.2	Hardware Design and Challenges	5
2.2.1	Aircraft design	6
2.2.2	Ground Control System	7
2.2.3	Data Link	7
2.3	Applications	8
2.3.1	Drones in defence	8
2.3.2	Drones for civil applications	8
2.3.3	Drones for photogrammetry	9
2.3.4	Drones for antenna calibration	9
2.4	Challenges	9
2.4.1	Technological gaps	9
3	Introduction of GNSS	11
3.1	Markets and Application	11
3.2	GNSS overview	12
3.3	GNSS error sources	14
3.3.1	Clock bias	15
3.3.2	Signal propagation errors	17
3.3.3	System errors	19
3.3.4	Intentional error sources	20
3.3.5	User equivalent error	22
3.3.6	Dilution of precision	22
3.4	Augmentations	23
3.4.1	Differential GNSS	24
4	GNSS Attitude	27
4.1	Reference Frames	27
4.1.1	The Body Frame	27
4.1.2	The Local Level Frame	28
4.1.3	The Earth Center Earth Fixed Frame	29
4.1.4	Geographic coordinate conversion: rotation transformations	29
4.1.5	Attitude estimation from ECEF coordinates	30
4.2	The choice of baseline length and antenna location	30
4.3	Heading angle	30
5	Methods for Antennas Under Test (AUT) calibration	34
5.1	Voltage standing wave ratio (VSWR)	37
5.2	Radiated emission measurement: antenna factor (AF)	38
5.2.1	Definition and use of Antenna factors	39
5.2.2	Antenna gain	41

5.2.3	Antenna calibration	42
5.3	Phase center corrections	43
5.4	Anechoic chamber overview	45
5.5	Theory behind the anechoic chamber	47
5.6	Types of RF absorbers	49
5.7	Experimental setup	50
6	Testing and Validation	53
6.1	Hardware and software technologies	53
6.1.1	Antennas	53
6.1.2	Swift Navigation Piksi Multi GNSS Module	57
6.1.3	u-blox C94-M8P-3	58
6.1.4	RTKLIB	59
6.1.5	Swift Navigation Console	60
6.2	RTK base station	62
6.3	Acquisition stage	63
6.3.1	Methodology	63
6.3.2	Experimental setup	64
6.3.3	Data collection	68
6.4	Post-processing of data	69
7	Results	78
7.1	Estimation parameter analysis	78
7.2	Normal configuration: static positioning technique	78
7.3	Reversed configuration: static positioning technique	84
7.4	Dynamic configuration: Kinematic positioning	90
7.5	Bearing angle estimation: experimental setup	101
7.6	Bearing angle estimation: UAV Platform.	103
7.7	Tests validation with anechoic chamber results	105
8	Conclusions	111
A	Appendix	113
A.1	Static mode - normal configuration: DGPS/DGNSS positioning	113
A.2	Static mode - normal configuration: Moving-Base positioning	118
A.3	Static mode - reversed configuration: DGPS/DGNSS positioning	125
A.4	Static mode - reversed configuration: Moving-Base positioning	131
A.5	Dynamic mode - normal configuration: Moving-Base positioning in stepped rotation	143
A.5.1	Dynamic mode - reversed configuration: Moving-Base positioning in con- tinuous rotation	149
A.6	Dynamic mode - reversed configuration: Moving-Base positioning in stepped ro- tation	154
B	Code	158

1 Introduction

In recent years Unmanned Aerial Vehicles (UAVs) have been the subject of extensive research and development. UAVs offer cost effective access to airspace for long periods. They are able to operate in dangerous environments avoiding the possibility of human injuries. Due to this, UAVs were mainly developed for military purposes. As an Army Officer, I personally saw the evolutionary process of the use of drones in the Armed Forces. In fact, this evolution process went from the simple surveillance of risk territories, through the use of "Predator MQ-9" by the Italian Air Force or "Raven B / DDL" by the Italian Army, to the use of drones with more advanced technologies, suitable for dealing with spoofing and jamming phenomena. However, increasingly UAVs are finding application in civilian environments. Their ability to offer low cost access to airspace at low risk to operators has meant they have found application in science, security and land management. Military UAV systems may be adapted to meet civilian roles or alternatively bespoke systems may be developed to meet a specific task such as archaeology, environmental monitoring, civil engineering, and assistance in natural disasters.

A sector that witnessed significant UAV impact is the emerging Information and Communication Technology (ICT) field, in particular the branch of UAV attitude and antennas calibration. Typically, unmanned aerial vehicle performances are evaluated using a high-grade Inertial Navigation System (INS) and a position from a Global Navigation Satellite System (GNSS) receiver. Hence, it is clear how, navigation and positioning of drones are a fundamental aspect for remote operations and flight safety.

Unfortunately, the acquisition of emitted satellite signals, performed by onboard drone antennas, are extremely affected by noise due to electromagnetic disturbances, radio interferences and other bias. Therefore, it is clear how the antennas calibration is extremely important, particularly the low-cost ones. Typically, antennas tests are performed inside anechoic chambers, where the radiation pattern can be estimated with high precision. However, high precision often requires the use of high-cost instrumentation. In this scenario is mandatory to develop cost-effective methods to characterize UAV antennas. A possible solution to this phenomenon is using a multi antenna GNSS measurement system.

These kinds of measurements, although less accurate than those performed in anechoic chambers, allow a more realistic performance analysis due to multipath contributions in ground, surrounding structures, and drastically reduce the equipment cost. The main objective of this thesis is to calibrate antenna under tests (AUTs) throughout the use of a non-conventional and cost-effective system, understanding what the possible impact of this calibration over attitude estimation in UAV platform is.

This thesis consists of eight chapters. After a general introduction, that describes the context of the research and the problem statement on which it is focused on, theory background and proposed solution to solve the problem are presented. In particular, some necessary background on UAV onboard technology and aerial design, their types and domain of application and finally a general overview on what are the main challenges and technological gaps are presented. Subsequently, a general overview on the Global Navigation Satellite System (GNSS) is given. Here are presented all the possible GNSS error sources like clock bias, system errors, signal propagation errors, intentional error sources and user equivalent error. Furthermore, some augmentations of GNSS system are presented. Particularly, the concept of Differential GNSS is taken into consideration. As a consequence, it is taken into account the theory behind the GNSS attitude estimation, particularly the main reference frames through which UAV platforms are referenced with respect to the globe are presented. Furthermore, some trigonometrical approaches to obtain

the attitude estimation from geographical coordinates, like heading angle, are treated. Following this path, different methods of calibration for Antennas Under Test (AUT) are analyzed. Principal factors like antenna gain and phase center corrections, with which checking the performance of antennas, are taken into consideration. In addition, a general overview about the anechoic chamber is given: background theory and different types of Radio Frequency (RF) absorbers. Once all the background theory is analyzed, the low-cost measurement system is presented. Firstly, it was decided to underline all the Hardware and software technologies used throughout the project, including antenna model and features, signal receivers and data acquisition and post-processing softwares. Furthermore, a detailed description of the experimental setup is provided, focusing on the baseline configurations, the place where the surveys were made and the different methodologies used for both data acquisition and post-processing phases. After data acquisition and post-processing phase, it was put emphasis on the estimation parameters comparison between the different acquisition modes, static and dynamic, and different baseline configurations, static and dynamic. Particularly, bearing angle estimation for both the experimental setup and UAV platform is given, comparing the performance of both measurement systems and validating the obtained results with anechoic chamber tests. The simulations showed how even through the use of unconventional methods it is possible to calibrate signal receivers. Clearly, as an experimental system, further development could be studied. However, being a method that uses low price equipment, the initial goal of this thesis has been achieved: we are able to provide a valid alternative to high-cost antenna calibrations.

2 Brief introduction of UAV system

Unmanned aerial vehicle (UAV) also known as remotely operated aircraft, can be operated autonomously or by remote pilot control [1], [2]. UAV is an integral part of the Unmanned aerial system which incorporates UAV, communication link and ground control station [3]. UAV overcomes the limitation of the terrestrial system in terms of accessibility, speed and reliability [4]. UAV can provide cloud-free and high-resolution images to serve the commercial applications such as agriculture, mining and monitoring. UAV was originated in defense for reconnaissance and combat purpose. Later on with the advent and integration of advanced navigation sensors UAV became an integral part of armed forces [4]. The emergence of technology not only removed the limitations of UAV exercises in the military but expanded their wings in commercial applications related to agriculture, scientific activities, recreation, servile, delivering goods, photogrammetry and many more [5].

In this chapter will be given a general classification of UAV platforms, what is the aircraft design and what type sensor technologies are integrated. Moreover, a brief overview on what are the main challenges that UAVs have to deal with will be provided. Finally, we will understand what is the main connection between UAVs and GNSS receivers.

2.1 Classification of UAV

UAVs are typically classified in sense of aerodynamics, landing, weight and range.

2.1.1 Based on Aerodynamics

A variety of UAV system has been developed and in the advancement phase, some of them includes the Fixed-wing aircraft, chopper, multi-copter, motor parachute and glider, UAV with Vertical takeoff and landing, congregating ready-made parts and commercialized UAV. All of them are specified for a specific mission and have their zeros and ones [4].

Fixed wing drones (see Figure 1) are very simple but saturated in designing and manufacturing, because of successful generalisation of larger fixed-wing planes with slight modifications and improvements [4].



Figure 1: Fixedwing NM& F300 UAV.



Figure 2: Multirotor OnyxStar HYDRA-12 UAV.

Typically, Fixed wing drones need a higher initial speed and the thrust to load ratio of less than 1 to start a flight. If fixed wing and Multirotor (see Figure 2) are compared for a same amount of payload, fixed-wing drones are more comfortable with less power requirement and thrust loading of less than 1 [4]. Rudder, ailerons and elevators are used for yaw, roll and pitch angles to control the orientation of aircraft.

Flapping wing drones (see Figure 3) are primarily inspired by insects such as small hummingbirds to large dragonflies [5; 6]. The lightweight and flexible wings are inspired from the feathers of insects and birds which demonstrate the utility of weight and flexibility of wings in aerodynamics [4]. However, these flapping wings are complex because of their complicated aerodynamics.



Figure 3: Flapping wing drone.

Flapping drones can support stable flights in a windy condition, unlike fixed-wing drone: light, flexible and flapper wings provide the flapper motion with an actuation mechanism [4]. Intensive research on flapping wings has been carrying out by drone community and biologist because of their exclusive manoeuvrability benefits [8].

Fixed/flapping-wing: Integrated effect of the fixed and flapping mechanism is used where fixed wings are used to generate lift whereas flagging wings are used for generation of propulsion [9]. These type of drones are inspired by dragonfly which uses two pairs of wings in order to increase the lift as well as thrust forces. Hybridisation using fixed and flapping wing increases overall efficiency and aerodynamic balance [9].

Multirotor: Main rotor blade produces a forceful thrust, which is used for both lifting and propelling. These are the most common types of drone available and make up the vast majority of commercial and consumer models available. Many different configurations are available but they generally follow the same design principle. There is a central chassis which connects up to eight fixed-pitched propellers to control the speed, direction and elevation of the aircraft.

These propellers control the direction and elevation of the aircraft by varying the speed of each propeller to alter the amount of thrust and torque produced. This gives the aircraft a unique set of handling characteristics, allowing it to fly with extreme precision in both enclosed and open space. Multirotor unmanned aerial vehicles are capable of vertical takeoff and Landing (VTOL) and may hover at a place unlike fixed-wing aircraft [10; 12]. Multirotor are designed by number and location of motors and propellers on the frame. Their hovering capability, ability to maintain the speed makes them ideal for surveillance purpose and monitoring [4]. The only concern with Multirotor is that they need more power consumption and makes them endurance limited. Abott equations are used for exact calculation of power and thrust requirements in multirotor aircraft [4].

$$Power[W] = Pitch \cdot Diameter^4 \cdot (RPM)^3 \cdot (5.33 \times 10^{-15}) \quad (1)$$

$$Thrust[OZ] = Pitch \cdot Diameter^3 \cdot (RPM)^2 \cdot (10^{-10}) \quad (2)$$

Multicopter is divided into specific categories based on number and positioning of motors, each category belongs to a specific type of mission [4], and based on the mission requirement they are classified in various configurations such as Monocopter, Tricopter, quadcopter, hexacopter and so on.

2.1.2 Based on landing, weight and range

Horizontal takeoff and landing (HTOL) and vertical takeoff and Landing (VTOL): HTOL may be considered as the extension of fixed-wing aircraft [4]. They have high cruise speed and a smooth landing. VTOL drones are expert in flying, landing and hovering vertically [14], but they are limited by cruise speed because of the slowing down of retreating propellers [13]. Some researchers and organisations have classified the drones based on weight and range [4]. Table 1 presents the list of the unmanned aerial vehicle based on the weight and range.

2.2 Hardware Design and Challenges

The designing of the Unmanned aerial system includes the unmanned aerial vehicle and other subsystems which includes communication link between UAV and user, ground control station and accessories like gimbal, payload [4]. The design of UAV itself integrates the parts evolving from vehicle frame to complete ready to fly the aerial vehicle. Selection of components like airframe, Controller, motor, propellers and the power supply is the crucial task and needs in-depth knowledge and full- fledged mathematical calculations to design a UAV for a specified mission [4]. Figure 4 and 5 describes the subsystems and modules for the design of UAS.

Type	Maximum Weight	Maximum Range [Km]	Category
Nano	200 g	5	Fixed wing, multirotor
Micro	2 Kg	25	Fixed wing, multirotor
Mini	20 Kg	40	Fixed wing, multirotor
Light	50 Kg	70	Fixed wing, multirotor
Small	150 Kg	150	Fixed wing
Tactical	600 Kg	150	Fixed wing
MALE	1000 Kg	200	Fixed wing
HALE	1000 Kg	250	Fixed wing
Heavy	2000 Kg	1000	Fixed wing
Super Heavy	2500 Kg	1500	Fixed wing

Table 1: Unmanned aerial Vehicles classification based on weight and range.

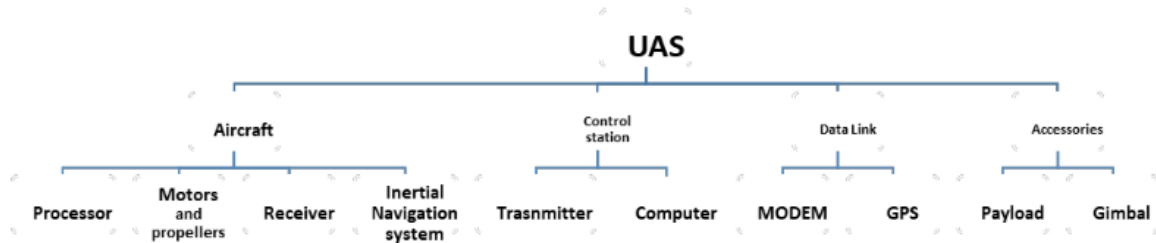


Figure 4: Unmanned Aerial System Subsystems.

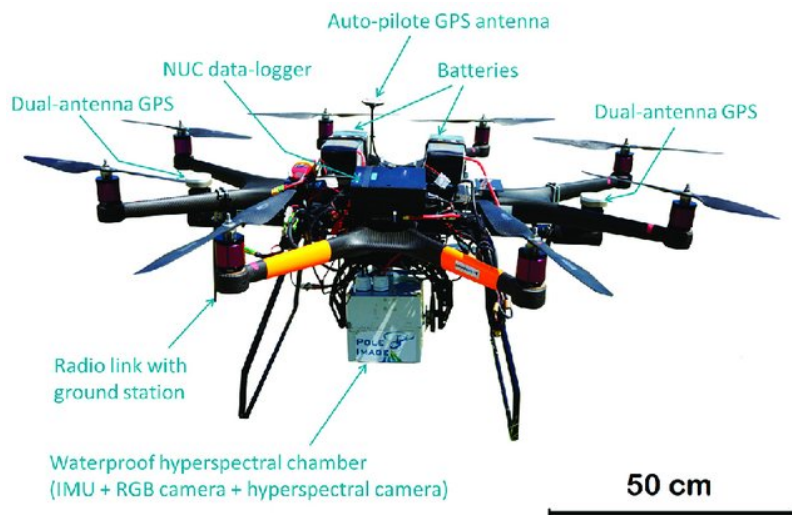


Figure 5: UAS details.

2.2.1 Aircraft design

The design challenges of an aircraft rely on the type of application which specifies the coverage area, maximum altitude, speed, climb rate, flight time or endurance, and stability [15]. All the specifications are prone to vary contingent on applications and the environmental effects. Higher

altitude specifies a large coverage area and improves survivability although maximum altitude is limited by the aviation regulations [4]. Climb rate also increases the survivability. Flight time is strictly dependent on the type of operation and aerodynamic design of aircraft [4].

The main components of aircraft subsystems are inertial measurement unit, motors, propellers and receiver, processor and an Airframe [4]. The most common metallic materials to manufacture aircraft are alloys, aluminium and titanium, whereas nonmetallic materials include transparent and reinforced plastic [16]. Multicopter have the N brushless motors with N propellers. Electronic speed controller serves their purpose by varying the power supplied to motor commanded from throttle stick [4]. They can fly in a particular direction and adjust their elevation, i.e. pitch (along X-axis, heading of quadcopter), roll (along Y-axis) and yaw (along Z-axis) by taking the inputs from Inertial Measurement Unit (IMU) consisting of three-axis accelerometer, gyroscope which provides 3-axis raw data and a GPS unit [4].

2.2.2 Ground Control System

The typical ground station consists of a wireless router along with a computer to capture, process and display of data [4]. Typically a ground control station should fulfil requirements such as open system architecture, compatible with different platforms like airborne, ship and ground, execution of data in real time, ability to control multiple UAVs, payload control and communication with other ground control stations [17; 18]. Other safety and a security function that can be expected from the ground control station include the warnings and emergency action plan in case of any failure, power outage restoration [4].

2.2.3 Data Link

It set up a communication channel between the Aircraft sensors and ground control station (GCS) [4]. A wireless link IEEE 802.11, is used to make a communication between aircraft central data unit and ground control station, for this purpose routers equipped with omnidirectional antennas with high gain can be used to minimise path loss and make a signal to noise ratio higher [4]. Now a day's typical antennas work on 2.4GHz and minimum 12dBi gain. Additional wireless link based on orthogonal frequency division multiplexing (OFDM) is used for online video and images transmission to a ground station [4].

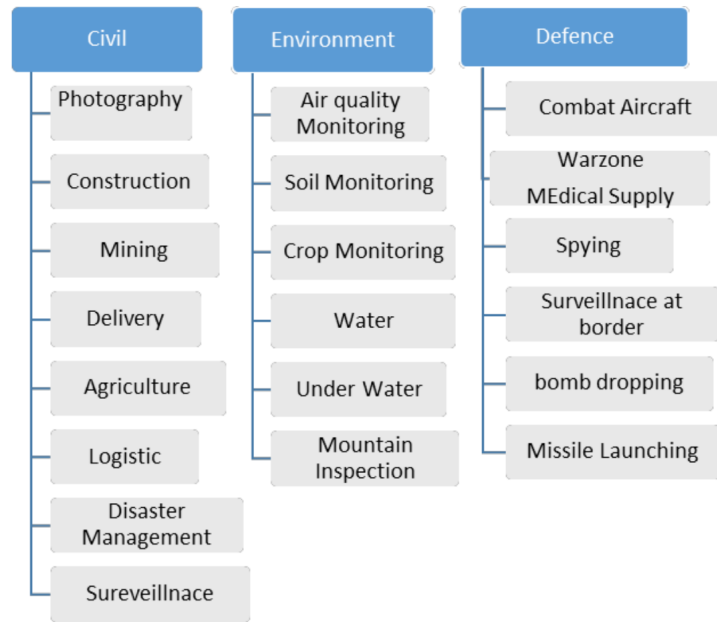


Figure 6: Potential applications of remote piloted drones.

2.3 Applications

Since Drones provide supremacy over conventional remote sensing technologies and their benefits lie in terms of less power consumption, less risk to human life, ease to data collection, hovering, and ultra-high spatial resolution forges them an excellent choice for surveying and mapping [4]. Following pioneer, studies demonstrate the relevance and uniqueness of drones in the civil, logistics, agriculture and Defense sectors [4]. Figure 6 shows the potential applications of UAV in civil, environment and defence sectors.

2.3.1 Drones in defence

The advent of UAV was started initially with the aim of transacting the war missions like intelligence, spying, reconnaissance vigilance and target detection; later they were introduced for civil and logistic applications [4]. USA, UK, Russia, India and Israel are the leading countries in the development and deployment of military drones. In 2017 the acceleration in the proliferation of military along with civilian drones was observed, and a maximum number of drone strikes by USA and UK were noted [4]. Breakthrough research and remarkable advancements in the area of swarming drones, jet-powered and Microdrones.

2.3.2 Drones for civil applications

Drones are being fascinated in all commercial stratum from electricity companies to the railway industry. Electrical companies are preferring drones for inspection of high tension lines with ease of risky task of climbs and power outages [4]. Railway companies have employed drones for monitoring and inspecting the track faults in constrained access areas. The Indian government is planning 3d mapping of thousands of kilometres long railway corridors and national highways [4]. Drones are helpful in performing search and locate operations of missing people during calamities condition. A trial to locate people in Donegal mountain range, Ireland and rescue

operation of 200 people in flood zone by Chennai police, India exemplifies the potential and necessity of drones [4]. Medical facility delivery using drones performed in many countries like the USA and electricity generation through high elevation and high-speed [4].

2.3.3 Drones for photogrammetry

Photogrammetry based on Unmanned Aerial Vehicles (UAV photogrammetry) is an irruptive technology that is being applied to obtain very-high-resolution Digital Surface Models, orthoimages, and point clouds which represent terrain morphology [59]. Most of the research issues related to UAV photogrammetry concern the adaptation of precedent classic photogrammetry from aircrafts, satellites, or even close-range photogrammetry to images captured with UAV. UAVs introduce new possibilities for photogrammetric projects thanks to their flexibility of route planning, on-board GNSS navigation devices, or inertial data synchronized with shotting. Photogrammetric software has experimented parallel development, especially with the implementation of the Structure from Motion (SfM) algorithm to efficiently manage imagery capture by sensors on-board UAVs, working not only in the visible spectrum but also the infrared, multispectral, and hyperspectral wavelengths.

2.3.4 Drones for antenna calibration

2.4 Challenges

2.4.1 Technological gaps

There is always a trade-off between Payload capacity and flight time in drone technology. Conventionally, onboard lightweight lithium-ion batteries are used to supply power to UAV, but their power backup is not comparable with other batteries [4]. In addition, with the increase in payload, endurance decreases and hence mission may not get its completion. Fixed wing drones are efficient in power usage, but they have the drawback of hovering and speed control [4]. Flying a single drone may also encounter a flight failure due to some technological and climatic reasons, so there is always a need to provide backup. Upcoming swarm flight of drones can execute this task, where in case of failure of one drone, others complete the mission. This technology is dependent on Swarm motion of insects, ants and birds and makes use of artificial intelligence, yet in developing phase [4]. Drones are still limited by controlling through human operators, integration of Artificial Intelligence will allow a drone to make smart decisions and operate accordingly instead of human controllers [4]. Possible gains and harms are yet to be explored in this direction.

Drones also suffer from windy conditions and adverse climate changes: Spraying Drones are efficient to spray less area, but for mass spraying, they become less efficient, and the operation cost becomes high [4].

Another concern is too technical learning of farmers to make use of drone-based precision farming and to make the drone-based system fully automatic from image acquisition to making complex statistical models and decision support system [4]. A GPS mounted on drone connects with four satellites to detect the position, velocity and elevation accurately. Since GPS signals are very much prone to noise and interference, there is a finite possibility of losing contact: at that time it is recommended that instead of emergency landing, their location should be estimated [4]. The inertial navigation system combined with GPS provide a solution for this situation. Efficient algorithms have to be designed and tested to estimate the position and elevation correctly.

Besides the drone hardware design challenges, the cameras used for precision agriculture applications also puts some limitations [4].

The multispectral images collection is very much prone to get affected by total irradiation along with sun angle and adverse weather conditions such as rain, heavy wind [4]. Comparison of UAV data and satellite data puts two significant limitations that data has to be resampled to make equal spatial resolution images and secondly, if there is a cloud cover then it is almost impossible to compare the images since the information beneath the ground gets shadowed [4]. Onboard thermal sensors can detect the water utilisation of plants based on radiated temperature. The temperature variations in plants are exiguous which makes it difficult to discriminate other factors which may affect plant water such as sun irradiation, therefore, further research is required [4].

In addition, the world of UAVs is increasingly gaining ground in the field of ICT technologies. In particular, fundamental aspects such as the estimation of the attitude and bearing of the UAV platform are carried out with new low-cost measurement systems. In fact, since these parameters are strictly linked to the onboard antennas, one of these is certainly the GNSS positioning system which, thanks to the robustness and accuracy of its measurements, allows to obtain very high levels of accuracy. Therefore, it is clear how, in recent years, studies of these innovative systems have increased.

3 Introduction of GNSS

Navigation is defined as the science of getting a craft or a person from one place to another. Each one of us uses some navigation techniques in our daily lives: driving to work, walking to a store, going to the gym are all actions that require fundamental navigation skills. For some people, these skills necessitate utilizing our eyes, common sense, and landmarks. Instead, for other people, a more accurate knowledge of our position, intended course, transit time to a desired destination is needed. These may be in the form of a simple clock to determine the velocity over a known distance or some tools like the odometer to keep track of the distance traveled. Other navigation aids transmit electronic signals and therefore, are more complex. These are referred to as *radionavigation aids*.

Signals from one or more radionavigation aids enable a person to compute their position. It is important to note that it is the user's radionavigation receiver that processes these signals and computes the position fix. The receiver performs the necessary computations (e.g., range, bearing, estimated time of arrival) for the user to navigate to a desired location.

Typically, various types of radionavigation aids exist and they are categorized as ground-based or space-based. For the most part, the accuracy of ground-based radionavigation aids is proportional to their operating frequency. Highly accurate systems generally transmit at relatively short wavelengths and the user must remain within line of sight, whereas systems broadcasting at lower frequencies (longer wavelengths) are not limited to line of sight but have less precision. A typical example of systems that use short wavelengths and are generally highly accurate and line-of-sight-limited are the satellite navigation (SATNAV) [19].

3.1 Markets and Application

Today's 4 billion GNSS deployed devices are projected to grow to over 9 billion by 2023. That is more than one unit for every person on Earth. It is anticipated that while the United States and Europe will grow at 8% per year, Asia and the Pacific Region will grow at 11% per year. The total world market is expected to grow about 8% over the next 5 years due primarily to GNSS use in smart phones and location-based services. Revenues can be broken into core elements like GNSS hardware/software sales and the enabled revenues created by the applications. With these definitions, annual core revenue is expected to be just over 100 billion euros by 2021 [19].

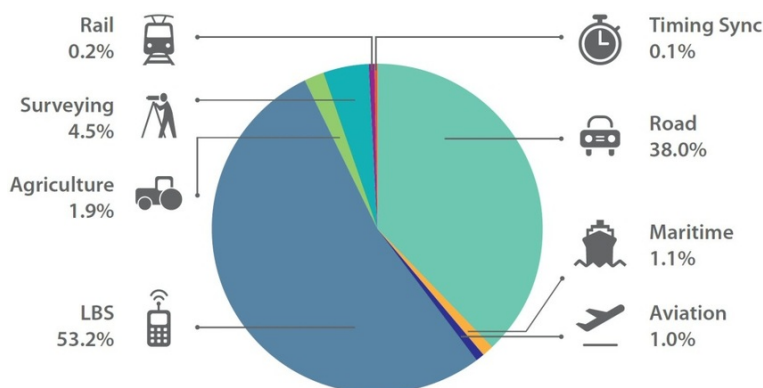


Figure 7: Cumulative core revenue 2013 to 2023 by market segment (billions of Euros).

GNSS revenue growth between now and 2023 was estimated to be dominated by both mobile users and location-based services as can be seen from Figure 7.

Applications of GNSS technology are diverse. These range from navigating a drone to providing a player’s position on a golf course and distance to the hole. While most applications are land-based such as providing turn-by-turn directions using a smartphone, there also aviation, maritime, and space-based usages [19]. Furthermore, for some years now, GNSS has been used as a support tool for attitude estimation in UAV platform and the characterization of some antenna models (microstrips, patches, geodesics, etc.) given its innovation, ease of implementation and cost-effectiveness.

3.2 GNSS overview

Today, there are numerous SATNAV systems operating around the world. Some are global and others only provide service within a certain region. The term *Global Navigation Satellite System* (GNSS) is defined as the collection of all SATNAV systems and their augmentations. The most important SATNAV systems are the Chinese BeiDou Navigation Satellite System (BDS), the European Galileo system, the Russian Federation GLObal Navigation Satellite System (GLONASS), the U.S. Global Positioning System (GPS) and the Japan’s Quasi-Zenith Satellite System (QZSS)[19].

The GNSS provides accurate, continuous, worldwide, three-dimensional position and velocity information to users with the appropriate receiving equipment; it also disseminates time within the Coordinated Universal Time (UTC) timescale. Global constellation within the GNSS, sometimes referred to as core constellations, nominally consist of 24 or more medium Earth orbit (MEO) satellites arranged in 3 or 6 orbital planes with four or more satellites per plane [19].

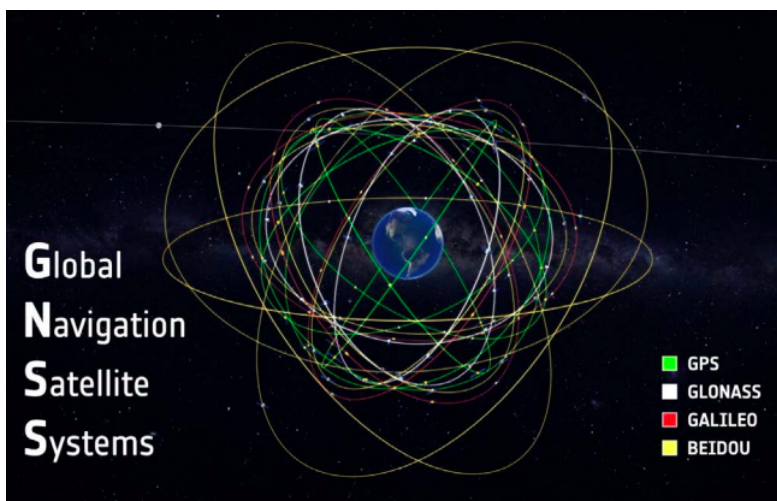


Figure 8: GNSS schematic representation containing all the SATNAV systems.

A ground control/monitoring network monitors the health and status of the satellites. This network also uploads navigation and other data to the satellites. With the exception of the radiodetermination service (RDSS) provided by a portion of the BDS, which relies on active ranging to geostationary satellites for positioning, the SATNAV systems just mentioned before provide service to unlimited number of users since the user receivers operate passively (i.e., receive only). These SATNAV systems utilize the concept of one-way time of arrival (TOA)

ranging. Satellite transmissions are referenced to highly accurate atomic frequency standards onboard the satellites, which are in synchronism with an internal system time base. All of these SATNAV systems broadcast ranging codes of navigation data on two or more frequencies using a technique called *direct-sequence spread spectrum* (DSSS). Each satellite transmits signals with the ranging code component precisely synchronized to a common timescale. The navigation data provides the means for the receiver to determine the location of the satellite at the time of signal transmission, whereas the ranging code enables the user's receiver to determine the satellite-to-user range [19]. Figure 9 shows the DSSS technique on both transmitter and receiver sides. But why the DSSS technique? It is used since:

- uses both time and frequency planes for transmission of information bits, effect of interference and fading can be minimized to great extent;
- it can be employed in point to point applications at the rate of 11 Mbps;
- it supports higher coverage range due to low SNR (signal-to-noise ratio) requirement at receiver.

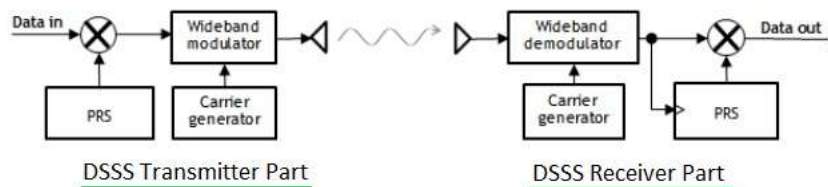


Figure 9: DSSS transmitter and DSSS receiver block diagrams.

In DSSS techniques, channel bandwidth complicates the process of decryption or decoding, because an original signal is spread into a wider bandwidth signal. In a typical DSSS system, the transmitter first modulates the data signal with a carrier signal, and then spreads the modulated signal, by applying modulo-2 addition to it with a spreading signal. The spreading signal is generated from a PN sequence running periodically at a much higher rate than the original data signal. The spreading operation is shown in Figure 10. Each individual digit in the PN sequence is called a chip to be differentiated from the bit in the data signal, and each period of the PN sequence is used to spread one data bit. Because the PN sequence is designed to resemble white noise, the spectrum of the original signal is spread out. Thus, the spectrum of the spread signal occupies a larger bandwidth than necessary and shows a lower power spectral density than that of the original signal.

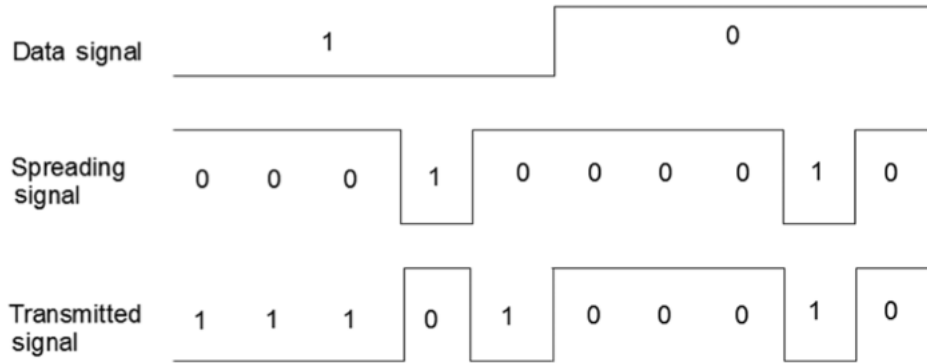


Figure 10: DSSS spreading operation: here is reported an example containing a pseudonoise (PN) sequence of 00010.

Symmetrically, the receiver first performs a correlation process on the incoming signal, that is, it applies the modulo-2 addition to the incoming signal with a synchronized copy of the spreading signal. The receiver then obtains the underlying modulated signal, which is in turn demodulated to recover the original data signal. The duplicating modulo-2 addition provides interference rejection for the DSSS signal if the interference is narrow band, because modulo-2 addition of the narrow band interference with the spreading signal will spread out the power of the interference, and hence will increase the receiving signal-to-noise (SNR) of the signal of interest.

A longer spread sequence must be employed in order to enhance the jam resistance. However, it reduces the communication efficiency accordingly, because a wider bandwidth is utilized to deliver the same amount of data bits. The spread sequence can be generated in two different ways: PN sequence, and orthogonal code. Two desirable features of the former are that auto-correlation is zero so that the synchronization at the receiver is easier, and that cross-correlation is zero too, therefore multiple codes can be used concurrently.

3.3 GNSS error sources

Typically, all the GNSS signals make a trip of thousand of kilometers between the satellite antenna and the ground receiver. Clearly, the longest part of this journey is done through space, where the signal obtains its characteristics. Unfortunately, the passage of the signal through the atmosphere layers makes it prone to undesirable errors. In fact, this medium add delays to signal propagation time, introducing some measurements imprecision.

Once the signal reaches the receiver, it usually senses some reflections leading it to bounce around the antenna surface and potentially causing multiple hits. This is the so-called *multipath* phenomenon. Multipath is one of the major error sources that a GNSS signal can run into. All the abovementioned signal interferences are caused by the nature of the signal or by a particular propagation mean characteristic and are unintentional.

But what are the consequences of these errors? Usually, GNSS signals have very low power, making them unrobust against noise and disturbances. The range measured by the GNSS receiver is full of errors and, for that reason, this is why it is called the *pseudorange*. The pseudorange can be expressed as follows:

$$P_r^s = \rho_r^s + c(dt_r - dT^s) + I_r^s + T_r^s + \epsilon_r^s \quad (3)$$

where P_r^s , represents the pseudorange between satellite s and receiver r . ρ_r^s is the real range, c the speed of light, dt_r and dT^s are respectively the receiver and satellite clock errors in unit of time (s). Variables I and T stand for the ionospheric and tropospheric delay, evaluated in meters. ϵ , the last variable, represents a combination of multipath and receiver noise errors.

GNSS errors can be categorized by following the nature of the error itself. Therefore, clock errors group all the timing-errors in both satellite and receiver. In contrast, the combination of multipath errors, atmospheric errors and the motion relative effect between the satellite and the receiver creates signal propagation errors. As regard the satellite orbit parameters (typically needed to evaluate the satellite position and velocity) are estimated at control segment level. These particular parameters are initially sent to the GNSS satellites to be broadcasted through the navigation message. This estimation error is combined with the receiver noise effect and considered as system errors. In addition, GNSS system can be affected by another type of errors called intentional errors. Those errors include signal spoofing and jamming.

3.3.1 Clock bias

Receivers generate measurements based mainly on measuring time [28]. Indeed, time is central to GNSS systems; therefore, GNSS satellites are equipped with very precise, and hence very expensive, clocks [29]. Despite their accuracy, satellite clocks still drift slightly from GNSS time. For affordability and size reasons, receiver clocks are usually much cheaper; as a consequence, they drift from GNSS time in a rapid way. This drift is the reason of dramatic range errors in receiver measurements. Therefore, correcting or compensating timing errors in the GNSS signal take a significant role. These clock errors can be summarized as follows:

- **Satellite clock errors;**
- **Receiver clock errors;**
- **Intersystem biases.**

GNSS satellite clock errors are typically introduced by: *stability*, *timing group delay* and *relativistic effects*.

The stability of onboard satellite clock is approximately 8.64 to 17.28 ns per day. This can be traduced as a range error of about 2.59m to 5.18m. The following equation describe the instability model:

$$dT^{s'} = a_{f0} + a_{f1}(t - t_{oc}) + a_{f2}(t - t_{oc})^2 \quad (4)$$

where t represents the receiver GPS time, t_{oc} the reference epoch time, a_{f0} is the clock offset, a_{f1} is the clock drift coefficient, and a_{f2} is the clock drift rate coefficient.

Relativistic effects are errors linked to relativity theories. This will result in a different perception of time. In fact, the onboard satellite clock will run faster than the same clock on Earth by 38.4 μ s/day. This is equivalent to a range error of about 11.512m. Thanks to the introduction of a proper offset to the satellite clock rate, it can be fixed. Unfortunately, some residual effects are still present due to the noncircular satellite orbit, which should be compensated by the user. This correction is expressed by:

$$\Delta t_r = -\frac{2}{c^2} \sqrt{\mu a} (e \sin E) \quad (5)$$

where, c is the speed of light, $\mu=3.86005 \times 10^{14} m^3/s^2$ is the Earth's gravitational coefficient for GPS, a is the Earth's semimajor axis, e is the eccentricity of the satellite orbit, E the eccentric

anomaly of the satellite orbit. Considering the orbit as a perfect circle, this effect would be zero as the eccentricity. Since it has a value of 0.015, the maximum threshold will be 16.8 ns, corresponding more or less to 5m. The previous formula should be written in a different way, taking into account the satellite position and velocity:

$$\Delta t_r = -\frac{2r^2 \times v^2}{c^2} \quad (6)$$

where the numerator is the product between, respectively, the satellite position and velocity vectors.

Timing group delay (TGD) are errors that refer to the satellite clock corrections inside the navigation message (typically a single GNSS signal or a signal combination). Considering the GPS, this signal is the ionospheric-free combination of codes at L1 and L2. In the case of a single-frequency operation, a correction should be made to compensate for the bias offset between L1 and the ionospheric-free combination signals. This correction is also provided in the navigation message, named as timing group delay (TGD) [30].

Once all the errors have been declared, the total satellite clock error can be estimated as the sum of the three:

$$dT^s = dT^{s'} + \Delta t_r + TGD \quad (7)$$

The second clock errors are the receiver-related clock errors. GNSS receivers are equipped with inexpensive crystal clocks, which have low accuracy compared to satellite clocks [31]. As a result, the receiver clock error is much larger than that of the GNSS satellite clock. There are two ways to fix this issue. One is to use external precise, usually cesium or rubidium, clocks which have superior performance, but the problem is that they are very expensive, as they cost between a few thousand dollars to about 20,000 dollars [32].

The other solution, which is much more common, is to remove this error through differencing between satellites or by estimating the error as an additional unknown parameter in the position estimation process. This later solution is meant to make receiver prices affordable [33]. If we add receiver clock bias to the set of unknowns, this will set the limitation to a minimum of four satellite in line of sight, instead of three, in order to obtain a clear solution from the receiver side.

To avoid the disproportionate growth of receiver clock error, manufacturers apply a clock-steering mechanism. Typically, two approaches are used to prevent this undesirable effect. The first method is continuous steering to keep the clock error within the acceptable range. The other method is clock jumping, where clock bias is adjusted only when the error reaches a certain threshold. Although the clock bias is estimated as an unknown parameter in the estimation filter, it should still be kept within a certain limit. The reason for this is that the receiver clock is used to time tag the receiver output. This time tag must have a minimum level of accuracy for time synchronization between different systems to occur [34].

Finally, intersystem biases are another way to enhance the accuracy of the GNSS receiver solution. In practical, all the observations from all available GNSS constellations are checked and intersystem clock biases are taken into account since we are dealing with a multi-constellation system. In this way, new unknowns are introduced, representing the time difference between the new GNSS constellation time and GPS time.

3.3.2 Signal propagation errors

During signal propagation time, the Earth would have rotated, causing a relative shift between the satellite and receiver locations at signal transmission time and signal reception time. If not accounted for, this relative distance, known as the Sagnac effect, will cause an extra error in the measured range [34].

Moreover, the GNSS signal makes a long trip between the satellite and the receiver. The first and longest part of the GNSS signal journey is through space where the signal preserves its original characteristics, foremost of which is its constant speed. At lower altitudes, however, the signal will experience some disturbances, e.g., ionosphere and troposphere effects. Furthermore, during the final part of the signal path, the GNSS signal arrives directly at the receiver or via single or multiple reflections from the surrounding objects. This multipath effect is not deterministic and can degrade the signal dramatically. This section covers the factors that affect the signal throughout its journey between the satellite and the receiver [34].

Let's now focus on the ionospheric effect. When the signal reaches 1000 km of altitude above the Earth's surface, it penetrates the upper layer of the atmosphere, the so-called ionosphere. This layer of atmosphere includes various types of gases that are readily ionized by the sun's radiation [29]. The intensity of solar activity is the key factor determining the condition of the ionosphere, but it is also affected by season and time of day. Accordingly, these three parameters define the level of ionization, thereby changing the refractive indices of the layers of the ionosphere, therefore, influencing the signal transit time measured by the receiver [32]. Figure 11 shows the signal propagation through the atmosphere's layers.

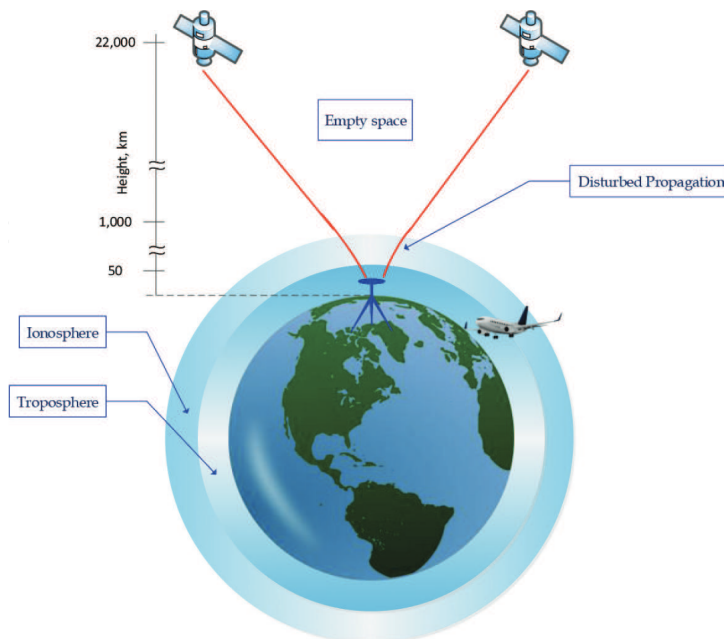


Figure 11: The GPS signal's propagation mediums.

The ionosphere acts as a dispersive medium, meaning that the ionospheric delay is frequency dependent. This delay represents one of the significant ranging errors in GNSS positioning and can reach a value of 300 ns (100 m) in some situations [35]. The first-order ionospheric delay I ,

in meters, is expressed by the following equation:

$$I = \frac{40.3 \times TEC}{f^2} \quad (8)$$

where TEC represents the total electron content, defined as the number of electrons in a tube of 1 m^2 cross section in the signal propagation direction, and f is the signal frequency.

For dual-frequency receivers, using the ionospheric-free signal combinations, this first-order error can be removed and with it 99.99% of the ionospheric delay [36]. On the other hand, in single-frequency receivers, the ionospheric delay must be modeled or estimated. The simplest way is to use the broadcast models transmitted in the satellite navigation message, such as GPS Klobuchar model [35] and Galileo NeQuick model [37]. Nevertheless, these models can correct for approximately 50% rms of the ionospheric error; even the most accurate theoretical model can only correct up to 80% of this error [35].

The other approach is to use a network of global or local dual-frequency receivers to estimate ionospheric corrections in a grid model. This network usually estimates the vertical TEC (VTEC) and sends these corrections to the users. The satellite-based augmentation network (SBAS) corrections provided by the American Wide Area Augmentation System (WAAS) are an example of such corrections. The VTEC can be used to obtain the total slant TEC through an obliquity factor that accounts for the effect of the satellite elevation angle [38]. If these corrections can be done at the single-frequency receiver, ionospheric error modelling will result more accurate compared to broadcast models.

As the signal exit from the ionosphere, it will pass through another atmosphere layer: the troposphere. It is considered as the lowest part of the atmosphere and it extends from the Earth's surface up to 20 km of maximum height above the sea level (see Figure 11). This part of the atmosphere is mainly composed of water vapor and dry gases. Since it is a refractive layer, the troposphere, too, delays GNSS signals; however, being electrically neutral, this layer is nondispersive for some GNSS frequencies [39]. The tropospheric delay has two components: wet and dry. The wet one is difficult to model, but luckily, it accounts for only 10 percent of the delay. The dry one, which is responsible for the rest of the delay, can be more easily modeled. The tropospheric delay is frequency independent; therefore, unlike the ionospheric delay, it cannot be removed by combining measurements from L1 and L2 GPS signals [34]. Depending on satellite elevation, the tropospheric delay adds up about 2.5 m to 25 m to range measurements [31].

For meter-level accuracy, several models can be used to mitigate the total tropospheric error, such as Hopfield model and Saastamoinen model. These models usually calculate the zenith delay (for elevation angle = 0) and then use a mapping function to obtain the total slant delay, depending on the satellite elevation angle [40]. If higher level of accuracy is requested in tropospheric error estimation, the dry component will be modeled, while the zenith wet component will be considered as an additional unknown in the navigation filter.

Once the signal overpasses the ionosphere and troposphere, it reaches the end of the trip. In fact, as the signal arrives nearby the antenna, often it can suffer further effects. In several scenarios, the signal may reach the receiver's antenna via more than one path (see Figure 12), owing to signal reflections from surrounding structures or the ground [41]. Usually, one of the received signals would be the direct line-of-sight (LOS) signal, along with one or more of its echoes, which are delayed versions of the original signal. Those delayed versions are superimposed on the LOS signal, which can significantly distort the desired LOS signal [34]. This is due to the fact that the multipath effect depends on the surrounding environment and the relative motion of the satellite-receiver. Moreover, in general, this effect cannot be canceled through differential positioning—even for closely spaced receivers. Therefore, the multipath error can limit positioning

accuracy even if the other error sources have been removed. In the most severe conditions, the multipath error can cause a pseudorange error of up to 100 m [28].

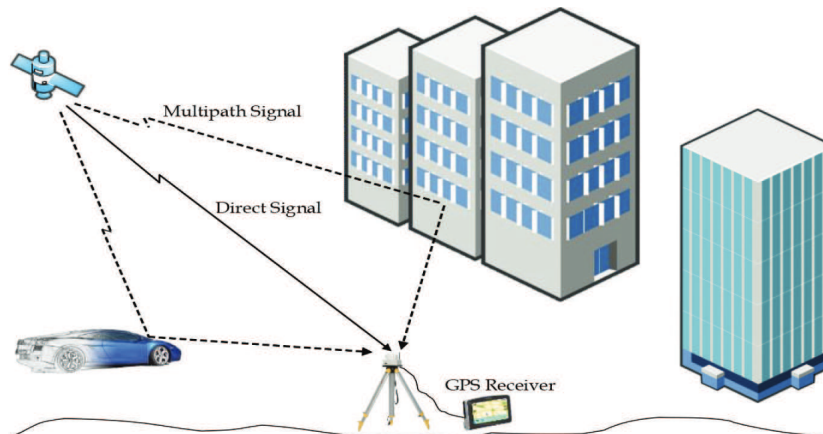


Figure 12: Line-of-sight (direct) and multipath (indirect) signals.

A possible solution to this effect is putting the receiver antenna in a reflection-free place; however, this is not always possible, particularly when the receiver is put on a moving stage. Another way to mitigate multipath error is through the receiver or antenna design. The “choke ring” antenna is one of the best-known antennas that mitigates multipath [42]. Other designs were made to keep the same high performance of the “choke ring” with lighter weight and smaller size [43]. Some modern receivers use techniques relying on multiple antennas or what is known as an antenna array. With such technology, the receiver can tune itself to track only the LOS signal and block all other replicas of the signal [44]. The multipath effect can also be mitigated at the measurement level while processing data [34]. The simple way is by weighting the measurements according to the elevation angle, since the multipath error increases at lower elevation angles [45]. A more advanced approach is to detect the multipath effect using code-phase information, such as the code minus carrier observation. This data can be used to adjust satellite weighting or even to reject some measurements with severe multipath effects [46].

3.3.3 System errors

System errors are related to the nature of the system, e.g. the receiver structure and the conformation of orbital planes.

Receiver noise is an error generated at the receiver’s side during the measurement of satellite signals. It covers a broad spectrum of noise types, including but not limited to microwave radiations sensed by the antenna in the band of interest unrelated to the signal; noise introduced by system components such as the antenna, cables, and amplifiers; and signal quantization noise [47]. Since receiver noise is considered as a white noise, it cannot be avoided at all. However, with modern receiver technology, this term is lessened to about 0.1–1% of a cycle in the carrier phase and d of centimeters in pseudorange measurements. The contradiction here is that receiver noise increases by $\sqrt{2}$ for single-differenced observations, while double-differenced ones have a noise amplification of two [48].

In contrast, satellite orbital errors are linked to the satellite conformation. Generally, receivers try to estimate satellite position with information contained in the navigation message known

as satellite ephemeris. Ephemeris parameters are calculated at the control segment and then uploaded to the constellation. Satellites broadcast updated ephemeris data every 2 hours; however, these parameters are estimated using a curve fit to predict the satellite orbit, which leaves residual errors relative to the actual orbit [33]. This error source introduces a root mean square (RMS) error of about 2 m [29]. A possible solution to this error is reached if global or network corrections for the satellite position are available. These corrections are used to refine the broadcast ephemeris corrections and, hence, improve accuracy. For post-processing, a more precise ephemeris, available from IGS [49], can be used if centimeter-level precision is required and a dual-frequency receiver was used [34].

3.3.4 Intentional error sources

These error sources are imposed by the service provider. Typically, they are divided into *selective availability*, *signal jamming* and *signal spoofing*.

Selective availability (SA) is associated with only the GPS system among the entire GNSS constellation. This is due to the fact that the US government has deliberately imposed these restrictions on its navigation system performance for national security reasons. In fact, the satellite clock corrections in the broadcast ephemeris were downgraded in order to reduce the precision for civilian use. However, the USA decided to completely remove these restrictions on 2 May 2000. Furthermore, the new generation of GPS satellites (GPS III) will not have this feature, meaning that SA cannot be used by the US government anymore [50].

Intentional interference is, in many cases, a significant source of GNSS signal degradation. Intentional interference, known as signal jamming, is caused by the broadcast of malicious radio frequency (RF) signals to prevent GNSS receivers in the area from tracking GNSS signals [51]. The typical direct consequences of jamming are signal frequency shifts in Hertz (Hz) and a drop in signal power in decibels (dB) [34]. These effects, in turn, have the potential to cause severe errors in position, velocity, and time calculations and even completely freeze the receiver causing a denial of service condition [34]. Attacking a GNSS signal through jamming requires neither sophisticated knowledge nor complex equipment: all that is needed is a signal of a higher power in the same frequency to defeat the target signal [52]. These concepts can be summarized by Figure 13 and Figure 14. In the first figure it is possible to observe the availability of satellites in a scenario in which there is no external interference. In the second, on the contrary, it can be seen that, with the introduction of a jamming signal, the visibility of the satellites appears disturbed between the 370 and 400 epoch. The jamming signal lasted for about 1 minute with a power of around -70 dBm and a bandwidth of 10 MHz around the central GPS L1 signal frequency. A slightly higher power jamming signal can completely block signals from all satellites in view [34].

A possible solution to this effect could be the introduction of the military (M-Code) receivers or receivers based on a multi-constellation. Another option is to completely switch to any other available navigation solutions [53].

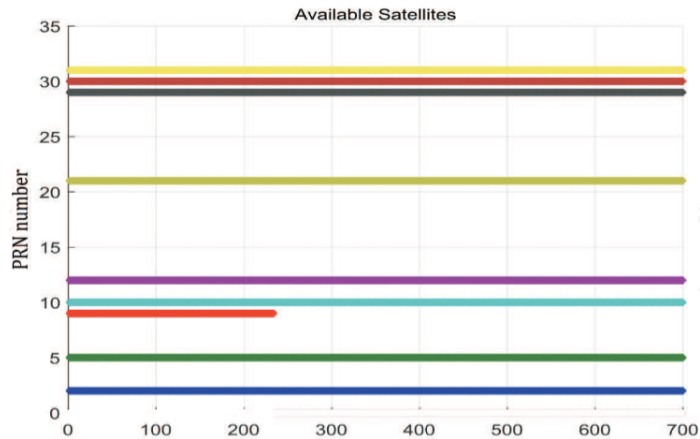


Figure 13: Satellite availability without external interference.

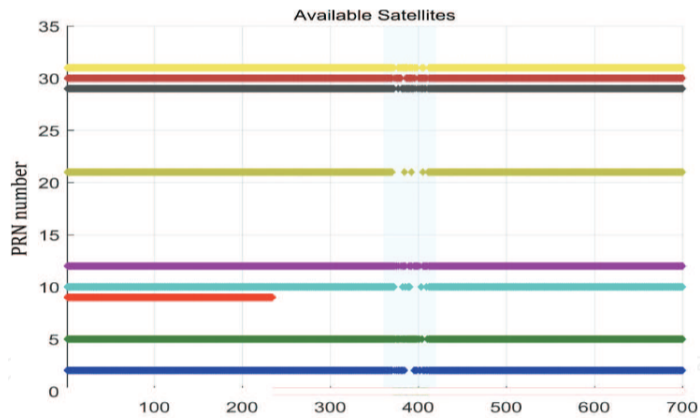


Figure 14: Satellite availability in a jammed scenario.

Among these is the long-range navigation system (Loran-C) which is not active now, but there is a noteworthy argument by the US Department of Defense to reactivate it for its significance as an alternative for GPS-based navigation [34]. Furthermore, a modernized version of the system, known as enhanced Loran (e-Loran-C), has been already established and tested [34]. The main aspect of this system is that the effective power of this signal is thousand times greater than the GPS signal. In addition, since it uses a different frequency range from GPS, it is safe from intentional GPS interference. Another alternative is the satellite-based augmentation systems (SBAS) and ground-based augmentation systems (GBAS), which are approved by the US Federal Aviation System (FAA) [34].

Last intentional error source is the so-called signal spoofing. GNSS signal is the creation of a faked GNSS signal that looks authentic to the GNSS receiver [34]. Signal spoofing is different from the jamming since it can not be directly detected. The receiver can be fooled by the spoofing signal, which in turn affects its navigation solution [34]. Furthermore, using correlation techniques to detect the spoofing is not feasible because the received signal is statistically correlated with the authentic GNSS signal, unlike the signal jamming case [54]. The effect of signal spoofing in degrading the navigation solution can have serious impacts in both military and civilian applications, especially those related to safety-of-life services [34]. Nowadays, plenty of studies are ongoing in order to find robust techniques able to protect systems from spoofing

attacks.

3.3.5 User equivalent error

After applying the appropriate models and the data in the navigation message to mitigate for the errors, one can use the so-called user equivalent range error (UERE) to quantify the total effect of the remaining errors on pseudorange measurements [33]. The metric, defined as the root sum square of the “unintentional” errors discussed above, is used to analyze the accuracy of the GNSS positioning solution under two assumptions [34]. First, the measurement errors for all the satellites are uncorrelated; second, the independent errors are affecting the pseudorange measurement equivalently [29]. It is worth mentioning that the UERE is typically combined with the dilution of precision (DOP) to meaningfully express the expected accuracy of the GNSS positioning solution [34]. The DOP measure is discussed in the next section.

3.3.6 Dilution of precision

The dilution of precision (DOP) is one of the most important measurement parameter for position accuracy. Its main characteristic is that it is totally independent from the cleanliness of measurements. In fact, it depends on the geometry of visible satellites. Practically speaking, a better satellite geometry and lead to a lower DOP factor, and, hence, a better position estimation. To better understand how the concept of DOP is, Figure 15 comes to our aid.

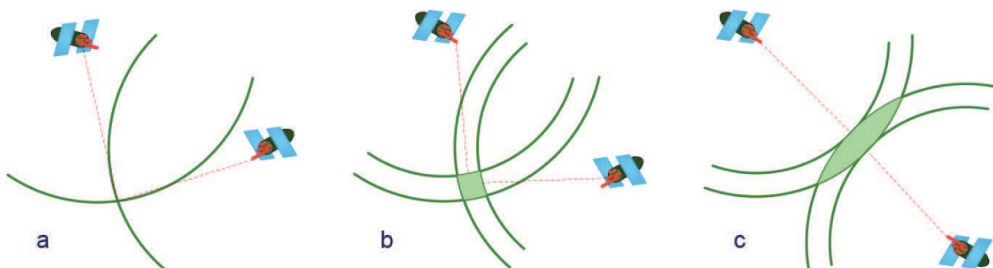


Figure 15: Dilution of precision with range measurements in 2D.

In the first case, Figure 29a, is shown the ideal scenario where signals from two satellites form circles that intersect at the receiver position, considering the receiver in ideal condition, without any error introduction (always false for a GNSS receiver). Figure 29b shows a more realistic case where uncertainty measurement makes the circuits radii ambiguous. The intersection area characterizes the possible region in which receiver could stay. Clearly, different shape of this area can be found as seen in Figure 29c. It mostly depends on the geometry of the available satellites. DOP is used to select which satellites should be included in position calculations [34]. An ideal receiver would select only the set of satellites with the minimum DOP [55]. The DOP number is unitless, and calculating it requires knowing only the receiver and satellites’ positions, i.e., no measurements are needed [29]. Hence, DOP could be computed before the journey to plan for trajectory data collection [33]. DOP or the geometric DOP (GDOP) is the general term to describe the geometry of satellites; however, there are subcategories of this [34]. Horizontal dilution of precision (HDOP), vertical dilution of precision (VDOP), and position dilution of precision (PDOP) are examples, to name a few [34]. Simulation DOP values, using GPS only

constellation, are shown in Figure 16 and 17, respectively, for low latitude (Equator) versus high latitude (North Pole) areas. It can be seen from both figures that DOP values at the Equator are always lower due to better satellite geometry [34]. Moreover, GPS provides better HDOP versus VDOP since it has a better arrangement of satellites and orbits. The accuracy of the obtained/expected GPS solution is expressed as the product of the pseudorange error factor (i.e., UERE) and the geometry factor (i.e., DOP) [51]:

$$Err. \text{ in GPS sol.} = \rho_{err} \times \text{geometry factor} = UERE \times DOP \quad (9)$$

As an example on this, a UERE value of 9 m and an HDOP value of 1.4 will indicate a horizontal position accuracy of 12.6 m at the two-sigma level [34].

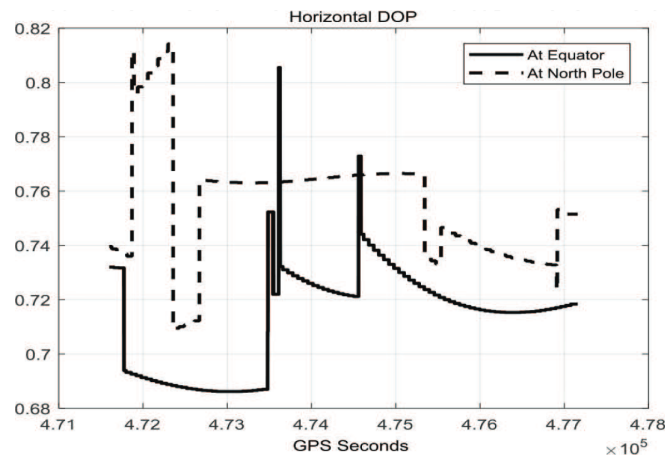


Figure 16: Horizontal DOP value at low vs high latitudes.

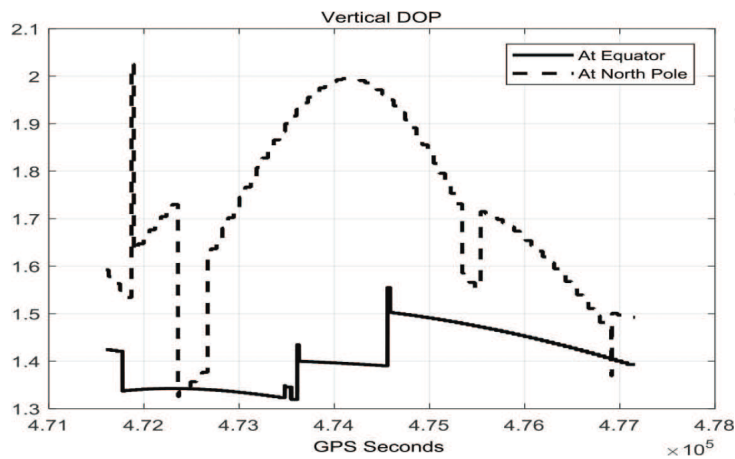


Figure 17: Vertical DOP values at low vs high latitudes.

3.4 Augmentations

Augmentations are available to enhance standalone GNSS performance. These can be space-based such as a geostationary satellite overlay service that provides satellite signals to enhance accuracy, availability and integrity or ground-based as in a network that assists embedded GNSS

receivers in cellular telephones to compute a rapid position fix. The need to provide continuous navigation between the update periods of the GNSS receiver, during periods of shading of the GNSS receiver's antenna, and through periods of interference, is the impetus for integrating GNSS with various additional sensors. The most popular sensors to integrate with GNSS are inertial sensors, but can be also included dopplerometers (Doppler velocity/altimeters), altimeters, speedometers, and odometers, just to provide few name. The most widely used method for this integration is the well-known Kalman filter.

In addition to integration with other sensors, it can also be extremely beneficial to integrate a GNSS sensor within a communications network. For example, many cellular handsets now include embedded GNSS engines to locate the user in the event of emergency, or to support a wide variety of location-based services (LBS). These handsets are often used indoors or in other areas where the GNSS signals are so highly attenuated that demodulation of the GNSS navigation data by the handset takes a long time or is not possible. However, with network assistance, it is possible to track weak GNSS signals and quickly determine the location of the handset. The network can obtain the requisite GNSS navigation data from other GNSS receivers with a clear-sky view or other sources. Further, the network can assist the handset in a number of other ways such as the provision of timing and a coarse position estimate. Such assistance can greatly increase the sensitivity of the GNSS sensor embedded in the handset enabling it to determine position further indoors or in other environments where the GNSS signal is highly attenuated [19].

Some applications, such as precision farming, aircraft precision approach, and harbor navigation, require far more accuracy than that provided by the standalone GNSS. They may also require integrity warning notifications and other data. These applications utilize a technique that dramatically improves standalone system performance, the so-called differential GNSS (DGNSS) [19].

3.4.1 Differential GNSS

DGNSS is a method of improving the positioning or timing performance of GNSS by using one or more reference stations at known locations, each equipped with at least one GNSS receiver to provide accuracy enhancement, integrity or other data to user receivers via a data link (see Figure 18).

There are several types of DGNSS techniques and depending on the application, the user can obtain accuracies ranging from millimeters to decimeters. Some DGNSS systems provide service over a local area (10-100 km) from a single reference station, while others service an entire continent. The European Geostationary Navigation Overlay Service (EGNOS) and Indian GAGAN system are examples of wide area DGNSS services [19].

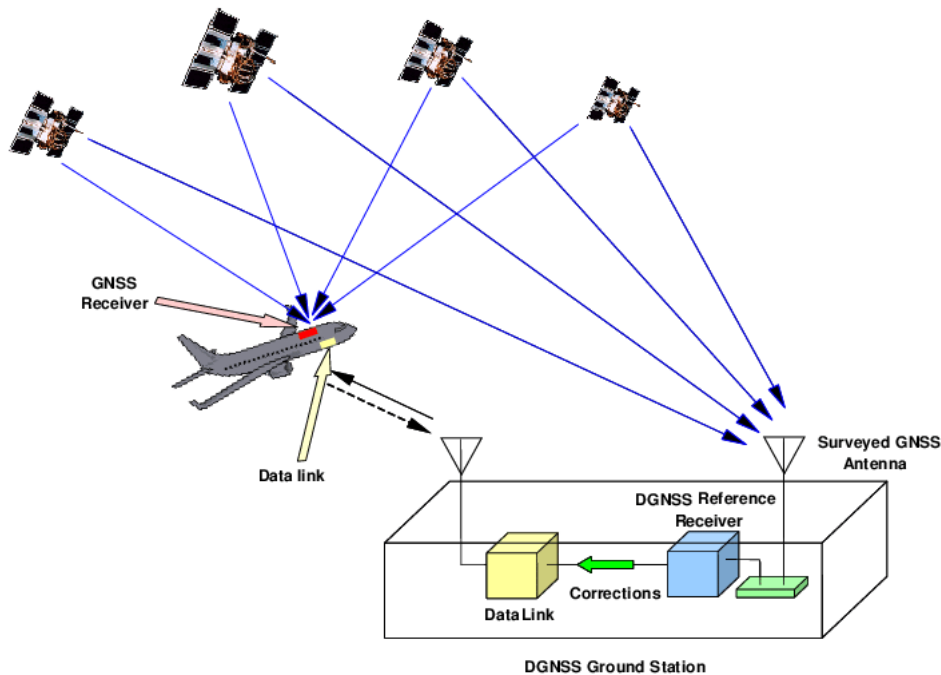


Figure 18: Typical DGNSS system architecture.

DGNSS was developed to meet the needs of positioning and distance-measuring applications that required higher accuracies than stand-alone GNSS could deliver [20]. DGNSS involves the use of a control or reference receiver at a known location to measure the systematic GNSS errors; and, by taking advantage of the spatial correlation of the errors, the errors can then be removed from the measurement taken by moving or remote receivers located in the same general vicinity [20]. There have been a wide variety of implementations described for affecting such a DGNSS system. The intent is to characterise various DGNSS systems and to compare their strengths and weaknesses [20]. Two general categories of DGNSS systems can be identified: those that rely primarily upon the code measurements and those that rely primarily upon the carrier phase measurements [20]. Using carrier phase, high accuracy can be obtained (centimetre level), but the solution suffers from integer ambiguity and cycle slips. Whenever a cycle slip occurs, it must be corrected for, and the integer ambiguity must be re-calculated. The pseudorange solution is more robust but less accurate (2 to 5 m). As it is not affected by cycle slips, there is no need for re-initialisation [20].

The system consists of a Reference Receiver (RR) located at a known location that has been previously surveyed, and one or more DGNSS User Receivers (URs) [20]. The RR antenna, differential correction processing system, and data link equipment (if used) are collectively called the Reference Station (RS). Both the UR and the RR data can be collected and stored for later processing, or sent to the desired location in real time via the data link. DGNSS is based on the principle that receivers in the same vicinity will simultaneously experience common errors on a particular satellite ranging signal. In general, the UR (mobile receiver) uses measurements from the RR to remove the common errors. In order to accomplish this, the UR must simultaneously use a subset or the same set of satellites as the reference station. Various DGNSS techniques are employed depending on the accuracy desired, where the data processing is to be performed,

and whether real-time results are required. If real-time results are required then a data link is also required. For applications without a real-time requirement, the data can be collected and processed later. The accuracy requirements usually dictate which measurements are used and what algorithms are employed. In the case of Differential GPS (DGPS), accuracy is independent of whether SPS or PPS is being used, although real-time PPS DGPS can have a lower data rate than SPS DGPS because the rate of change of the nominal system errors is slower than the rate of change of SA. However, the user and the Reference Station must be using the same service (either PPS or SPS). The clock and frequency biases for a particular satellite will appear the same to all users since these parameters are unaffected by signal propagation or distance from the satellite. The pseudorange and delta-range (Doppler) measurements will be different for different users because they will be at different locations and have different relative velocities compared to the satellite, but the satellite clock and frequency bias will be common error components of those measurements.

As said before, the signal propagation delay is truly a common error for receivers in the same location, but as the distance between receivers' increases, this error gradually de-correlates and becomes independent. The satellite ephemeris has errors in all three dimensions. Therefore, part of the error will appear as a common range error and part will remain a residual ephemeris error. The residual portion is normally small and its impact remains small for similar observation angles to the satellite.

There are two primary variations of the differential measurements and equations. One is based on **ranging-code** measurements and the other is based on **carrier-phase** measurements. There are also several ways to implement the data link function.

Taking everything into account, what are the main advantages in using DGNSS compared to the classic relative positioning? Before listing all pros, it must be declared what is the Standalone, Single Point Positioning or Standard GNSS. Standalone is the standard GNSS practice, also known as Single Point Positioning. While using this method, there are no error corrections made. The GNSS satellites just provide you with the best standard signals available. With this positioning techniques, an accuracy around 1.5 meters is guaranteed. Conversely, Differential GPS/GNSS or DGPS/DGNSS is essentially a system to provide positional corrections to regular GPS/GNSS signals. DGPS uses bases with a fixed known position to adjust realtime GPS signals to eliminate errors. These DGPS corrections improve the accuracy of the Standalone position data. The receiver makes distance measurements in real time to each satellite in use. The difference between the known and measured range for each satellite is the range error. This error is the amount that needs to be removed from each satellite distance measurement. The base-station transmits the range error corrections to the receiver in real-time. The receiver corrects its satellite range measurements using these differential corrections, giving a much more accurate position. Thanks to this technique, receiver provides a horizontal accuracy of maximum 40 centimeters while using DGPS. The advantage of DGPS is that it is useful over a longer baseline and it's usually less expensive than RTK. In addition, DGNSS systems can be designed to serve a limited area from a single reference station, or can use a network of reference stations and special algorithms to extend the validity of the DGNSS technique over a wide area. The result is that there is a large variety of possible DGNSS system implementations using combinations of these design features.

4 GNSS Attitude

GNSS attitude determination is the name given to deriving platform attitude from the GNSS observables [57]. It has existed since the advent of GPS [56] but only in recent times it has become accurate and practical enough for UAV applications. If multiple antennas are positioned around a rigid platform, in this case the UAV, their relative position will be related to the platform's attitude at a given measurement epoch [57].

If two antennas are used they will be capable of providing two dimensions of the attitude, usually heading and roll or pitch [57]. Conversely, if three or more are used, it will be possible to determine all three dimensions of the platform attitude.

In this chapter will be discussed the main procedures and reference frames needed to estimate platform attitude from GNSS observables.

4.1 Reference Frames

Here are presented the main Cartesian reference frames and the existing relationships between them.

4.1.1 The Body Frame

As can be easily understood from the name itself, the body frame is attached to, and moves with, the UAV body. It is defined as an orthogonal cartesian system, having its origin at a certain point on the platform. Axes can be related either relative to the body or to the navigation system.

The body frame (see Figure 19) can be linked to the UAV center of gravity. Practically speaking, the x_b axis points towards the nose of the aircraft, the y_b axis through the right wing and the z_b axis points down forming a right handed system [57].

A second body frame, termed as *sensor frame* (see Figure 20), is affixed to and moves with the platform but is relative defined to the navigation sensors, in particular the antennas used in the GPS attitude system [57]. In systems like that, one antenna works as the "Base" antenna. This antenna defines the sensor frame origin and can be attached on top of the wing (over the gravity center) or on the top of the leftmost wingtip [57]. The y_n axis direction is defined as running from the center of the base antenna through the "Rover" antenna on the rightmost wingtip, while the z_n axis is defined as being normal to the plane which passes through the base and roving antenna with its positive direction down [57]. The right hand orthogonal system is then completed by the x_n axis.

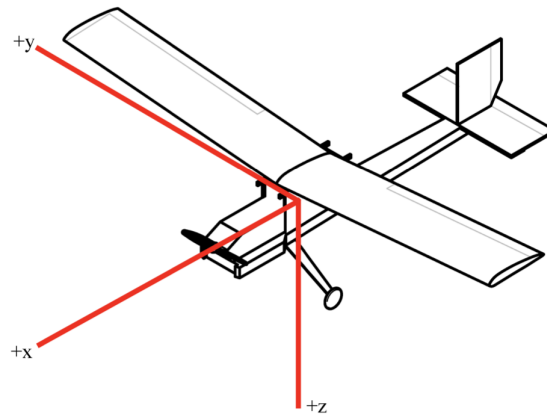


Figure 19: Body Frame of UAV platform.

The transform between body and sensor frame can be achieved using a translation and rotation operation: the translation required will be known as the lever arm, while the rotation is known as the boresight [57]. Since the relationship between the sensor and body frame is constant, the lever arm and boresight are constants which may be obtained by survey of the platform.

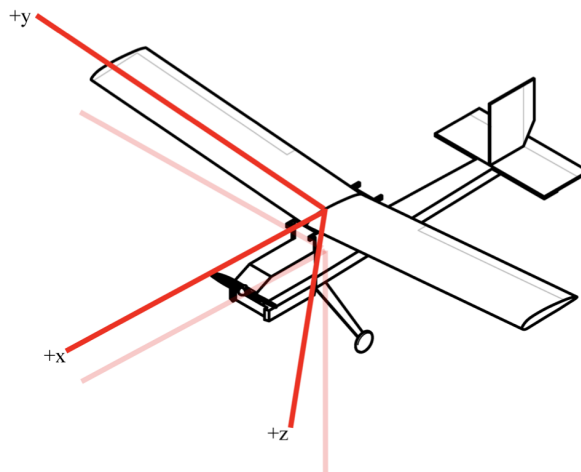


Figure 20: The Sensor Frame, body frame axes are shown as reference [57].

4.1.2 The Local Level Frame

This type of frame takes an important role when talking about the motion and orientation of UAV platform. Local level frame's origin can be fixed in the UAV center of gravity. The y_{ll} axis points the geodetic north and the z_{ll} axis points away from the center of the earth through the center of gravity (up) [57]. The right hand orthogonal system is then completed by the x_{ll} axis, pointing east.

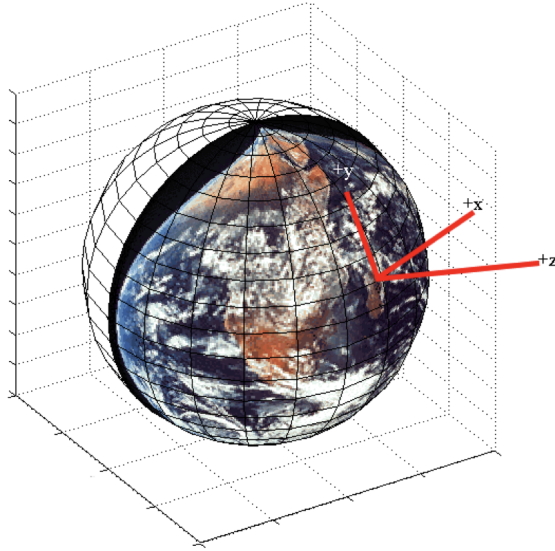


Figure 21: Local Level Frame and its relative orthogonal reference system.

4.1.3 The Earth Center Earth Fixed Frame

The origin of this particular frame is related to the Earth's center of mass. Since it rotates with the Earth at $\sim 7.3 \times 10^{-5} \text{ rads}^{-1}$ of rate, it can not be considered as a true inertial frame. As regard the orthogonal system, the z_e axis runs along the mean rotation axis towards the north celestial pole; the x_e and y_e axes run through the equatorial plane with the x_e axis pointing in the direction of the Greenwich meridian and the y_e axis complete the overall system [57].

Typically, the realisation of the Earth-centered, Earth-fixed coordinate system is done using the WGS84 datum since it is referred to the GPS satellite constellation. There are two ways of representing a position using the WGS84 datum: first, there is the cartesian system using the axis defined above; secondly, a position on an ellipsoid defined in WGS84 may be used [57]. This is the well known latitude and longitude. Adding to this the relative height above the ellipsoid, the position is completely described. Clearly, a mathematical relationship exists between the latitude (ϕ), longitude (λ), height (h) system and the reference system.

4.1.4 Geographic coordinate conversion: rotation transformations

Conversions between reference frames, like the ones discussed above, and geographic coordinates (latitude and longitude) are strictly necessary since different geographic coordinate systems are used across the world and over time. Coordinate conversion is composed of a number of different types of conversion: format change of geographic coordinates, conversion of coordinate systems, or transformation to different geodetic datums.

To transform a vector from the ECEF frame to the local level frame or to pass from local level frame to body frame, a translation and rotation is required. Clearly, there are many ways of representing the rotation between two reference frames. In geometry, various formalisms exist to express a rotation in three dimensions as a mathematical transformation. According to Euler's rotation theorem, a rigid body rotation (or three-dimensional coordinate system with the fixed origin) can be described by a single rotation about some axis. Typically, at least three real parameters are needed to uniquely describe this rotation. Examples of alternatives used for rotation transformations are:

- **Rotation matrix:** transformation matrix used for transformation in Euclidean space. Since we are dealing with latitude, longitude and height, it is clear how it will consist of a 3×3 matrix;
- **Euler axis and angle:** a three rotation process, where the first rotation is around an axis of the reference frame, the second around an intermediate axis and the third around an axis of the rotated frame [57];
- **Quaternions:** a less intuitive rotation transformation based on Euler's rotation theorem. They give big improvements in computational speed and accuracy, despite the singularity inherent in Euler angle system [57].

4.1.5 Attitude estimation from ECEF coordinates

Once possible rotation transformations have been declared, attitude determination can be given. To obtain attitude values from a baseline vector in the ECEF frame, the baseline is first rotated to the local level frame [57]. This is done using mathematical formulas from the rotation matrix approach. The heading, pitch and roll of the sensor frame may now be determined using basic trigonometric functions and the baseline coordinates in the local level frame [57]. This is then corrected to the body frame using the boresight / lever arm calibration [57]. Typically, when rotation matrix is used, latitude and longitude of local frame level are needed and it could be related to the UAV platform gravity center. Clearly, since the estimation of this precise place is always affected by some errors, they will be propagated even to the rotation matrix. The magnitude of this error is dependent on the latitude and longitude of the platform but will not be significant if the position error is kept small [57]. Problems like that can be avoided by obtaining the antenna position using the stand alone GPS positioning technique.

4.2 The choice of baseline length and antenna location

The precision of the attitude parameters, possibly derived from an ambiguity fixed baseline, will change according to the baseline length. Given a baseline precision, the estimation of attitude parameter precision will decrease with baseline length [57]. Therefore, a maximization of attitude parameters precision can be reached by maximizing the physical platform limits. To do that, correct positioning of the antennas must be established. Suitable antenna locations on the UAV include the wingtips, nose and tail [57]. It is not a coincidence that these positions could be chosen. In fact, all of these locations have a high level of sensitivity to weight since they exert a large lever force around the UAV center of gravity [57]. A possible solution of lever forces minimization should be putting the receivers away from the antennas, possibly in the main payload, and as close as possible to the UAV center of gravity.

4.3 Heading angle

Bearing or heading angle is used to define navigation generally in the field of aircraft or marine or Vehicle navigation or while working for land surveying.

Bearing can be defined as direction or an angle, between the north-south line of earth or meridian and the line connecting the target and the reference point. While Heading is an angle or direction where you are currently navigating in. This means to reach a particular destination you need to

adjust your heading direction with the bearing. Generally a 'compass' is an instrument, which gives you the direction information for navigation.

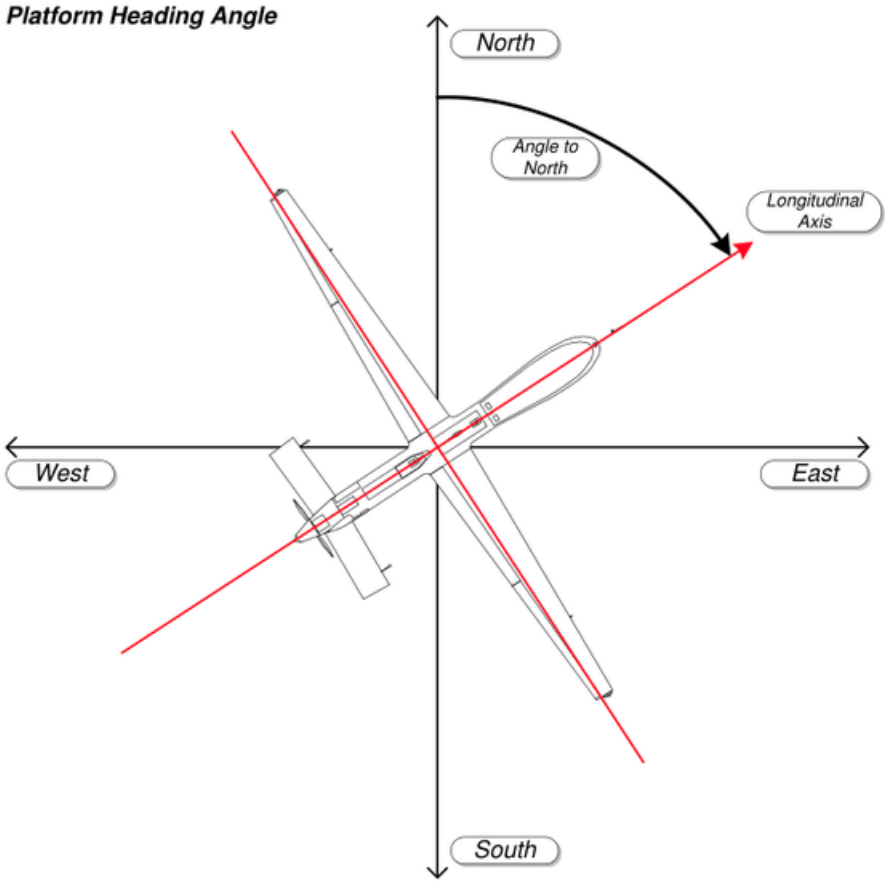


Figure 22: Identification of heading angle in Unmanned Aerial Vehicle platforms.

Figure 22 show how is the heading angle is identified in UAV platforms. As can be seen, it is evaluated as the direction in which the longitudinal axis of an aircraft is pointed, usually expressed in degrees, from North (true, magnetic, compass or grid). Geographic north (also called “true north”) is the direction towards the fixed point we call the North Pole. Conversely, Magnetic north is the direction towards the north magnetic pole, which is a wandering point where the Earth’s magnetic field goes vertically down into the planet. The north magnetic pole is currently about 400km south of the north geographic pole, but can move to about 1,000km away.

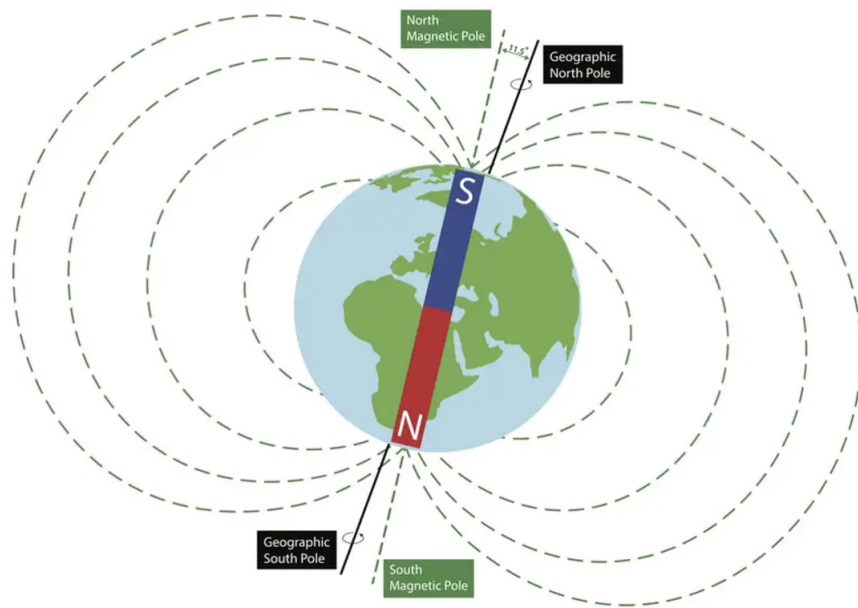


Figure 23: The lines of the Earth's magnetic field come vertically out of the Earth at the south magnetic pole and go vertically down into the Earth at the north magnetic pole.

Magnetic north and geographic north align when the so-called “angle of declination”, the difference between the two norths at a particular location, is 0° .

Declination is the angle in the horizontal plane between magnetic north and geographic north. It changes with time and geographic location. On a map of the Earth, lines along which there is zero declination are called agonic lines. Agonic lines follow variable paths depending on time variation in the Earth's magnetic field. Currently, zero declination is occurring in some parts of Western Australia, and will likely move westward in coming years.

Thanks to "ngdc.noaa.gov" website, it was possible to verify the magnetic declination of Turin by putting the Latitude and Longitude of the city (see Figure 24)



Declination

Date	2021-12-07
Latitude	45° 4' 0" N
Longitude	7° 42' 0" E
Elevation	0.0 km GPS
Model Used	WMM-2020
Declination	2° 49' E changing by 0° 9' E per year
Uncertainty	0° 21'



Compass shows the magnetic bearing of the magnetic north (MN)

Figure 24: Magnetic declination of Turin.

The heading angle can be easily calculated with trigonometric formulas and it can be estimated from both E/N/S coordinates and Latitude and Longitude. Considering the Latitude and Longitude of two points, it is given by the following formulas:

$$\beta = \arctan(X, Y) \quad (10)$$

where, X and Y are two quantities given by:

$$X = \cos\theta_b \cdot \sin\Delta L Y = \cos\theta_a \cdot \sin\theta_b - \sin\theta_a \cdot \cos\theta_b \cdot \cos\Delta L \quad (11)$$

where, ΔL is the difference between Longitudinal coordinates

5 Methods for Antennas Under Test (AUT) calibration

An antenna calibration is a verification of performance and the measurement of the antenna's properties. Antenna calibration is important to ensure repeatable, reliable data and the calibration interval should be set depending on the quality system policy of the organization, conformance to your testing procedures/standard and also on the reliability of the antenna.

All antennas are characterized by a few performance metrics: input impedance, polarization, directivity, gain, radiation efficiency, and the radiation pattern. All but the first property can be measured either on an antenna range or in an anechoic chamber. An anechoic chamber is a room constructed to eliminate all reflections at the frequencies of interest. If tests take place on an antenna range that is not an anechoic chamber, the range must first be analysed for any sources of reflections (for example, from the ground). Then these reflections are eliminated before the test (sometimes easier said than done on outdoor ranges).

The general approach to antenna tests is to put a known transmitter and antenna at a known distance away from the tested antenna. The tested antenna is connected to a known receiver. The magnitude of the transmitter output is known, as is the loss of any cabling. Similarly, the sensitivity of the receiver attached to the antenna under test is also known. The path loss over the distance between the two antennas can be calculated.

The use of anechoic chamber is fundamental to calibrate and characterize antenna's features. As said before, there are lots of information that can be retrieved by analysing the antenna's performance. Typically, **antenna parameters** could be identified by:

- Polarization;
- Input impedance and VSWR;
- Directivity;
- Gain;
- Efficiency;
- Effective Isotropically Radiated Power (EIRP)
- Radiation pattern;
- Antenna Noise Temperature.

Polarization is the property of the electric field vector that defines variation in direction and magnitude with time. If we observe the field in a plane perpendicular to the direction of propagation at a fixed location in space, the end point of the arrow representing the instantaneous electric field magnitude traces a curve. In the general case, this curve is an ellipse (see Figure 25).

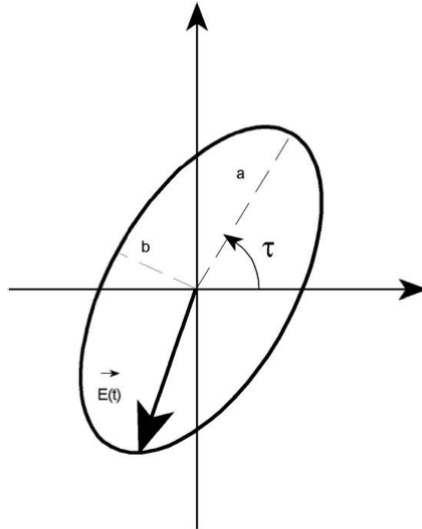


Figure 25: Elliptical polarization.

The ellipse can be characterized by the axial ratio (AR), the ratio of the two major axes and its tilt angle t . Polarization may be classified as linear, circular or elliptical according to the shape of the curve. Linear and circular polarization are special cases of elliptical polarization, when the ellipse becomes a straight line or circle, respectively. Clockwise rotation of the electric field vector is designated as right- hand polarization (RH) and counterclockwise rotation is left-hand polarization (LH), for an observer looking in the direction of propagation.

Input impedance is defined as the impedance presented by the antenna at its terminals or the ratio of the voltage to current at its terminals. If the antenna is not matched to the interconnecting transmission line, a standing wave is induced along the transmission line. The ratio of the maximum voltage to the minimum voltage along the line is called the Voltage Standing Wave Ratio (VSWR).

The directivity is a measure that describes the directional transmitting properties of the antenna. It is defined as the ratio of the antenna radiation intensity in a specific direction in space over the radiation intensity of an isotropic source for the same radiated power. There are cases in which the term directivity is implied to refer to its maximum value.

The gain of the antenna (see Figure 26) is closely related to the directivity, but takes into consideration the losses in the antenna as well as its directional capabilities.

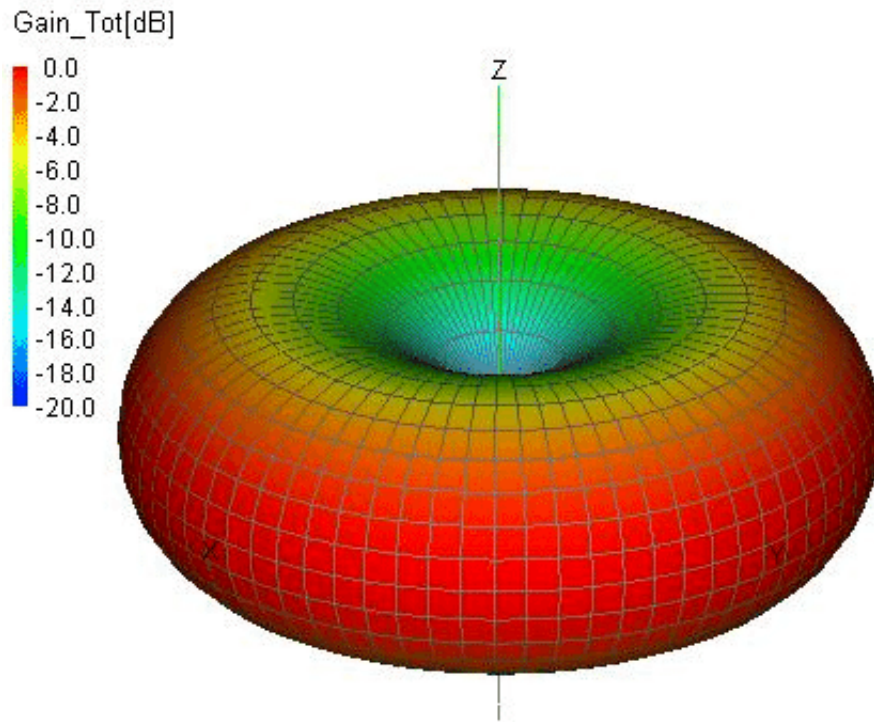


Figure 26: Example of antenna's gain: radiation pattern of a dipole omnidirectional antenna.

The antenna efficiency is the ratio of directivity to gain. It takes into consideration all the power lost before radiation. The losses may be due to mismatch at the input terminals, conduction losses, dielectric losses and spillover losses.

The Effective Isotropically Radiated Power (EIRP) is a figure of merit for the net radiated power in a given direction. It is equal to the product of the net power accepted by the antenna and the antenna gain.

The antenna radiation pattern is the display of the radiation properties of the antenna as a function of the spherical coordinates (θ, Φ) . In most cases, the radiation pattern is determined in the Far-Field region for constant radial distance and frequency. A typical radiation pattern is characterized by a main beam with 3 dB beamwidth and sidelobes at different levels (see Figure 27). The antenna performance is often described in terms of its principal E- and H-plane patterns. For a linearly polarized antenna, the E- and H-planes are defined as the planes containing the direction of maximum radiation and the electric and magnetic field vectors, respectively.

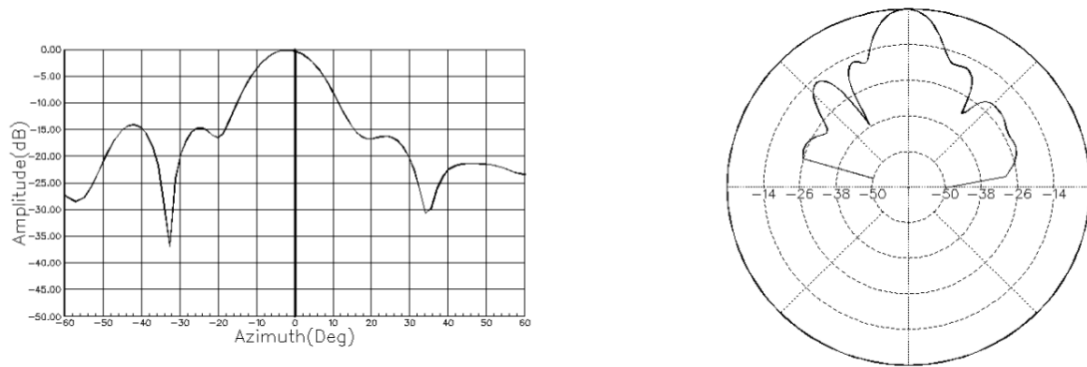


Figure 27: Rectangular and Polar form of radiation patterns.

5.1 Voltage standing wave ratio (VSWR)

With this setup, the amplitude of the signal measured at the receiver will indicate the gain of the antenna under test. The antenna radiation pattern can be determined by placing the antenna under test on a rotating platform and measuring the magnitude of the received signal at increments as the platform rotates.

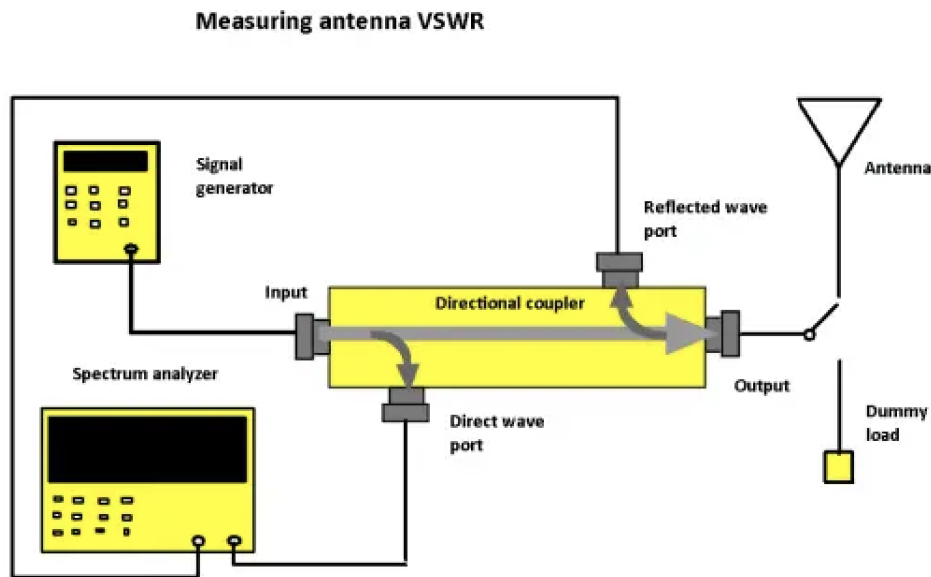


Figure 28: Measuring antenna VSWR.

The antenna noise temperature is a measure that describes the noise power received by the antenna at a given frequency. It can be obtained by integrating the product of the antenna directivity and the brightness temperature distribution of the environment over the entire space. The brightness temperature of the environment is dependent on many noise sources: cosmic, atmospheric, man-made and ground. The noise power received at the antenna terminals is equal to KT_aB in which K is Boltzman coefficient, T_a is the antenna noise temperature and B is the bandwidth of the system receiver. Antenna VSWR (voltage standing wave ratio) is a measure of how much energy sent to the antenna is reflected back. Its measurement usually involves a

directional coupler, signal generator, and the spectrum analyzer mode of an oscilloscope. The signal generator puts out a known signal into the coupler that feeds to the coupler output port. A baseline reading is taken by connecting a dummy load of a known impedance (usually the same impedance as the target impedance of the antenna) to the output. The amplitude of the reflected and direct signals are noted. Then the antenna under test is connected to the output. The difference in the reflected wave amplitude with the antenna attached and the reflected wave during the baseline is the figure of interest. It is usually expressed as a ratio of the input amplitude over the reflected amplitude. A perfectly matched antenna/cable system will have a $VSWR = 1$. Real VSWRs are typically in the 1.1 to 1.2 range.

Finally, there are a few other specialized measurements for more exotic antennas. Active phased arrays, for example, have a transient response that arises when switching between beam directions as well as switching between frequencies. This response is a function of internal antenna interactions such as coupling and VSWR, active circuitry, and components such as phase shifters and attenuators. These sorts of measurements are quite specialized and generally depend on the specifics of the antenna being measured.

5.2 Radiated emission measurement: antenna factor (AF)

Radiated emission measurements are required worldwide as one type of EMI measurement to demonstrate product compliance with regulatory requirements. In addition, such measurements are very often performed to evaluate prototypes of products, subassemblies or design changes during the product design phase with the goal to achieve compliance before products are marketed.

In either situation a receiving antenna as a transducer of the measurement system is used to measure the electric or magnetic field strength at a certain distance from the equipment under test (EUT) and using a defined test procedure. For compliance testing such antennas must meet certain specifications as well as calibration requirements. Whereas the antenna types to be used are obvious to most EMI test laboratories the calibration requirements are known to a much lesser degree and are often felt to be difficult to determine. The situation is compounded further by the complexity of applicable antenna calibration standards and the interaction between the test laboratory and the antenna calibration laboratory.

The very basic measurement system for radiated emission measurements consists of an antenna, a cable which connects the antenna to the measuring instrument and the measuring instrument itself, as shown conceptually in Figure 29.

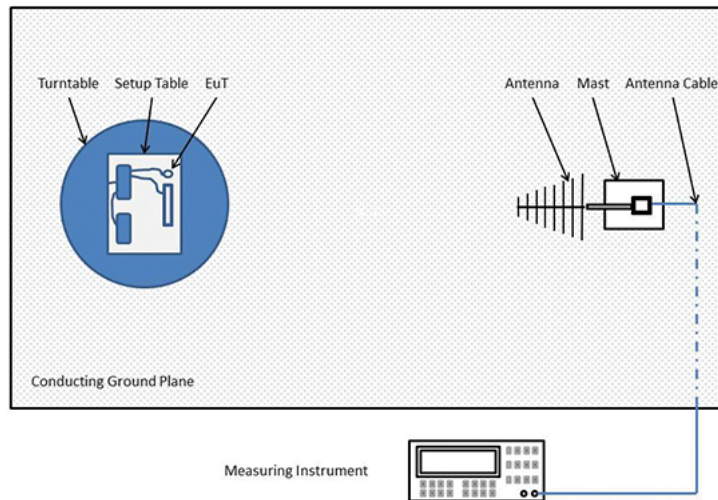


Figure 29: Measuring antenna VSWR.

This setup is used for measurements of the electric field strength of an EUT in the frequency range 30 MHz to 1 GHz in accordance with commercial EMI standards. These standards also require that measurements are to be performed over a conducting ground plane. The actual test environment, which the ground plane is a part of, can be an Open Area Test Site (OATS), a weather-protected OATS or a semi-anechoic chamber. Any test environment chosen for such measurements must be validated by determining its Normalized Site Attenuation (NSA) values in the measurement axis that is used for EUT measurements. A test site yielding NSA values of less or equal to ± 4 dB (relative to the theoretical normalized site attenuation for an ideal site) in the frequency range 30 MHz to 1 GHz is deemed suitable to conduct radiated emission measurements.

The NSA determination must follow a specified procedure and setup which involves the use of two antennas. Furthermore, CISPR 16-1-4 Amendment 1 (2012) offers a second test site validation method: the Reference Site Method (RSM). This method accounts for mutual coupling of the antennas, antenna radiation patterns and near field effects, which can have a significant influence at a 3 m test distances. Since this site validation method does not rely on the use of antenna factors to determine the test site performance the method is inherently more accurate than the NSA method.

In addition to requirements for the test environment specifications do exist for the measuring instrument which can be an EMI receiver or spectrum analyzer as well as the antennas. These specifications must be met for instruments and antennas to be used in radiated emission measurements.

5.2.1 Definition and use of Antenna factors

The purpose of radiated emission measurements is the determination of the electric or magnetic field strength arriving at the receiving antenna at a certain distance from the EUT and based on a defined measurement process. As shown in Figure 29 an antenna is connected to a measuring instrument (i.e., EMI receiver or spectrum analyzer) with a coaxial cable. The mea-

measuring instrument measures voltages frequency-selectively but does not measure field strength directly. However, these measured voltages are directly related to the field strength and hence must be converted to field strength values since the applicable limits in the standards the EUT is tested to are given in units of field strength. Common field strength units are: V/m (or dB μ V/m) for electric field strength and A/m (or dB μ A/m) for magnetic field strength. The relationship of the incident plane wave that illuminates the antenna (this describes the far field condition) in the direction of the antenna's polarization E_R or H_R to the received voltage V_R is described by the antenna factor (AF).

The antenna factor of a well-designed and well-built antenna should not change provided the antenna is handled with care. If repeat calibrations show that the antenna factor does not deviate by more than the uncertainty of measurement, the calibration interval can be extended. Calibration laboratories can suggest intervals but, in most cases, they are not familiar with the details of the antenna or its application.

The antenna factor is defined as follows:

- for electric field strength:

$$AF_{electric} = \frac{E_R}{V_R} [1/m] \quad (12)$$

- for magnetic field strength:

$$AF_{magnetic} = \frac{H_R}{V_R} [S/m] \quad (13)$$

If the antenna factor AF is known and the voltage V_R is measured and displayed, then the measured value of the electric field strength at the antenna is:

$$E_R [V/m] = AF_{electric} [1/m] * V_R [V] \quad (14)$$

or in logarithmic terms:

$$E_R [dBV/m] = AF_{electric} [dB/m] + V_R [dBV] \quad (15)$$

The magnetic field strength can be determined in a similar way:

$$E_R [A/m] = AF_{magnetic} [S/m] * V_R [V] \quad (16)$$

or in logarithmic terms:

$$E_R [dBA/m] = AF_{magnetic} [dBS/m] + V_R [dBV] \quad (17)$$

It is clear from these equations that the accurate knowledge of the antenna factor AF is essential to the accurate determination of the electric or magnetic field strength.

The antenna factor includes balun losses, mismatches between the antenna elements and the balun, the balun and the matching network as well as the electric length (also referred to as the effective height) of the antenna. Usually the insertion loss of the cable connecting the antenna to the measuring instrument is not included in the antenna factor. Therefore the cable loss L_{cable} (as well as the gain of a preamplifier or the attenuation of an attenuator, if used) needs to be taken into account separately when calculating the field strength. In this case the electric field strength is calculated (in logarithmic terms) as:

$$E_R [dBA/m] = AF_{electric} [dBS/m] + V_R [dBV] + L_{cable} [dB] \quad (18)$$

It should be noted that the antenna factor is also affected by mutual coupling to its surroundings, for example the proximity of other antennas and buildings. Furthermore, the antenna factor also depends on the angle of incidence of the field arriving at the antenna as well as the antenna impedance which is constant in free space. However, when performing emission measurements over a conducting ground plane the antenna impedance is affected by the antenna's proximity to the ground plane as well as the orientation relative to the ground plane. The proximity and the orientation (i.e., polarization) are changed due to the required measurement process: For radiated emission measurements, for example, an antenna height variation between 1 m and 4 m is to be performed for both horizontal and vertical polarization which directly influences the antenna factor.

The antenna factors used in EMI measurements to calculate the field strength are defined as free-space antenna factors which are single values at each frequency, independent of the antenna height, polarization and the distance to the EUT. The free-space antenna factor was chosen as the best compromise since the antenna factor varies quasi-periodically around the free-space antenna factor during a height scan. The effects of the antenna height, polarization and the distance to the EUT are included in the measurement uncertainty estimate for radiated emission measurements.

5.2.2 Antenna gain

The gain of an antenna (in any given direction) is defined as the ratio of the power gain in a given direction to the power gain of a reference antenna in the same direction. It is common to use an isotropic radiator as the reference antenna in this definition. An isotropic radiator is assumed to be lossless and radiates its energy equally in all directions. This means that the gain of an isotropic radiator is $G = 1$ (or 0 dB). It is customary to use the unit dBi (decibels relative to an isotropic radiator) for gain compared to an isotropic radiator. Gain expressed in dBi is computed as follows:

$$G[dBi] = 10 * \log\left(\frac{G_{numeric}}{G_{isotropic}}\right) = 10 * \log(G_{numeric}) \quad (19)$$

The numeric gain $G_{numeric}$ is the linear representation of power gain.

Sometimes, a theoretical dipole is used as the reference, so the unit dBd (decibels relative to a dipole) will be used to describe the gain compared to a dipole. This unit tends to be used when referring to the gain of omnidirectional antennas of higher gain. In the case of these higher gain omnidirectional antennas, their gain in dBd would be an expression of their gain above 2.2 dBi. Therefore, if an antenna has a gain of 5 dBd it represents a gain of 7.2 dBi. It is to be noted that in case a single number is stated for the gain of an antenna, it is assumed that this is the maximum gain (the gain in the direction of the maximum radiation).

The antenna factor AF and the antenna gain can be related to each other using the following relationship (in linear terms):

$$AF = \frac{9.73}{\lambda * \sqrt{G}} \quad (20)$$

with G being the numeric gain of the antenna with respect to an isotropic radiator and λ being the wavelength.

This simplified equation is only applicable if the antenna is lossless, has an impedance of 50 Ω and is used in a 50 Ω system in the far field. If any one of these assumptions does not apply then more complex equations must be used to relate the antenna factor to the gain.

Antenna gain is required for example when performing substitution measurements to determine the effective radiated power of an EUT.

Once both antenna factor and antenna gain have been described, it is possible to concentrate the treatment to the real antenna calibration.

5.2.3 Antenna calibration

The accuracy of the antenna factor directly affects the measurement uncertainty of radiated emission measurements. In order to preserve accuracy and traceability of measurement results antennas are periodically calibrated. Commonly used standards for the calibration of EMI antennas are ANSI C63.5, SAE ARP 958 and CISPR 16-1-6.

An EMI test laboratory must define the calibration requirements for all test equipment, including the requirements for antenna calibration. In order to request the proper calibration service the EMI test laboratory should first consider the following.

First of all, the EMI standards used to perform radiated emission measurements on products often call out antenna calibration requirements (e.g., ANSI C63.4:2014, 4.5.1 or EN 55025, 6.4.2.1) which are mandatory and must be complied with. If an antenna were to be used for radiated emission measurements in accordance with different standards like CFR 47 Part 15 using ANSI C63.4:2014 and EN 55025 the same antenna may have to be calibrated in two different ways which will result in different antenna factors.

ANSI C63.5:2006 includes two main methods for the calibration of antennas in the frequency range 30 MHz to 40 GHz. In principle, either of the two calibration methods can be chosen by the test laboratory. However, there are significant differences between the two methods and the antenna factors derived with these methods have a different meaning.

One method, called Reference Antenna Method (RAM), is suitable for the calibration of antennas used for radiated emission measurements in the frequency range 30 MHz to 1 GHz. This method is a substitution method that tends to yield larger uncertainties since the requirements for the antenna calibration site are less stringent and the uncertainty of the reference antenna directly impacts the uncertainty of the antenna factors of the antenna under calibration. This antenna factor is essentially a height dependent factor but due to the required calibration height (minimum 2.5 m) and required horizontal polarization the influence of the conducting ground plane is reduced. RAM requires less effort during the calibration process than the second method in ANSI C63.5:006, the Standard Site Method (SSM).

SSM does require an antenna calibration site of a defined quality which is specified in ANSI C63.5:2006. The method can be used in the frequency range 30 MHz to 40 GHz and does not rely on the availability of a suitable reference antenna. A set of three antennas is required for the basic method to determine the individual antenna factors of each of these three antennas. Since SSM involves an antenna height scan between 1m and 4 m which means the antennas are calibrated a way similar to their use during product measurements. SSM tends to yield lower antenna factor uncertainties.

In addition, per ANSI C63.5:2006 Annex G, a correction factor must be applied to antenna factors of biconical antennas that were determined using SSM. If the antenna meets certain size requirements of the standard and the balun of the biconical antenna is 50 Ω or 200 Ω such numerical corrections must be performed. The correction factor is to be applied to obtain the free-space antenna factor for a biconical antenna in the frequency range 30 MHz to 200 MHz. This correction only applies to biconical antennas that do meet the aforementioned criteria related to size and balun impedance. For other antennas like log-periodic antennas no

correction is available in the standard and the antenna factor of SSM is to be used for product measurements.

Secondly, if an antenna is also to be used for NSA measurements for the purpose of site validation in the frequency range 30 MHz to 1 GHz then additional requirements are to be observed. ANSI C63.5:2006 is cited in ANSI C63.4:2014 as the only permissible antenna calibration standard which in turn includes requirements for antennas used for NSA measurements.

For other antenna types like log-periodic antennas, no correction for an antenna pair is available in the standard. For such antennas a measurement process is defined in Annex H to determine the Geometry-Specific Correction Factor (GSCF). The calibration laboratory will have to perform such measurements with the antenna pair that is used by the EMI test laboratory to perform NSA measurements. This means that the test laboratory must submit both antennas to the calibration laboratory since the GSCF is applicable to the antenna pair only. ANSI C63.5:2006 provides an equation how the GSCF is to be combined with the antenna factors. It is important to note that the GSCF is only applicable to NSA measurements. When one log-periodic antenna out of the pair is used for product testing, then the GSCF is not to be applied and the antenna factor for the individual antenna, derived by SSM, has to be used.

Thirdly, the number of frequencies the antenna factor has to be determined since it has a direct impact on the measurement uncertainty of the emission measurement, related to the interpolation error. In general, the larger the number of frequency points the smaller the error contribution due to interpolation. Of course the actual error magnitude also depends on the antenna factor characteristics versus frequency. If the antenna factor is fairly constant or linear with frequency, then fewer points are sufficient. If there are rapid changes of the antenna factor over small frequency segments then more points should be used to avoid larger interpolation errors. The number of frequency points is also affected by array size for the correction factors in the test automation software.

Finally, different antenna calibration procedures yield different uncertainties of the resultant antenna factors. The consideration of the antenna factor uncertainty is important when a test laboratory is required to calculate and report (and sometimes even apply) the uncertainty of radiated emission measurements. The uncertainty of the antenna factor is a key contributor to the uncertainty calculation and lower antenna factor uncertainties do improve the overall uncertainty of the emission measurement. Antenna factor uncertainty is also significant when validating radiated emission test sites using NSA measurements. The test site must meet an acceptance criterion (calculated NSA $\leq \pm 4$ dB). The calculation of the NSA values requires the use of the antenna factors of both the transmit and receiving antenna. Larger uncertainty values of the calibration process may lead to a test site failing the criterion – not due to site imperfections but due to uncertainties related to the antenna factors.

5.3 Phase center corrections

The GNSS receiver antenna is the connecting unit between the GNSS satellite and the GNSS receiver which transform the incoming signal from satellites into an electrical signal that can be treated by the receiver. The GNSS signal is received at a point called Antenna Phase Center (APC) but this point is not identical with the antenna physical center [21]. Therefore, it is necessary to calculate a mean position of the electric antenna phase center (MPC) for the offset calibration (as can be seen from Figure 30)

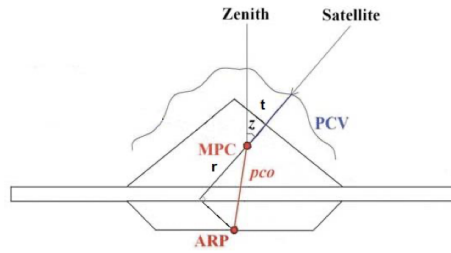


Figure 30: Diagram of locations of the GNSS antenna phase center variations.

The point used by the receiver manufacturer to measure the vertical antenna height is called antenna phase reference point (ARP) [22; 23; 24]. These are produced from the junction of the symmetrical vertical axis of the antenna with the bottom of the antenna. Hence, the antenna phase center offset (PCO) is estimated as the difference between the ARP and the MPC [25; 26]. Deviations that arise as a result of comparing the electricity of an individual measurement with the mean electrical antenna phase center are called the antenna phase center variations (PCV) (see Figure 31). There are three offset components (east, north and up).

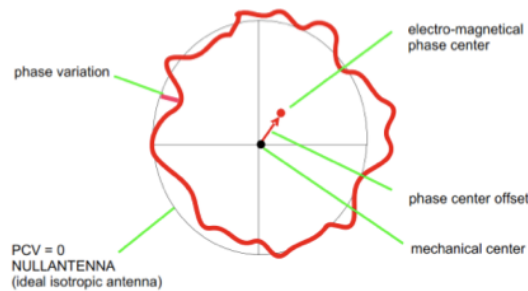


Figure 31: Variations and offset of antenna phase center (PCV).

Different studies were done on the evaluation of phase center variations of antennas. During the 2003, Schmid and Rothacher used the GPS data to estimate PCV of GPS satellite antennas using two methods. First estimations have between the satellite of the same block and second estimations have two different satellite antenna for Block IIR and for Block II/IIA. They collected the data used for more than 100 IGS stations for the days (14 to 19 July) of the year 2002.

In 2014, the researcher Dawidowicz studied the influence of the different calibration models on the height differences in GPS/GLONASS observations processing. He used three types of calibration models (absolute, relative, absolute converted) for receiver antennas and two types of calibration models (absolute and standard) for satellite antennas. He used data collected at three points on one day 24 hour observation sessions (on 20 November) of the year 2012. For this study he used two types of antenna (JAVAD RINGANT G3T and *TPSHIPER – PLUS*). In 2013, researcher EL-Hattab used data collected from static and kinematic field experiments to evaluate the effect of using the manufacturer's recommended antenna phase offset. The baseline length was limited (in range of 27 m - 70 m). He treated this data using two types of commercial software (LGO and TBC) using the manufacturer's recommended PCO and ignore the effect of PCV. His results showed that the height component of the PCO is larger than horizontal components. The height component and north component were about 8 and 4 cm in the maximum variations. Moreover, results showed that the mean phase center offsets and

phase and amplitude patterns for L1, L2 express the GNSS antenna phase center were shifted. On one hand, it is clear that the PCO plus the azimuth and elevation dependent PCV are affecting the total antenna phase center correction for an individual phase measurement [27]. On the other hand, to determine the antenna phase center variation for GNSS receiver antennas there are three ways:

- **Relative field calibration:** the antenna offsets and phase center variations are calculated with respect to a reference antenna (AOAD/M-T antenna);
- **Absolute field calibrations:** the antenna phase center variations were obtained by using a high precision robot which tilts and rotates the antenna while the reference antenna remains fixed;
- **Anechoic chamber measurements:** obtained by placing the robot which rotates and tilts in an anechoic chamber.

The most challenging thing is that some GNSS users ignore the effect of the antenna phase center variation (PCV) and others take the effect of the antenna phase center variation into account using calibration results or by estimating the antenna phase center.

What we have just seen explains how much the calibration of antennas is a subject that has been somewhat studied by university researchers. Precisely for this reason, this paper aims to investigate this issue and find possible methods for the characterization of signal receivers.

5.4 Anechoic chamber overview

All measurements are influenced by outside interferences (every electromagnetic wave radiated in space with sufficient energy or objects in area for measurements). Electromagnetic waves are reflected from object to all direction and cause interferences with measured waves. Ideal area for measurements must be completely shielded from outer influences and completely anechoic. As a consequence, this means there is no reflection of waves from walls, floor and ceil. Since antenna system receives only waves radiated from source it is clear how an ideal area does not exist. Therefore a room for measurements called anechoic chamber was invented.

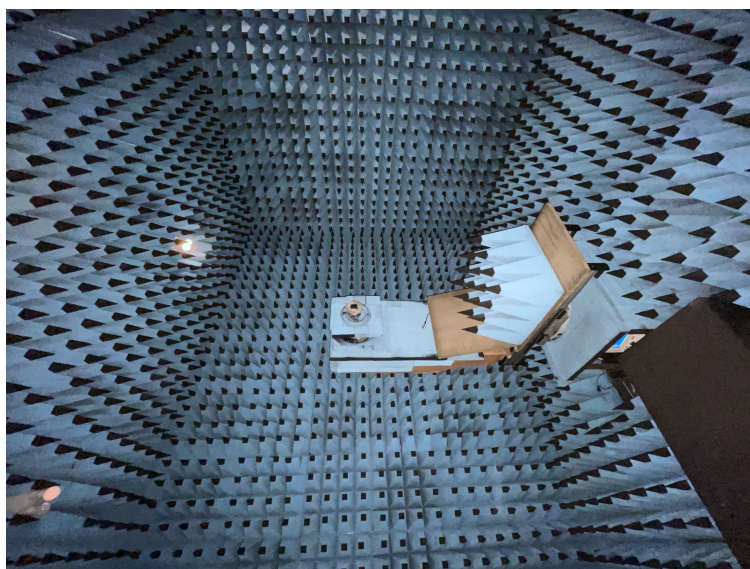


Figure 32: Anechoic chamber of "Politecnico di Torino".

Anechoic chamber (see Figure 32) creates space similar to ideal area. There is only a small reflection from walls and interior is partially shielded from outside interferences. Equipment for measurements (spectrum analysers, oscilloscopes, signal generators, PC, vector network analysers etc.) are placed outside this chamber. Since this room is full of specialized tools, common anechoic chambers are very expensive and of complex construction. In general, there are two common types of anechoic chambers based on operating frequency range. First types are acoustic chambers. They attenuate a mechanical wave – acoustic wave. Frequency range is around 10Hz - 30kHz. Second types are anechoic chambers for radio signal purposes. Constructions of acoustic chambers are very similar to RF chambers, but not the same at all. They are similar only from outside look. They use absorber as RF chambers but from totally different materials, dimensions and shapes. Uses for radio frequency anechoic chambers are:

- Antenna diagrams measurements;
- Measurements of influences object to antenna system;
- Electromagnetic compatibility measurements;
- Measurements antenna close and far field;
- Reflection and through loss of radio wave from different materials and objects;
- Output power measurements;
- Influences of electromagnetic radiation to cable path;
- Immunity for radio waves measurements

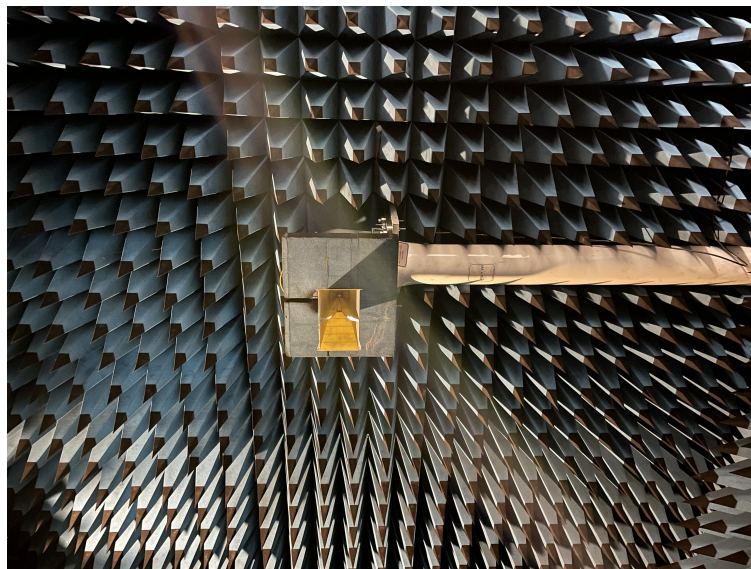


Figure 33: Probe antenna: this antenna is used for the far-field characterization of radiation pattern.

These types of measurements demand precision laboratory devices since a very small energy of waves must be detected. Very high level of isolation from outer space is needed in this case. Anechoic chambers create a space with defined characteristics and these characteristics should

be similar as free space characteristics. Free space has impedance of 377Ω and free space can be thought as a very extensive meadow with no trees, no shrubs and no objects. In the middle of meadow is our measurements stand. Radiated waves from stand are spread around meadow without reflection.

5.5 Theory behind the anechoic chamber

To better understand the functioning of such particular room, we can consider the following example.

Suppose a plane wave, radiated from a source, hits the wall. In this case we know that the free space impedance is about 377Ω . To describe the theory behind the operating principle of the anechoic chamber we need the theory of line transmission. In this circuit (see Figure 34 there is no power consumption at the load, but the whole power is reflected back to the source. However, if the wall is packed with some material, a load for radiated waves is obtained. The transmission line will be ended with an impedance of this packing material.

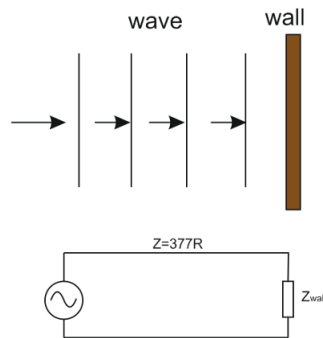


Figure 34: Equivalent circuit of plane wave radiated throughout the free space.

To demonstrate these types of materials, it was used the Salisbury screen. Salisbury screen was a way of reducing the reflection of radio waves from a surface. It was one of the first concepts in radar absorbent material, an aspect of "stealth technology", used to prevent enemy radar detection of military vehicles. Salisbury screen is typically a sheet of paper coated with a material having 377Ω as surface resistivity. This material is exactly placed a quarter of wavelength from the wall. Its main goal is to create an anechoic effect and avoid the signal reflection form the wall. The only problem with this particular material is that it is thought for just one tuned frequency. For other frequencies or different frequency ranges, it does not work at all. The only way to achieve a frequency range response is to use Salisbury sheets of different resistivity values, always put with a distance between the sheet of $\frac{\lambda}{4}$. When circuits are built following the previous details, it is possible to reduce the reflection coefficient from 1 to less than 0.1. This will result in more than 20dB loss of energy and an increment of frequency range from 1 to 2.5 multiple of wavelength is sensed.

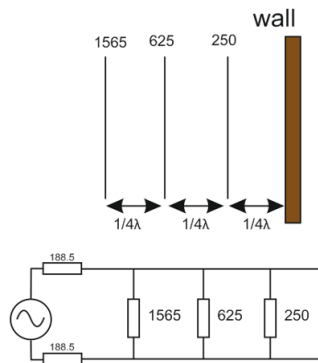


Figure 35: Equivalent circuit containing the Salisbury screen.

Figure 35 shows what has just been described. Another solution is the Jaumann sandwich. Here both the resistances and the distances from the metal wall are tapered (see Figure 36). The Jaumann Sandwich can achieve a 20dB reduction in reflection over a 5:1 bandwidth.

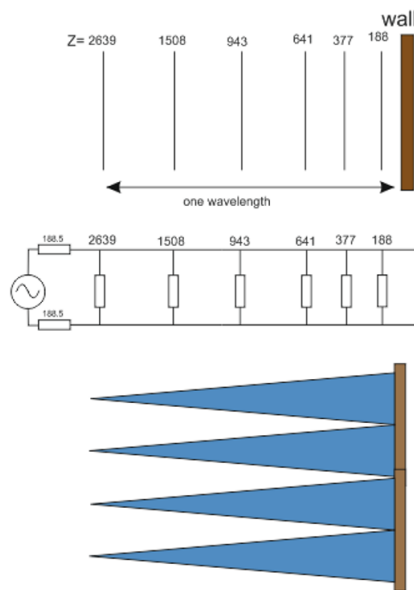


Figure 36: The Jaumann Sandwich uses a staggered array of resistive sheets and reportedly achieves a 20 dB reduction in reflected signal over a 5:1 bandwidth.

Clearly, a modern implementation of these techniques can be found. In fact, pyramidal absorbers perform a role similar to the tapered resistances of the Jaumann Sandwich. A bunch of small reflections are created as the electromagnetic wave passes into the pyramid and these reflections are slowly cancelled. However, in order to reach the most effective result, pyramids must be at least a half wavelength long at the lowest frequency of interest. Since the wavelength of the radio frequency signal is shorter than the free space as it goes through the pyramidal absorber material, the size of the pyramid, necessary to achieve this effect, is

mitigated. It is typically reduced by a factor of:

$$\lambda_r = \frac{1}{\sqrt{\epsilon_r}} \quad (21)$$

where, the term λ_r represents the wavelength in media (within the absorber) and ϵ_r the permittivity relative to free space.

For frequencies under the 100 MHz threshold, very large dimensions of absorbers are got. Therefore, using another absorbing material would be a better choice. One of the best choice we can made is certainly the ferrite. In the last 20 years, ferrite tiles have become widely used as an absorbing mechanism. The fundamental aspect of this material is its impedance, that is close to 377 Ohms. This can be accomplished by making sure the ratio of the permeability to permittivity equal to that of free space:

$$Z = \sqrt{\frac{\mu}{\epsilon}} \quad (22)$$

$$Z_{free\ space} = \sqrt{\frac{\mu_0}{\epsilon_0}} = 377\Omega \quad (23)$$

$$Z_{in\ media} = \sqrt{\frac{\mu_r}{\epsilon_r}} \quad (24)$$

As can be seen from Equation 13, the ratio between μ_r and ϵ_r is equal to 377 Ω .

Moreover, the ferrite is considered as a lossy material since both permeability and permittivity are complex and it can be seen throughout the following formula:

$$\mu_r = \epsilon_r = 60(2 - j1) \quad (25)$$

And this will result in a characteristic impedance value:

$$Z = 377\sqrt{\frac{\mu_r}{\epsilon_r}} = 377\Omega \quad (26)$$

For 100MHz of frequency and 1cm depth of ferrite sheet, the loss can be evaluated as:

$$Loss = e^{ad} = e^{-\left(\frac{120\pi}{\lambda}\right)(.01)} = e^{-1.26} = .28 = 11dB \quad (27)$$

This means, waves passing through ferrite sheet will have 11dB less energy as incoming waves. Thanks to a combination of ferrite sheet and pyramidal absorbers we can obtain anechoic chambers with large frequency range.

5.6 Types of RF absorbers

Before the design phase of an anechoic chamber, an important step is choosing the absorbing materials. This is due to the fact that such materials must absorb as much signal as possible from the reflection surface. The most used RF absorbers can be classified as follows:

1. Ferrite plate
2. Microwave pyramidal absorber

3. Hybrid absorber

Microwave pyramidal absorbers usually works in the range of 80 MHz to 200MHz. Typically, it has a blue foam and it is a mix of polyurethane and carbon. The size of pyramid is proportional to electric parameters.



Figure 37: Respectively: ferrite absorber, foam absorber and hybrid absorber.

These types of materials can still be found in some chambers where electromagnetic compatibility measurements are performed. The length of pyramidal absorbers is over than 2.4cm, allowing to reach an absorption and reflection value lower than 30MHz. Despite their features, they are significantly find in chambers designed for satellite and antennas tests, where a high-working frequency range is reached (from 500MHz to 40GHz).

Ferrite plates are non-linear absorption material: plates with a thickness of 5-7mm can maintain great absorbing properties despite its height. Typically they stop absorbing around 1.5GHz frequency. A well-known issue is that using ferrite plates increases both cost and payload of the anechoic chamber, leading to add some additional supports.

Hybrid absorbers, instead, are built combining both technologies. It has to be thought not as a combination of blue foam glued on ferrite walls, since it will eliminate the ferrite function. The basic principle behind this material is that when a signal passes throughout the material, it spreads with a different impedance compared to the open space one. Once the wave hits the ferrite plate with a different impedance from the absorber, it is reflected by the ferrite instead of passing through it, therefore making the ferrite inefficient. A solution to this problem is adding carbon or by making hollow pyramids.

5.7 Experimental setup

The antennas were characterized following the principles expressed above. In particular, the measurements were carried out in far-field, using the probe antenna shown in Figure 33. The probe antenna rotates along the azimuth and zenith plane while the antenna under test moves only along the azimuth plane. The scan of the signal describes diameters and, from a linear polarization, it passes to a circular polarization by combining the module and phase of the antenna.

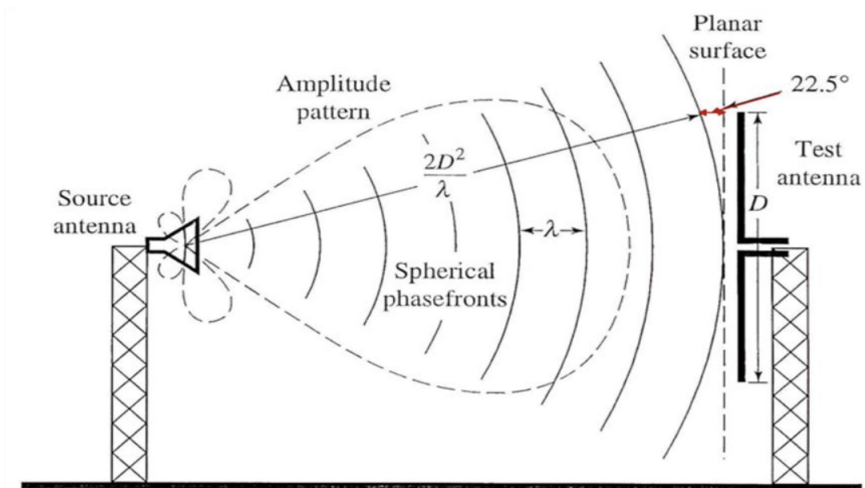


Figure 38: Schematic representation of AUT characterization.

Figure 38 shows how the signal is radiated by the probe antenna. As regard the setup, both antennas were fixed to a ground plane in order to obtain measurements as precise as possible. Figure 39 and 40 show the omnidirectional and patch setup.

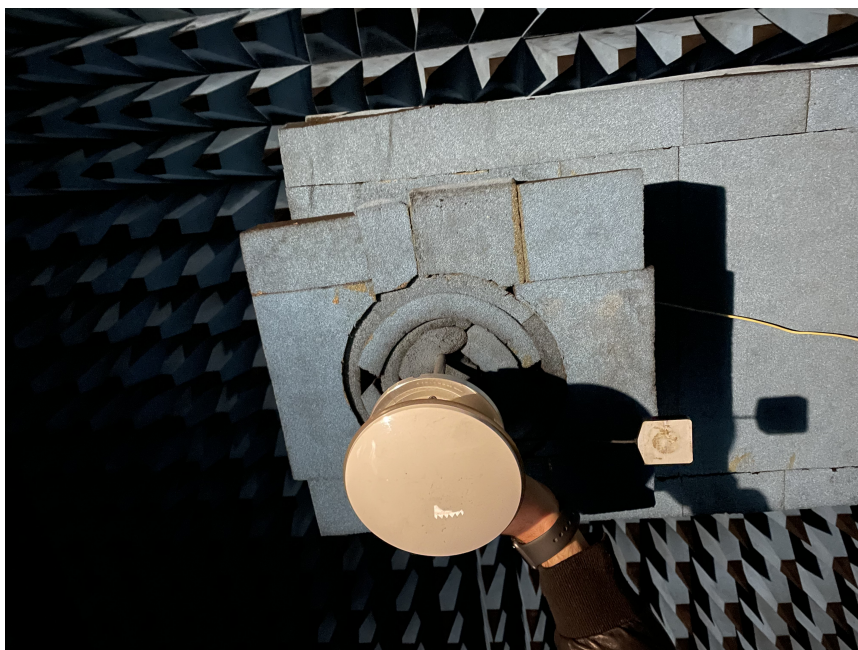


Figure 39: Geodetic antenna's setup.

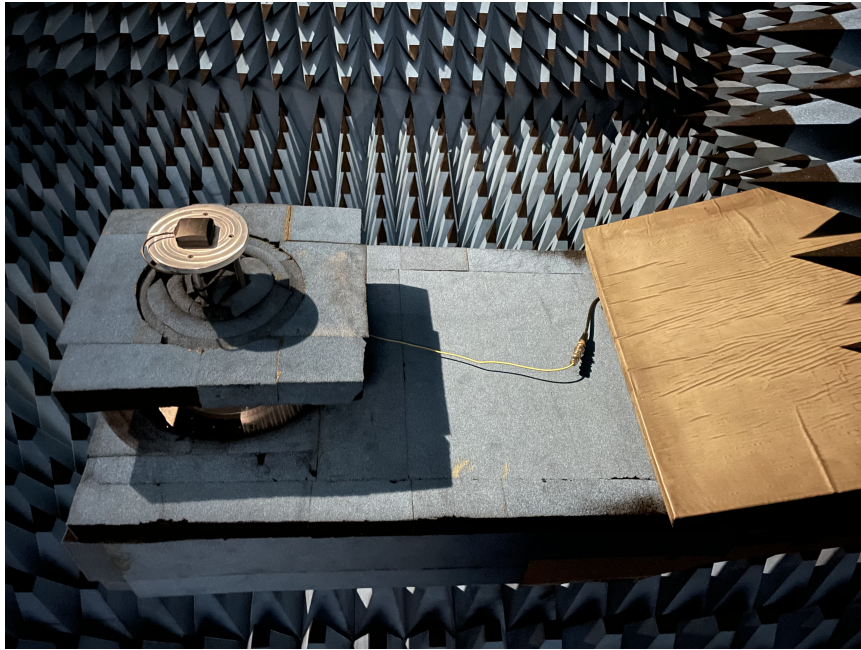


Figure 40: Patch antenna's setup.

The measurements were carried out with a rotation of over 90° , lower than the horizon, in order to visualize any scattering and multipath phenomena.

6 Testing and Validation

This section is the heart of the thesis. In particular, we will first see the hardware and software technologies used in the project, the concept of RTK station, a detailed analysis of the experimental setup and the main methodologies with which the tests were carried out. Finally, the post-processing modalities will be presented.

6.1 Hardware and software technologies

In the following section we want to give a general overview of the main technologies used throughout the project, both at the software and hardware level, also reporting the main specifications of each component.

6.1.1 Antennas

Antennas play a very important role in communication systems. By definition, an antenna is a device used to transfer an RF signal, which is traveling on a conductor, into an electromagnetic wave in free space. Antennas demonstrate a component known as reciprocity, which means that an antenna will maintain the same characteristics while transmitting or receiving the data. An antenna must have the same frequency band of the radio system to which it is connected. When a signal is transmitted into an antenna, the antenna will emit radiation distributed in space in a certain way. A graphical representation of the relative distribution of the radiated power in space is called a radiation pattern.

There are different types of antennas which are named as:

- Wire antenna;
- Aperture antenna;
- Microstrip antenna;
- Array antenna;
- Reflector antenna;
- Lens antenna.

In this thesis, only two types of antennas were used: **microstrip** (patch) and **geodetic** antennas.



Figure 41: Magnet Mounted GPS-GLONASS Antenna: mod AA.161.

Microstrip antenna Microstrip antennas became very popular in 1970's famous for space applications. Today these antennas are used for government and commercial applications and they consist of a metallic patch on a grounded substrate. The metallic patch can take many different forms which may vary from rectangular to circular patches. These are the most popular because of ease of analysis and fabrication and their attractive radiation characteristics especially low cross polarization radiation. These antennas can be mounted on the surface of high performance aircraft, satellites, missiles, cars and even can be used in mobile telephones. In this case was used a *Magnet Mounted GPS-GLONASS Antenna* (Figure 41), made by "Tao-glas" company. This antenna is designed for applications which require high positioning accuracy by combining signals from GPS and GLONASS systems. High gain wide-band patch antenna on a large integral ground delivers maximum performance.

ELECTRICAL			
Centre Frequency	1574~1610MHz		
Antenna Gain	26 ± 3dBic @ zenith @ 1575.42MHz 27 ± 3dBic @ zenith @ 1602MHz		
Axial Ratio	3.0dB max. @ zenith @ center frequency		
Polarization	RHCP		
VSWR	2.0 max.		
Impedance	50Ω		
DC input	1.8V (min.)	3.0V (typ.)	5.5V (max.)
LNA Gain	22dB	28dB	31dB
Noise Figure	2.6dB	2.6dB	2.6dB
Power Consumption	5mA	10mA	23mA
MECHANICAL			
Antenna Dimensions	65.7 x 49.7 mm		
Housing Material	ABS		
Cable	3m RG174 (fully customizable)		
Connector	SMA(M) (fully customizable)		
ENVIRONMENTAL			
Operation Temperature	-40°C to 85°C		
Storage Temperature	-40°C to 105°C		
Relative Humidity	40% to 95%		

Figure 42: Main antenna's specifications.

As can be seen from Figure 42, the main specifications of the antenna are reported. Among these, we can certainly underline the antenna and LNA gain, impedance, DC input, power consumption as regard the electrical one and the operating temperature as regard the environmental.

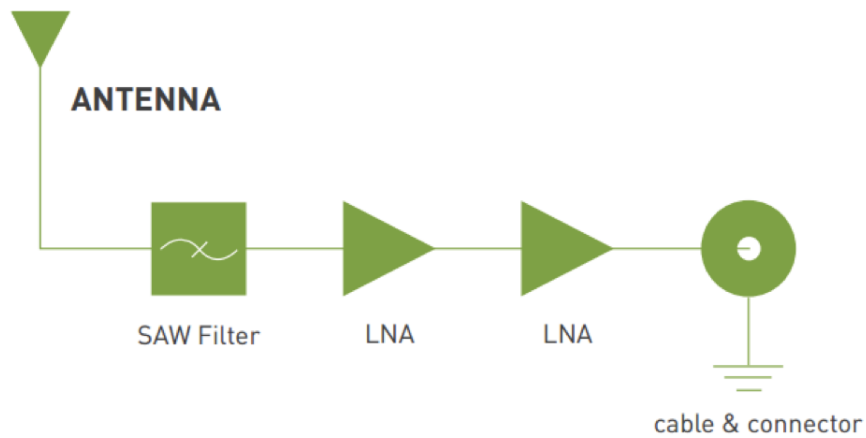


Figure 43: Block diagram.

Thanks to the block diagram shown in Figure 43, it is possible to have a rough idea about the functioning of the system. The antenna at the transmitter generates the radio wave. A voltage at the desired frequency is applied to the antenna. The voltage across the antenna elements and the current through them create the electric and magnetic waves, respectively. At the receiver, the electromagnetic wave passing over the antenna induces a small voltage. Thus, the antenna becomes the signal source for the receiver input.



TOP VIEW

(a) Antenna's top view



BOTTOM VIEW

(b) Antenna's bottom view

Figure 44: Top and bottom views of the antenna.

Geodetic antenna: GNSS Antenna GPS500 A GNSS antenna is a device designed to receive and amplify the radio signals transmitted on specific frequencies by GNSS satellites and convert them to an electronic signal for use by a GNSS or GPS receiver. The output of the GNSS antenna is fed into a GNSS receiver that can compute the position.

**ANTENNA STRUCTURE AND PHASE CENTERS DRAWING
(DIMENSIONS IN MM)**

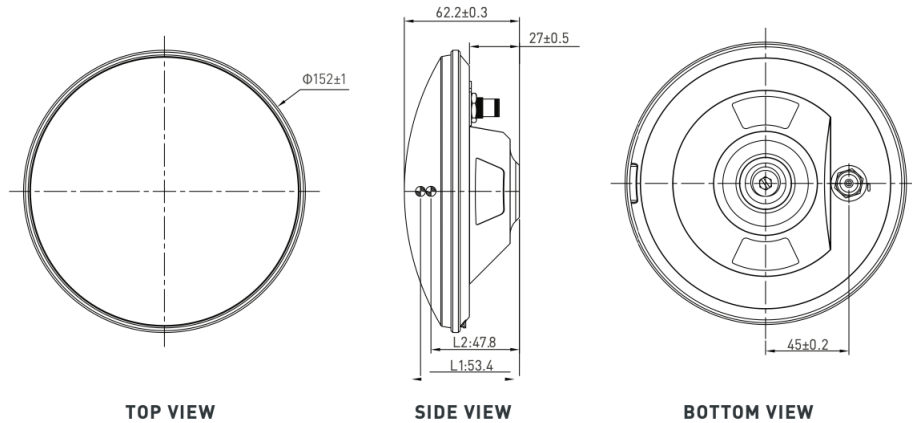


Figure 45: GNSS Antenna GPS500's mechanical specifications.

This type of antenna provides different capabilities compared to the microstrip one. In fact, it guarantees a *high center phase stability* since it provides a multi-point feeding design, effectively improving measurement accuracy and a better RTK solution; a better *tracking in challenging environments* due to its ability to receive low elevation signals with high gain and wide beam width, providing the positioning solutions with precision and reliable data. It can be widely used in autonomous vehicles, construction, agricultural equipment, field base stations and GIS surveying where high-precision operations are needed. Finally, a strong *anti-interference performances* is reached since the LNA antenna features an excellent out-of-band rejection performance, which can suppress the electromagnetic interference, to provide stability and reliability of GNSS signals. It also effectively avoids the dangers of disconnection when receivers are operated under complex electromagnetic environments such as a communication tower and in busy urban areas. To this can also be added a *small form factor*: this lightweight and small sized antenna can lighten the loads of small unmanned vehicles. Moreover, its IP67 ruggedized design protects it from dust and water.

6.1.2 Swift Navigation Piksi Multi GNSS Module

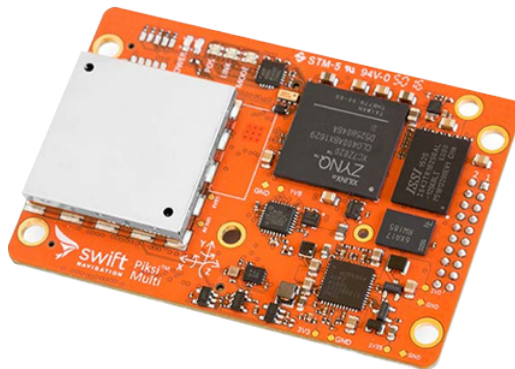


Figure 46: Piksi Multi Board.

Piksi Multi is a low-cost, high-performance GNSS receiver with Real Time Kinematics (RTK) technology for centimeter-level positioning accuracy. Its small form factor, fast position solution update rate and robust feature set make Pixsi Multi ideal for integration into autonomous vehicles and robotics. Multi-band and multi-constellation support enable Pixsi Multi to offer fast RTK convergence times. Integrated inertial measurement unit (IMU) and magnetometer enable sensor fusion techniques.

In particular, Pixsi Multi supports GPS L1/L2, GLONASS G1/G2, BeiDou B1/B2, Galileo E1/E5b for RTK measurements and positioning and SBAS for robust sub-meter positioning in non- RTK mode. Additional constellations create more robust positioning performance in a variety of challenging skyview environments.

6.1.3 u-blox C94-M8P-3



Figure 47: u-blox C94-M8P-3 receiver.

The C94-M8P module provides centimeter-level GNSS positioning for the mass market with integrated real time kinematics (RTK) for fast time-to-market. This small, light, and energy-efficient RTK module is a complete and versatile solution thanks to its base and rover variants and moving baseline technology for attitude-sensing and follow-me applications.

C94-M8P modules are compatible with a wide range of communication technologies (Cellular, Wi-Fi, Bluetooth, UHF) enabling the user to select the communication link best suited to their application. With u-blox's RTK technology, integration and software development efforts can be reduced, ensuring a minimal cost of ownership.

6.1.4 RTKLIB

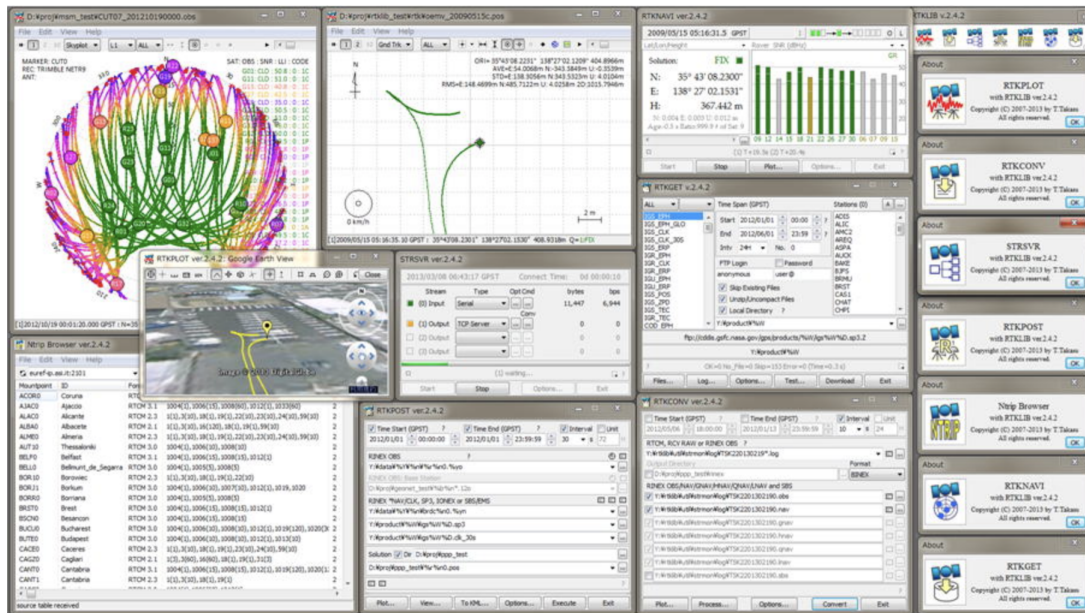


Figure 48: Preview of the main functions of the RTKLIB software.

RTKLIB is an open source program package for standard and precise positioning with GNSS (global navigation satellite system). RTKLIB consists of a portable program library and several APs (application programs) utilizing the library. The features of RTKLIB are:

- It supports standard and precise positioning algorithms with: GPS, GLONASS, Galileo, QZSS, BeiDou and SBAS;
- It supports various positioning modes with GNSS for both real-time and post-processing: Single, DGPS/DGNSS, Kinematic, Static, Moving-Baseline, Fixed, PPP-Kinematic, PPP-Static and PPP-Fixed;
- It supports many standard formats and protocols for GNSS: RINEX 2.10, 2.11, 2.12 OBS/NAV/GNAV/HNAV/LNAV/QNAV, RINEX 3.00, 3.01, 3.02 OBS/NAV, RINEX 3.02 CLK, RTCM ver.2.3, RTCM ver.3.1 (with amendment 1-5), ver.3.2, BINEX, NTRIP 1.0, RTCA/DO-229C, NMEA 0183, SP3-c, ANTEX 1.4, IONEX 1.0, NGS PCV and EMS 2.0;
- It supports several GNSS receivers' proprietary messages: NovAtel: OEM4/V/6, OEM3, OEMStar, Superstar II, Hemisphere: Eclipse, Crescent, u-blox: LEA-4T/5T/6T, SkyTraq: S1315F, JAVAD: GRIL/GREIS, Furuno: GW-10 II/III and NVS NV08C BINR;
- It supports external communication via: Serial, TCP/IP, NTRIP, local log file (record and playback) and FTP/HTTP (automatic download);
- It provides many library functions and APIs for GNSS data processing: Satellite and navigation system functions, matrix and vector functions, time and string functions, coordinates transformation, input and output functions, debug trace functions, platform dependent functions, positioning models, atmosphere models, antenna models, earth tides

models, geoid models, datum transformation, RINEX functions, ephemeris and clock functions, precise ephemeris and clock functions, receiver raw data functions, RTCM functions, solution functions, Google Earth KML converter, SBAS functions, options functions, stream data input and output functions, integer ambiguity resolution, standard positioning, precise positioning, post-processing positioning, stream server functions, RTK server functions, downloader functions;

- As shown in Figure 48, it includes lots of GUI and CUI APs since it has to satisfy different functions.

6.1.5 Swift Navigation Console

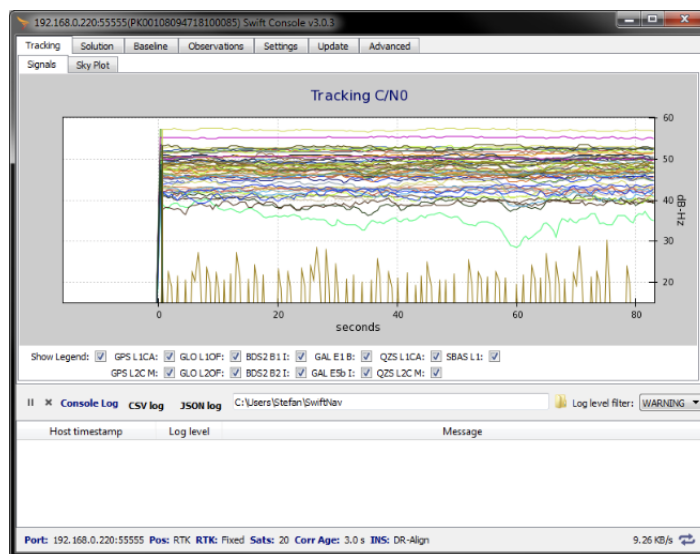
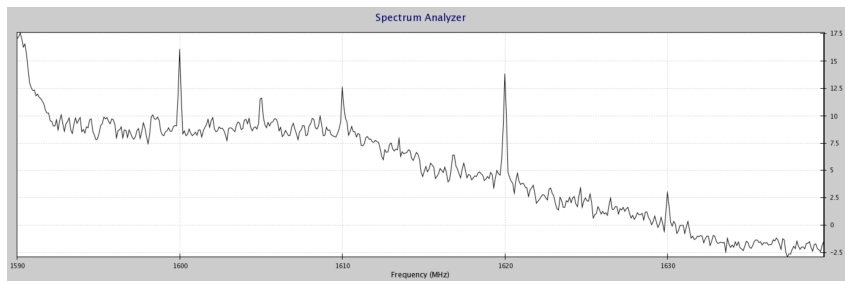


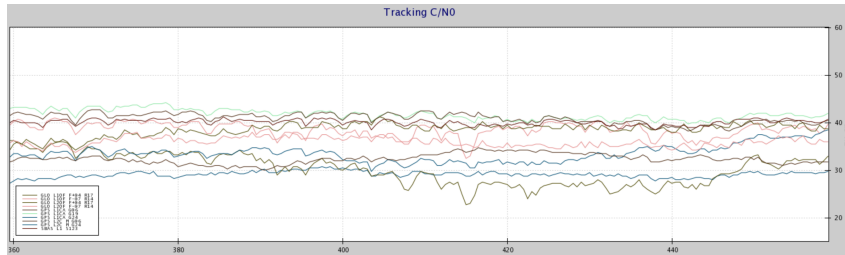
Figure 49: Swift Navigation Console.

The Swift Navigation Console is a Graphic User Interface (GUI) program providing visual representation of what's happening inside the Swift Navigation Piksi Multi and Duro GNSS receiver. Console displays information and allows to adjust the settings on the hardware. It is able to display the position and status information and also allows you to change the receiver's configuration.

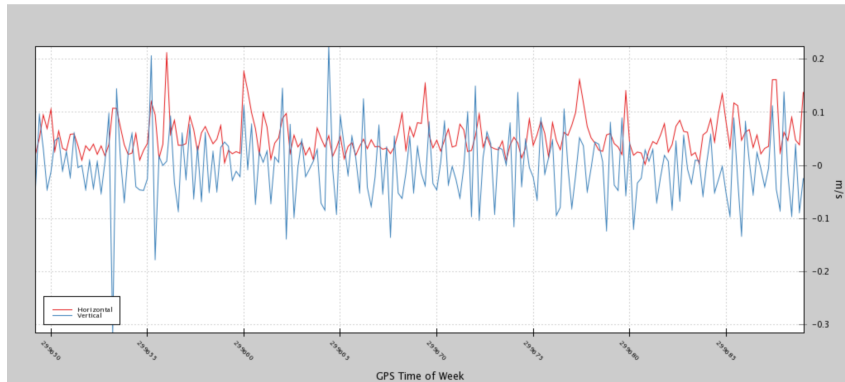
It has a bunch of functionalities like: monitor the GPS/GNSS satellites' track that are present; evaluate the solution of the constellation; display the satellites SkyPlot; exploit different features to better understand the tracking (see Figure 50).



(a) Spectrum analyzer



(b) Tracking C/NO



(c) Velocity

Figure 50: Other features implemented in the console.

6.2 RTK base station

Before going into details of the experimental setup, it is right to provide some more information about the theory background of an RTK system architecture.

In an RTK system, both the reference station and roving station consist of a single- or dual-frequency GPS receiver, the associated antenna, a data radio (sometimes called a radio modem), and its associated antenna (see Figure 51).



Figure 51: In RTK positioning, a GPS reference station transmits carrier-phase and pseudorange data over a radio link to a rover station. Either single- or dual-frequency GPS receivers can be used, with dual-frequency systems typically affording faster ambiguity resolution and higher and higher positioning accuracies over long distances.

Typically, users employ identical GPS receivers and data radios at the base and roving stations, although one must obviously use the reference station data radio for transmitting and the rover station data radio for receiving. High-power transmitters and less costly receive-only radios are available. Often, the transmitting antenna has higher gain than the receiving antenna, although it is common for both to be omnidirectional whip antennas. Sometimes users opt for "rubber duck" (helical, quarter-wavelength) antennas for receiving and low-power transmitting.

Some RTK systems integrate the GPS receiver and data radio into one package, with the GPS and radio link antennas even sometimes sharing a common enclosure.

To achieve the best results, the reference station GPS antenna should be mounted in a location free, as much as possible, of multipath and the radio link antennas should be as high as possible to maximize the link's coverage.

Some RTK installations use combined GPS/GLONASS receivers at the reference and roving stations. Using GLONASS data in addition to GPS can provide faster ambiguity resolution and higher positioning accuracies.

The **data link** used to support RTK operations is usually a radio channel or some sort, although an optical data link could conceivably be used in some environments. For RTK operations that carry out double differencing using Message Types 18 and 19, the data must be updated every 0.5-2 seconds, rather than the more leisurely 10 seconds or more used with code differential operation. So, whereas the RTCM SC-104 messages for code DGPS are typically transmitted

by marine radionavigation beacons at 200 bits per seconds (BPS), the data links for RTK use need data rates of at least 2,400 bps and preferably 9,600 or even 19,200 bps. The bandwidths required to support such data rates can be found in the VHF and UHF part of the radio spectrum.

Regarding the **propagation distances**, since RTK data links operate at VHF/UHF frequencies, their use is limited, for the most part, to line of sight with the maximum distance, d , in kilometers that can be theoretically achieved given approximately by:

$$d = 3.75\sqrt{k}(\sqrt{h_t} + \sqrt{h_r})$$

where h_t and h_r are the heights in meters of the transmitting and receiving antennas above their common horizon. In many cases, the heights can be approximated as heights above average terrain. The term k is the effective earth radius factor that accounts for the fact that the distance to the radio horizon because of atmospheric refraction.

For a transmitting antenna at 30 meters above the terrain and a receiving antenna at 2 meters, the computed maximum propagation distance is 28 kilometers. It can be difficult to achieve such maximum distances in practice. Any obstructions along the propagation path will affect the signal's range. Signals might be blocked or reflected by buildings or other objects, or even travel much longer distances than normal because of anomalous atmospheric ducting.

Furthermore, even in the absence of obstructions, the signal suffers an attenuation, according to the inverse square law, as it spreads out from the transmitting antenna. This is the so-called *free-space loss*. But in addition to the direct path signal, the receiver often obtains a signal that is reflected from the ground and combined with the direct-path signal. So, the total signal path loss depends on several factors, including ground reflection characteristics, terrain, and the presence of buildings and other structures.

It is difficult to accurately predict the path loss unless one has a detailed description of the environment through which the signal travels.

Once the basic knowledge about the theory behind an RTK station has been declared, it is possible to go deep in the description of the system.

6.3 Acquisition stage

The acquisition phase is undoubtedly one of the most important part of the whole thesis project. The importance is due to the fact that through this, it was performed a verification of the reliability and accuracy of the measurement system for receivers calibration.

6.3.1 Methodology

The acquisition phase can be mainly divided into two parts: **static** and **dynamic** acquisition. For the purposes of a possible data post-processing phase, it is clear how important the acquisition of raw data is for both antennas. Therefore, the settings of the respective data collection software were checked even before the setup was prepared. For the microstrip antennas the reception of *RAWX messages* has been activated through the u-Center message console; on the other hand, for the dual frequency antennas, the data stream was created through a *STR2SVR connection*, a RTKLIB tool, using NTrip client and server.

For the static acquisition the following approach was used:

- Two different types of configuration: normal baseline configuration, considering both microstrip patch antennas with the cable facing inwards and the configuration with the right patch antenna with the cable facing outwards;
- 20 minutes of continuous data acquisition: simple collection of incoming data stream;
- 3 different modes: Static, DGNSS/DGPS and Moving-Base.

In contrast, the dynamic acquisition was organized in this way:

- Same baseline configurations as the static one in order to better compare the results;
- Introduction of rotating platform plus ground plates for microstrip patch antennas;
- Introduction of a tripod for better position accuracy and oscillation reduction;
- Different data collection compared to the static mode:
 1. 180° rotation, back and forward, at a rate of $\omega = 5^\circ/\text{s}$;
 2. 90° rotation, back and forward, in steps of 10° at $\omega = 5^\circ/\text{s}$.

Since the dynamic acquisition setup is much more complex than the static one, the data were first collected in static mode and then in the other configuration.

6.3.2 Experimental setup

The study area is considered a place free of obstructions, such as trees and buildings, and it was defined on the rooftop of the "Institute of Electronics, Information Engineering and Telecommunications (IEIIT) Consiglio Nazionale di Ricerca (CNR)" laboratory, located at the Politecnico di Torino University. The rooftop has approximately 15 m height and it has a strategic position for GNSS data acquisition since it already had some stationary points.

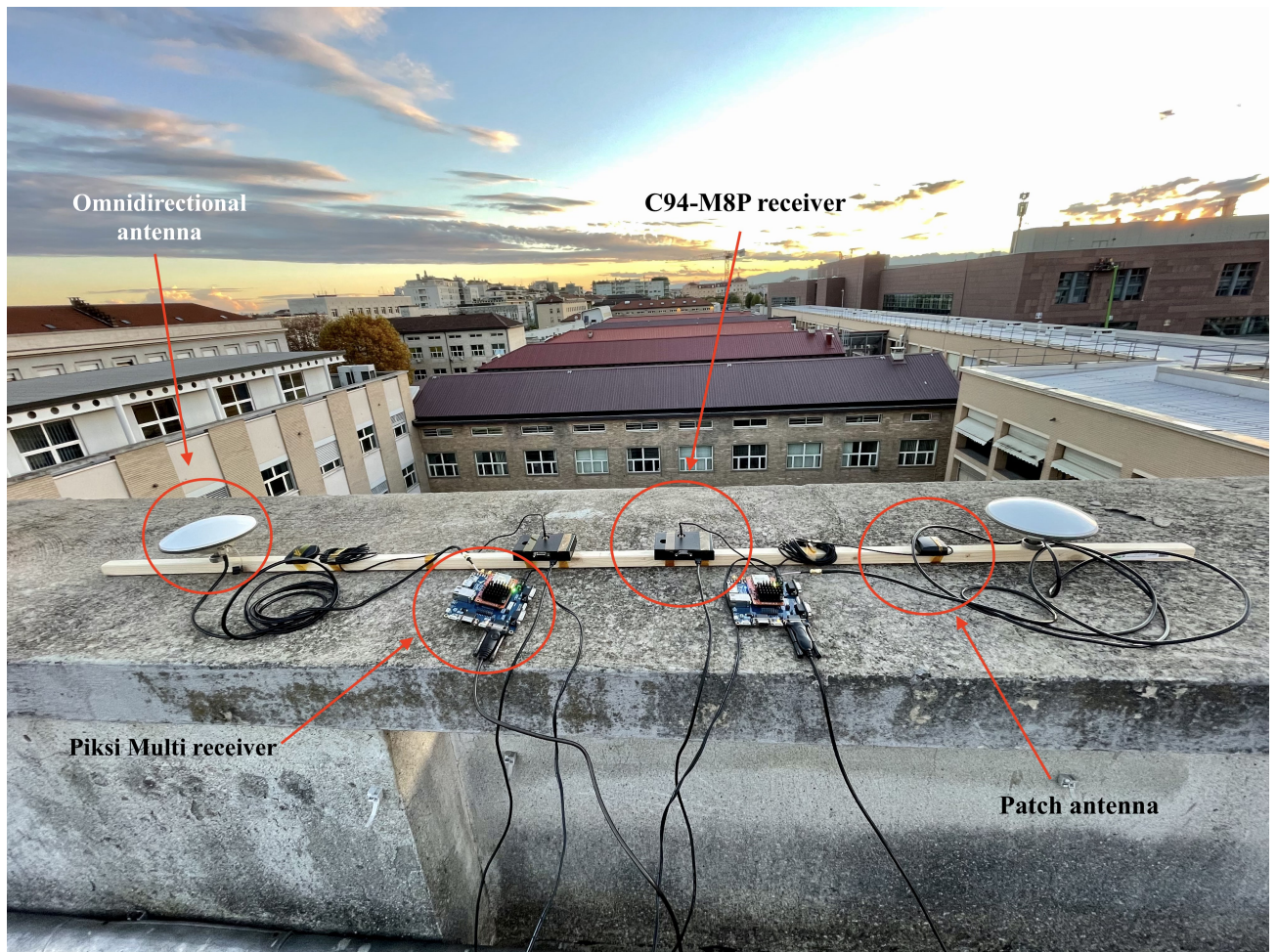


Figure 52: Experimental setup for static data acquisition.

Figure 52 depicts the experimental setup used for static acquisitions. At the base of everything there is a support made of wood, customized for the needs of the tests. The setup baseline was calibrated a priori, thus making the measurement system mirror: both microstrip and dual frequency antennas are at the same distance from each other from the midpoint of the support. This is due to the fact that we did not want to create too much noise between the two receivers. To make the baseline even more robust, the dual-frequency antennas were anchored to the rod by means of a metal support, while the microstrip antennas and receivers were fixed by means of bio-adhesive. Data acquisition was made possible by connecting each antenna to a receiver: u-blox C94-M8P for the microstrips and Piksi Multi by SwiftNav for the dual-frequency ones.



Figure 53: Particular of static setup: cable connections between antennas and receivers.

Figure 53 shows cable connections between antennas and receivers: in particular it shows the second baseline configuration, having the right antenna rotated. Once this connection was made, the receivers were connected to two different computers: one to manage the data acquisition with .ubx format and one for the swiftnav format. In this way, the data collection time was halved. To complete the ensemble, the two Piksi receivers have been connected to a power source as they are not capable of self-powered via USB connection.

In the experimental setup for dynamic acquisition, we find the same baseline as the static one. The big difference lies in the introduction of two parts: the tripod and the rotating platform. Since, during the dynamic data collection phase, the baseline rotated by a certain angle at a fixed speed, the tripod was introduced to make the calibration system more robust towards oscillations and to achieve greater precision. The anchoring of the support was possible thanks to the realization of a thread placed in the center of the rod. Finally, the rotating platform was fixed to the tripod by means of a particular support base made by the laboratory technician.



Figure 54: Experimental setup for dynamic data acquisition.



Figure 55: L-611 rotation platform.



Figure 56: Complete dynamic setup: everything is connected and controlled by PCs.

The rotation stages, often called *index tables* or *rotary tables*, are mechanisms used to precisely rotate a sample or specimen with high angular accuracy. Motorized rotary stages make use of a motion controller and stepper motor or - when higher performance is required - closed-loop servo motor, position feedback and computer control. Better performance, speed control and higher acceleration is achieved when using a direct-drive rotary table.

In this case was used the **L-611 rotation stage** (see Figure 55), a high-positioning rotation stage due to low-play preloaded worm gear. Preloaded pivot bearings for high travel accuracy. It has a clear aperture with \varnothing 35 mm and an unlimited travel range in both directions of rotation. It has been fixed to the tripod by using a plastic support by means of screws. This was able to guarantee no fluctuations during the kinematic acquisitions.

The control of any type of movement of the platform has been achieved through a program created in MatLab. In fact, thanks to this software, it was possible to set few parameters like angular speed, angle rotation and automatic referencing.

6.3.3 Data collection

The GNSS data collection was performed during the 5th November, starting from 9 a.m. up to 5 p.m. Before reviewing the entire data acquisition phase, a priori considerations can be made on the observation site. This operation is usually called **GNSS planning** and it is typically used to understand the impact of obstacles to GNSS signals and distribution of



(a) GPS and GLONASS elevation during the observation period.

(b) Number of satellites (GPS and GLONASS) during observation period.

Figure 57: Elevation degree and number of satellites of GPS and GLONASS.

satellites over that specific part of the world. To do that, it was used an online website (<http://www.trimble.com/GNSSPlanningOnline>), where user is simply asked to put the site coordinates (latitude and longitude). Coordinates allow the website to understand the exact position and provide useful information about the observation site. With this preventive technique users can determine the optimal moment in which satellite measurement can be done. In fact, we need at least four satellites in line-of-sight to take a position measurement, but more satellites we have a better estimation we can achieve.

A general overview is given by the following figures. In particular, Figure 57a shows the elevation angle of GPS and GLONASS satellites. Note that the *cut-off angle* (around 15°) defines the elevation angle under which tracked satellites are not considered. Figure 57b shows the number of satellites visible during the observation period. Figure 59a, 59b and 59c show respectively the sky view at 9 am, 12 and 4.30 pm. Once the conditions of the observation site have been visualized, we can analyze in detail the acquisition methods. The data stream was collected using two open-source softwares: u-Center and RTKLIB. These programs give access to GNSS data from multi-constellation like GPS, GLONASS, Galileo, QZSS and BeiDou, and multiple frequencies, and converts it to output files in RINEX format.

Just two data collection campaigns, lasting approximately 5 hours and 3 hours, were performed in static and dynamic mode, following the methodology in section 6.3.1.

6.4 Post-processing of data

As can be seen from the name itself, the post-processing is a specific phase, done after the data collection. Post-processing is used in GPS or GNSS to obtain precise positions of unknown points by relating them to known points such as survey markers [58].

The GPS measurements are usually stored in computer memory in the GPS receivers, and are subsequently transferred to a computer running the GPS post-processing software [58]. The software computes baselines using simultaneous measurement data from two or more GPS receivers. The baselines represent a three-dimensional line drawn between the two points occupied

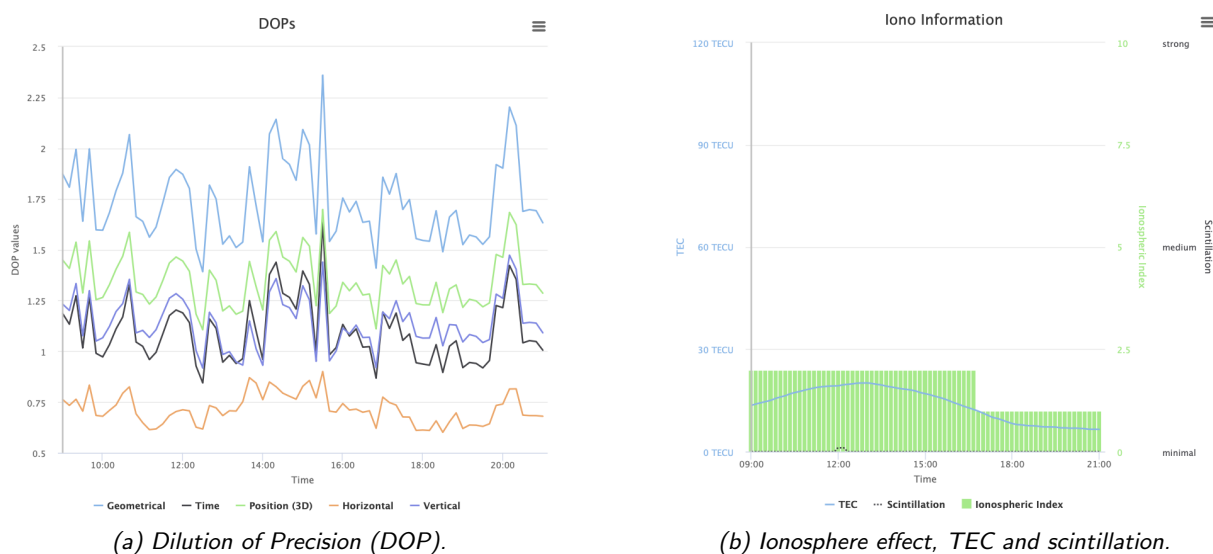


Figure 58: DOP and space effects.

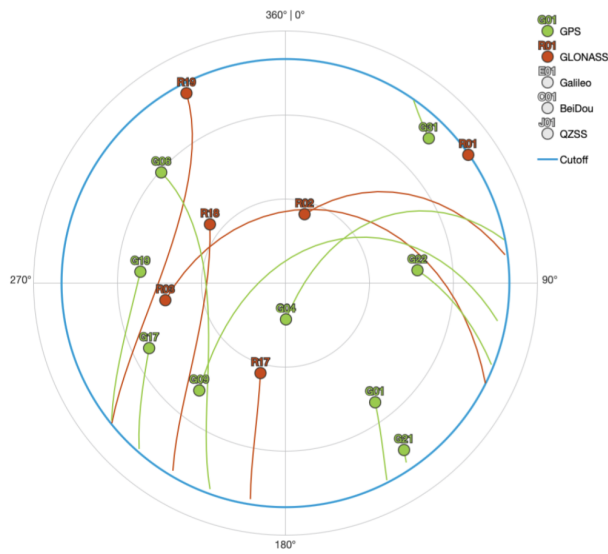
by each pair of GPS antennas. The post-processed measurements allow more precise positioning, because most GPS errors affect each receiver nearly equally, and therefore can be cancelled out in the calculations [58]. Differential GPS measurements can also be computed in real time by some GPS receivers if they receive a correction signal using a separate radio receiver, for example in Real Time Kinematic (RTK) surveying or navigation [58]. The improvement of GPS positioning doesn't require simultaneous measurements of two or more receivers in any case, but can also be done by special use of a single device [58]. In the 1990s when even handheld receivers were quite expensive, some methods of quasi-differential GPS were developed, using the receiver by quick turns of positions or loops of 3-10 survey points [58].

The data processing by relative positioning method, in both static and dynamic mode, was performed using the same software as the acquisition stage, RTKLIB, but by means of three different libraries: RTKCONV, RTKPOST and RTKPLOT. These allowed post-processing and visualization of data from the GPS and GLONASS constellations, and from the frequencies L1 and L2.

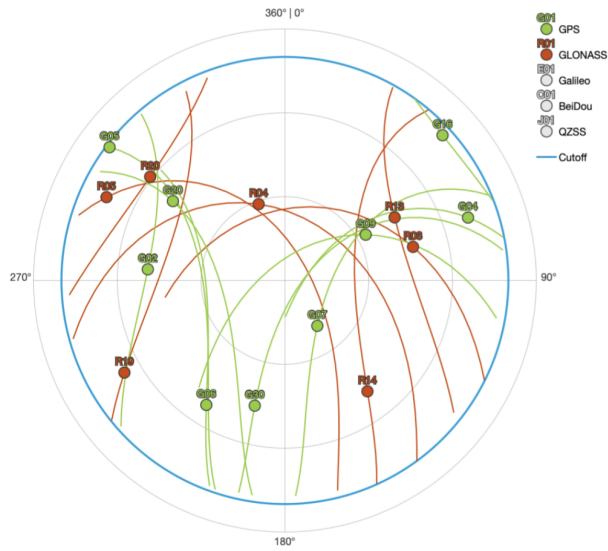
Successful post-processing of raw data using RTKLIB requires a number of specialized files, only one of which is produced by the GNSS Surveyor.

- A RINEX log (.obs) from the GNSS Surveyor;
- A RINEX log (.o or .obs) and nav (.n or .nav) file from a base station;
- (Optional) precise ephemeris and clock files from the IGS (.clk and/or .sp3 files).

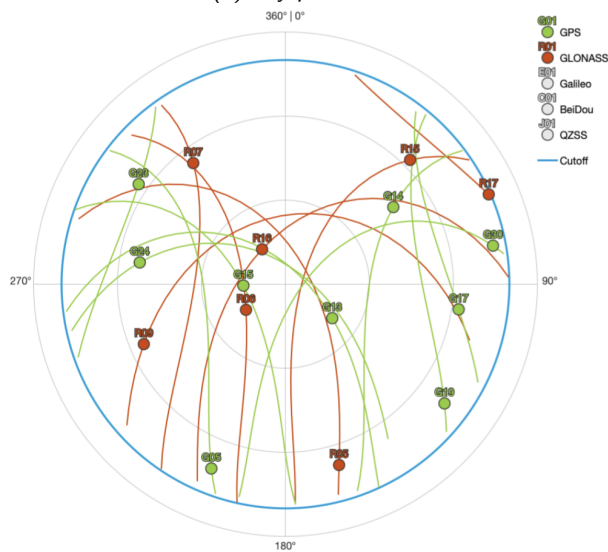
For purposes of clarity, the GNSS Survey is referred to as the Rover. The Base is typically a CORS station (Continuous Operating Reference Station) or a fixed reference station that stores recorded satellite data in RINEX format. Most countries have a network of reference stations and observations that are publicly available.



(a) Sky plot at 9 am.

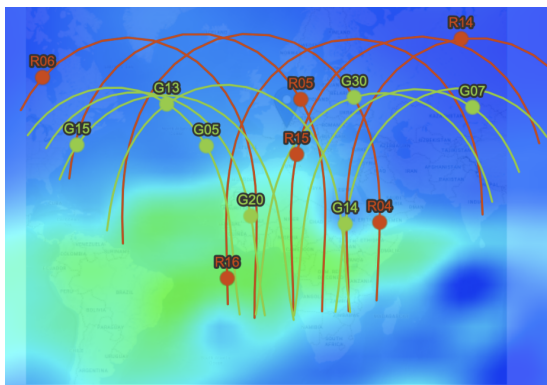


(b) Sky plot at 12.

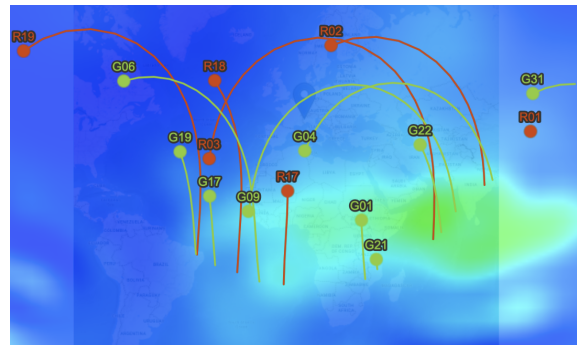


(c) Sky plot at 4.30 pm.

Figure 59: Sky view of GPS and GLONASS constellation.



(a) Ionospheric, effect around the world, at 9 am.



(b) Ionospheric effect, around the world, at 4.30 pm.

Figure 60: Behaviour of ionospheric effect during the observation period.

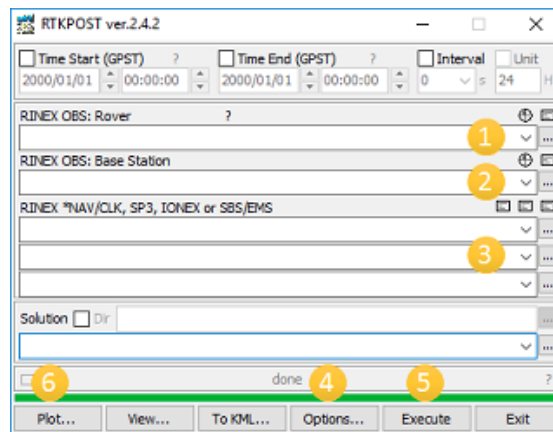


Figure 61: RTKPost primary GUI.

Once RTKPOST software has been launched, a GUI such as that shown in Figure 61 appears. From this GUI, the first step is to configure the options used for post-processing. These option will remain set unless they are changed at a future time. RTKPost also has a means to save and load configuration files. As a good measure, you should save your initial configuration in order to create alternate configurations in the future.

The following steps provide for basic configuration and setup of the RTKPOST application. Once configured, steps 4 and 6 are not required unless one desires to make changes to the configuration.

1. Click on the ellipses “...” next to RINEX OBS: Rover. Select the RINEX file obtained during the data collection;
2. Click on the ellipses “...” next to RINEX OBS: Base Station. Select the RINEX file downloaded from your base station;
3. Under RINEX *NAV/CLK, SP3... click on the ellipses “...” on the first line and select the NAV file from your base station. On the second line, optionally, select the SP3 or CLK file. SP3 and CLK files can be found on the IGS web site. The additional CLK and SP3 files provide precise ephemeris and clocks. They are required for long baselines.

4. Click on the button labeled “Options” in order to set your positioning technique and how to consider the ambiguity resolution for both GPS and GLONASS;
5. Click “Execute” to have RTKLIB process your data files;
6. Click “Plot” to see your solution on a map. Alternatively click on “View” to see a text file containing the solution.

As already stated inside section 6.3.1, three approaches were used to perform the data processing, therefore different combinations between Rover station and Master station were performed. As Master station, it was considered the Turin virtual station (“TORI”, see Figure 63), whose .nav and .obs files were easily downloaded from the “SPINGNSS” portal (see Figure 62) and the baseline was always maintained fix.

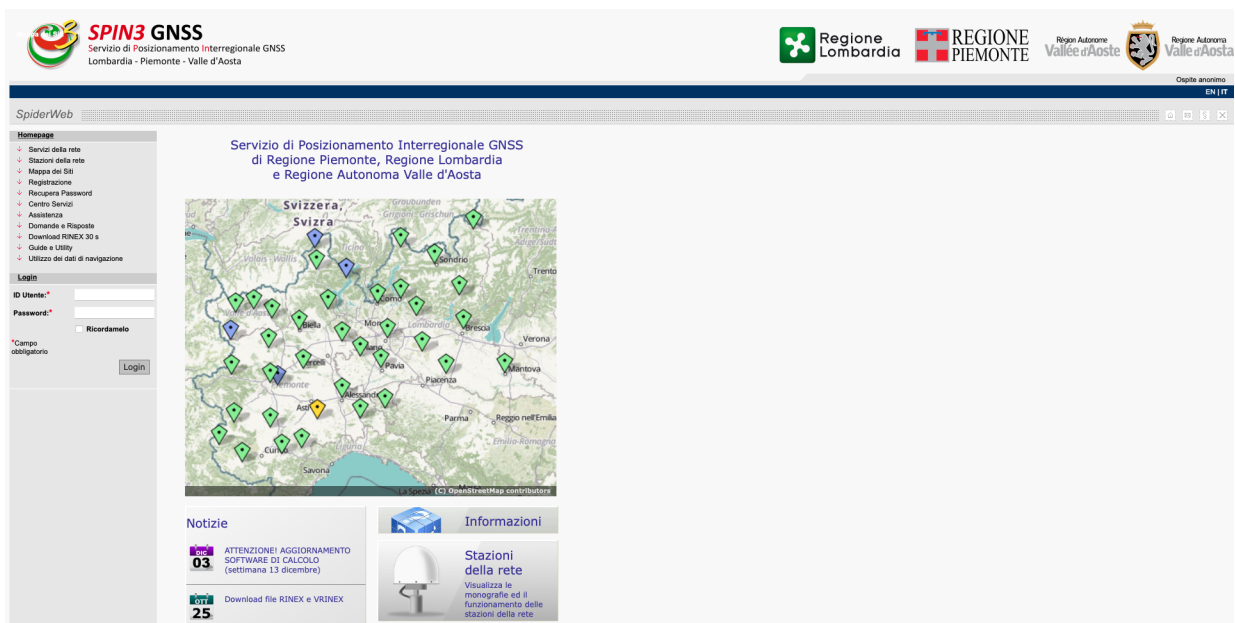


Figure 62: SPINGNSS website (www.SPINGNSS.it).



Figure 63: “TORI” reference station.

Particularly, the workflow was organized through the following way:

1. For both Static and DGPS/DGNSS positioning mode, the virtual station "TORI" was set as Master base station, alternating microstrip patch and omnidirectional antenna as Rover;
2. In Moving-base positioning mode, the role of Master and Base station was alternated between microstrip patch and dual-frequency antenna.

Normal configuration	
Static	Dynamic
Static positioning: Master fixed (TORI) - Rover: patch/omnidirectional	Kinematic positioning: Master fixed (TORI) - Rover: patch/omnidirectional
DGPS/DGNSS positioning: Master fixed (TORI) - Rover: patch/omnidirectional	DGPS/DGNSS positioning: Master fixed (TORI) - Rover: patch/omnidirectional
Moving-Base positioning: Master omnidirectional - Rover patch and viceversa	Moving-Base positioning: Master omnidirectional - Rover patch and viceversa

Figure 64: Acquisition methodology: normal configuration.

Reversed configuration	
Static	Dynamic
Static positioning: Master fixed (TORI) - Rover: patch/omnidirectional	Kinematic positioning: Master fixed (TORI) - Rover: patch/omnidirectional
DGPS/DGNSS positioning: Master fixed (TORI) - Rover: patch/omnidirectional	DGPS/DGNSS positioning: Master fixed (TORI) - Rover: patch/omnidirectional
Moving-Base positioning: Master omnidirectional - Rover patch and viceversa	Moving-Base positioning: Master omnidirectional - Rover patch and viceversa

Figure 65: Acquisition methodology: reversed configuration.

Figure 64 and 65 show the different configurations used for the post-processing phase. To better understand what "Reversed configuration" stands for, see Figure 53. Here, the right patch antenna is internally rotated by 180°. This type of rotation was taken into consideration since we wanted to verify if a possible change in the baseline configuration had influenced the performance of the system.

From all the previous configurations, it was decided to give a more detailed analysis of only two cases: the static acquisition with the Static positioning approach and the dynamic acquisition with the Kinematic approach. In particular, for the static case, it was decided to vary two parameters: the **Filter type** (combined and forward) and the resolution of the **Phase Ambiguity** (Fix&Hold and Continuous for GPS and Fix&Hold and Off for GLONASS). But, to be exact, what kind of parameters are they?

The "Filter Type" can be selected during the post-processing phase and can be set to forward, backward, or combined. Forward is the default and this is the only mode that can be used in real-time solutions. In forward mode, the observation data is processed through the well-known Kalman filter in the forward direction, starting with the beginning of the data and continuing through to the end. Kalman filtering is an algorithm that provides estimates of some unknown variables given the measurements observed over time [60]. Kalman filter algorithm consists of two stages: prediction and update. Note that the terms "prediction" and "update" are often called "propagation" and "correction," respectively [60]. The Kalman Filter has inputs and outputs. The inputs are noisy and sometimes inaccurate measurements. The outputs are less noisy and sometimes more accurate estimates. The estimates can be system state parameters that were not measured or observed. In short, we can think of the Kalman Filter as an algorithm that can estimate observable and unobservable parameters with great accuracy in real-time [60]. Estimates with high accuracy are used to make precise predictions and decisions. For these reasons, Kalman Filters are used in robotics and real-time systems that need reliable information [60].

Backward mode is the opposite, data is run through the filter starting with the end of the data

and continuing to the beginning. In Combined mode, the filter is run both ways and the two results are combined into a single solution. Since we are dealing with real time positioning solution, it was decided to use only the combined and forward.

As stated before, for the phase ambiguity computation mode, it was decided to use the "Fix&Hold" and "Continuous" technique for the GPS constellation and "Fix&Hold" and "Off" for the GLONASS. To get a high precision fixed solution in RTKLIB, the integer ambiguities, that come from the carrier phase measurements, must be resolved. Resolving the integer ambiguities for the GLONASS satellites is more challenging than resolving them for the other constellations. This is because, unlike the other constellations, the GLONASS satellites all transmit on slightly different frequencies. As a consequence, this introduces an additional bias error in the receiver hardware. These hardware biases are constant, generally the same for all receivers from the same manufacturer, are proportional to carrier frequency and are similar between L1 and L2. If GLONASS AR is set to "Off", then the raw measurements from the GLONASS satellites will be used for the float solution but ambiguity resolution will be done only with satellites from the other constellations. If GLONASS AR is set to "Fix&Hold", this is an extension to the "fix-and-hold" method used for other constellations but instead of using the additional feedback to track the ambiguities, it uses it to null out the hardware biases. It uses the difference between the fixed and float solutions to push the phase-bias estimates toward integer values, then uses integer ambiguity resolution to determine how good the answer is based on how close to integers it is. In short, having a FIX solution means that the receiver calculated a correct solution. It determined that the coordinates you see, have a certain accuracy with corresponding dilution with an accuracy between 1 to 3 centimeters in regular conditions. In a Float solution, the algorithm has not been solved (yet) and can not produce an acceptable FIX solution (yet). Since there is no FIX solution, a Float one is provided, which is always a less accurate position than a fixed solution and in general can not be used for measurements with centimeter accuracy.

However, the Fix&Hold, will usually improve the phase-bias estimates since it is very likely the chosen integers are the correct actual biases, but it will always improve the confidence in the result as determined by the integer ambiguity resolution, even when the result is wrong.

Continuous phase ambiguity resolution means that static integer ambiguities are estimated and resolved continuously through the post-processing phase. However it can be only applicable to Kinematic, Static, Moving-baseline and Fixed modes.

Further information can be obtained from the Phase ambiguity resolution. In fact, once the AR has been set, by looking at the RTKPLOT **AR ratio** for validation, it can be understand if the overall performances have been improved. The AR ratio factor is the residuals ratio between the best solution and the second best solution while attempting to resolve the integer cycle ambiguities in the carrier-phase data. In general, the larger this number, the higher confidence we have in the fixed solution. If the AR ratio exceeds a set threshold, then the fixed solution is used, otherwise the float solution is used. To sum up the post-processing phase, Tables 2, 3, 4 and 5 help us to better understand how data have been post-processed. Here are reported all the possible settings adopted through the post-acquisition phase, divided by static and dynamic acquisitions and by normal and reversed configuration. These methodologies will be further analysed in the following section.

Static acquisitions: normal configuration	
Filter type: Combined	Ambiguity resolution: GPS (Fix&Hold)GLONASS (Fix&Hold) Ambiguity resolution: GPS (Fix&Hold)GLONASS (Off) Ambiguity resolution: GPS (Continuous)GLONASS (Fix&Hold) Ambiguity resolution: GPS (Continuous)GLONASS (Off)
Filter type: Forward	Ambiguity resolution: GPS (Fix&Hold)GLONASS (Fix&Hold) Ambiguity resolution: GPS (Fix&Hold)GLONASS (Off) Ambiguity resolution: GPS (Continuous)GLONASS (Fix&Hold) Ambiguity resolution: GPS (Continuous)GLONASS (Off)

Table 2: Static acquisitions - Normal configuration: post-processing methodologies.

Static acquisitions: reversed configuration	
Filter type: Combined	Ambiguity resolution: GPS (Fix&Hold)GLONASS (Fix&Hold) Ambiguity resolution: GPS (Fix&Hold)GLONASS (Off) Ambiguity resolution: GPS (Continuous)GLONASS (Fix&Hold) Ambiguity resolution: GPS (Continuous)GLONASS (Off)
Filter type: Forward	Ambiguity resolution: GPS (Fix&Hold)GLONASS (Fix&Hold) Ambiguity resolution: GPS (Fix&Hold)GLONASS (Off) Ambiguity resolution: GPS (Continuous)GLONASS (Fix&Hold) Ambiguity resolution: GPS (Continuous)GLONASS (Off)

Table 3: Static acquisitions - Reversed configuration: post-processing methodologies.

Dynamic acquisitions: normal configuration	
Continuous rotation	Stepped rotation
Velocity: 5deg/s Baseline configuration: 1. Master dx omnidirectional Rover sx omnidirectional; 2. Master sx omnidirectional Rover dx omnidirectional; 3. Master dx patch Rover sx patch; 4. Master sx patch Rover dx patch.	Velocity: 5deg/s, 4s for each step Baseline configuration: 1. Master dx omnidirectional Rover sx omnidirectional; 2. Master sx omnidirectional Rover dx omnidirectional; 3. Master dx patch Rover sx patch; 4. Master sx patch Rover dx patch.

Table 4: Dynamic acquisitions - Normal configuration: continuous and stepped methodologies.

Dynamic acquisitions: reversed configuration	
Continuous rotation	Stepped rotation
Velocity: 5deg/s Baseline configuration: 1. Master dx omnidirectional Rover sx omnidirectional; 2. Master sx omnidirectional Rover dx omnidirectional; 3. Master dx patch Rover sx patch; 4. Master sx patch Rover dx patch.	Velocity: 5deg/s, 4s for each step Baseline configuration: 1. Master dx omnidirectional Rover sx omnidirectional; 2. Master sx omnidirectional Rover dx omnidirectional; 3. Master dx patch Rover sx patch; 4. Master sx patch Rover dx patch.

Table 5: Dynamic acquisitions - Reversed configuration: continuous and stepped methodologies.

7 Results

In this section we will see what are the main results obtained between the post-processing phase and the calibration of antennas obtained inside the anechoic chamber. As regard the experimental acquisitions, we will focus on the "Static" positioning approach for static acquisitions and on "Moving-Base" positioning for dynamic acquisitions. We will further compare how the main estimation parameters and the heading angle vary among different combinations of baseline. Finally, the heading estimation for UAV Platform will be discussed, comparing the estimation of experimental setup and the recorded data from UAV rotation tests.

7.1 Estimation parameter analysis

To compare the performance of the various methodologies used in the post-processing of the data, it was decided to focus on the following parameters:

- Position solution;
- Position and Velocity variation over coordinates;
- Number of available satellites among observation window;
- Pseudorange Residuals (mean and standard deviation);
- Carrier-Phase Residuals (mean and standard deviation).

In addition, the parameters will be compared by displaying antennas belonging to the same side within the same baseline configuration. To make the concept clearer, the right side omnidirectional antenna will be compared with the right side patch antenna having the same post-processing settings (same type of filter and same resolution of ambiguity) and vice versa with the opposite side.

7.2 Normal configuration: static positioning technique

As already mentioned in the table, the acquisitions were processed by setting different parameters regarding the type of Kalman filter as well as different ways of fixing the resolution of the ambiguity. Following the post-processing it has been seen how by fixing both ambiguities, GPS and GLONASS, slightly better results have been obtained using a "Combined" filter approach. Tables 6 and 7 show what has just been said.

Omnidirectional antennas		
	DX	SX
Position solution	Q=1(100%)	Q=1(100%)
N° of satellites	8, then 7	8, then 7
Pseudorange residuals(m)	//	AVE = -0.037m; STD = 0.0852m ; RMS = 0.0853m
Carrier-Phase residuals(m)	//	AVE = 0.0004m; STD = 0.0003m ; RMS = 0.0005m

Table 6: Omnidirectional antennas: "Combined" filter, Fix&Hold ambiguity resolution approach for both GPS and GLONASS.

Patch antennas		
	DX	SX
Position solution	Q=1(8.8%); Q=2(91.2%)	Q=1(100%)
N° of satellites	8, then 7	8, then 7
Pseudorange residuals(m)	AVE = -0.794m; STD = 3.967m; RMS = 4.046m	AVE = 1.571m; STD = 1.875m; RMS = 2.447m
Carrier-Phase residuals(m)	AVE = 0.001m; STD = 0.075m; RMS = 0.075m	AVE = -0.002m; STD = 0.009m; RMS = 0.010m

Table 7: Patch antennas: "Combined" filter, Fix&Hold ambiguity resolution approach for both GPS and GLONASS.

Unfortunately, during the post-processing phase, RTKLIB software was unable to provide the Pseudorange and Carrier-Phase residuals value for the right geodetic antenna. Even by significantly reducing the scale of the plot, it was not possible to obtain this data. This is certainly due to the considerable computational effort that the program had to make to process the data but also to the power of the graphic card in which the analysis was carried out.

Below are reported the graphs of Ground Track, Number of available satellites and Pseudorange and Carrier-Phase residuals of the best performing case. As can be seen from Figure 66 and 67, the antennas on the right have a more scattered quality of solutions than those on the left which have the totality of fixed solutions ($Q = 1$). This is also confirmed by the graph of the number of satellites available (see Figure 68) which has a much less stable trend than the one in Figure 69.

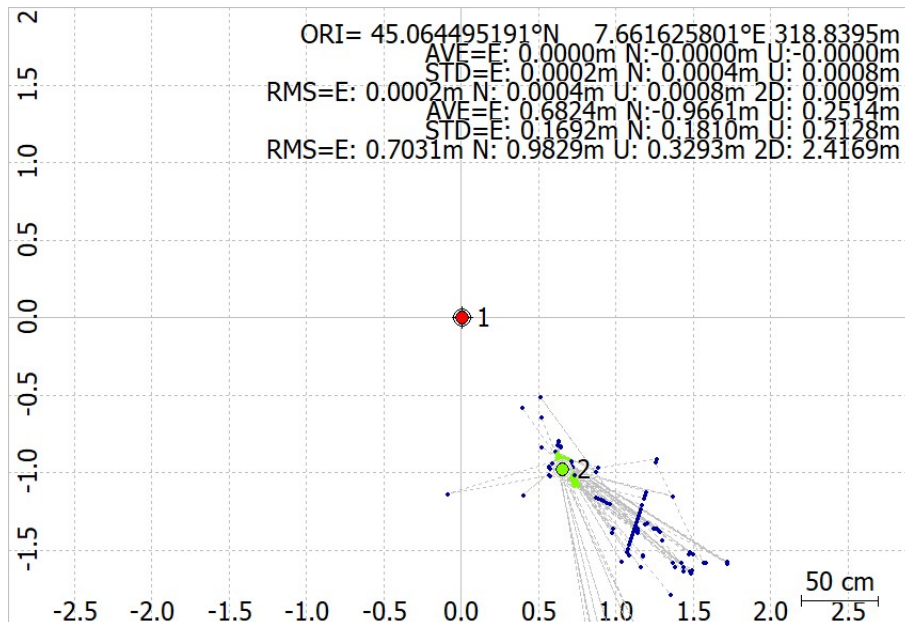


Figure 66: Ground Track of right antennas: omnidirectional in red and patch in green-blue.

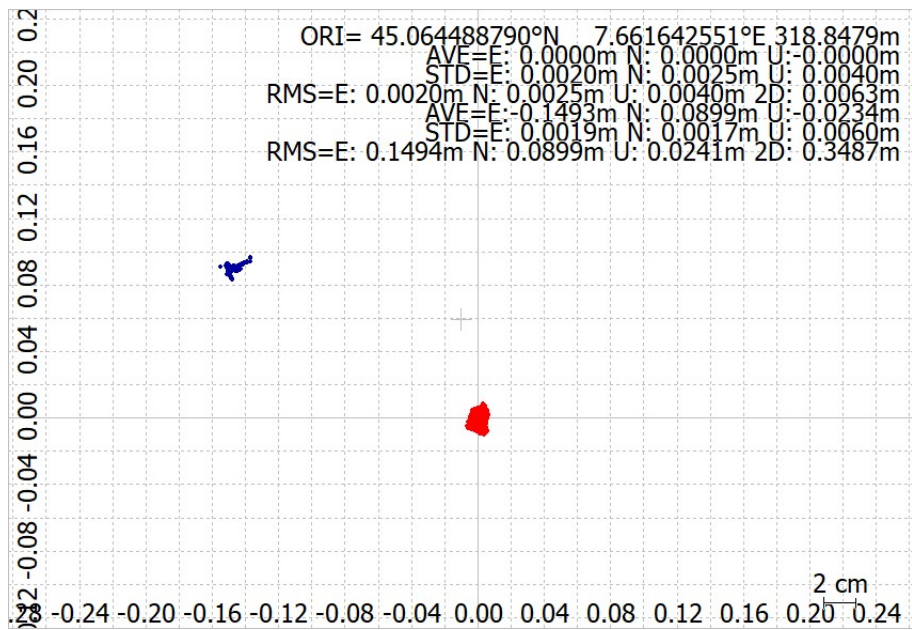


Figure 67: Ground Track of left antennas: omnidirectional in red and patch in blue.

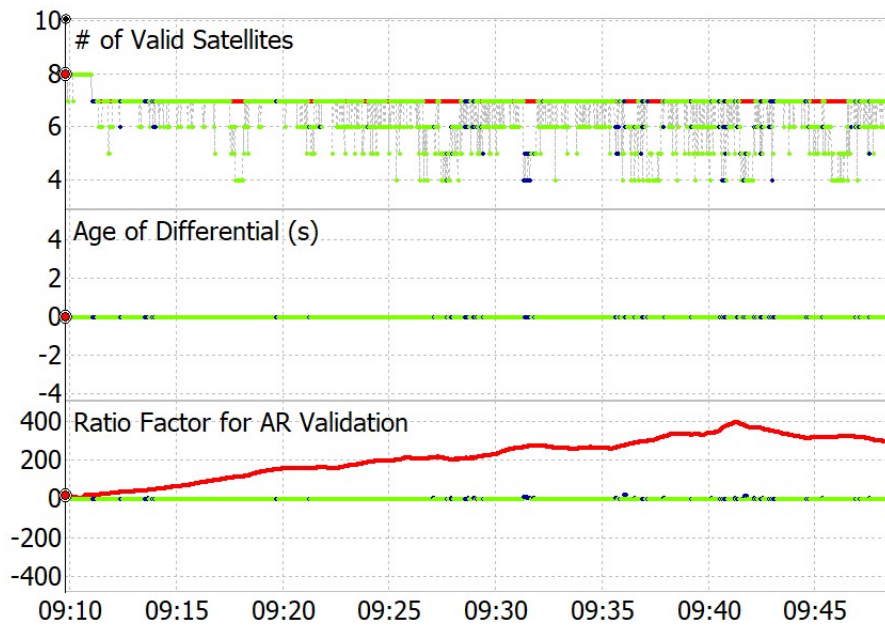


Figure 68: Number of available satellites of right antennas: omnidirectional in red and patch in green-blue.

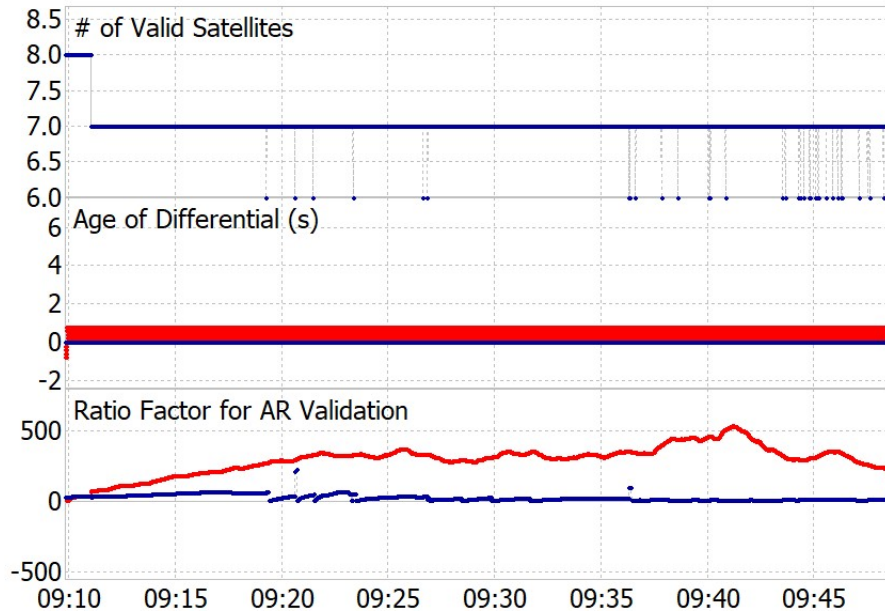


Figure 69: Number of available satellites of left antennas: omnidirectional in red and patch in blue.

Figure 70, 71 and 72 show the Pseudorange and Carrier-Phase residuals of both geodetic and patch antennas. As can be seen, the geodetic is more robust and does not display a noisy behaviour. This is further confirmed by the Mean, Standard deviation and RMS values. Moreover, the deviation of pseudorange residuals is between the range of ± 5 , achieving a good result.

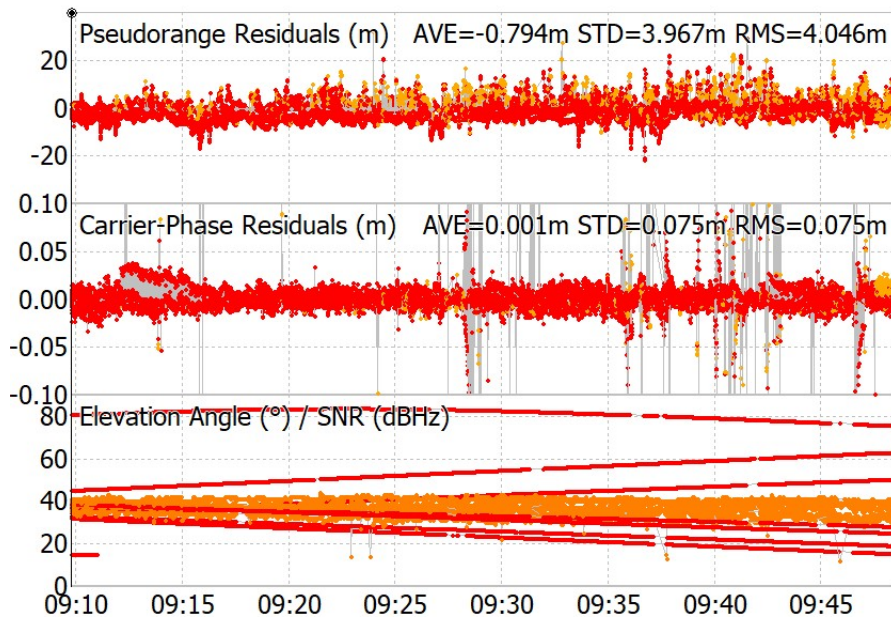


Figure 70: Pseudorange and Carrier-Phase residuals of right patch antenna.

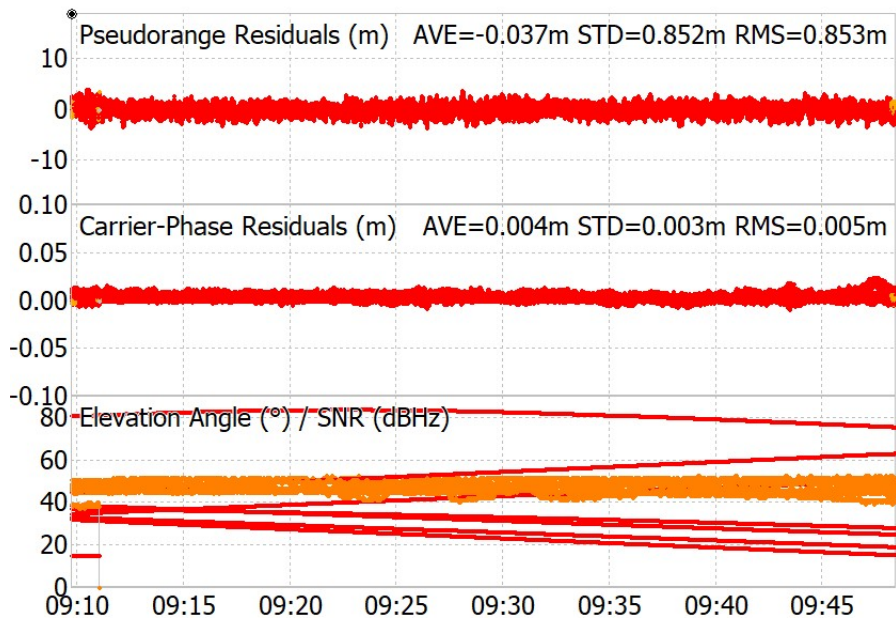


Figure 71: Pseudorange and Carrier-Phase residuals of left omnidirectional antenna.

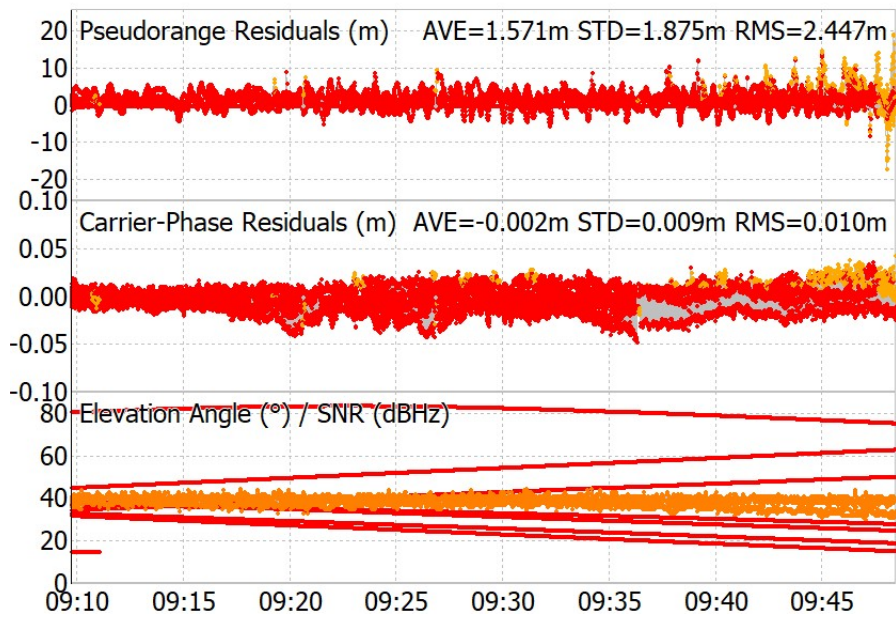


Figure 72: Pseudorange and Carrier-Phase residuals of left patch antenna.

From these very first results, it can be seen that omnidirectional antennas have a much lower estimation parameter value than patch antennas. This is certainly also due to the value of the position solutions obtained during data acquisition.

This is even more confirmed by looking at other approaches. In fact, in the case of "Forward" approach, both the patch and geodetic antennas perceive very high trend variation among velocity and position, almost touching one meter of RMS value on N-S and U-D coordinate for the right patch (see Figure 73 and 74).

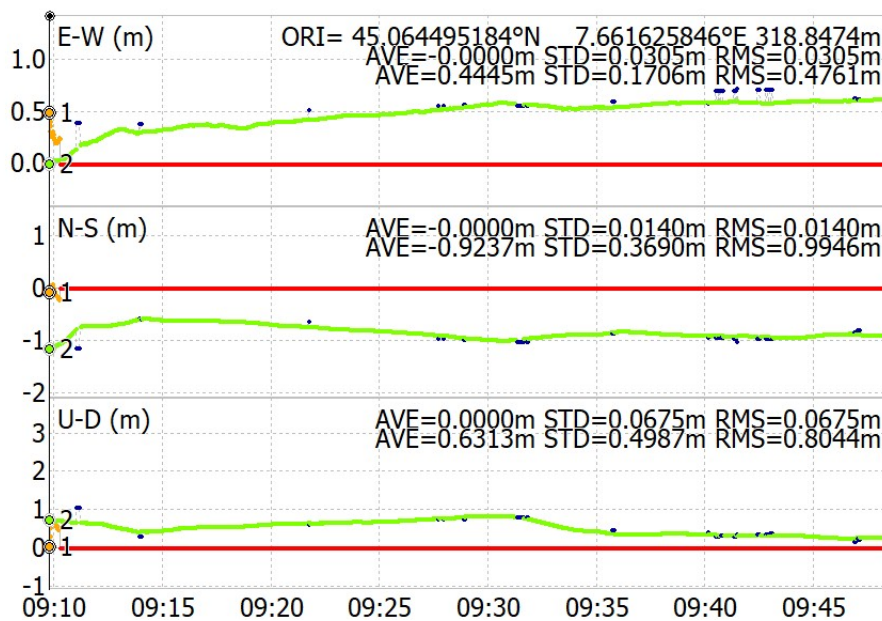


Figure 73: Position variation of right omnidirectional and patch antenna with "Forward" filter.

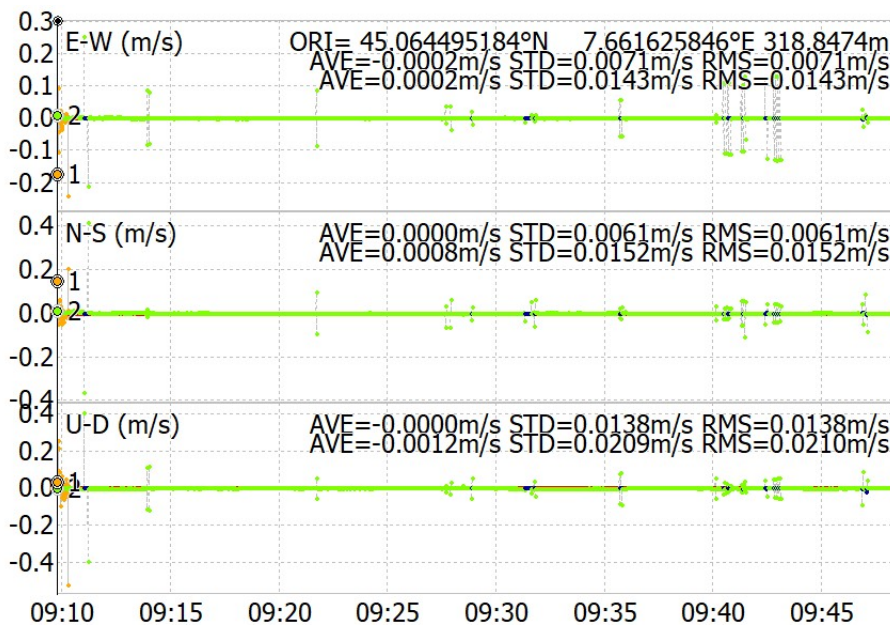


Figure 74: Velocity variation of right omnidirectional and patch antenna with "Forward" filter.

However, unlike what has just been said, the **limit case** of this configuration was obtained using the "Combined" approach as a Kalman filter and setting "continuous" for the GPS and Fix& Hold for the GLONASS ambiguity resolution. Tables 8 and 9 display what mentioned above.

Omnidirectional antennas		
	DX	SX
Position solution	Q=1(100%)	Q=1(100%)
N° of satellites	8, then 7	8, then 7
Pseudorange residuals(m)	//	AVE = -0.040m; STD = 0.0854m ; RMS = 0.0855m
Carrier-Phase residuals(m)	//	AVE = 0.004m; STD = 0.004m ; RMS = 0.005m

Table 8: Omnidirectional antennas: "Combined" filter, Continuous and Fix&Hold ambiguity resolution approach for GPS and GLONASS respectively.

Patch antennas		
	DX	SX
Position solution	Q=1(40.2%); Q=2(59.8%)	Q=1(100%)
N° of satellites	8, then 7	8, then 7
Pseudorange residuals(m)	AVE = -0.691m; STD = 4.047m; RMS = 4.105m	AVE = 1.625m; STD = 1.880m; RMS = 2.485m
Carrier-Phase residuals(m)	AVE = 0.001m; STD = 0.075m; RMS = 0.075m	AVE = -0.004m; STD = 0.010m; RMS = 0.011m

Table 9: Patch antennas: "Combined" filter, Continuous and Fix&Hold ambiguity resolution approach for GPS and GLONASS respectively.

7.3 Reversed configuration: static positioning technique

Here is presented the second configuration, that is, the patch antenna on the right is internally rotated by 180°, in order to verify whether such a change can modify the performance of the baseline. Even in this case, as in the previous one, the data post-processing was conducted using two different types of Kalman filters and setting the resolution of ambiguity in different combinations.

Despite what we saw in the just analysed case, in the reversed configuration, the best performance was obtained using the "Combined" approach but setting the ambiguity resolution for GPS and GLONASS to "Continuous" and "Fix& Hold". It is not a surprise that other cases show worse results, where the GLONASS ambiguity is turned off (set to "Off").

Omnidirectional antennas		
	DX	SX
Position solution	Q=1(100%)	Q=1(100%)
N° of satellites	6, then 7	6, then 7
Pseudorange residuals(m)	AVE = 0.072m; STD = 0.901m ; RMS = 0.904m	AVE = -0.151m; STD = 0.0847m ; RMS = 0.0861m
Carrier-Phase residuals(m)	AVE = 0.001m; STD = 0.001m ; RMS = 0.006m	AVE = 0.002m; STD = 0.005m ; RMS = 0.005m

Table 10: Omnidirectional antennas: "Combined" filter, Continuous and Fix&Hold ambiguity resolution approach for GPS and GLONASS respectively.

Patch antennas		
	DX	SX
Position solution	Q=1(63.2%); Q=2(36.8%)	Q=1(100%)
N° of satellites	6, then 7	6, then 7
Pseudorange residuals(m)	AVE = -2.766m; STD = 5.974m; RMS = 6.583m	AVE = 0.609m; STD = 2.449m; RMS = 2.523m
Carrier-Phase residuals(m)	AVE = 0.000m; STD = 0.050m; RMS = 0.050m	AVE = -0.001m; STD = 0.035m; RMS = 0.035m

Table 11: Patch antennas: "Combined" filter, Continuous and Fix&Hold ambiguity resolution approach for GPS and GLONASS respectively.

From Tables 10 and 11 can be seen a tremendous rise of patch parameters estimation. In fact, taking in consideration the right side of the baseline, patch antenna has both standard deviation and RMS value six times higher than the geodetic one. This is further confirmed by the number of available satellites and the quality of position solution.

Below are reported the graphs of Ground Track, Number of available satellites and Pseudorange and Carrier-Phase residuals of the best performing case. As can be seen from Figure 75 and 76, the antennas on the right have a more scattered quality of solutions than those on the left which have the totality of fixed solutions ($Q = 1$). This is also confirmed by the graph of the number of satellites available (see Figure 77) which has a much less stable trend than the one in Figure 78.

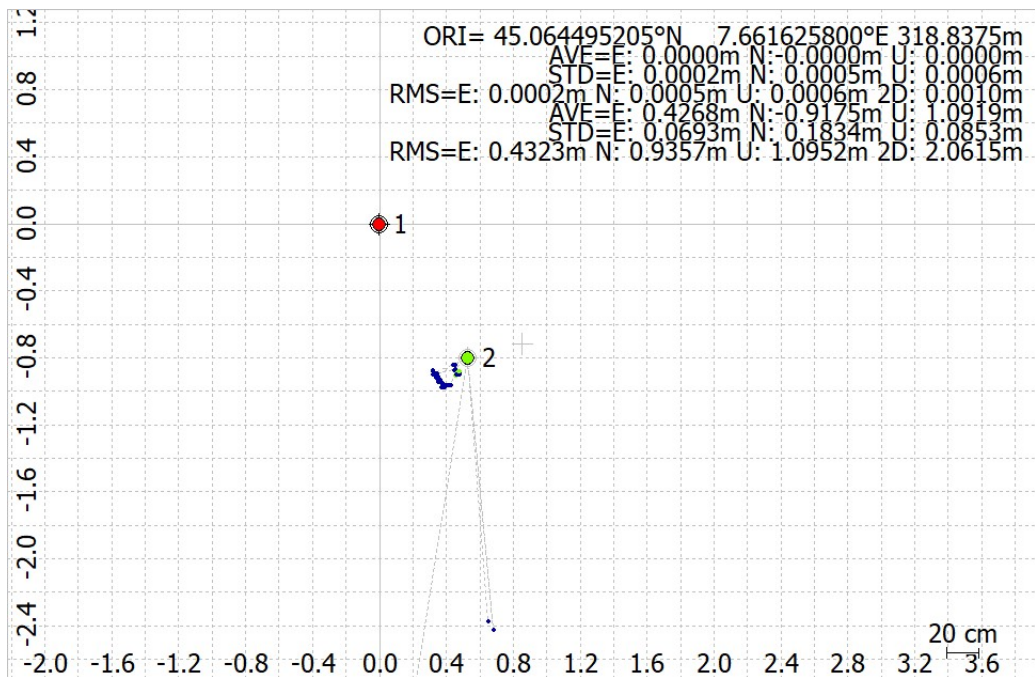


Figure 75: Ground Track of right antennas: omnidirectional in red and patch in green-blue.

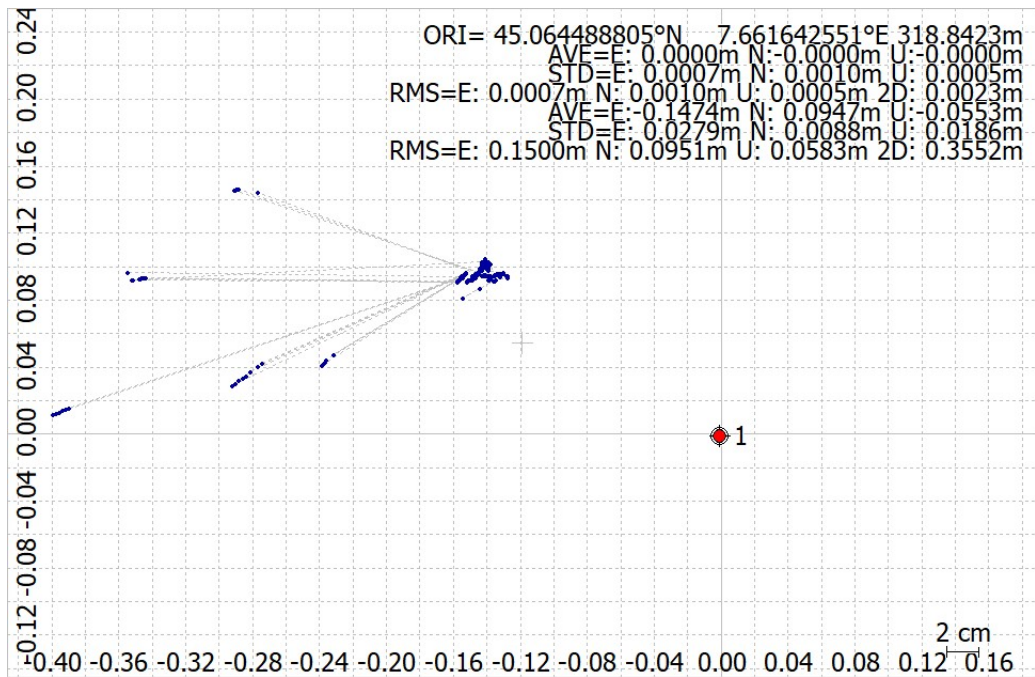


Figure 76: Ground Track of left antennas: omnidirectional in red and patch in blue.

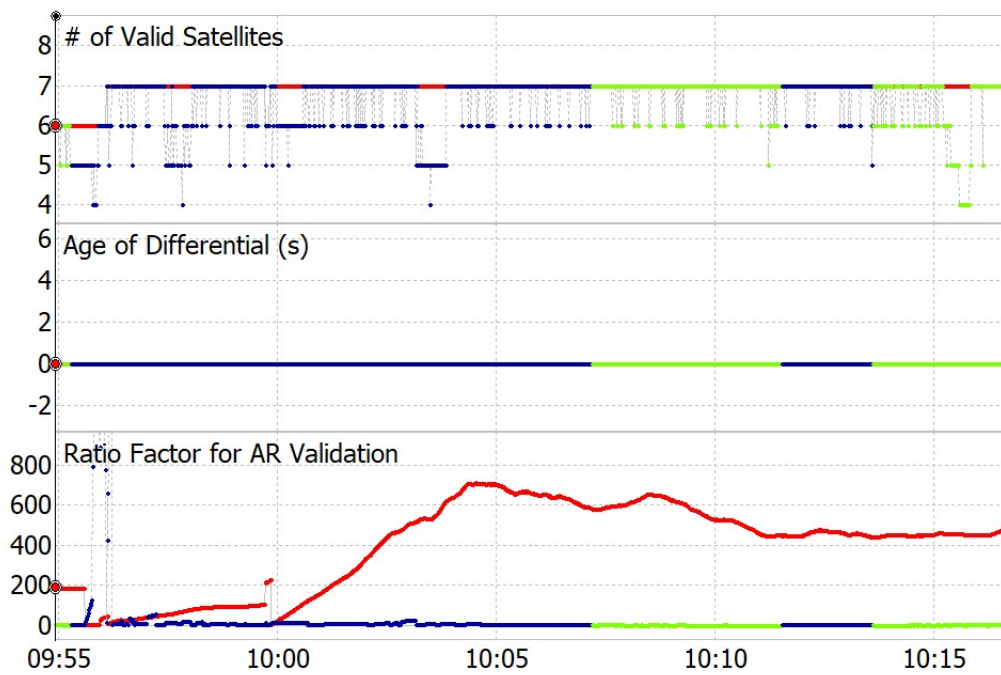


Figure 77: Number of available satellites of right antennas: omnidirectional in red and patch in green-blue.

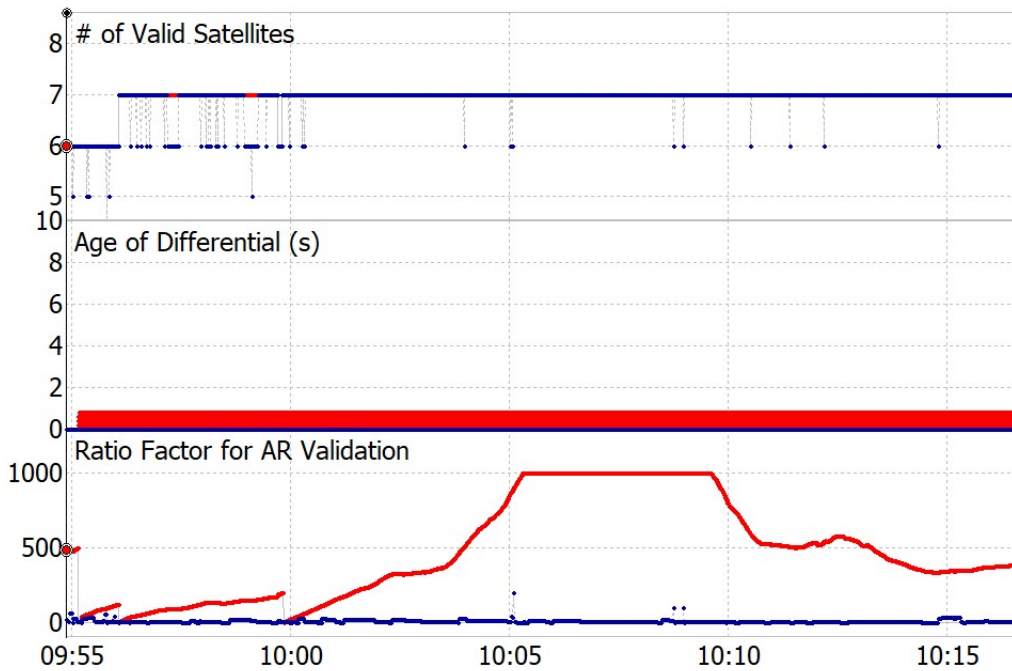


Figure 78: Number of available satellites of left antennas: omnidirectional in red and patch in blue.

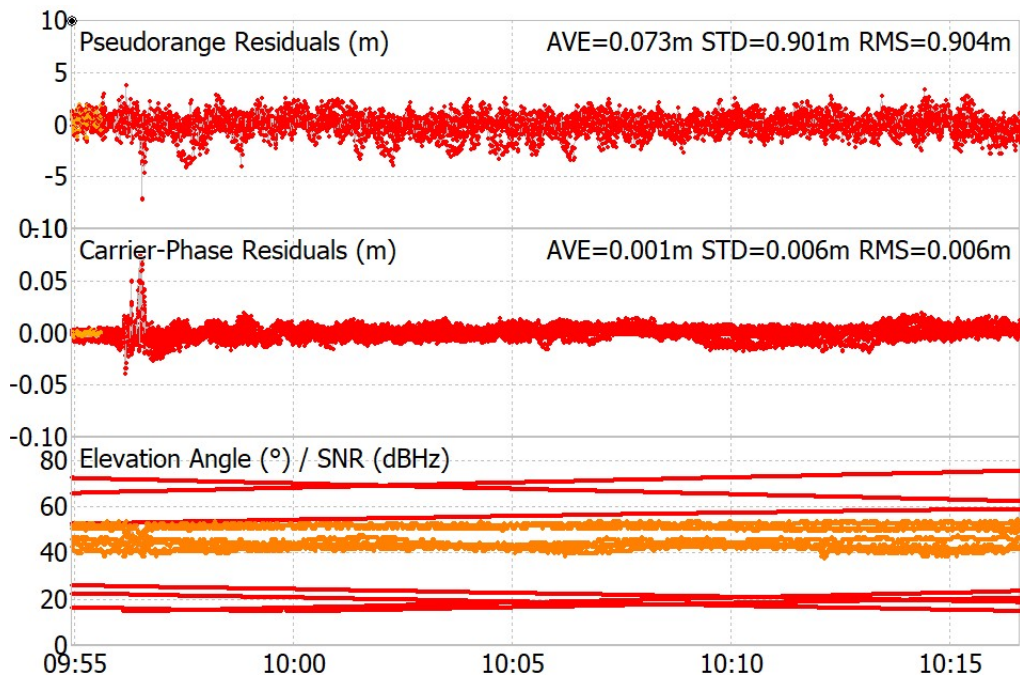


Figure 79: Pseudorange and Carrier-Phase residuals of right omnidirectional antenna.

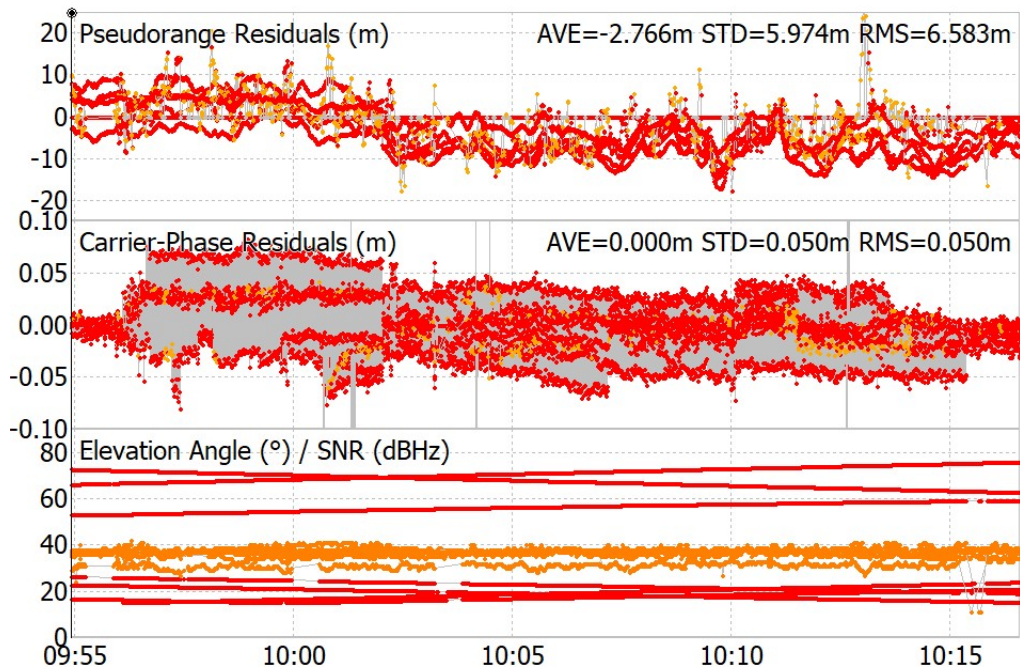


Figure 80: Pseudorange and Carrier-Phase residuals of right patch antenna.

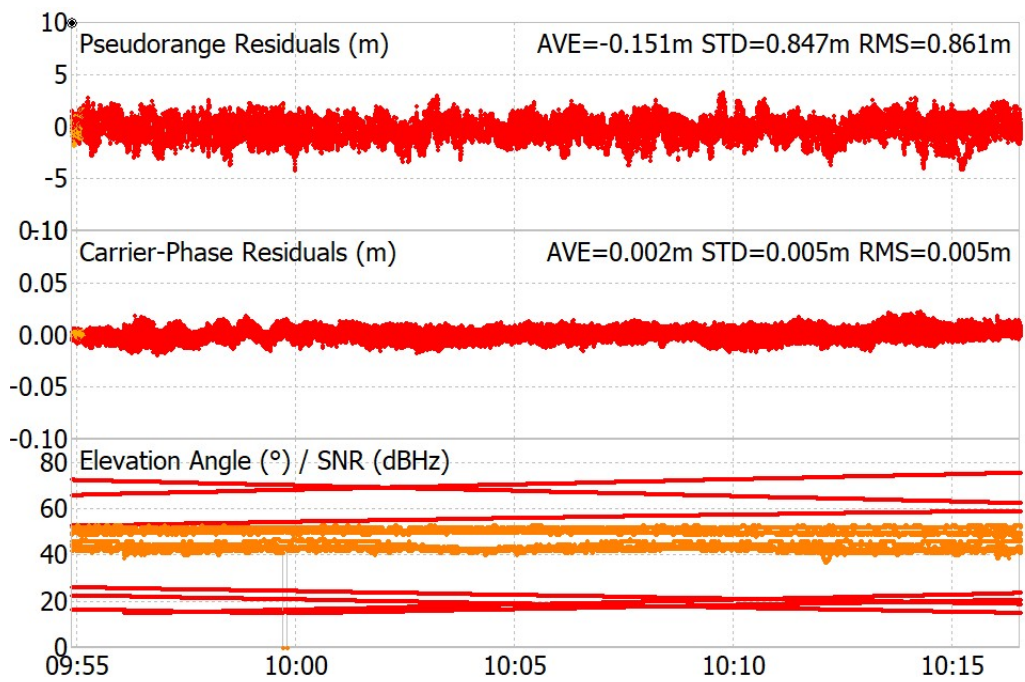


Figure 81: Pseudorange and Carrier-Phase residuals of left omnidirectional antenna.

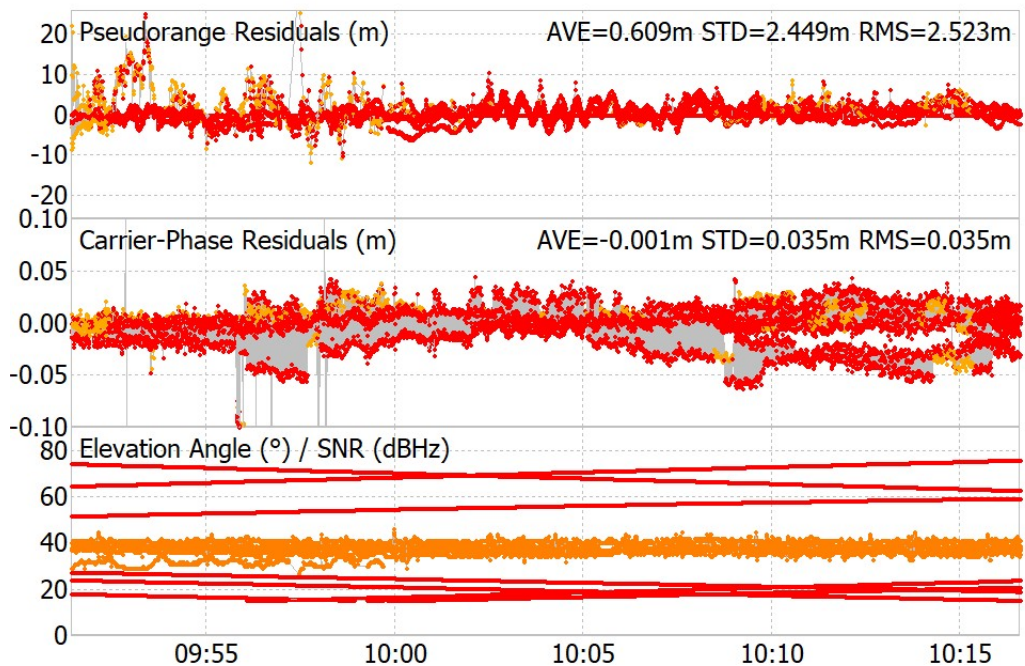


Figure 82: Pseudorange and Carrier-Phase residuals of left patch antenna.

Continuing the analysis, the case with the worst estimate values is certainly the one with the "Forward" approach with both resolutions of ambiguity fixed. This is attributable to the filter itself. In fact, using the Forward approach, certainly more suited for the type of surveys carried out (real-time solutions), the data are filtered from the beginning to the end of the observation

window. This means that, when anomalies should occur during data acquisition, user could run into the loss of fixed solutions. However, this does not happen with the Combined approach since these anomalies are checked both in forward and backward, and subsequently discarded in both directions.

Omnidirectional antennas		
	DX	SX
Position solution	Q = 1 (96.9%); Q = 2 (3.1%)	Q = 1 (96.9%); Q = 2 (3.1%)
N° of satellites	6, then 7	6, then 7
Pseudorange residuals(m)	AVE = 0.074m; STD = 0.902m ; RMS = 0.905m	AVE = -0.151m; STD = 0.0847m ; RMS = 0.0861m
Carrier-Phase residuals(m)	AVE = 0.001m; STD = 0.006m ; RMS = 0.006m	AVE = 0.002m; STD = 0.005m ; RMS = 0.005m

Table 12: Omnidirectional antennas: "Forward" filter, Fix&Hold ambiguity resolution approach for both GPS and GLONASS.

Patch antennas		
	DX	SX
Position solution	Q = 1 (8.4%); Q = 2 (91.6%)	Q = 1 (34.4%); Q = 2 (65.6%)
N° of satellites	6, then 7	6, then 7
Pseudorange residuals(m)	AVE = -3.131m; STD = 6.086m; RMS = 6.844m	AVE = 0.562m; STD = 2.447m; RMS = 2.510m
Carrier-Phase residuals(m)	AVE = -0.003m; STD = 0.042m; RMS = 0.042m	AVE = -0.001m; STD = 0.034m; RMS = 0.034m

Table 13: Patch antennas: "Forward" filter, Fix&Hold ambiguity resolution approach for both GPS and GLONASS.

Tables 12 and 13 show the estimation parameters of geodetic and patch antennas. What can be underlined is that the difference in both standard deviation and RMS values is not that high. In fact, the variation between the two approaches is minimal but still noteworthy.

7.4 Dynamic configuration: Kinematic positioning

In this section we will talk about the results obtained in dynamic acquisitions, therefore with the baseline anchored to the rotating platform, resting on the tripod to stabilize the setup. Unlike static acquisitions, here a Kinematic approach has been used since the baseline is no longer static but moves with uniform circular motion.

What came out from the analysis was that the best solution has been achieved by the Normal configuration, particularly the right antennas of the baseline.

Figure 83 show the Ground Track in a 180° continuous rotation at 5°/s rate. Here we are dealing

with the Kinematic positioning technique: TORI virtual station is alternated as Master Station between patch and omnidirectional antenna in order to verify the Rover Station behaviour.

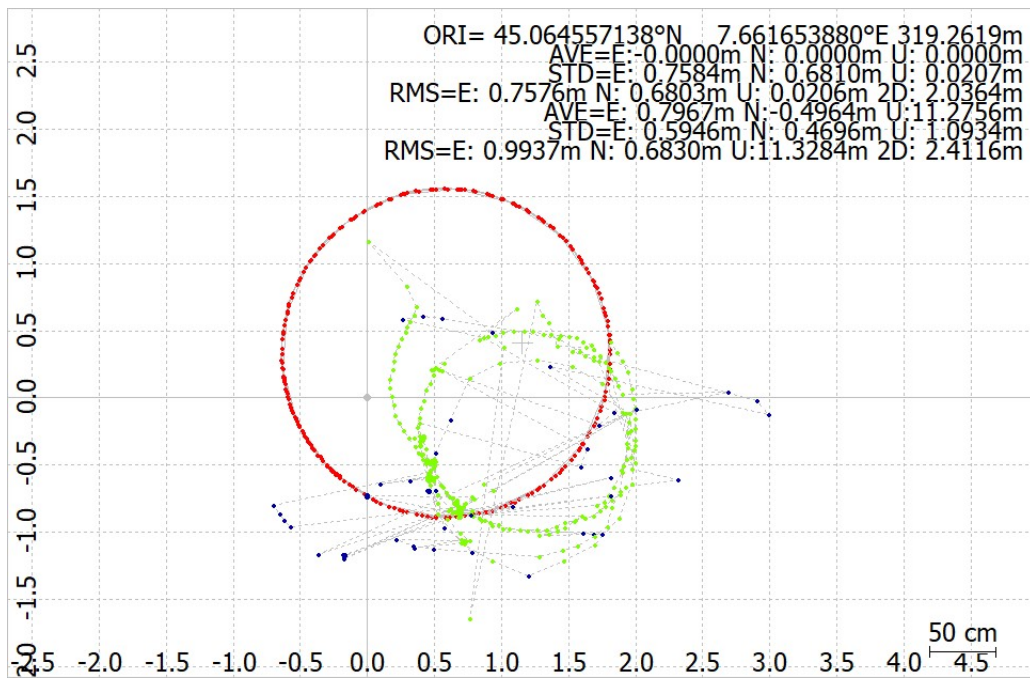


Figure 83: Right side continuous rotation: ground track.

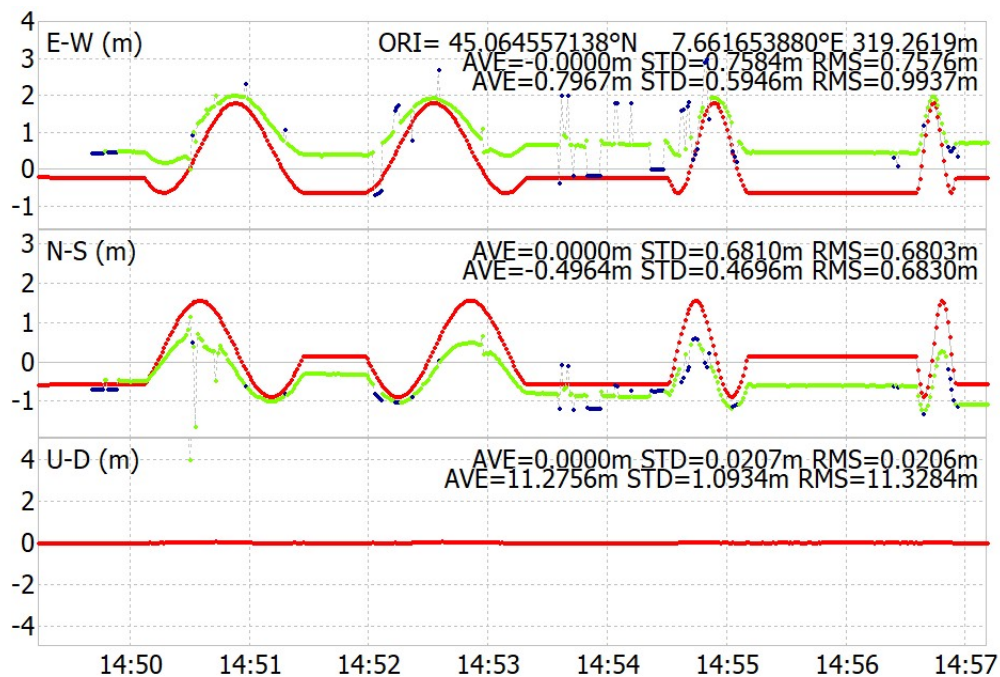


Figure 84: Right side continuous rotation: position variation over coordinates.

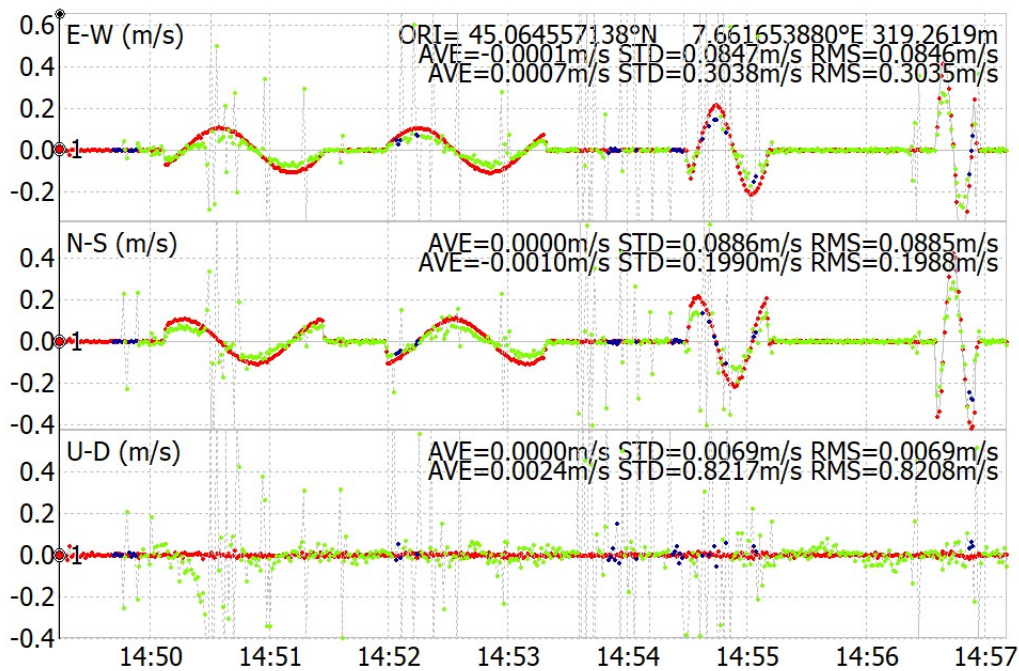


Figure 85: Right side continuous rotation: velocity variation over coordinates.

Omnidirectional antennas maintain a 100% of fixed solution during all the observation time while microstrips only 14.3%. The rest 85.7% is a float solution ($Q = 2$). What can be underlined is that unexpectedly, the trajectories described by both antennas should have been two concentric circles. The fact that they are not is certainly due to the poor quality of the patch antenna. In fact, the geodetic antenna describes a perfect circumference as opposed to what happens in the other. In a hypothetical scenario where this type of baseline is mounted on a drone, the high speed, sudden changes of position and the noise introduced by the engine, would cause further introductions of noise. This would result in an even more disturbed and imprecise system.

In this case, the most interesting observations are certainly visible in the graphs of the variation of speed (see Figure 85) and position (see Figure 84). In fact, unlike the previous acquisition mode, in this one the baseline moves in a circular motion. Thanks to the simple theory of physics, we know that circular motion can be decomposed into two components: sine and cosine. Therefore, it is clear that both trends assume a sinusoidal trend in time and space. From the point of view of statistical parameters, small differences can be found between the two sides of the baseline. In fact, both the standard deviation and the Root Mean Square take on an almost equal value. In addition to what has been said, we can underline that the moment of inversion of the platform corresponds to the flat trends of the sinusoid. In fact, once a turn angle was described, the platform was reset to make the same journey but in reverse. Figure 86 show the number of visible satellites during the observation window. As for static acquisition, we may also see some similarities in dynamic acquisition. In particular, the number of valid satellites stay constant over time for omnidirectional antenna while variable for the microstrip. The number of valid satellites assumes a very interesting behaviour. In fact, despite to what was expected, among the observation window, it has a higher number of available satellites.

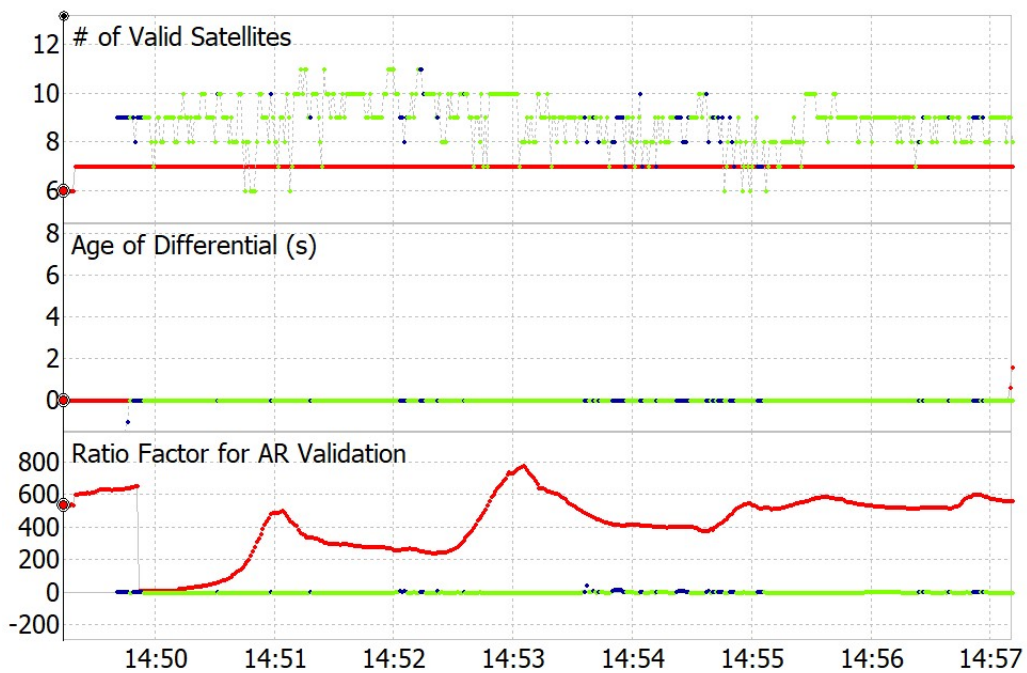


Figure 86: Right side continuous rotation: available satellites over time.

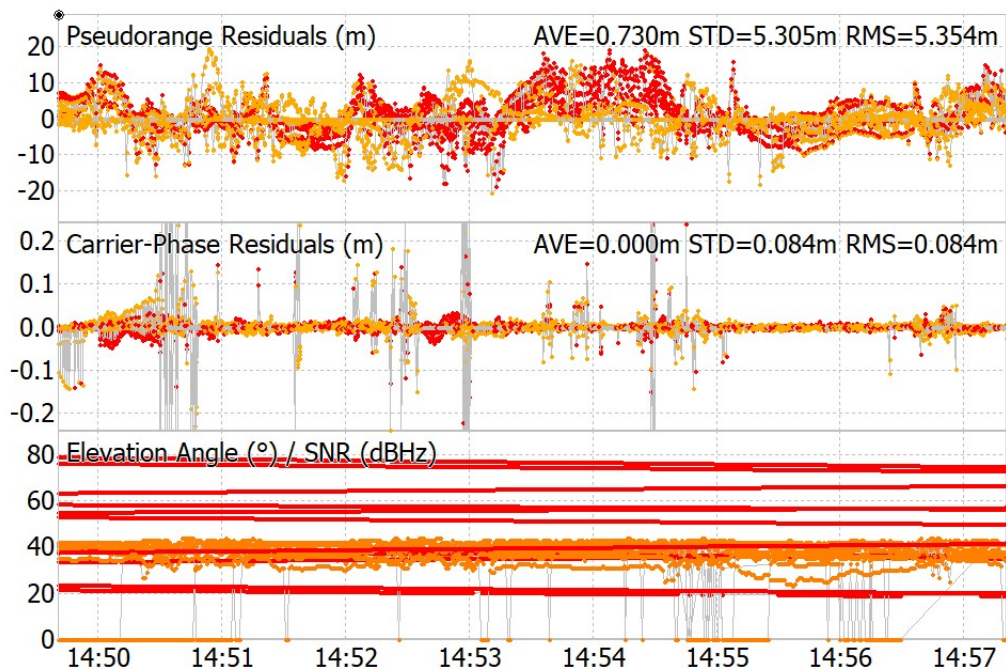


Figure 87: Pseudorange and Carrier-Phase residuals of patch antenna.

Figure 87 show the Pseudorange and Carrier-Phase Residuals with their related Elevation Angle over SNR. Unfortunately, the Pseudorange Residuals for the right omnidirectional antenna is not shown. In fact, RTKLIB was not able to provide this data during the post-processing phase. Conversely, the right microstrip residuals are shown. As can be seen from the figure, patch

residuals never remains between the range of ± 5 , therefore having a noisy result.

Right side baseline antennas		
	Omnidirectional	Patch
Position solution	Q = 1 (100%)	Q = 1 (14.3%); Q = 2 (85.7%)
N° of satellites	6, then 7	From 6 to 10
Pseudorange residuals(m)	//	AVE = 0.730m; STD = 5.305m; RMS = 5.354m
Carrier-Phase residuals(m)	//	AVE = 0.000m; STD = 0.084m; RMS = 0.084m

Table 14: Right baseline antennas: best performance case for dynamic continuous acquisition mode.

Table 14 show the estimation parameters of the best performance case in dynamic continuous acquisition.

Within the same configuration, as already explained in the Post-processing section, a stepped acquisition of the baseline was performed (see Tables 4 and 5). In this mode the best performance was recorded from the left side of the setup.

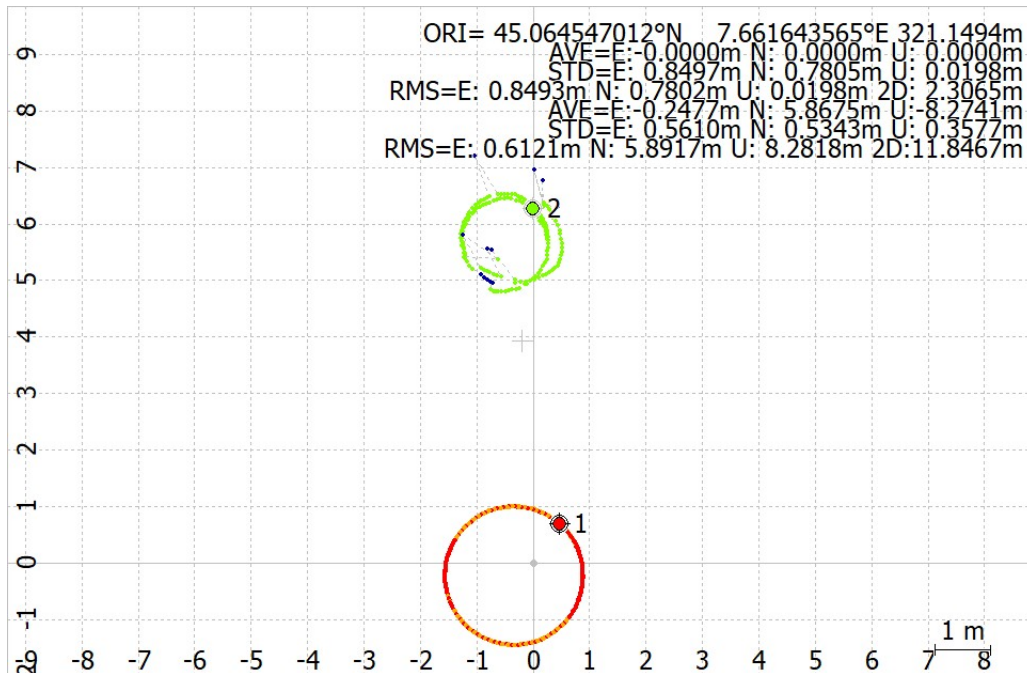


Figure 88: Left side continuous rotation: Ground track.

Even in this case, as in the previous one, the trajectories described by the antennas are not concentric (see Figure 88). The geodetic antenna always maintains an optimal behavior, describing a perfect circumference. With the introduction of a stepped and non-continuous movement, the system seems to suffer even more. In fact, the two antennas are 3 meters apart,

which is not true since their real distance in the baseline is only few centimeters. In fact, due to the momentum and fluctuations of the baseline support, there is a further introduction of disturbances and noises that make the system less accurate.

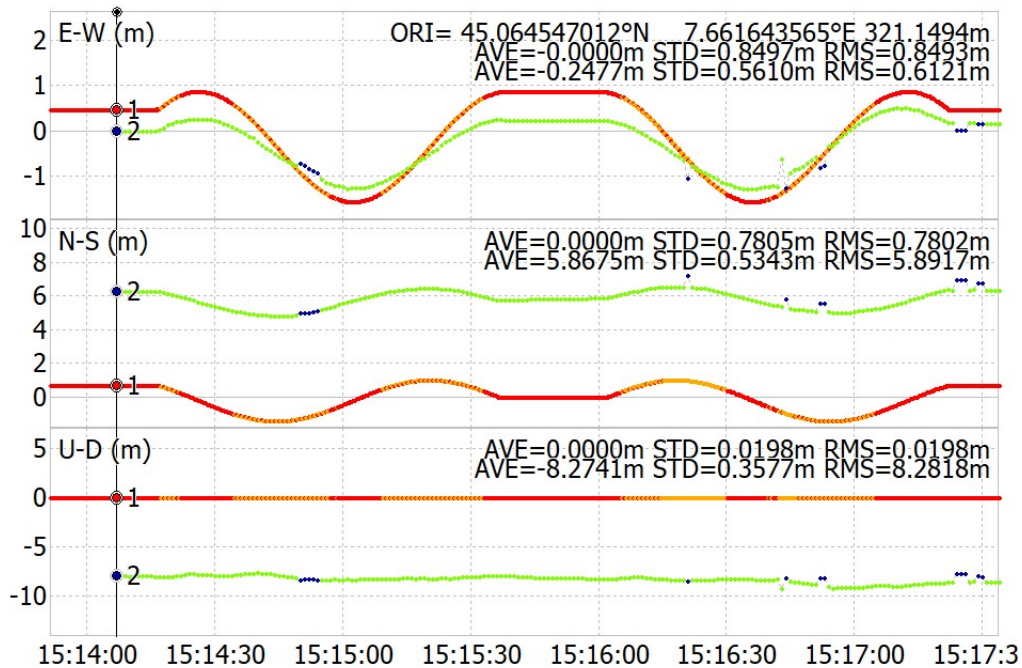


Figure 89: Position variation over coordinates of left side baseline antennas.

Figure 89 shows the change in position during the observation window. Even in this case, the variations give on the E-W and N-S coordinates describe sinusoidal curves. Result more than expected since it moves in a circular motion. It should be emphasized that, in the middle of the acquisition, there is a stationary moment in which both antennas do not perceive any type of variations. This is not a coincidence as it corresponds to the moment in which, after the 180° turn, the rotating platform was reset to perform the same movement and return to the initial position.

This behavior is further confirmed by the speed variation graph. Even in this case the two antennas move with the same speed but with different wavelengths since the radius of circumference described is not the same. In addition, the static condition of the system is visible in the center of the graph.

As already verified in most of the cases analyzed, Figure 91 shows how the omnidirectional antenna receives a greater number of satellites than the patch and also in a clean and undisturbed way.

Finally, Figure 92 show the Pseudorange and Carrier-Phase residuals. Having only the graph of the patch antenna residuals available, we notice how it has a very disturbed trend and does not fall within the range of ± 5 m, therefore reaching high variation of parameter estimation.

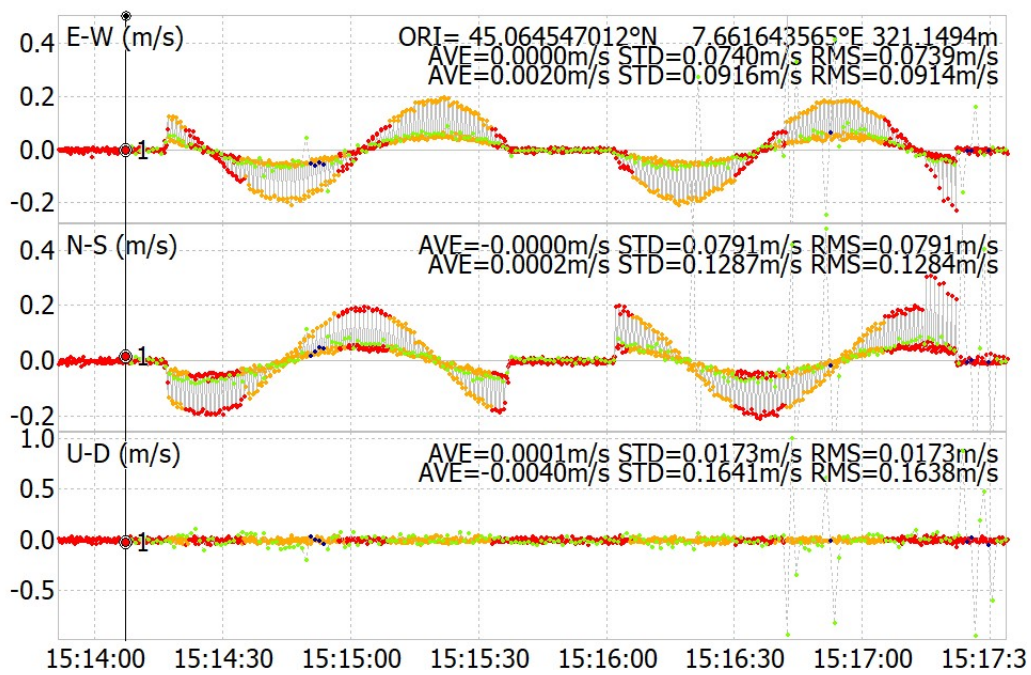


Figure 90: Velocity variation over coordinates of left side baseline antennas.

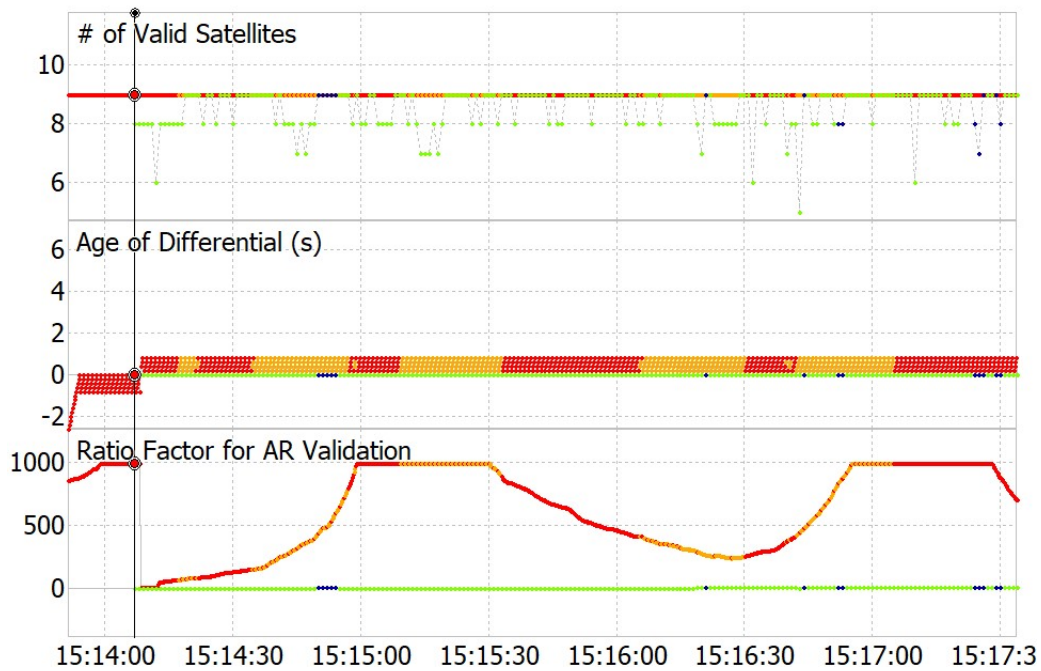


Figure 91: Number of available satellites through observation window.

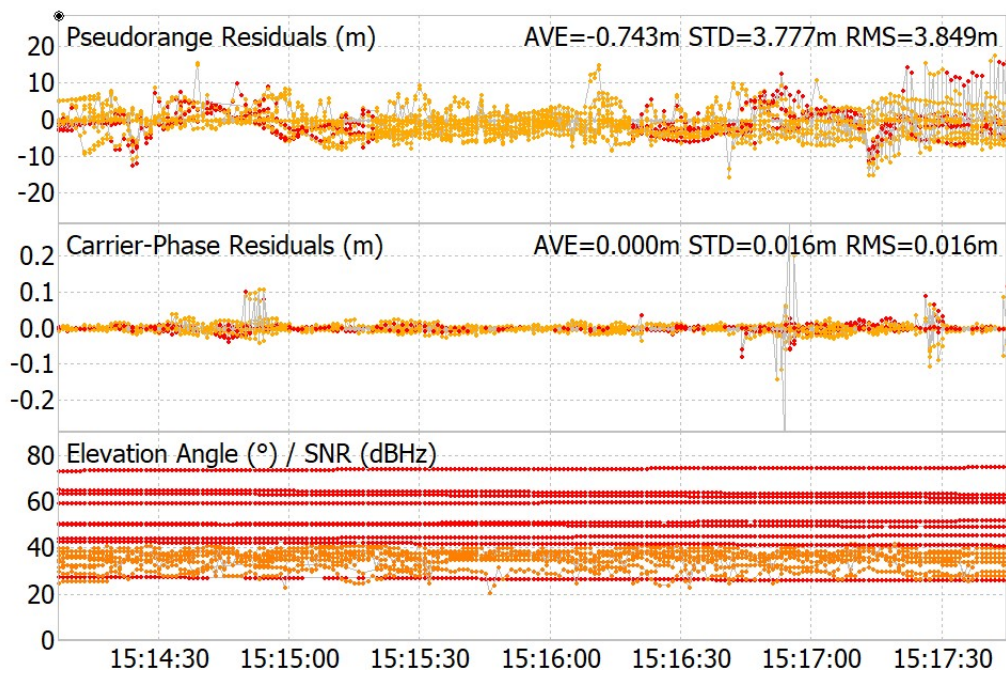


Figure 92: Pseudorange and Carrier-Phase residuals of left patch antenna.

Right side baseline antennas		
	Omnidirectional	Patch
Position solution	Q = 1 (64.2%); Q = 2(35.8%)	Q = 1 (7.3%); Q = 2 (92.7%)
N° of satellites	9	From 7 to 9
Pseudorange residuals(m)	//	AVE = -0.734m; STD = 3.77m; RMS = 3.849m
Carrier-Phase residuals(m)	//	AVE = 0.000m; STD = 0.016m; RMS = 0.016m

Table 15: Left reversed baseline antennas: best performance case for dynamic continuous acquisition mode.

Table 15 summarizes what has just been said.

To complete the analysis of dynamic acquisitions, lasts only one case in which the acquisitions were made with the stepped approach. The platform was programmed to turn with an angular velocity of $5^\circ/s$ for a trajectory of 200° . In this way we wanted to make the description of an angle of 180° visible as much as possible. The best performance was obtained by the left antennas of reversed baseline configuration.

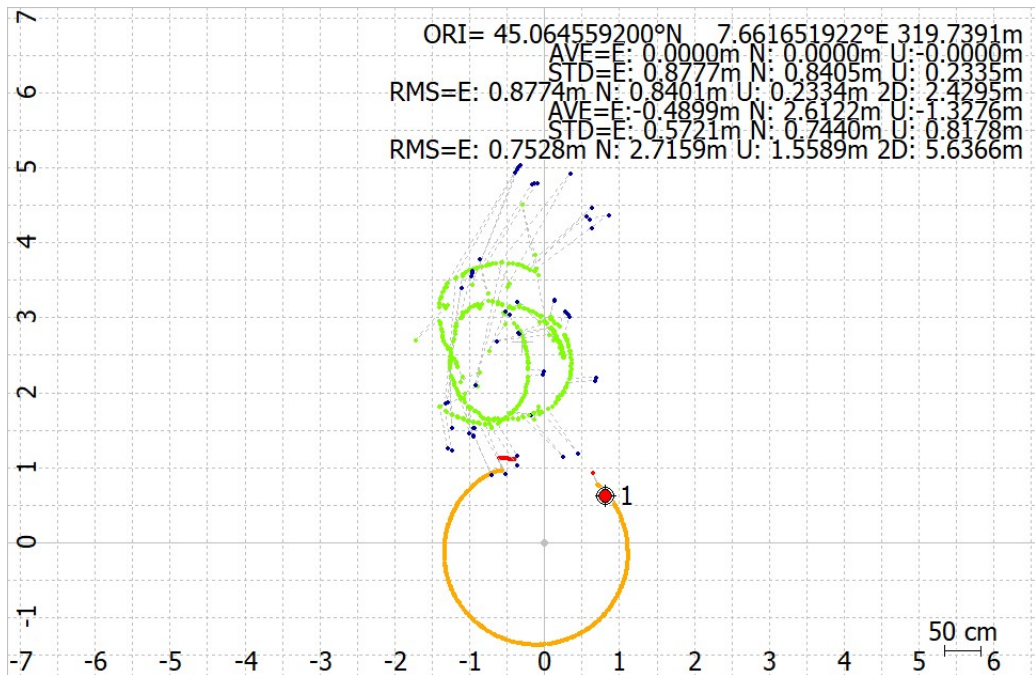


Figure 93: Left side stepped rotation: Ground track.

According to what has just been said, Figure 93 shows how the described trajectory of omnidirectional antenna is not equal to 360° but rather 200° . The same behavior should be seen in the patch antenna but, again due to the poor quality, it is not possible to find this data.

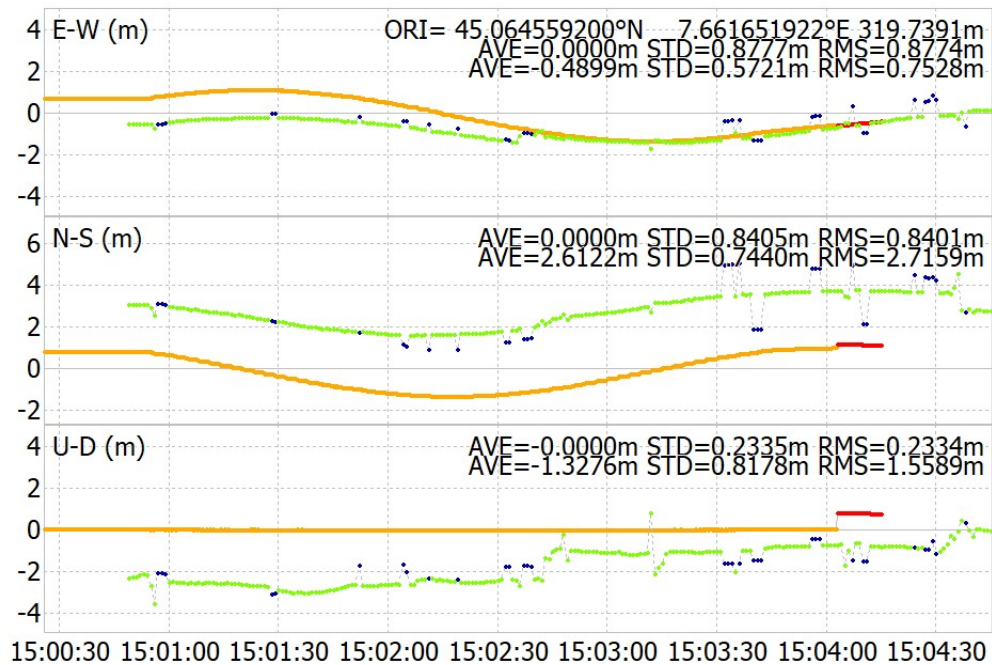


Figure 94: Position variation over coordinates of left side baseline antennas.

From Figure 94 is possible to see the position variation through coordinates. As can be seen,

the patch antenna shows a delay at the beginning of the graph. This is due to the fact that, during the acquisition phase, geodetic antenna's acquisition have been started 20s before the patch ones.

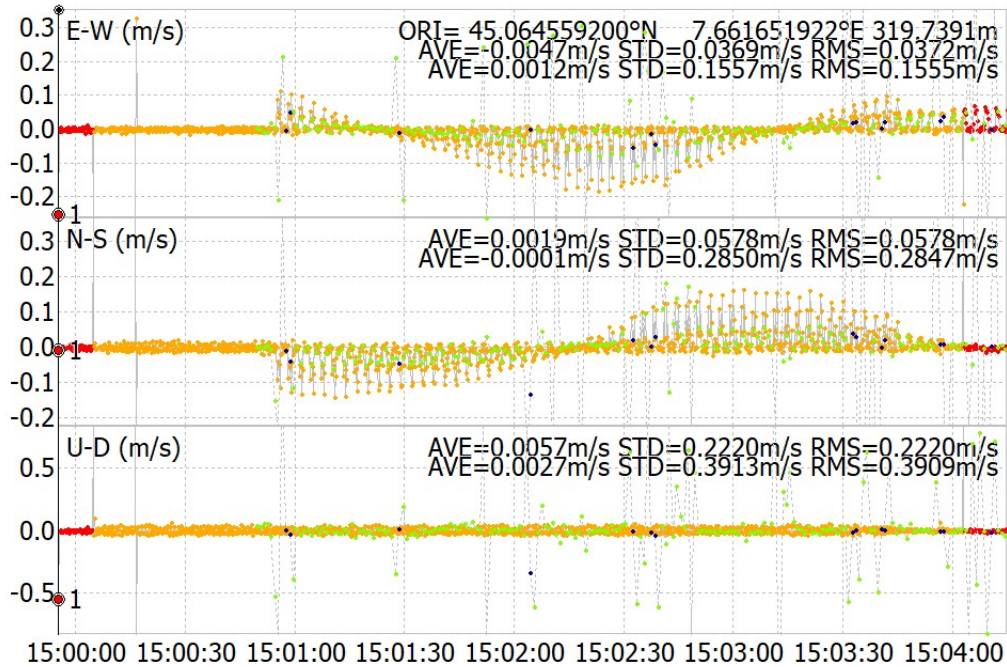


Figure 95: Velocity variation over coordinates of left side baseline antennas.

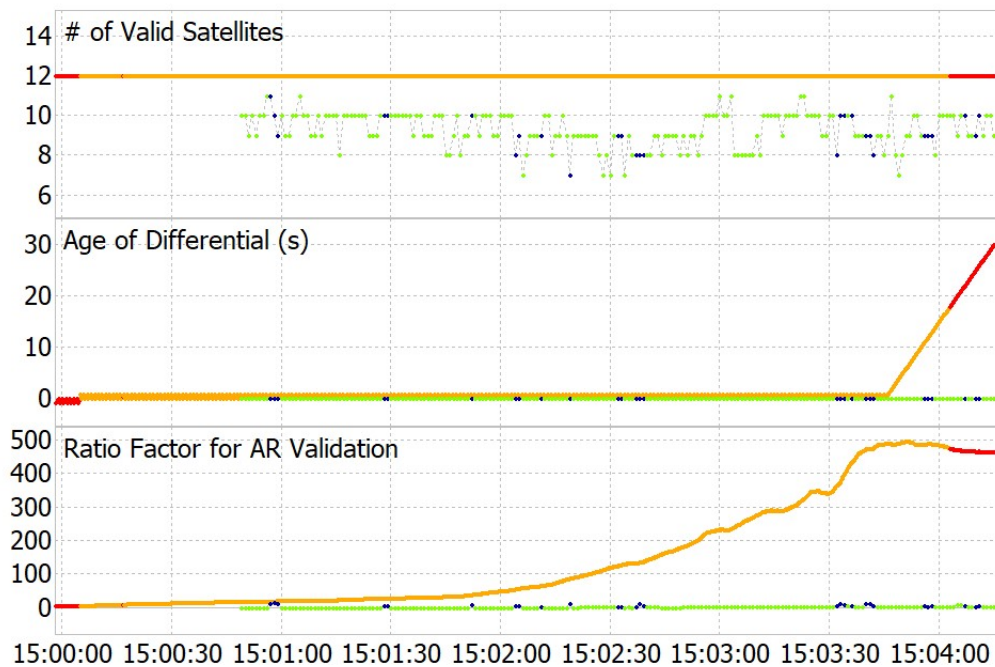


Figure 96: Number of available satellites through observation window.

As expected, patch antenna has same position variations of geodetic ones. The only thing is

that over U-D coordinate, omnidirectional antenna does not sense any type of changes (there is only a rotation, the tripod is fixed to the ground) instead the patch antenna senses a negative variation of quote, reaching 2 meters of value.

This strange behaviour is confirmed even by the number of available satellites. In fact, during the data acquisition, the available satellites for patch antenna never reached a constant trend but continuously oscillates through the time.

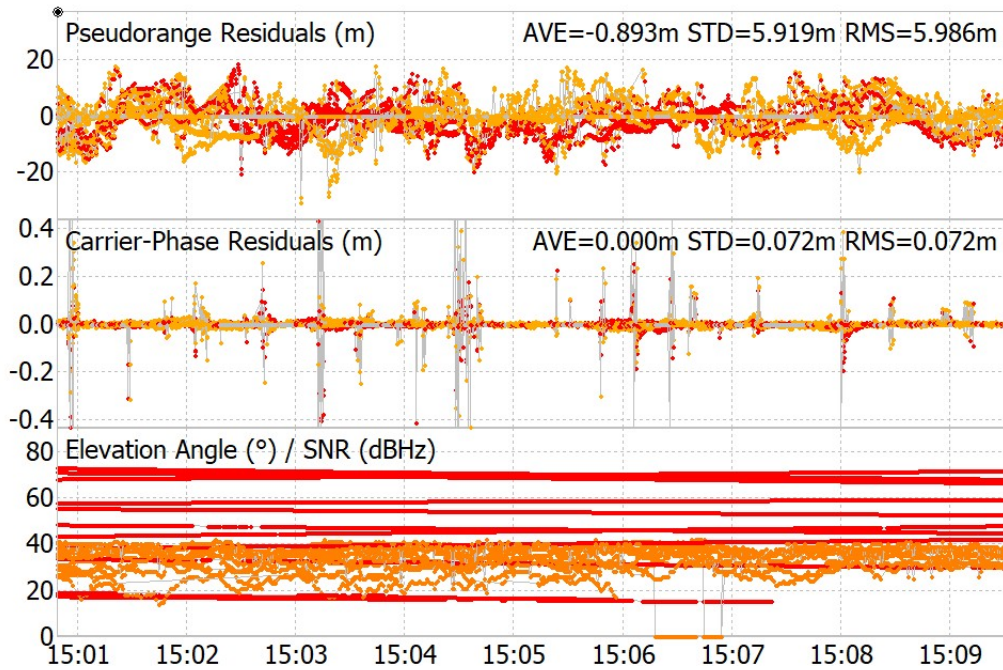


Figure 97: Pseudorange and Carrier-Phase residuals of left patch antenna.

Right side baseline antennas		
	Omnidirectional	Patch
Position solution	Q = 1 (88.9%); Q = 2(11.2%)	Q = 1 (7.3%); Q = 2 (92.7%)
N° of satellites	12	From 7 to 10
Pseudorange residuals(m)	//	AVE = -0.893m; STD = 5.919m; RMS = 5.986m
Carrier-Phase residuals(m)	//	AVE = 0.000m; STD = 0.072m; RMS = 0.072m

Table 16: Left reversed baseline antennas: best performance case for dynamic stepped acquisition mode.

To sum up, Table 16 displays the discussed results.

7.5 Bearing angle estimation: experimental setup

Bearing estimation has been done as expressed in GNSS Attitude section. The evaluation was conducted following two approaches:

- Bearing estimation from rotation of Multi-GNSS antennas setup;
- Bearing estimation from UAV platform rotation using a single receiver, combined with onboard sensors (magnetometer and gyroscope).

Clearly it was considered only the omnidirectional baseline since it was able to provide better post-processed results has already explained before.

Bearing angle for evaluated by following these steps:



Diagram : Bearing estimation workflow.

Dataset has been imported by using the *pandas* Python library. Since it was full of "not a number" (NaN), it was filtered in order to obtain clear input datas. Subsequently, variables have been initialized: in particular, three variables have been created: "baseline", " V_n " and "theta". They represent, respectively, the baseline vector (distance between the two antennas), North vector (a vector that points to the magnetic North) and bearing angle vector (it is formed between the North vector and the antennas' baseline).

Once variables have been declared, parameters have been estimated. As regards the calculation of the baseline, at each epoch the quadratic distance between the North and East coordinates of the two antennas is estimated.

$$Baseline[i] = \sqrt{(E1[i] - E2[i])^2 - (N1[i] - N2[i])^2} \quad (28)$$

In this way, at each instant of time, the baseline length variation, over time, is obtained.

The north vector, on the other hand, is estimated as the difference between the north coordinates of the two antennas.

$$Northvector[i] = N1[i] - N2[i] \quad (29)$$

Finally, the bearing angle is evaluated, given by the cosine of the ratio between the north vector and the baseline. In this way, we obtained a final vector, containing, at each time epoch, the bearing angle variation.

$$\theta[i] = \cos \frac{V_n[i]}{Baseline[i]} \quad (30)$$

What came out is that the estimation of the bearing angle, using the experimental setup, is very different from reality. In fact, the baseline estimation, during the rotation of the platform, deviates about 20 cm compared to the real distance (see Figure 98). On the other hand, the bearing angle does not assume an optimal behavior, showing a very disturbed trend. As expected, the bearing angle should have started from 0° , reached 180° and, after a short period of steadiness, it should have dropped again and returned to 0° (see Figure 99). This is certainly due to the oscillations of the setup, the additional noise of the patch antennas and an inappropriate movement of the antenna and receiver cables during rotation.

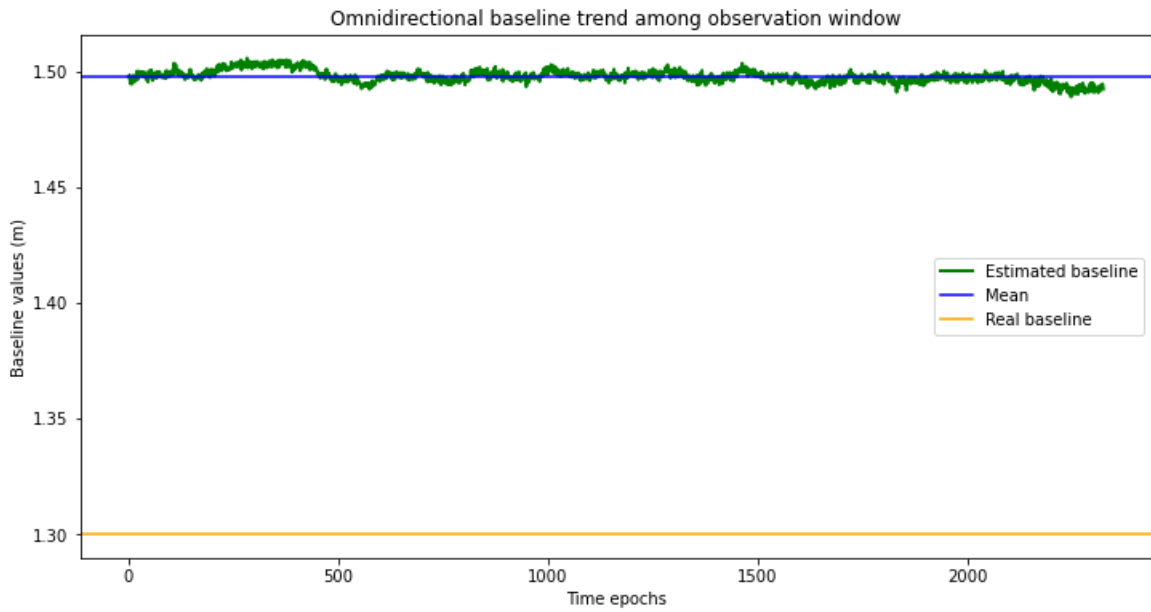


Figure 98: Baseline estimation of omnidirectional antennas in continuous rotation.

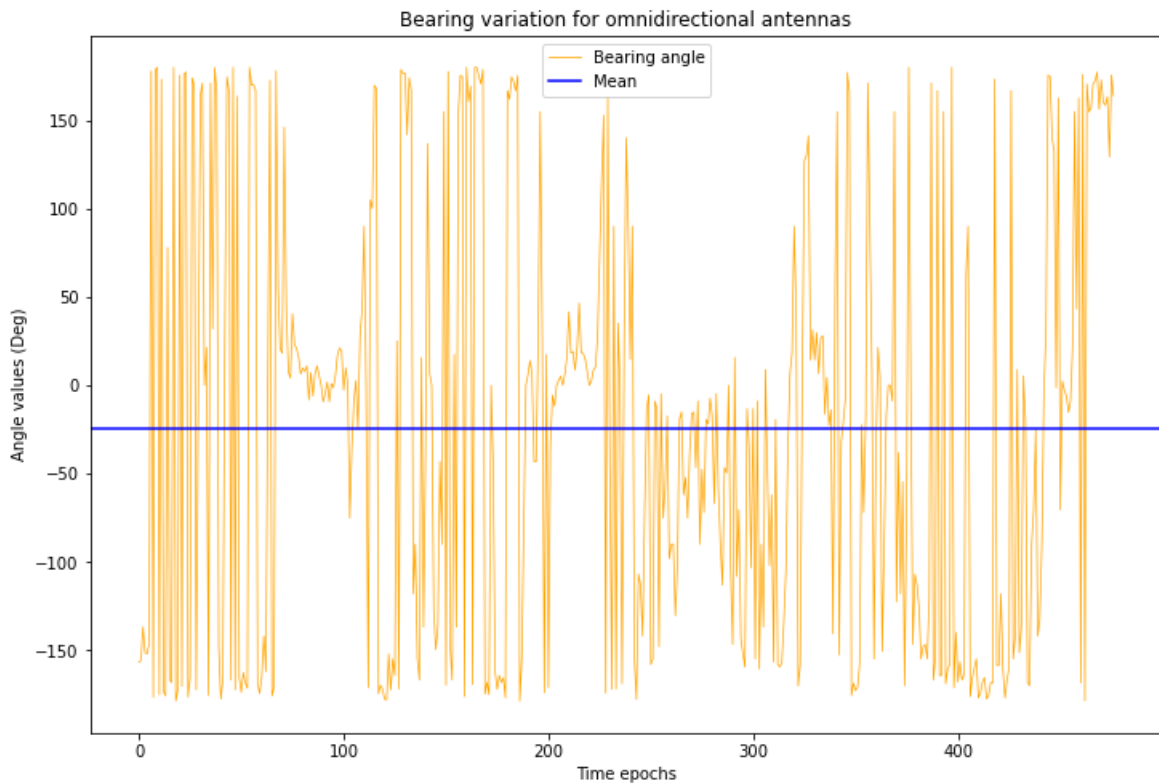


Figure 99: Bearing estimation of omnidirectional antennas in continuous rotation.

Putting all these factors together, it is not possible to obtain an optimal estimation. This underlines how, in systems like these, where a high accuracy of the measurements is required,

a perfect setting of the baseline configuration is necessary. In addition, even high performance antennas, such as the geodetic antenna, can be affected by the proximity of inferior quality antennas such as the patch one.

7.6 Bearing angle estimation: UAV Platform.

If on one hand the baseline and bearing angle estimation differs considerably from the real case, the tests carried out on the UAV platform have provided excellent results. In fact, through the use of a less complex setup and the addition of on-board sensors such as magnetometer and gyroscope, it is clear how the performance acquisition is significantly increased. Figure 100 shows a 180° continuous rotation. As can be seen, the RTK solution perfectly follows the magnetometer trend over the entire observation window. Same behaviour is shown in Figure 101. Here is presented a 90° stepped rotation: the bearing angle varies in correspondence of the platform rotation and remains constant when the platform is stopped. At the peak of the slope, a steady behaviour is displayed. This is due to the fact that the rotating platform was being reset to return to the initial position.

Finally, Figure 102 shows a 180° A/R continuous rotation. As already seen before, even in this case, the steady trend is assumed at the trend top.

What can be added is that we were able to obtain a quantization of RTK data with an accuracy of 1 cm and that the data from the magnetometer and gyroscope are very clean. However, it must be taken into account that we are in absence of engines power and also of vibrations. In reality, the current draw of the motors can degrade the quality of the magnetometer measurements while vibrations can degrade the quality of the gyroscope readings.

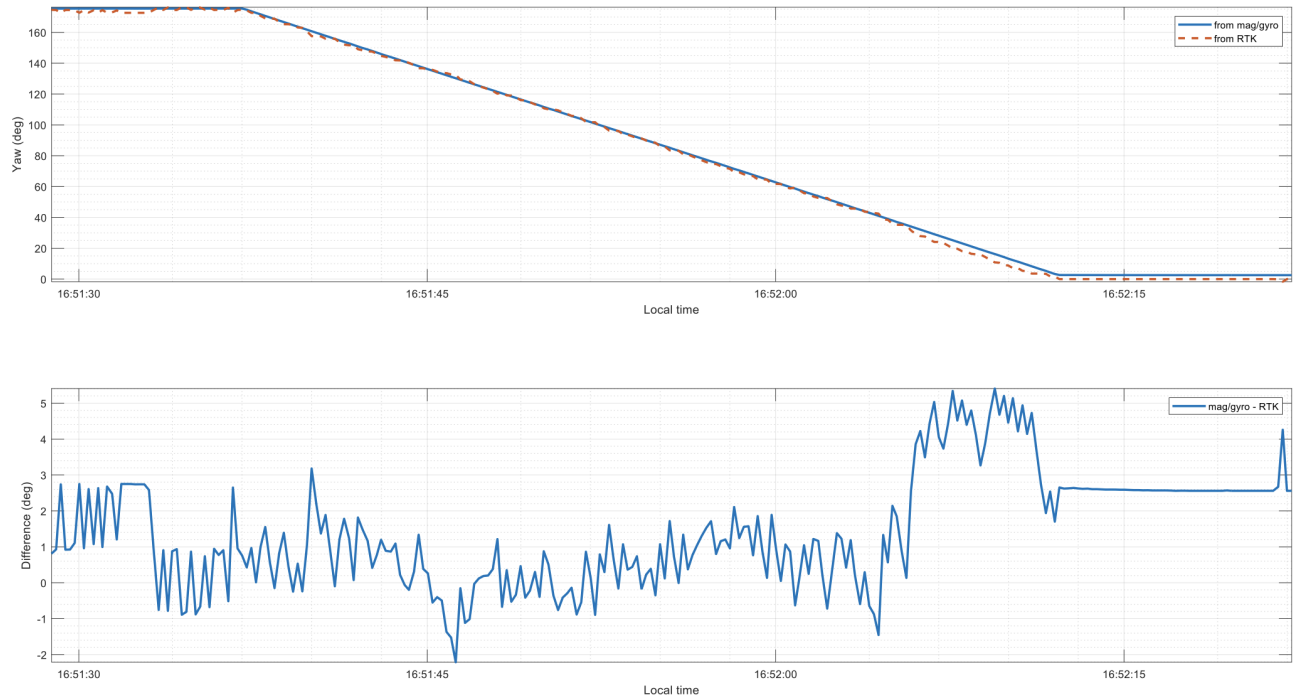


Figure 100: 180° continuous rotation: comparison between magnetometer and RTK receiver solution.

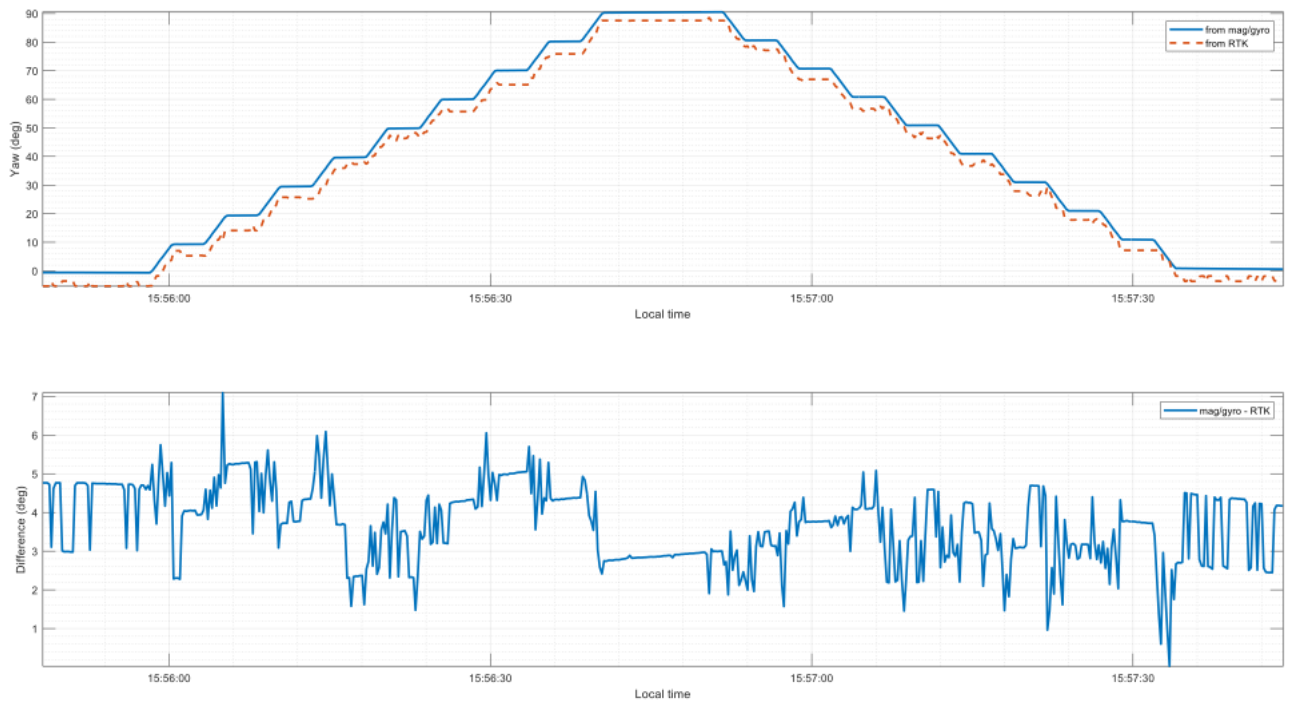


Figure 101: Stepped 90° rotation: comparison between magnetometer and RTK receiver solution.

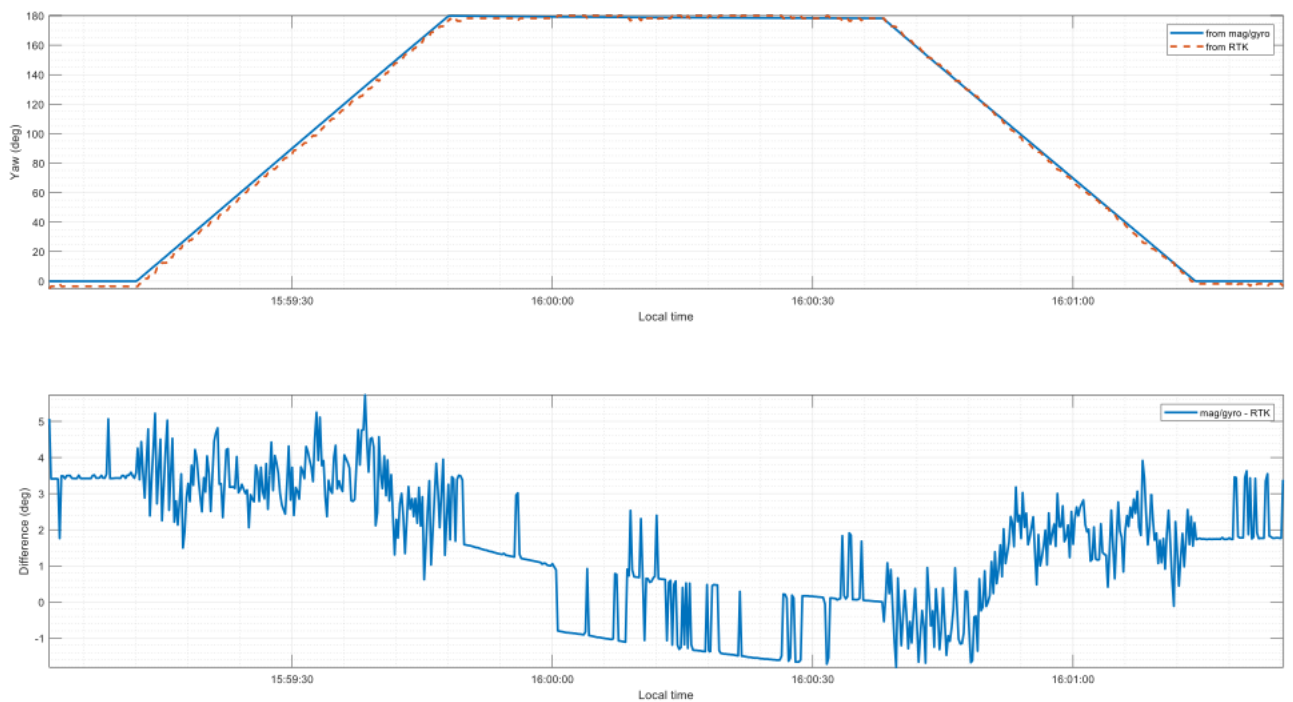


Figure 102: 180° A/R continuous rotation: comparison between magnetometer and RTK receiver solution.

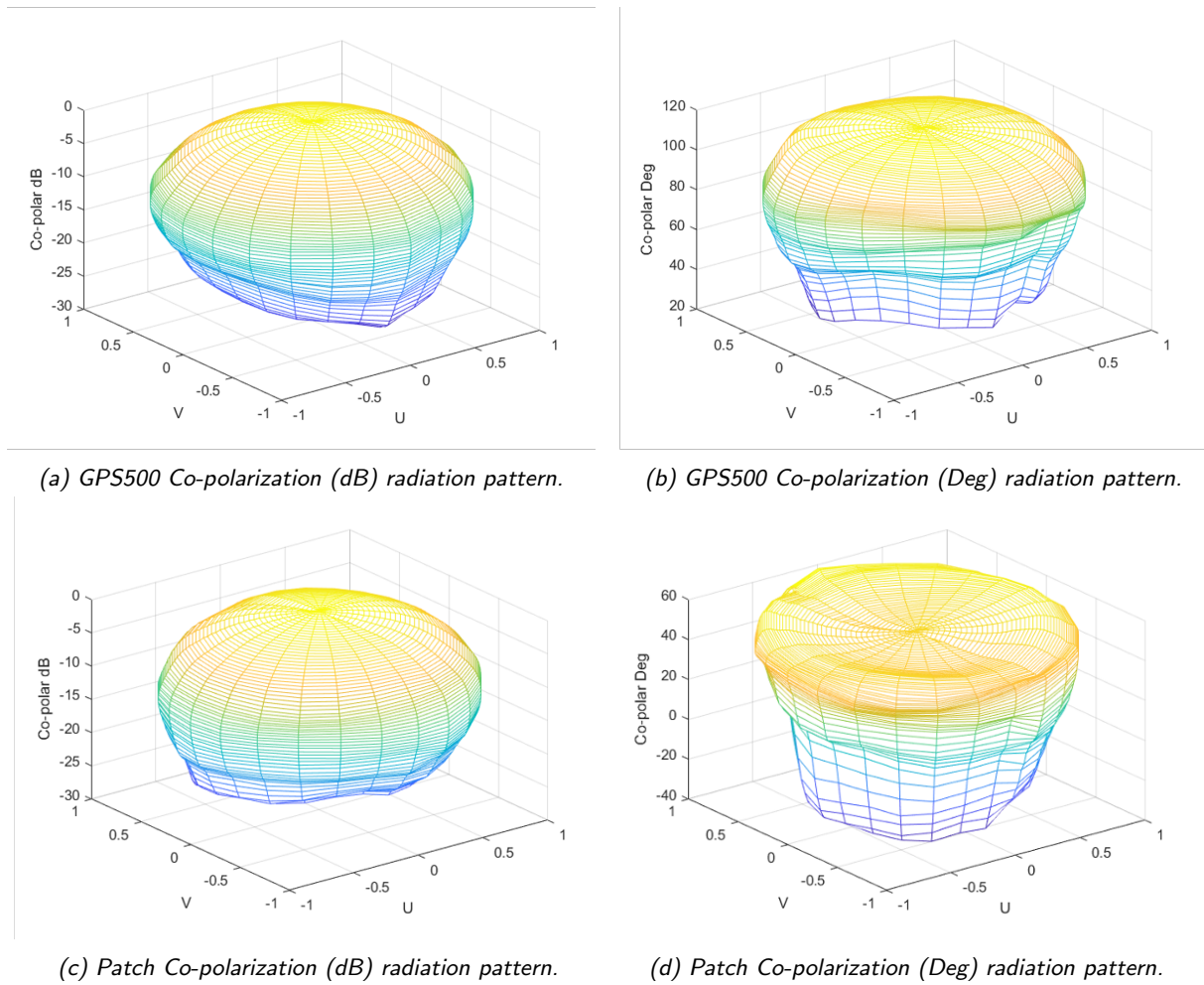
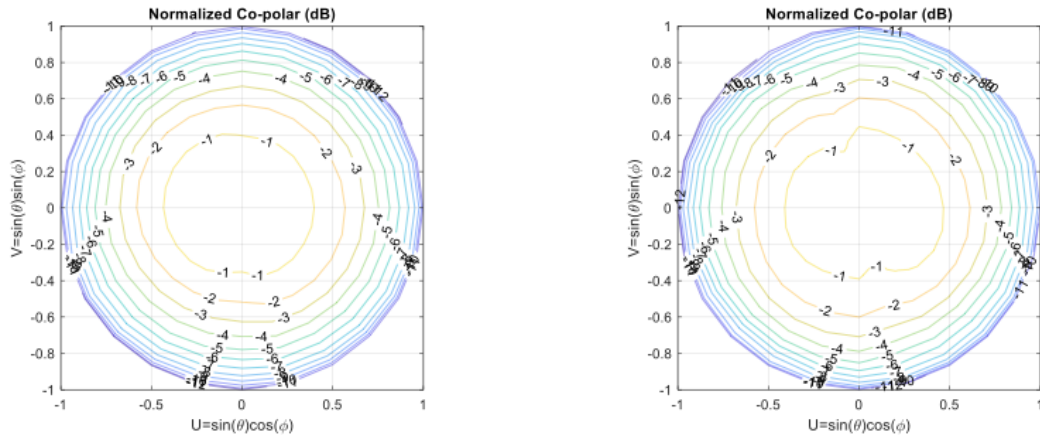


Figure 103: Geodetic and patch Co-polarization radiation pattern.

7.7 Tests validation with anechoic chamber results

Thanks to the results obtained from the performance analysis of the antennas in an anechoic chamber, we were able to validate the results obtained during the tests of the experimental setup. One aspect that has always been emphasized throughout the post-processing analysis of the data was the poor quality of the patch antenna compared to the dual frequency omnidirectional one. A difference that greatly influenced the tests and that we wanted to verify in order to further confirm the validity of our measurement system.

Here are presented results in terms of Cross polarization and Co-polarization and phase center mean. Cross-polarization is defined as the difference in decibels between the maximum radiation intensity of the required polarization (Co-Polarization) and cross-polarizations. The cross polarization is specified for an antenna as a power level. The value is represented in negative dB. In practice, it indicates how many decibels (dB) the cross-polarization power level is below the desired polarization. Phase center mean has already been treated in "Phase center corrections" section.



(a) GPS500 Normalized Co-polarization (dB) radiation pattern. (b) Patch Normalized Co-polarization (dB) radiation pattern.

Figure 104: Geodetic and patch Normalized Co-polarization (dB)

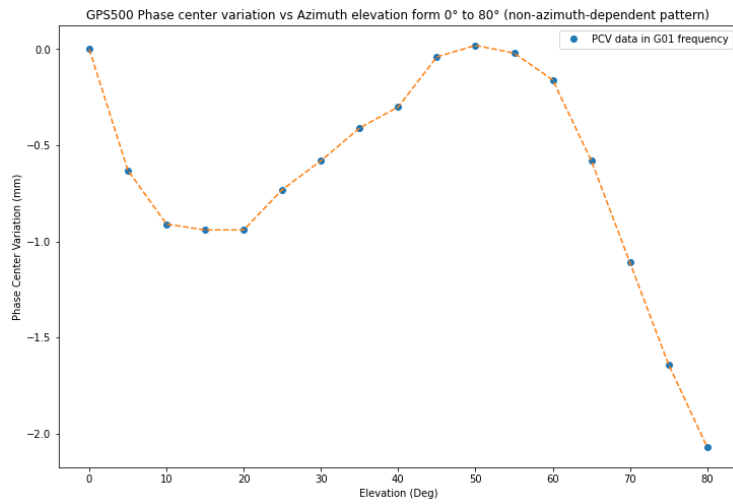
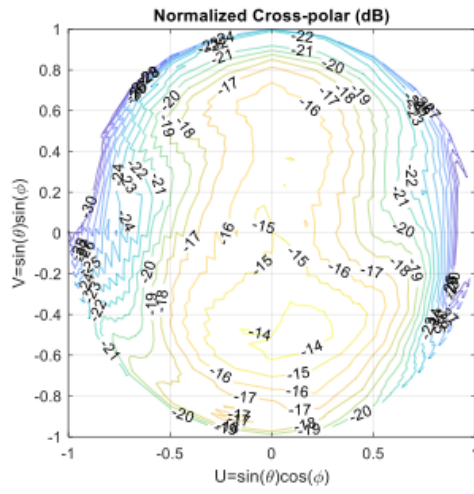
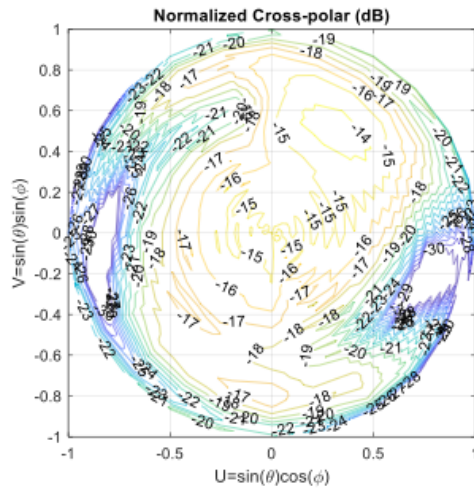


Figure 107: GPS500 Phase Center Variation of G01 frequency provided by SwiftNav.

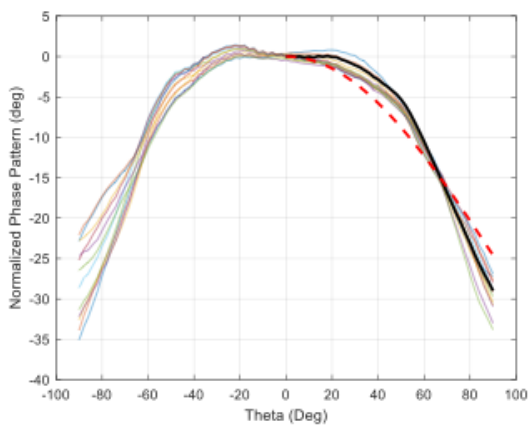


(a) GPS500 Normalized Cross-polarization (dB).

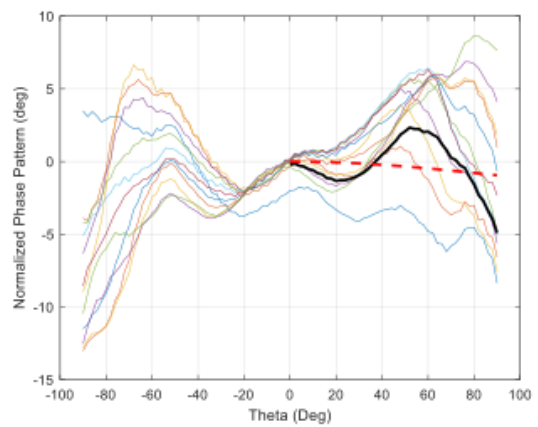


(b) Patch Normalized Cross-polarization (dB).

Figure 105: Geodetic and patch normalized Cross-polarization (dB).



(a) GPS500 Normalized Phase Pattern (Deg).



(b) Patch Normalized Phase Pattern (Deg).

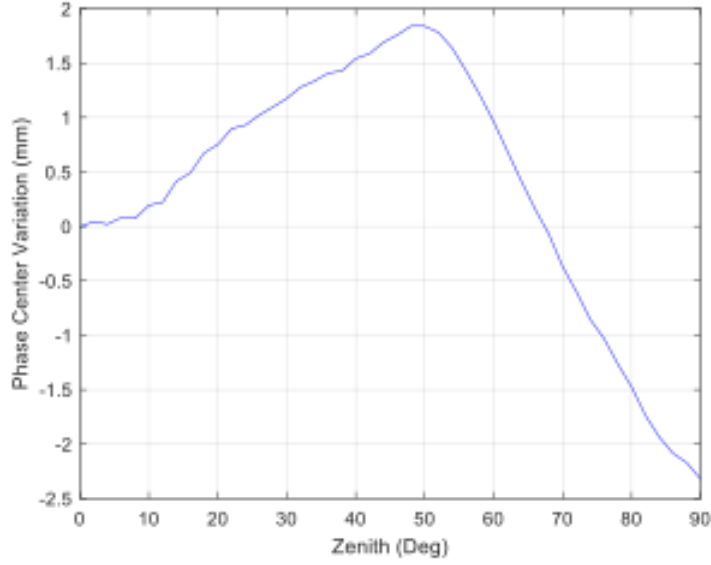


Figure 108: GPS500 Phase Center Variation obtained from anechoic chamber tests.

Measurements were made in "Far-field", with the probe antenna rotating along the horizontal and vertical axis. The scan describes diameters and a linear polarization is obtained. By modifying the module and phase, a switch from linear to a circular polarization can be achieved. The vertical and horizontal planes are described by the following mathematical relationship:

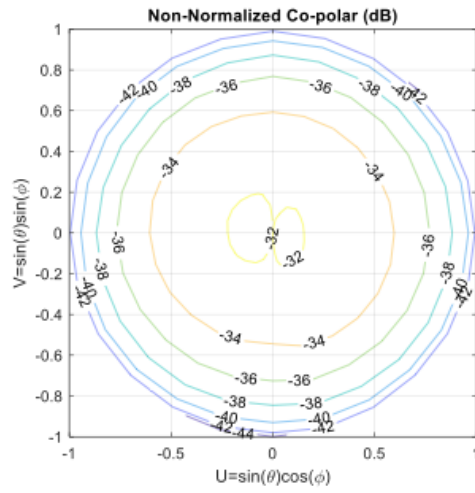
$$\begin{cases} U = \sin\theta\cos\phi \\ V = \sin\theta\sin\phi \end{cases} \quad (31)$$

By putting $U = 0$, the position is set to the Zenith. Viceversa, imposing $V = 0$, a variation of θ will provide the mapping of the sphere in the plane.

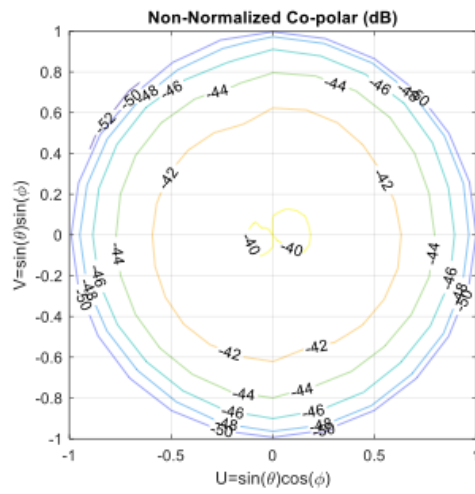
What can be seen from below figures is that the GPS500 antenna assumes an isotropic behaviour along Azimuth. Particularly, measures were taken not only at 90° but until 130° in order to verify scattering and multipath phenomenon.

As regard the antenna phase, it set between the range of 90° - 115° since the antenna boundary was considered as the reference system center. In addition, the antenna phase is not perfectly centered since it could be caused by some construction issues or depending on how it was fixed during tests (antenna cable should cause the introduction of some disturbances). As regard the patch antenna, its phase center is set on the ground plane, having a Cross-polarization of about $[-15,-20]$ dB. As can be seen from Figure 103c the patch antenna does not show a perfect isotropic behaviour and this is further confirmed by the Normalized Cross-polarization (see Figure 104b). As regard the Mean Phase Center, it is obtain by cutting ϕ angle with 5° of θ variation. The black slope represents the Mean; conversely, the red one represents the phase front of the beam. The red trend was obtained by considering a diverse center of phase. In fact, as regard the geodetic antenna, it was set back by approx $d = -13$ mm compared to the boundary ring. In the patch antenna, it was set back of $d = -5$ mm.

Figure 109a and 109b show the final comparison between geodetic and patch antenna. The gain of geodetic antenna is 8-10 dB larger than the patch. This could lead to higher signal-to-noise ratio of the measurement and partially explain its better performance. However, taking everything into account, as far as phase center stability is concerned the two antenna exhibit similar



(a) A230GRB Normalized Phase Pattern (Deg).



(b) Patch Normalized Phase Pattern (Deg).

Figure 109: Non-normalized Co-polarization comparison between Geodetic and Patch antenna.

performance. The residual variation of ± 2 mm are not significant for a real-time orientation measurement system. The patch does not receive L2, therefore we can investigate that the impact of L2 is relevant by removing the L2 observations from the acquisitions with the geodetic antenna. In addition, what can be underlined is that a fair comparison can be performed only when antennas share same mounting/placement conditions.

Finally, Phase Center Variation has been evaluated, converting the phase from degrees to millimeters with the following formula:

$$K_0 \cdot r = \frac{2\pi r}{\lambda} = \frac{2\pi r}{c \cdot r} \quad (32)$$

where K_0 is the radiation constant (rad/mm). What came out is that the anechoic chamber test perfectly matches the Phase Center Variation provided by the SwiftNav company (see Figure 107 and 108). The only difference from the company specifications is that it has been test only in a range of $[0^\circ, 80^\circ]$, while we performed a 90° elevation angle variation.

8 Conclusions

In this thesis work, we focused on the possible impact of GNSS antenna calibration model for the estimation of attitude in UAV platforms. Particularly, the main aim of this thesis was to provide a new cost-effective measurement system through which perform onboard antennas calibration. Firstly, a description of UAVs was given, showing their classification, the different types of onboard hardware and software technologies, military and civil applications and their challenges. From this description, we gave a general overview of the Global Navigation Satellite System and its ongoing evolution process. Here we put attention on what are the main GNSS error sources since the onboard antennas are signal receivers, therefore deeply sensitive to clock bias, signal propagation errors and user equivalent error. Subsequently, we studied what is the theory behind the UAV's platform attitude, focusing on the main reference frames and the trigonometric formulas with which retrieve a coherent heading angle estimation. Furthermore, different high-cost antenna calibration methods has been described and in particular we provided a general overview of anechoic chamber since different test has been conducted through the thesis work. This is due to the fact that this experimental method needed an a priori robust comparison model.

After exposing the main thesis theory background, it has been provided the main hardware and software technologies used throughout the project, including antenna model and features, signal receivers and data acquisition and post-processing softwares. Clearly, a detailed description of the experimental setup was provided, focusing on the baseline configurations, the place where the surveys were made and the different methodologies used for both data acquisition and post-processing phases.

Finally, a detailed results review has been exposed. Here we put emphasis on the estimation parameters comparison between the different acquisition modes, static and dynamic, and different baseline configurations, static and dynamic. Furthermore, we provided bearing angle estimation for both the experimental setup and UAV platform, comparing the performance of both measurement systems, and we validated the obtained results with anechoic chamber tests. What emerged from the analysis of the results is that it is possible to carry out a calibration of onboard antennas, from which it is possible to obtain an attitude estimation of UAV platforms. In particular, thanks to the study of the various baseline configurations, it was noted how the rotation of the patch antenna affects the data acquisition performance of the opposite antennas. This is visible in almost all of the post-processed data. In addition, omnidirectional antennas maintain an almost constant behavior in all observations: they have a greater number of available satellites, they do not show variations in position or speed among static acquisitions and the estimation parameters such as standard deviation and RMS of Pseudorange and Carrier-Phase residuals are always low. On the other hand, patch antennas almost never have a fixed number of satellites during the acquisitions, in static cases they feel variations even greater than one meter in the position or perceive brutal speed changes along the coordinates. Consequently, the standard deviation and RMS values of Pseudorange and Carrier-Phase residuals are very high. These results were further confirmed by the results obtained from the calibration of the antennas in anechoic chamber. In fact, thanks to the co-polarization and cross-polarization graphs, the geodetic antennas assume an almost isotropic behavior, with higher gains of about 8-10 dB more than the patch antennas.

However, as regard the heading angle, this project has recorded very good results. In fact, considering the tests carried out on the rotating platform with the remotely piloted drone on top, the RTK solutions perfectly follow the angular variations recorded by the onboard sensors

(magnetometer and gyroscope) obtaining a quantization of RTK data with an accuracy of 1 cm. This is clearly due to the lower complexity of the system and a more optimal configuration. In reality, the current draw of drone engines would degrade the quality of the magnetometer sensor while vibrations can degrade the quality of the gyroscope.

At the end of the work, the objective of this thesis has been completed. The question that has always been asked to us, even before starting this long journey, was whether it was possible to design a low-cost calibration system, therefore composed of low-level antennas and receivers, from which to draw important contributions in order to calibrate onboard antennas and determine the attitude of UAV platforms. We knew from the beginning that it was going to be a very difficult job and that there might be some difficulties. The key to all this was a careful and effective analysis of the enormous amount of data that we collected. In fact, thanks to the detailed analysis of the data obtained both in post-processing and from the estimation of the bearing angle, we were able to understand the true potential of this system. In particular, we understood how, in the design of these systems it is essential to approach with precision and accuracy and to take care of every single detail. Clearly this is only the beginning of a project that may have future implications, thanks to which students, researchers or technicians of all kinds will be able to develop their own calibration system without requiring a significant economic effort. Precise and detailed measurements such as those obtained in an anechoic chamber would be replaced by simpler and more accessible systems.

Taking everything into account, several potential directions can extend our future research in this domain. The aspects that could be taken into consideration in the future are listed as follows.

Future experiments could be implemented in order to obtain a better setup configuration. This ambiguous behaviour of patch antennas could be avoided by putting on the same plane the entire baseline, preventing any type of signal shields between receivers. The setup support itself can be adapted in a more optimal way, in order to minimize any kind of vibration due to the oscillation of the rotating platform. A better cable management of the whole setup would exponentially improve the quality of the acquisitions since, during the dynamic cases, often and willingly, the cables of both antennas and receivers did not remain well anchored but were put under tension. Since the world of ICT is experiencing a continuous and unstoppable phase of development, I am sure that in the future all the problems encountered during this thesis project will be easily solved.

A Appendix

A.1 Static mode - normal configuration: DGPS/DGNSS positioning

DGNSS (Differential GNSS) is essentially a system to provide positional corrections to GPS signals. DGNSS uses a fixed, known position to adjust real time GPS signals to eliminate pseudorange errors. An important point to note is that DGNSS corrections improve the accuracy of position data only. Therefore, a different behaviour is expected to have compared to the previous one.

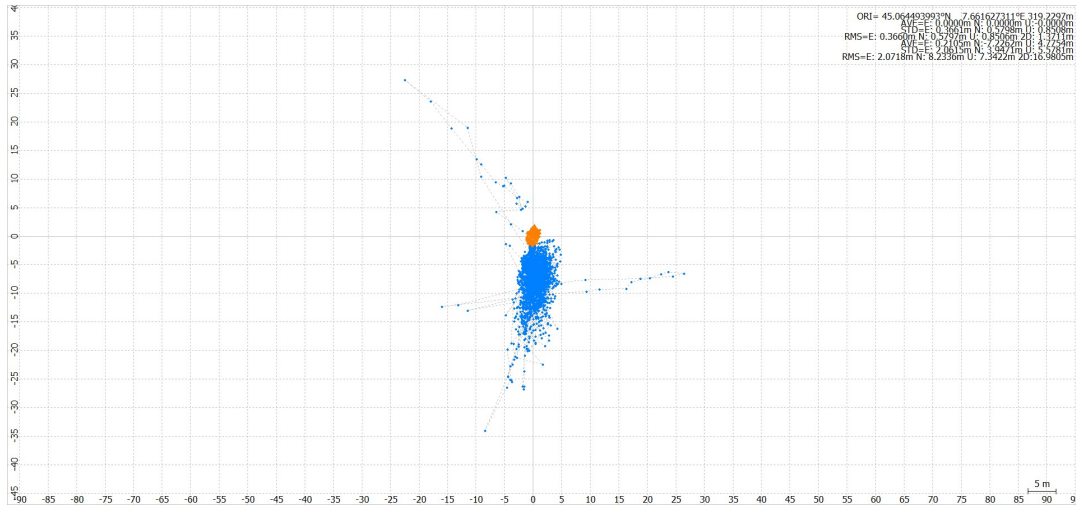


Figure 110: Ground tracking of right antennas.

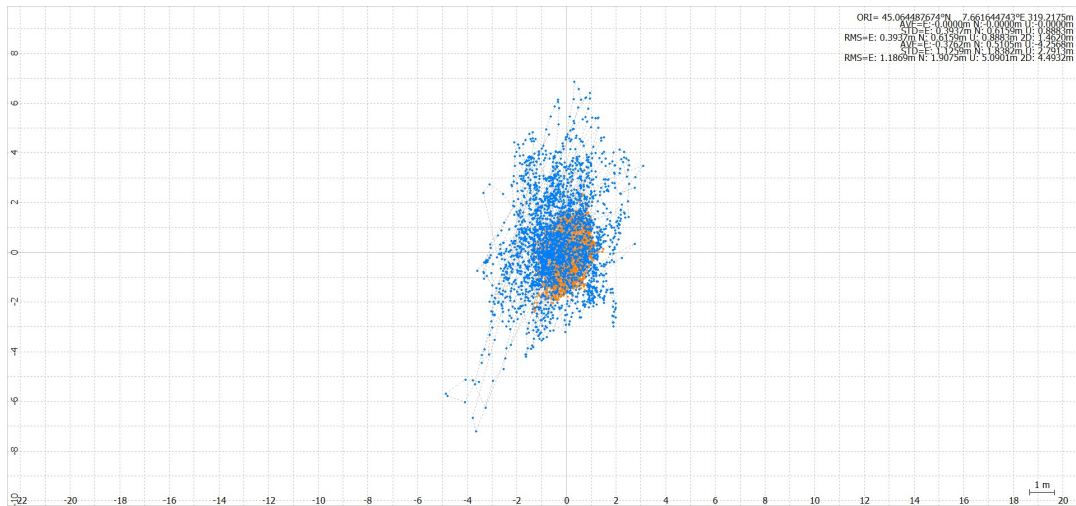


Figure 111: Ground tracking of left antennas.

As can be seen from Figure 110 and 111, both positioning solutions have the 100% of differential solution ($Q=4$). What can be underlined is that right antennas gained worst positioning performances. This is due to the fact that right patch antenna sensed a higher position variation in N-S and U-D direction during the observation window.

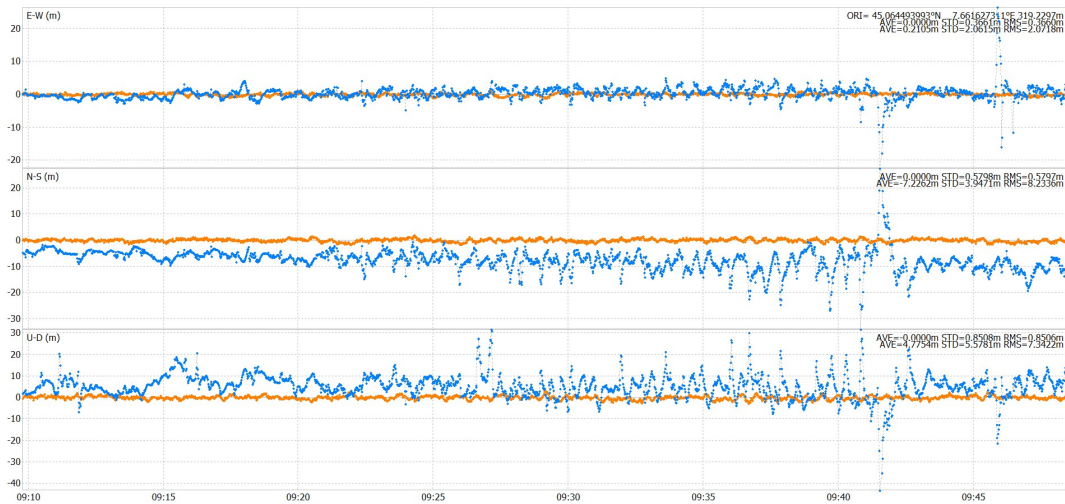


Figure 112: Right side antennas: position variation over coordinates.



Figure 113: Left side antennas: position variation over coordinates.

Figure 112 and 113 show the position variation. Even if the right omnidirectional antenna maintains a stable trend among time, a big amount of error is introduced by the patch variation. Conversely, the strong oscillation of left dual-frequency antenna is contained by the lower patch trend.



Figure 114: Right side antennas: velocity variation over coordinates.



Figure 115: Left side antennas: velocity variation over coordinates.

What has just been said is also confirmed by the speed variation graph (see Figure 114 and 115). In fact, the omnidirectional antenna on the left, even if in static acquisition, has a strong variation in speed over time, which is largely compensated by the relative patch antenna. Clearly, this loud noise heard from the right antenna can also be seen in the graph of the number of satellites available. In fact, Figure 116 shows how, during the acquisition, the number of available satellites does not remain fixed over time but rather varies abruptly.

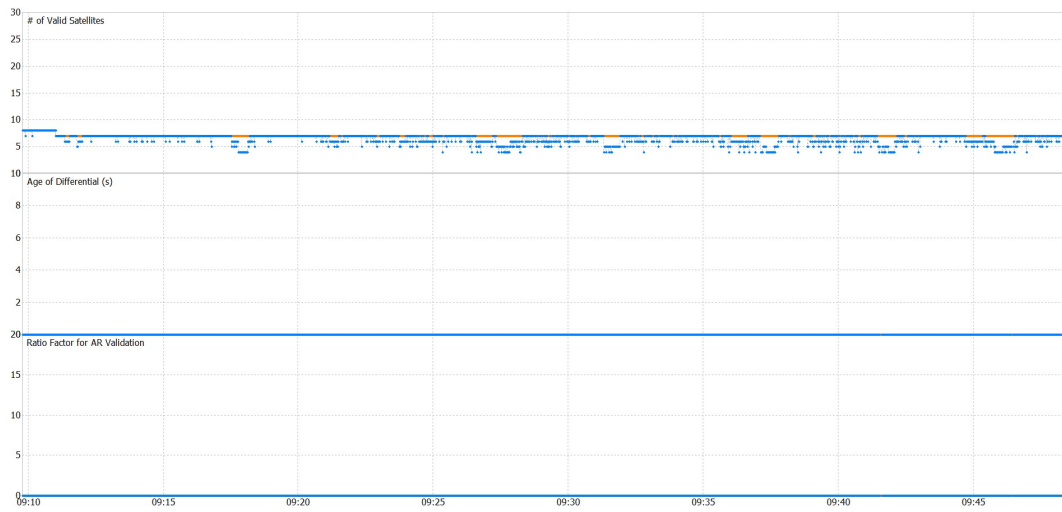


Figure 116: Right side antennas: available satellites over time.

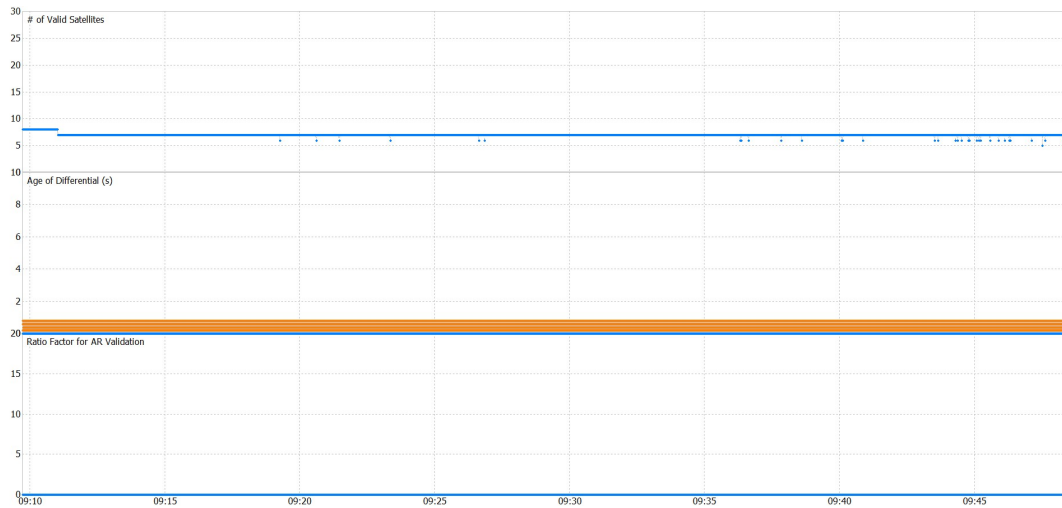


Figure 117: Left side antennas: available satellites over time.

Figure 116 and 117 do not provide relevant information about the Age of Differential and the Ratio Factor for Validation. The only tangible thing is that we are working in a DGPS/DGNSS positioning mode, therefore a $Q=1$ solution is never reached by the system.

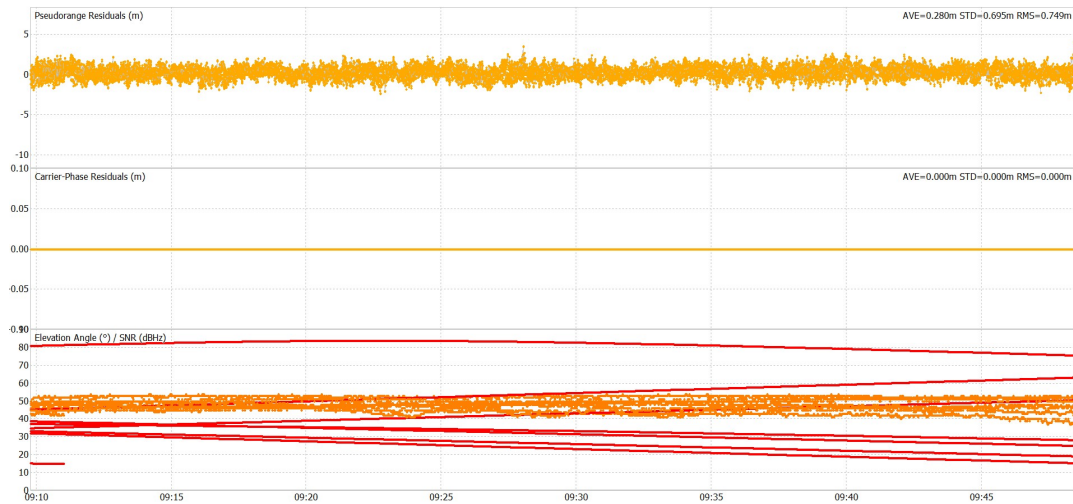


Figure 118: Pseudorange and Carrier-Phase of right omnidirectional antenna.



Figure 119: Pseudorange and Carrier-Phase of right patch antenna.

As for the Kinematic positioning mode, the Differential GNSS pseudorange residuals maintain good values for almost all antennas. The most estimation error is introduced by patches as usual. Even from this case we find further confirmation with what has been previously verified. In fact, the behavior of the right patch is quite noisy, resulting in a significant reduction of accuracy.



Figure 120: Pseudorange and Carrier-Phase of left omnidirectional antenna.



Figure 121: Pseudorange and Carrier-Phase of left patch antenna.

Same considerations can be done for the left side (see Figure 120 and 121): omnidirectional antenna maintains a variation between ± 5.0 m in Pseudorange Residuals and a constant value of Carrier-Phase Residuals.

A.2 Static mode - normal configuration: Moving-Base positioning

The Moving-Base positioning technique differs from the more common fixed-based solutions since the base station is allowed to move in addition to the Rover. Although it could be used to track the distance between two moving rovers, it is more commonly used in a configuration with two receivers attached to a single rover and used to determine heading. In this case, it is not really correct to use this type of solution since the acquisitions were carried out in static, therefore without the presence of any movements. The main reason why it was decided to propose this solution was to further characterize this calibration system.

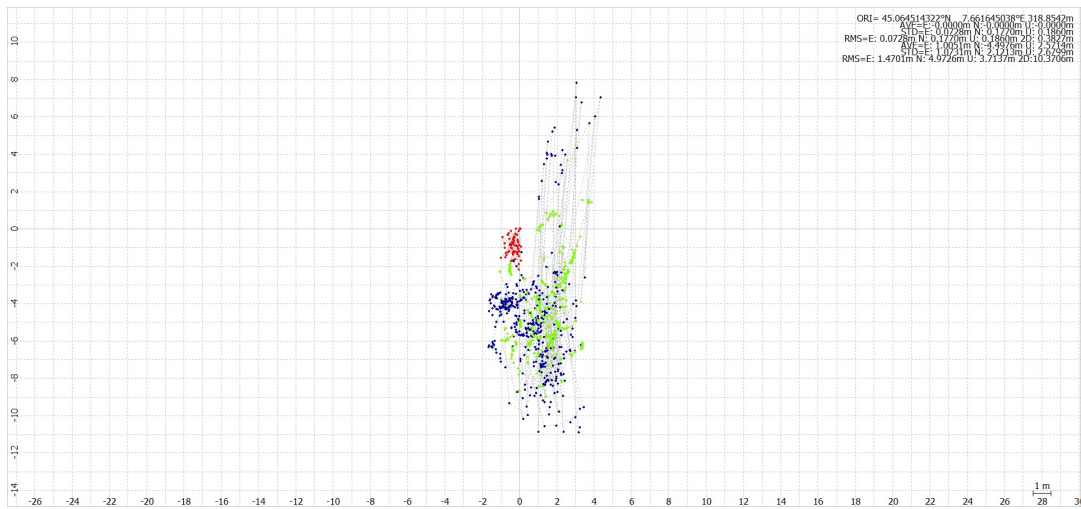


Figure 122: Ground tracking of right antennas.

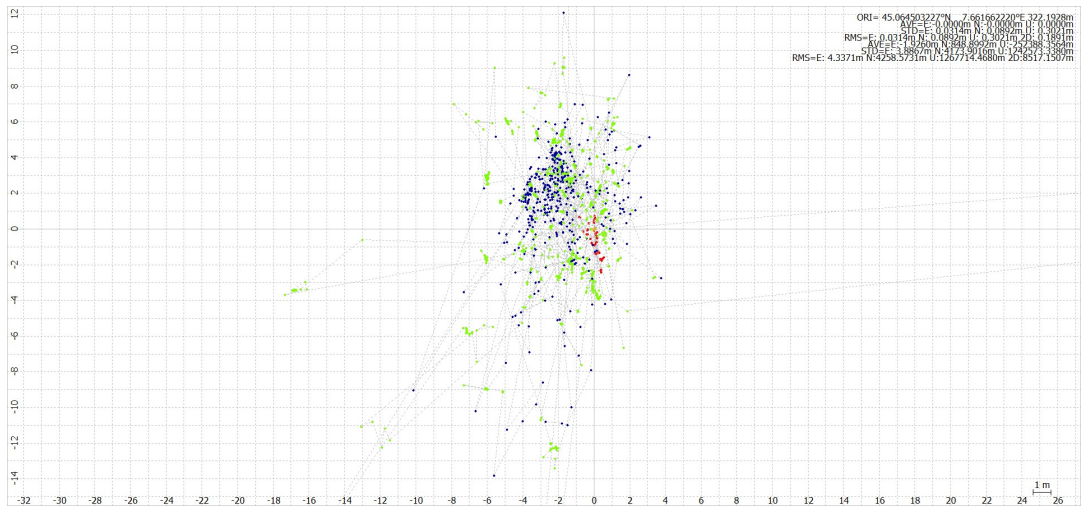


Figure 123: Ground tracking of left antennas.

Figure 122 and 123 show the Ground Track of the Moving-Base solution. In the first case we are comparing the right patch and omnidirectional antennas acting as Master station. Viceversa for the second case. As can be seen, this approach introduces big changes compared to the previous solutions. In fact, positioning estimation is based on false assumptions as said before. This results in a worst and scattered solution since most of it is float ($Q = 2$) and not fixed.

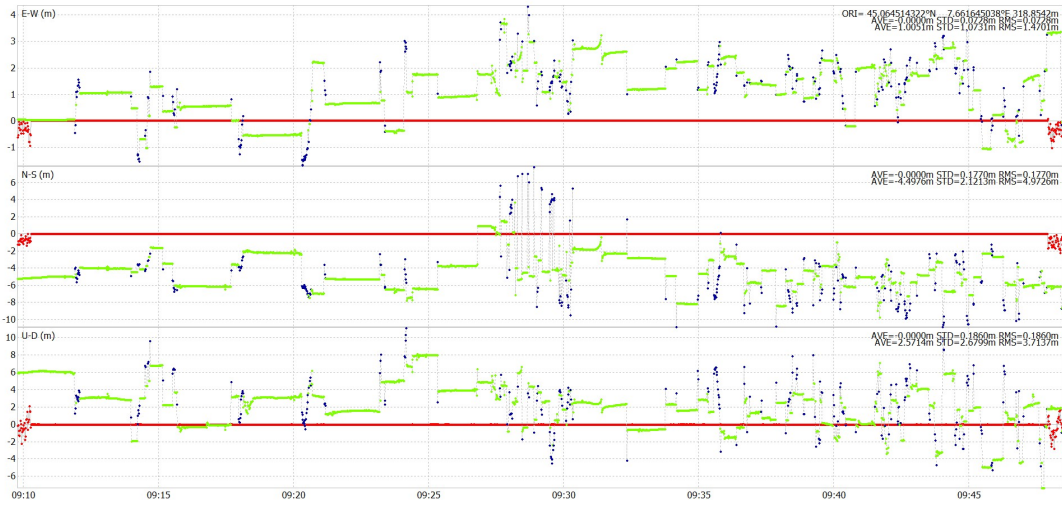


Figure 124: Right side antennas: position variation over coordinates.

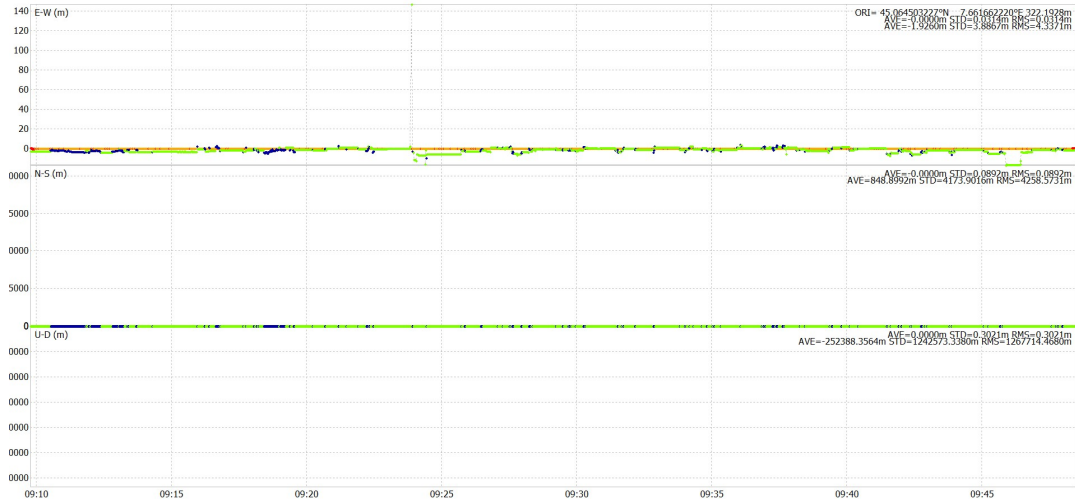


Figure 125: Left side antennas: position variation over time.

Figure 124 and 125 display the Position variation over coordinates. Figure 124 shows exactly what has just been stated: right patch antenna varies tremendously over all three coordinates, introducing a big quantity of estimation errors. A curious observation can be done: the behavior of the left patch antenna should be emphasized compared to the right one. In fact, unlike the second, it undergoes great variations, over time, on the E-W coordinate while remaining constant over N-S and U-D coordinates.

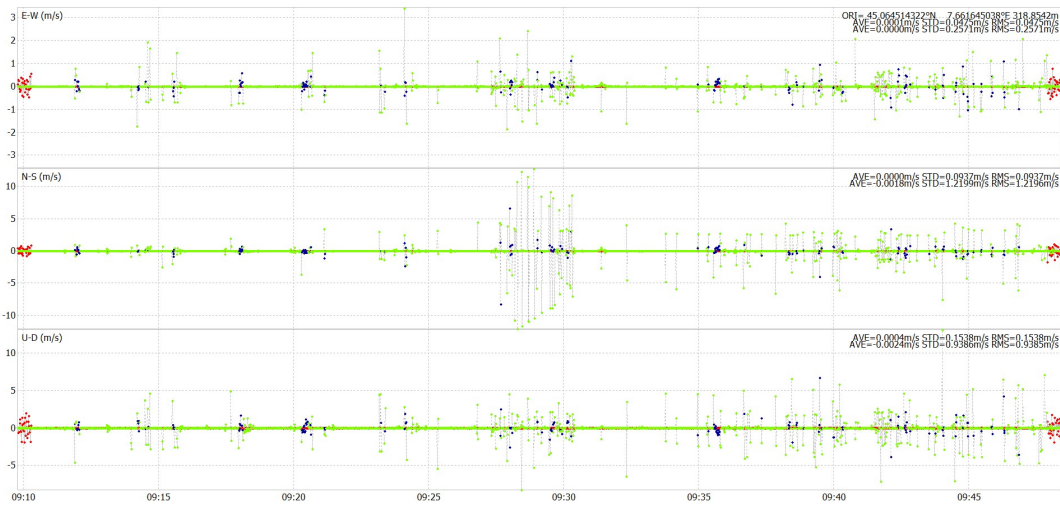


Figure 126: Right side antennas: velocity variation over coordinates.

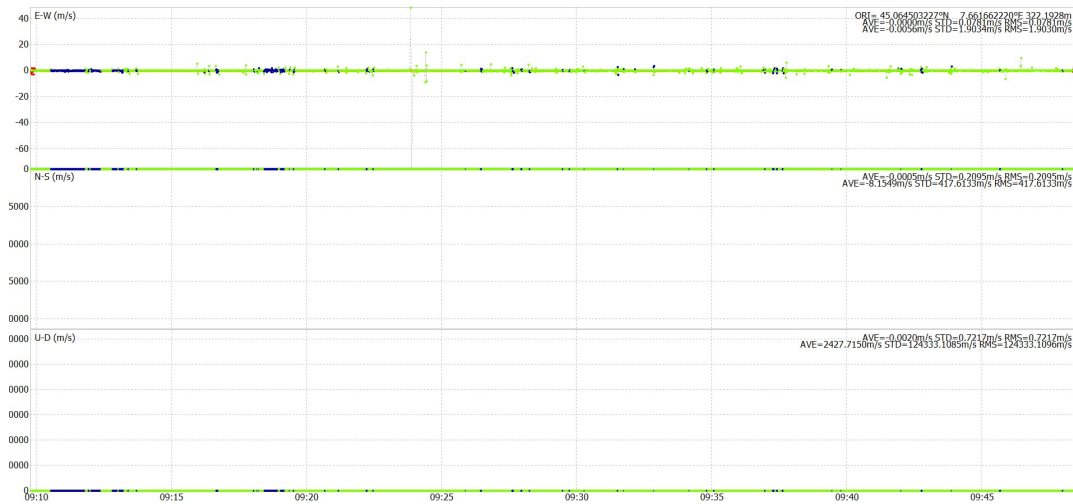


Figure 127: Left side antennas: velocity variation over coordinates.

As a consequence, errors are propagated among all other estimation parameters. In fact, even velocity variations confirm the assumptions. In particular, Figure 126 shows a continuous trend change of the right patch antenna. Even if big amount of errors are sensed at right side, lower standard deviation and Root Mean Square (RMS) values are observed, making the solution better.

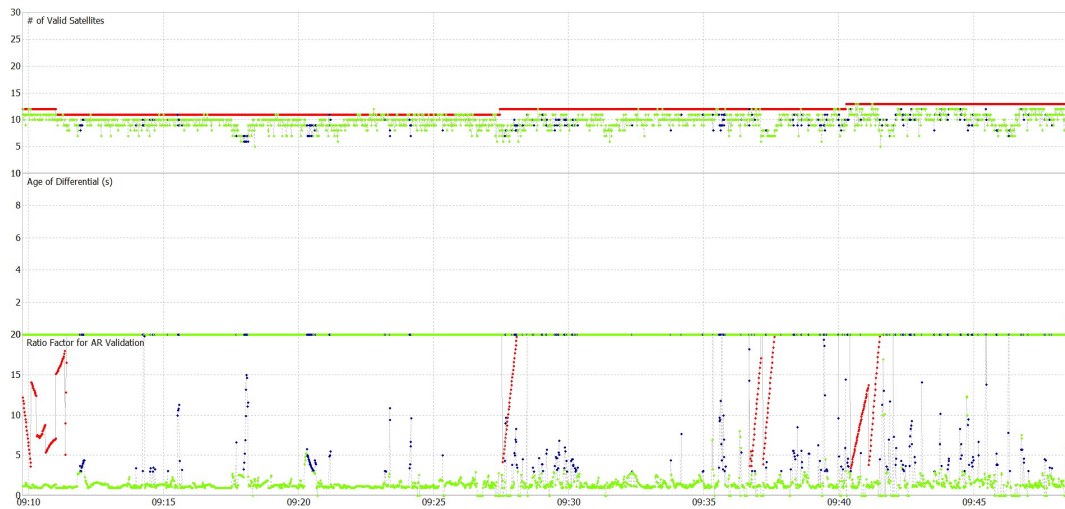


Figure 128: Right side antennas: available satellites over time.



Figure 129: Left side antennas: available satellites over time.

Figure 128 and 129 show the number of available satellite among the observation period. With the Moving-Base solution, this graph reminds the previous solution obtained with Kinematic positioning technique, giving great variations of both Ratio Factor for AR Validation. Omnidirectional antennas maintain the same number of visible satellites over time.

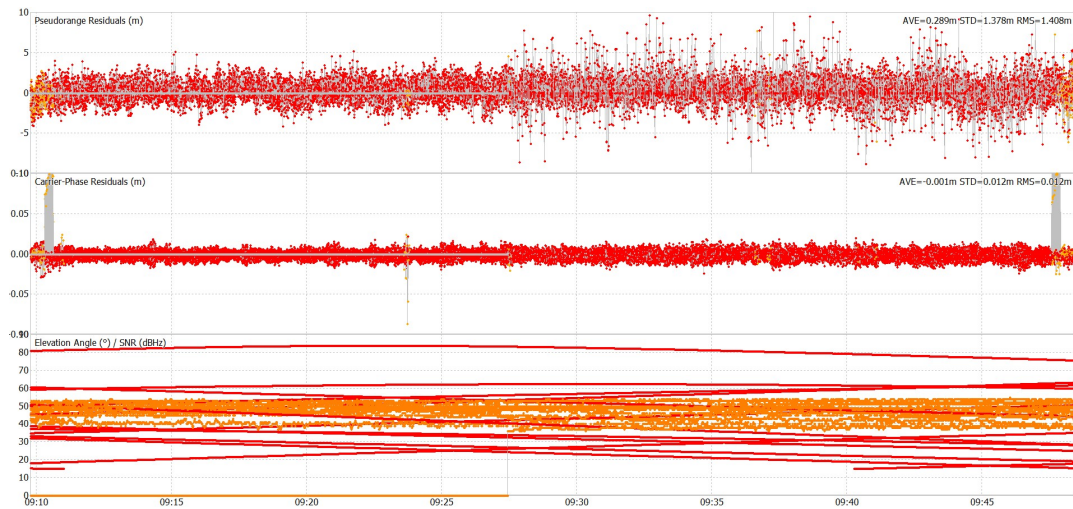


Figure 130: Pseudorange and Carrier-Phase of right omnidirectional antenna.

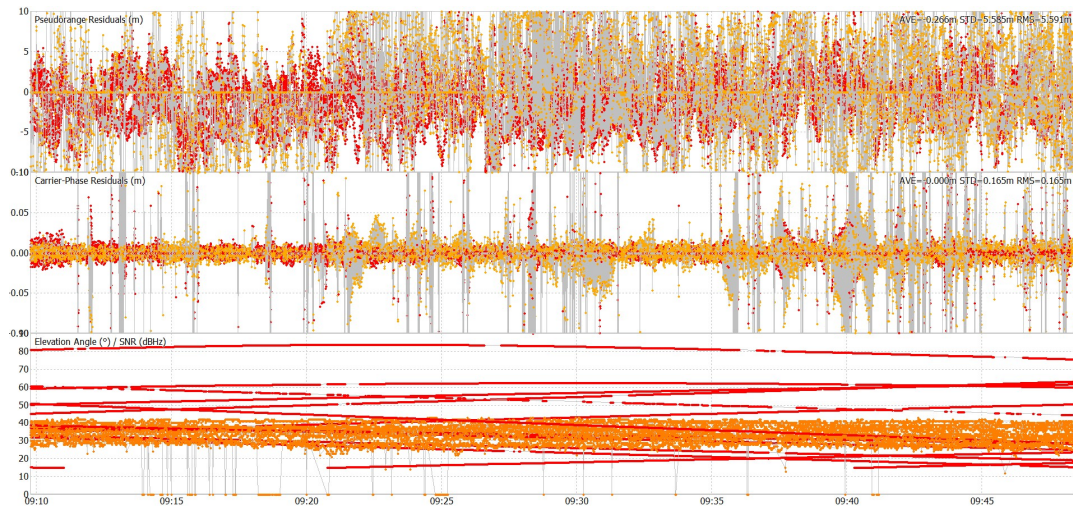


Figure 131: Pseudorange and Carrier-Phase of right patch antenna.

Finally, Pseudorange Residuals and Carrier-phase residuals are shown. Figure 130 and 132 show the ones related to dual-frequency antennas. As can be noticed, the antenna on the right maintains a less chaotic trend over time. This is due to the fact that it has 100% of fixed solution ($Q = 1$) as opposed to the second one which keeps 93.3% of a float ($Q = 2$) and just 6.7% of $Q = 1$.

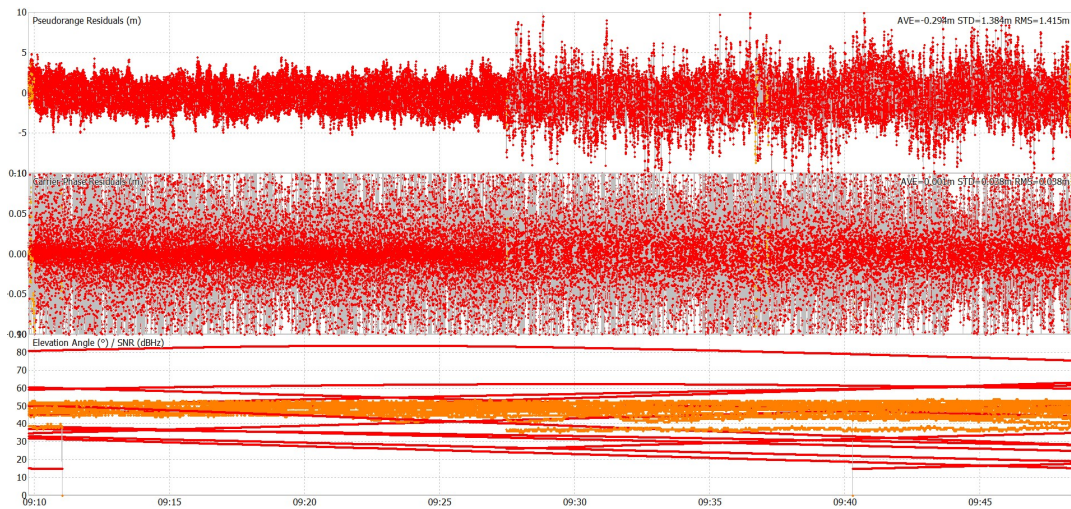


Figure 132: Pseudorange and Carrier-Phase of left omnidirectional antenna.

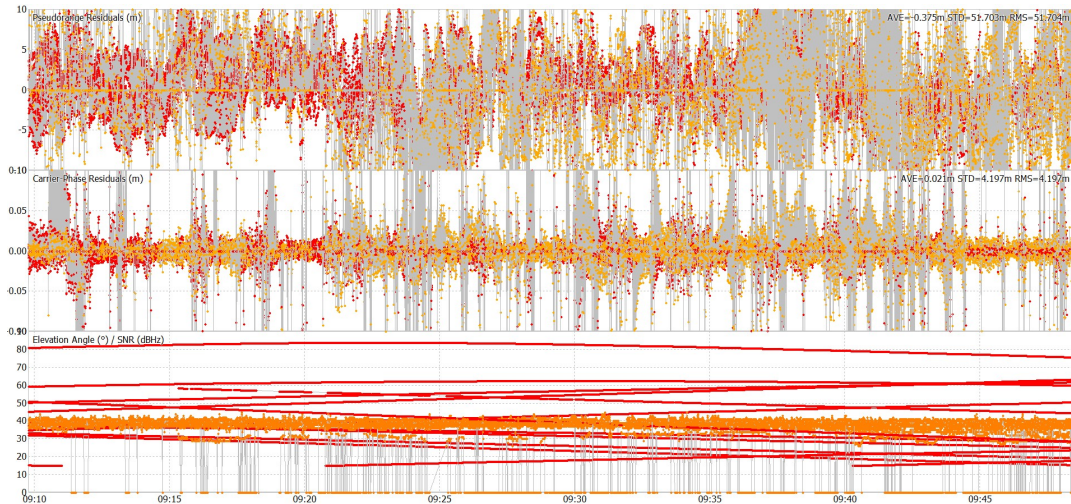


Figure 133: Pseudorange and Carrier-Phase of left omnidirectional antenna.

Regarding the results obtained for the patch antennas, bad standard deviation and RMS values are recorded for the left antennas, respectively of $STD = 51.703m$ and $RMS = 51.704m$. The same type of data analysis will be presented in subsequent sections. In particular we will see the three positioning techniques equally but within the Reversed configuration, therefore with the patch antenna on the right rotated inwards. The objective of this analysis is to verify whether a change in the baseline configuration can actually affect the acquisition system.

A.3 Static mode - reversed configuration: DGPS/DGNSS positioning

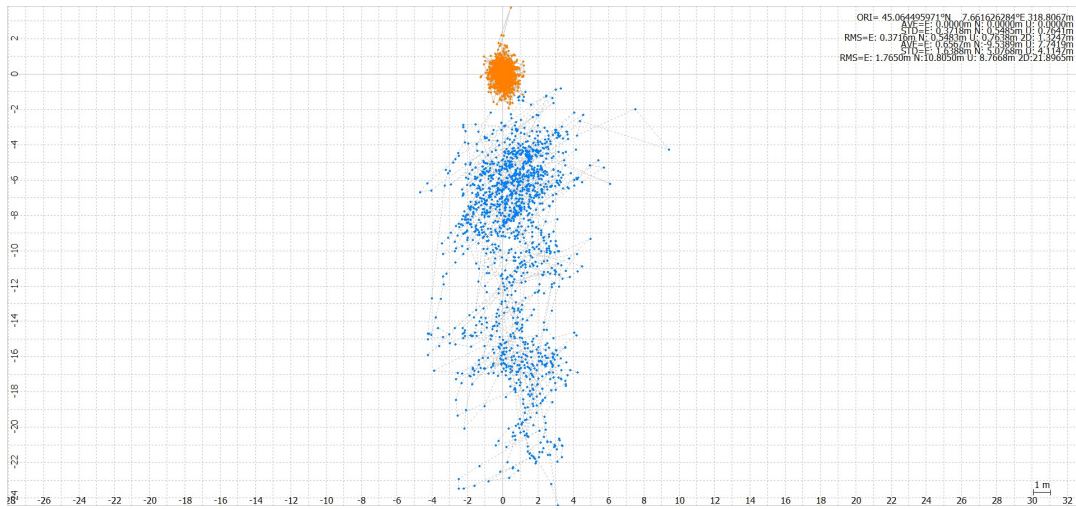


Figure 134: Ground tracking of right antennas.

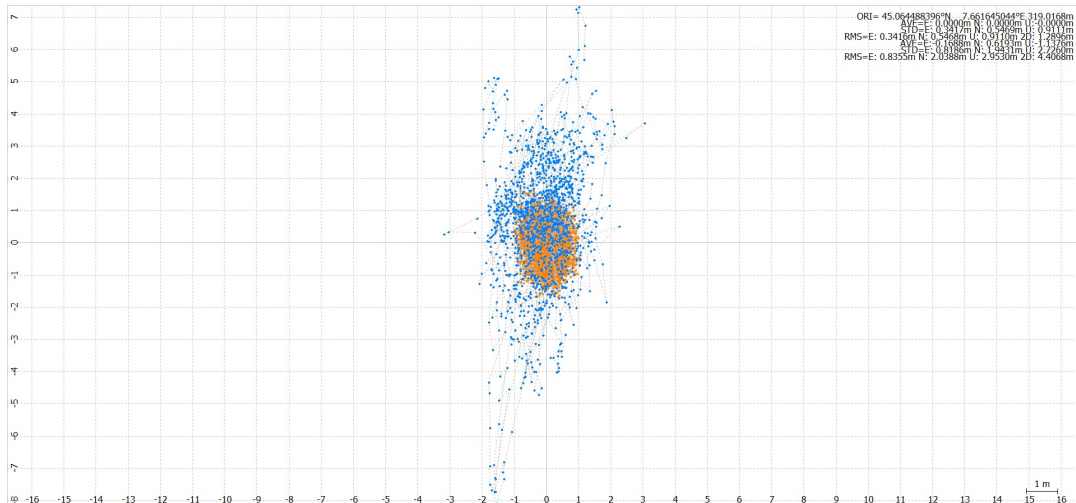


Figure 135: Ground tracking of left antennas.

Figure 134 and 135 show the Differential positioning technique. No fixed or float solution are present: in both cases, a 100% of differential solution ($Q=4$) is obtained. What can be underlined is that the right side results more scattered compared to the left side. This is due to the fact that the number of available satellites continuously changes over time.

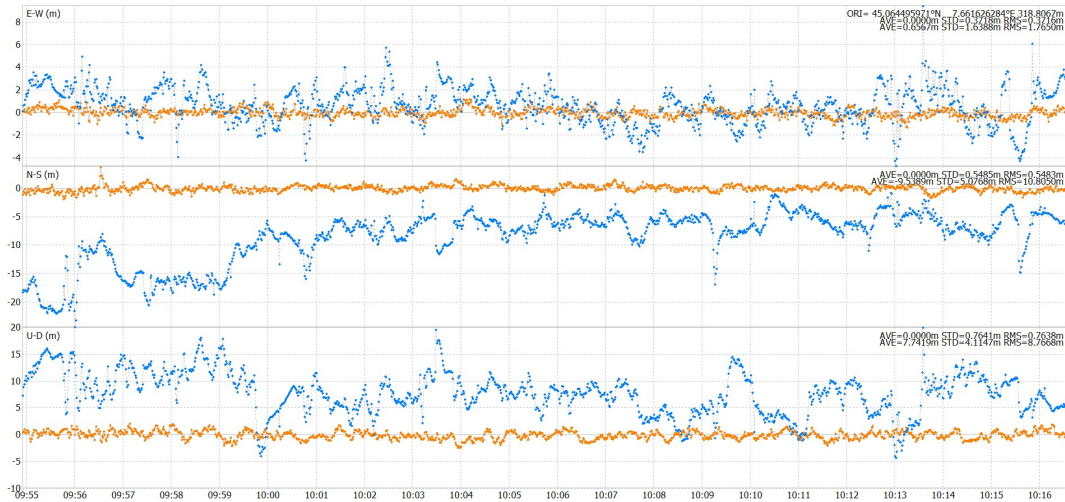


Figure 136: Right side antennas: position variation over coordinates.

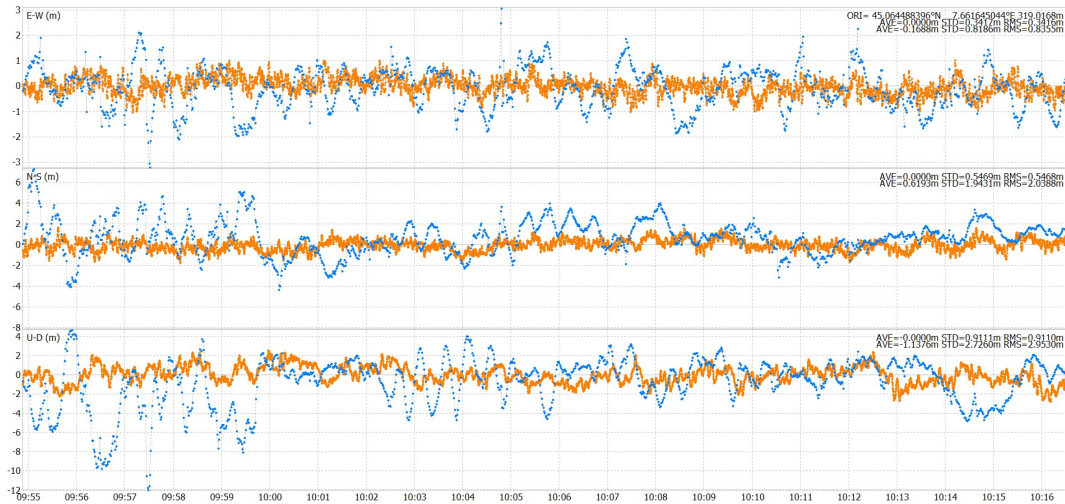


Figure 137: Left side antennas: position variation over coordinates.

In addition, this is confirmed by Figure 136 and 137. Right patch antenna senses high position variations in both N-S and U-D coordinates:

- N-S coordinate: RMS = 10.805 m for the right one and RMS = 2.0388 m for the left one;
- U-D coordinate: RMS = 8.767 m for the right one and RMS = 2.953 m for the left one.

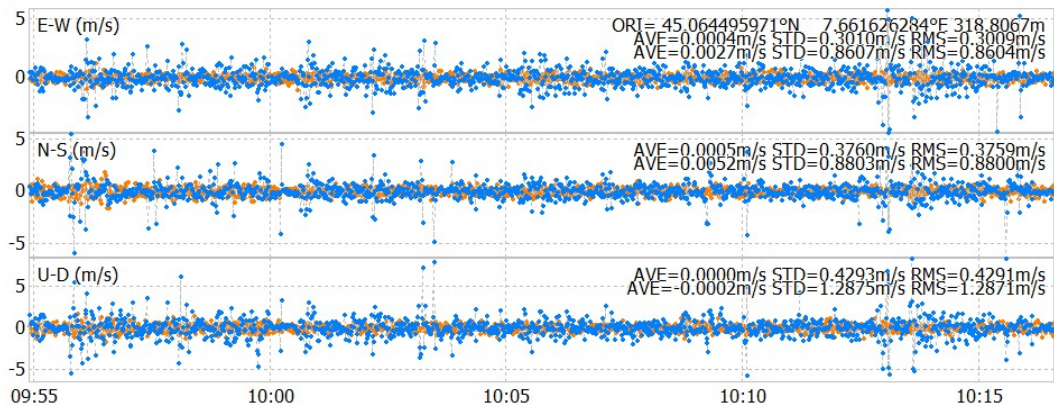


Figure 138: Right side antennas: velocity variation over coordinates.

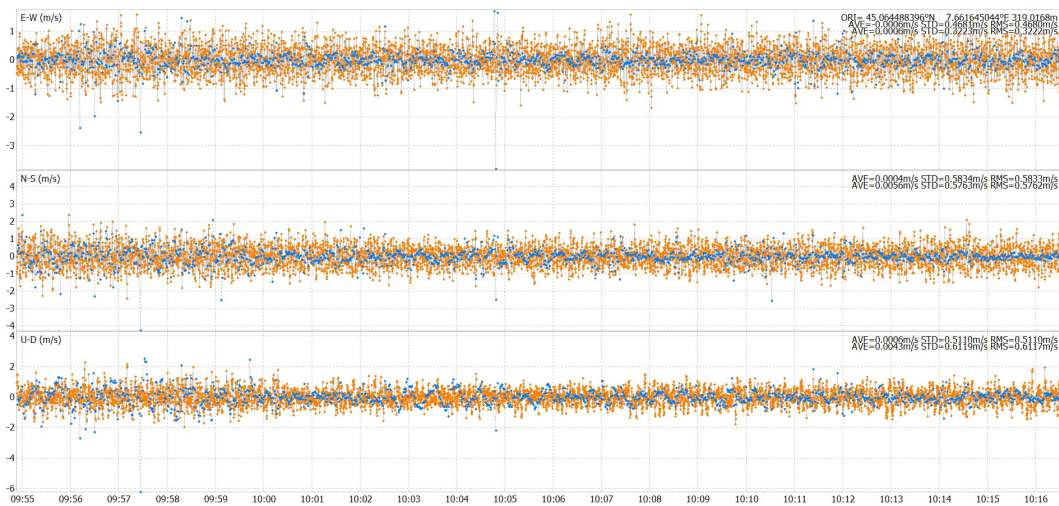


Figure 139: Left side antennas: velocity variation over coordinates.

As previously stated, the dispersion of the positioning solution strictly depends on the number of satellites available. Figure 141 shows that, starting from 10 am, the number of satellites remains constant over time. Conversely, Figure 140 shows how right patch antenna constantly loses its visible satellites, leading it to introduce error estimations.

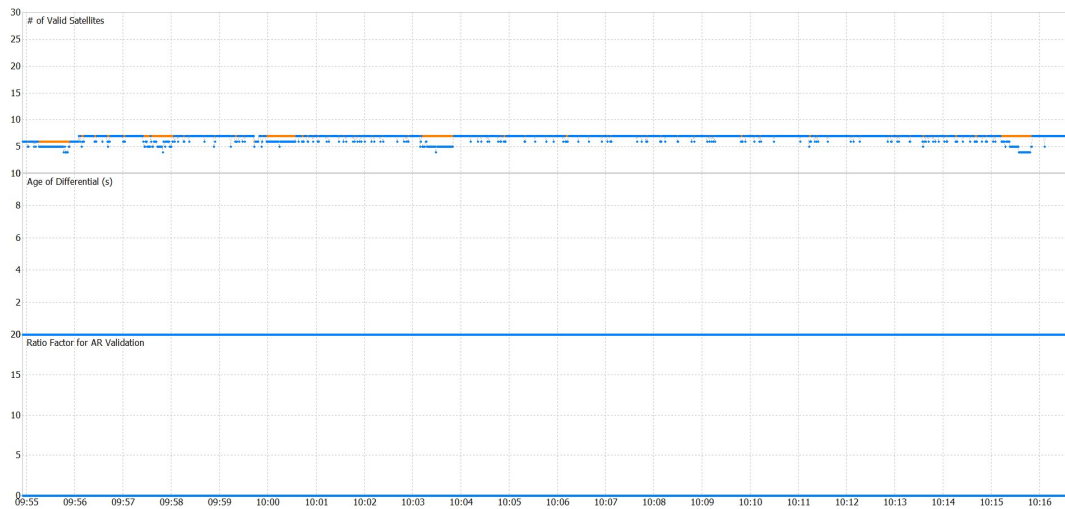


Figure 140: Right side antennas: available satellites over time.

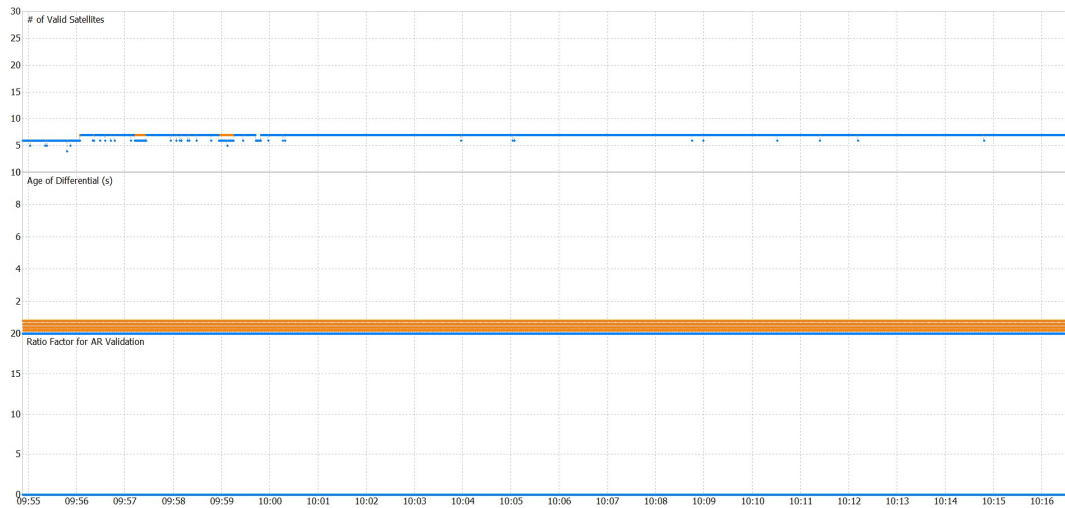


Figure 141: Left side antennas: available satellites over time.

Finally, Figure 142 and 143 shows the right residuals. According to what as just been said, the propagation of error estimation and the high level of noise can be clearly seen. This effect is strongly perceived by the left patch antenna which, unlike the normal configuration, has a higher value of the statistical parameters (see Figure 145).

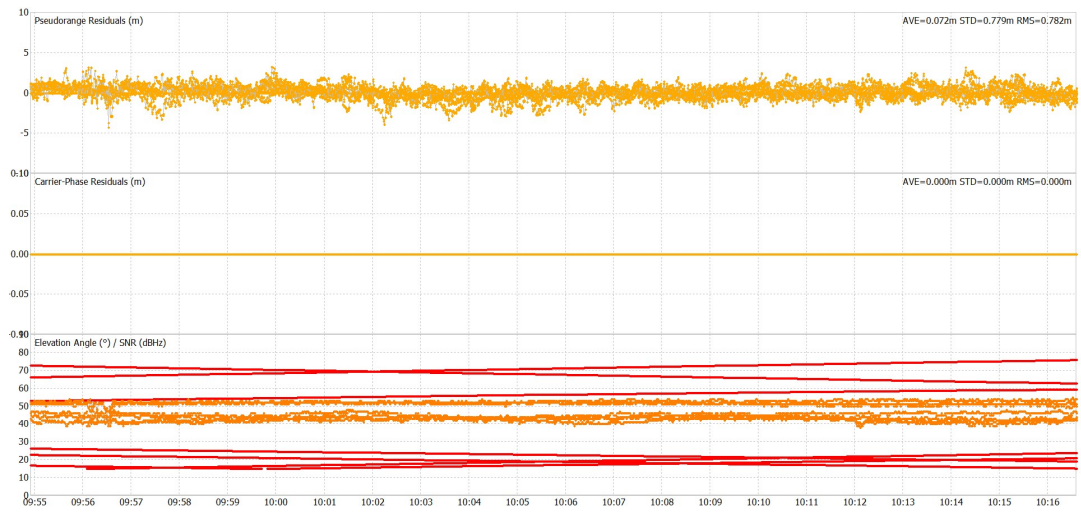


Figure 142: Pseudorange and Carrier-Phase residuals of right omnidirectional antenna.

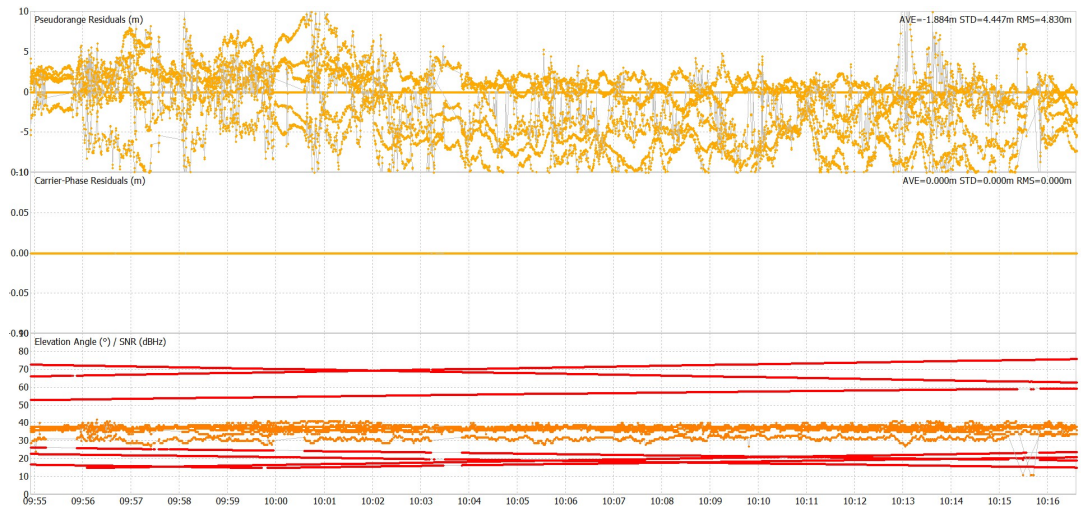


Figure 143: Pseudorange and Carrier-Phase residuals of right patch antenna.

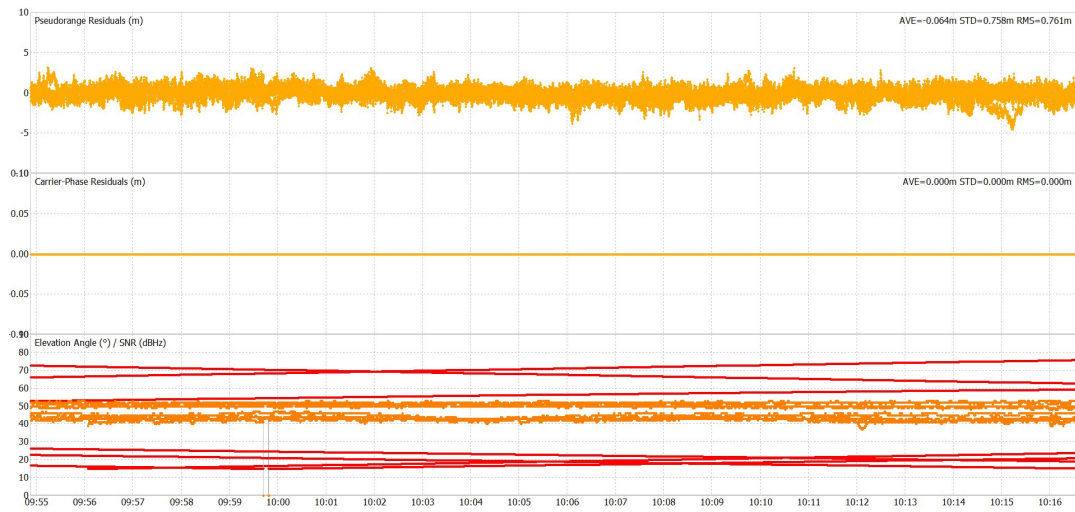


Figure 144: Pseudorange and Carrier-Phase residuals of left omnidirectional antenna.

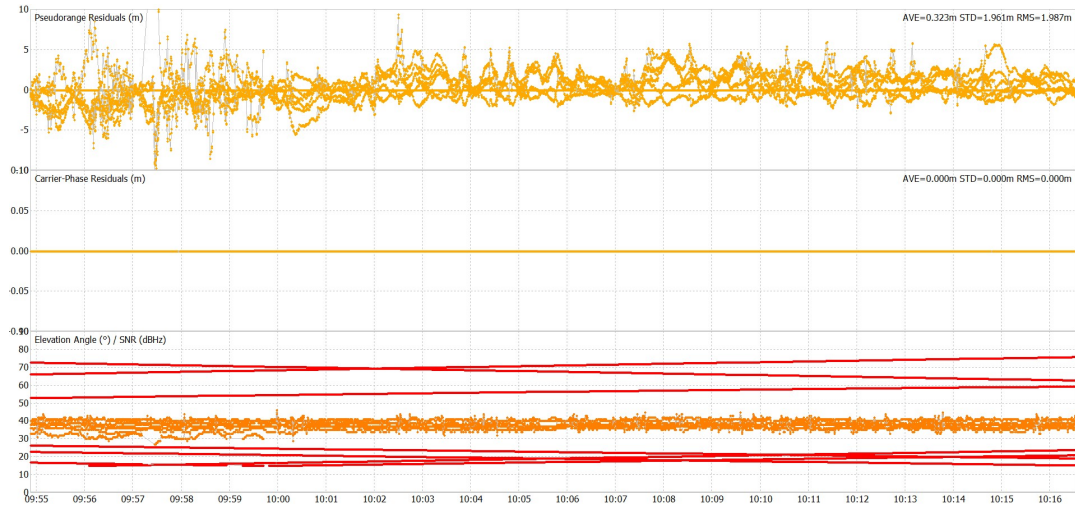


Figure 145: Pseudorange and Carrier-Phase residuals of left patch antenna.

Finally, with the Moving-Base positioning technique we finish the post-processing analysis in static acquisitions.

A.4 Static mode - reversed configuration: Moving-Base positioning

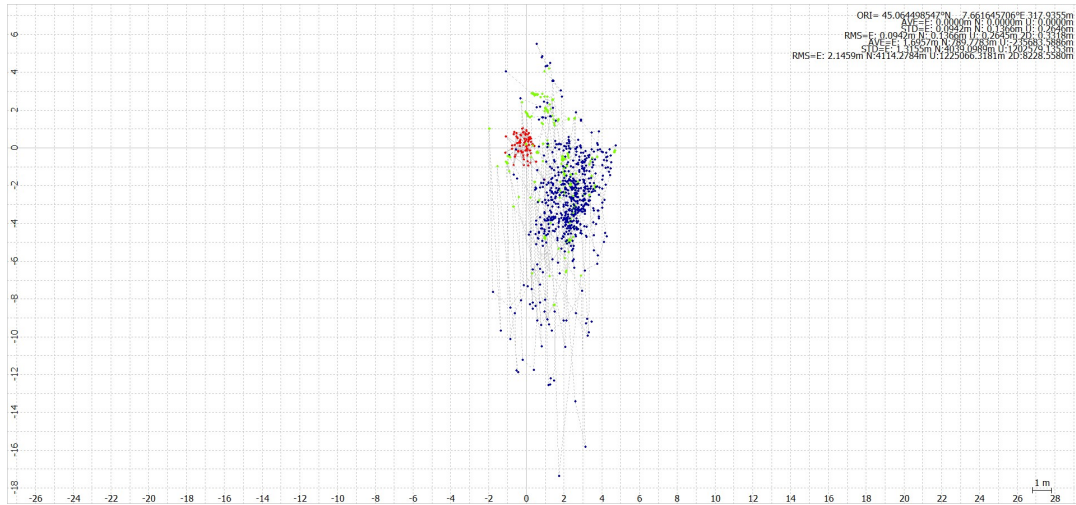


Figure 146: Ground tracking of right antennas.

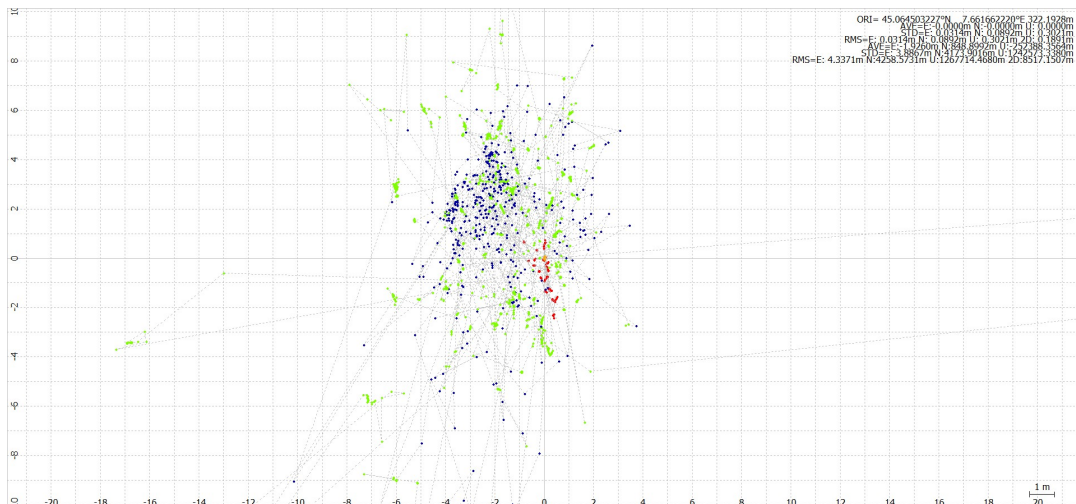


Figure 147: Ground tracking of left antennas.

Figure 146 and 147 show the Ground Track of the reversed configuration, using the Moving-Base positioning technique. We immediately notice how the solution of the antennas on the left is more dispersed than those on the right. This is also confirmed by the solution itself: the right dual-frequency antenna has 100% of fixed solution while the left one only 13.3%. In addition, the patch antenna on the right has 39.7% of fixed solution while the left one only 11%.

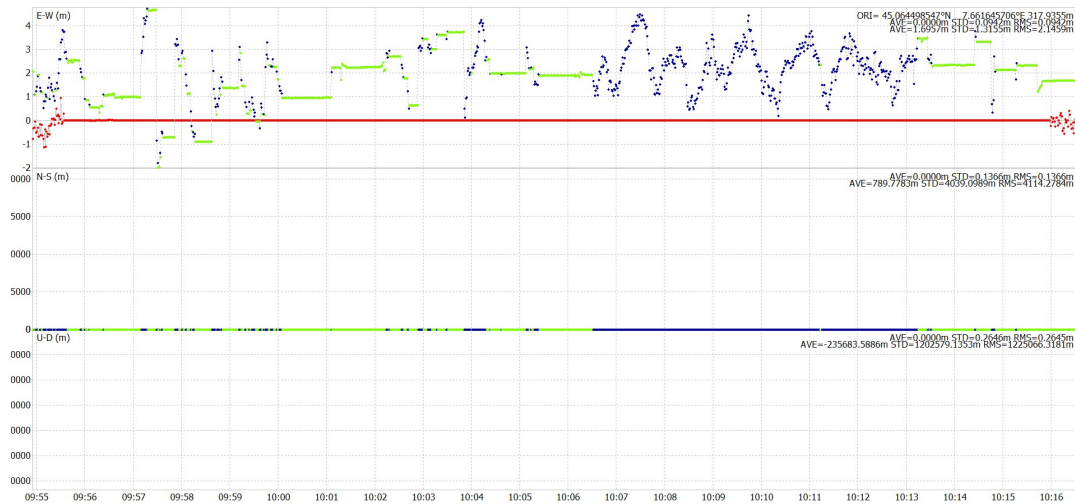


Figure 148: Right side antennas: position variation over coordinates.

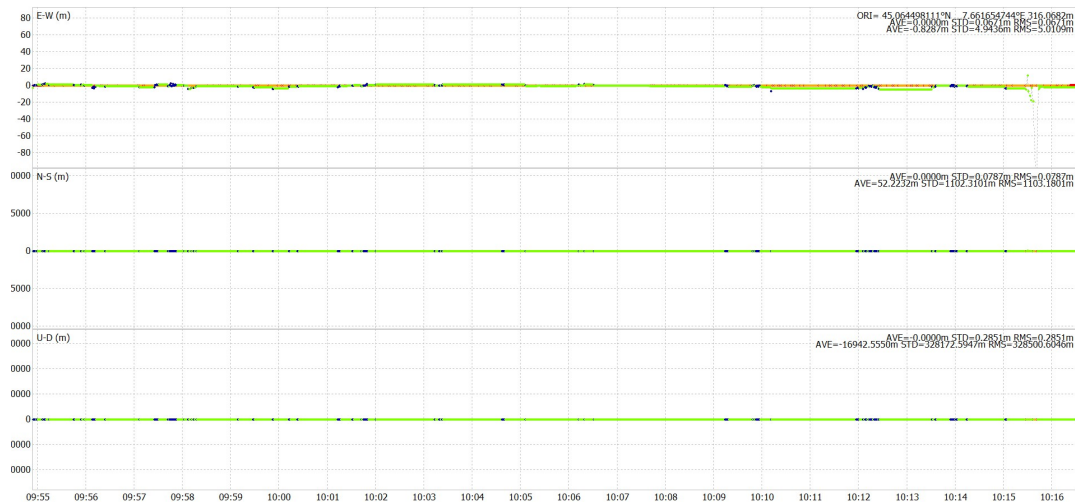


Figure 149: Left side antennas: position variation over coordinates.

In contrast, looking at Figure 148 and 149, the statistical information of the position variation over time is impressive. In fact, compared to the normal configuration, the left patch antenna registers a decrease of the order of magnitude of 10^3 for the N-S and 10^5 for U-D coordinates. It is not new that there is a general deterioration in performance for this antenna, but such a result would never have thought.

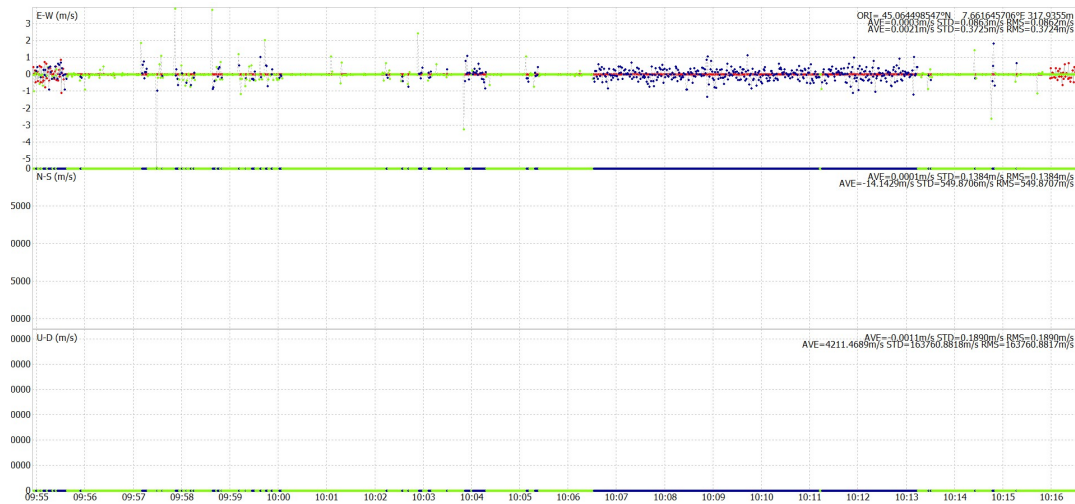


Figure 150: Right side antennas: velocity variation over coordinates.

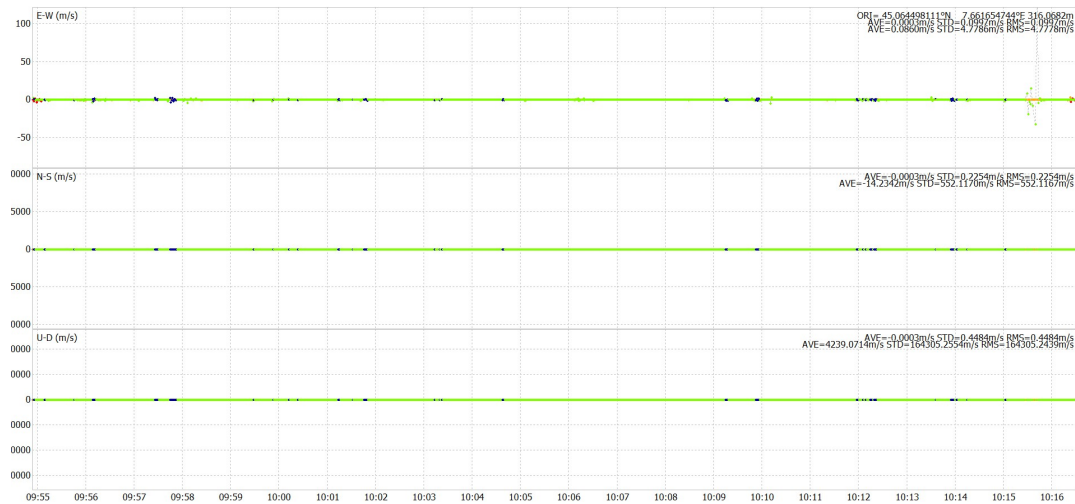


Figure 151: Left side antennas: velocity variation over coordinates.

Similar results are obtained in Figure 150 and 151. The level of error estimation is really high for both baseline configurations, making the initial assumptions right. In fact, this kind of positioning solution does not fit properly for this case study.

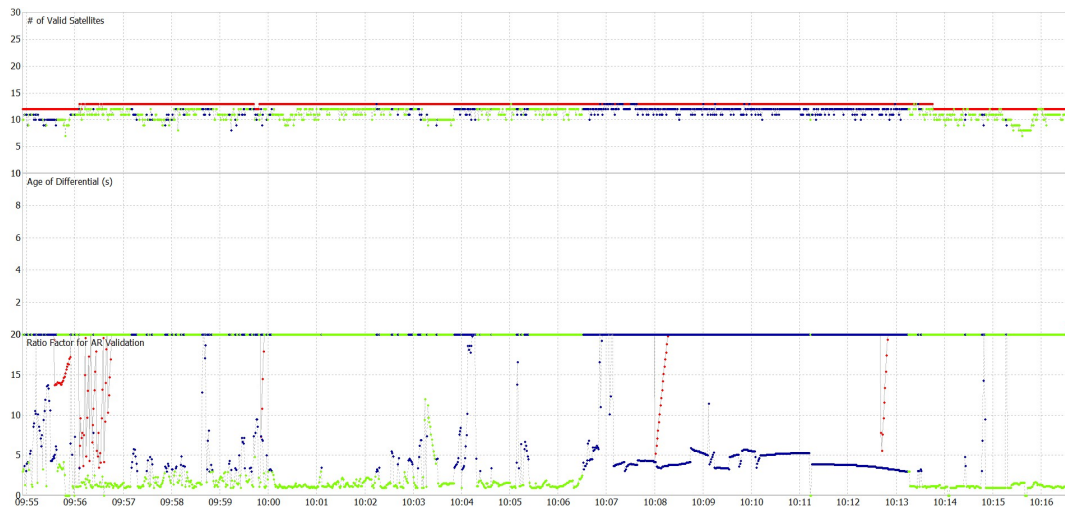


Figure 152: Right side antennas: available satellites over time.

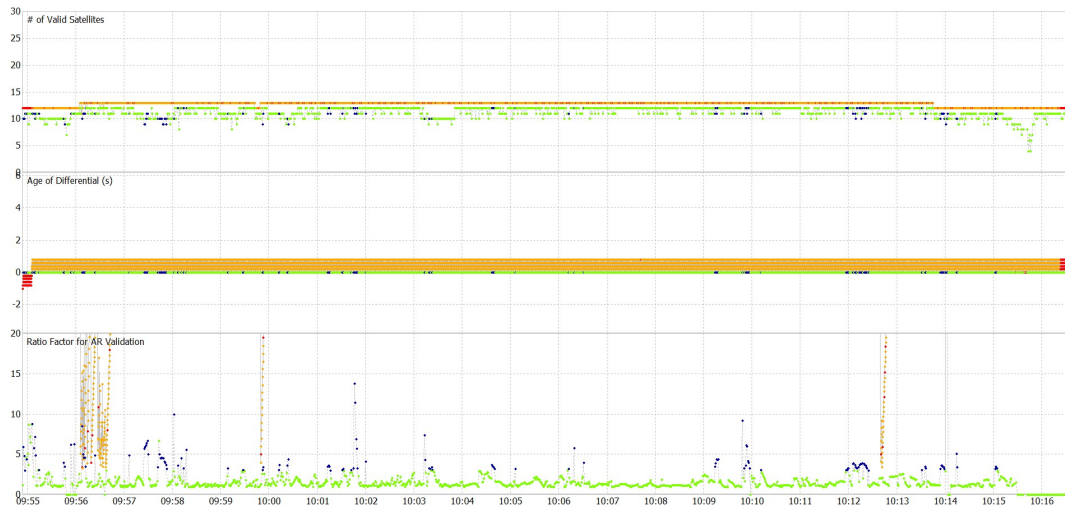


Figure 153: Left side antennas: available satellites over time.

This phenomenon is further confirmed by the plots where information about the number of valid satellites, Age of Differential and Ratio Factor for Ar Validation can be obtained. As always, the omnidirectional antennas maintain an almost constant number of satellites, lower only when the system is switched on and off. Conversely, the left patch antenna almost never reaches the fixed solution, introducing a high number of cycle sleeps during the observation period.

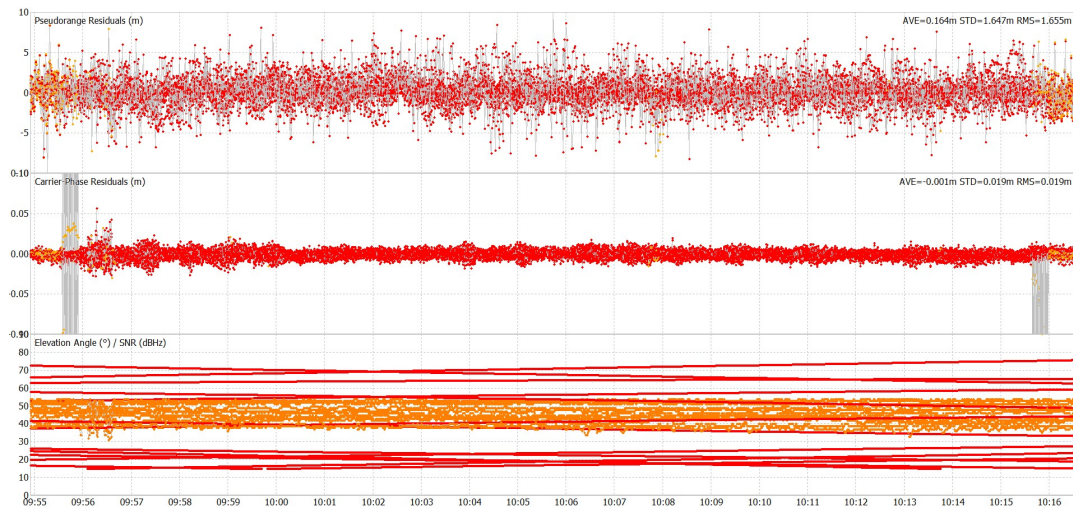


Figure 154: Pseudorange and Carrier-Phase residuals of right omnidirectional antenna.

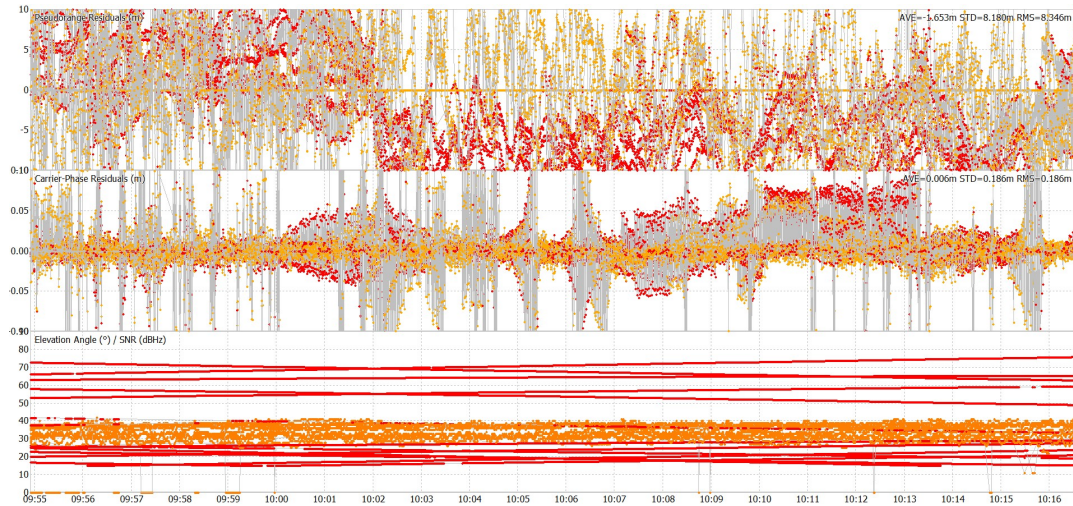


Figure 155: Pseudorange and Carrier-Phase residuals of right patch antenna.

To conclude the analysis, last figures show the antennas' Pseudorange and Carrier-Phase residuals. Even in this case, omnidirectional antennas maintain a better solution compared to the patch antennas. However, even in this case it is tangible how there is the influence of the right antenna on signal reception. In fact, microstrip residuals appear tremendously noisy, reaching RMS value of 15.854 m compared to the 4.197 m value for the left patch antenna in normal configuration. Thanks to the analysis of the reversed configuration we were able to compare the data obtained from both static acquisitions and understand whether the inversion of the right antenna could actually affect the performance of the measurement system.

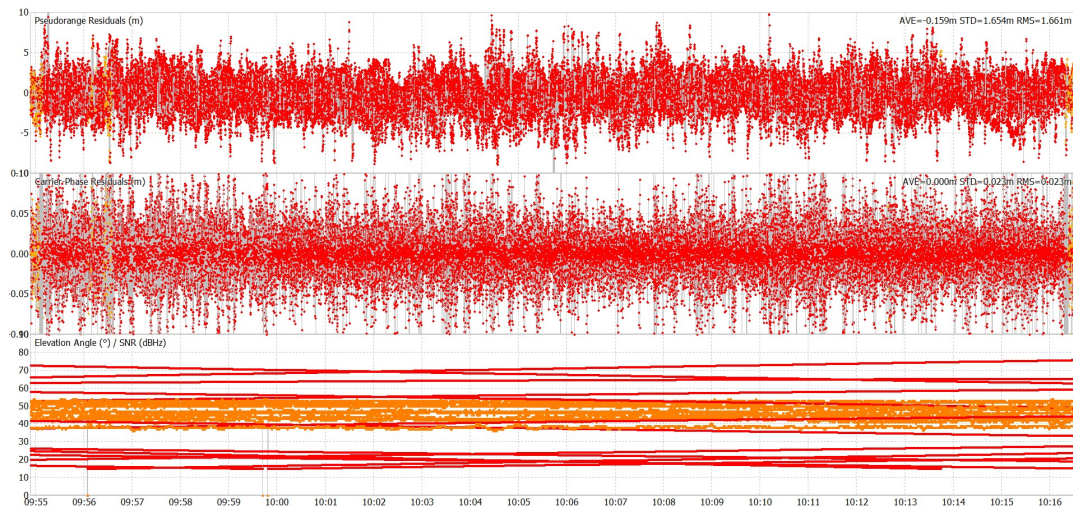


Figure 156: Pseudorange and Carrier-Phase residuals of left omnidirectional antenna.

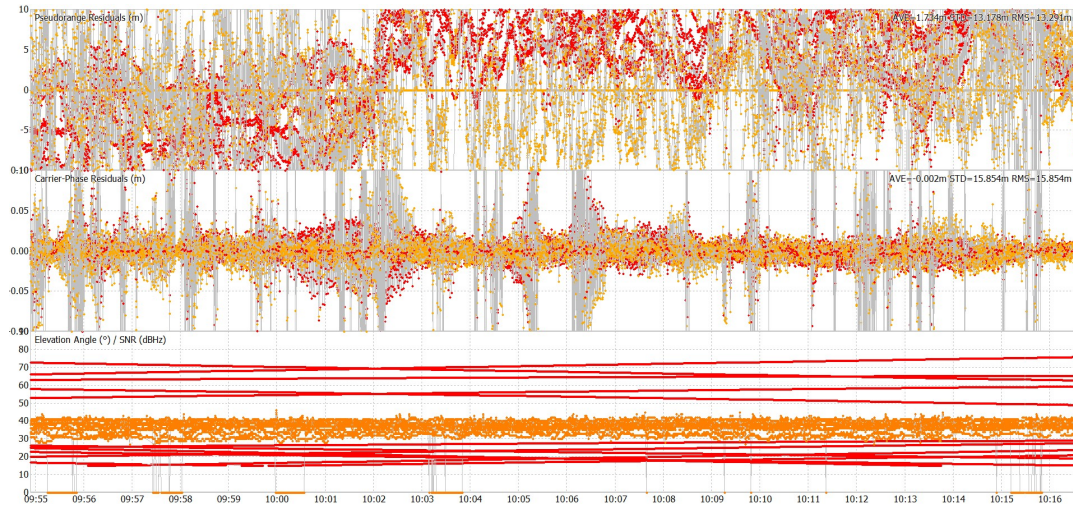


Figure 157: Pseudorange and Carrier-Phase residuals of left patch antenna.

Clearly, further conclusions and results will be provided after the analysis of the dynamic acquisitions. Therefore let us move to the following baseline configuration. Figure 158 and 159 show the Ground track of satellites using the K positioning solution. As expected, the positioning solutions are almost float ($Q = 2$), therefore reducing the fixed ones. Oddly, the right omnidirectional antenna does not maintain a reasonable float solution value at all. In fact, about 99.8% of his solution is fixed. It is a very special case since we are working with the Moving-Base approach, therefore considering moving stations.

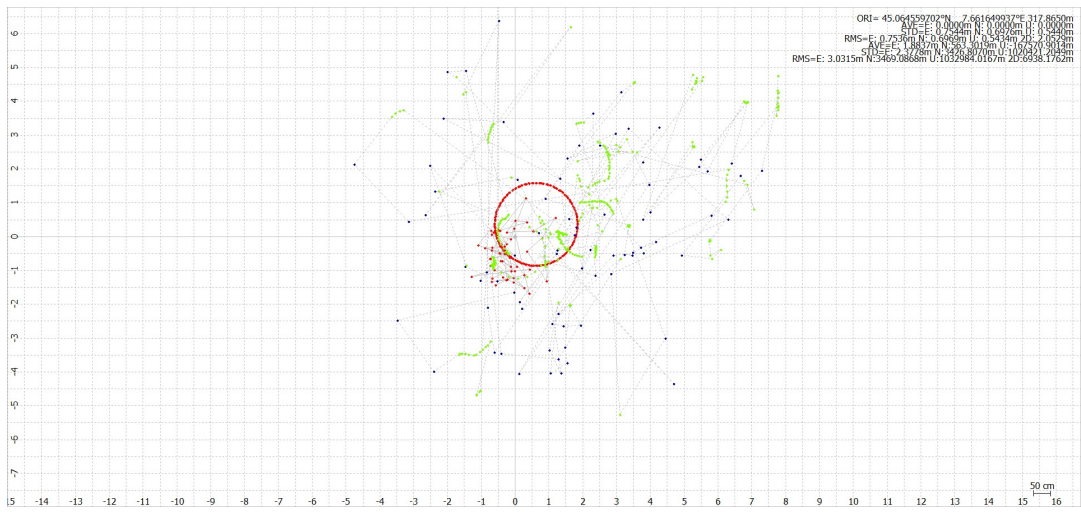


Figure 158: Right side continuous rotation.

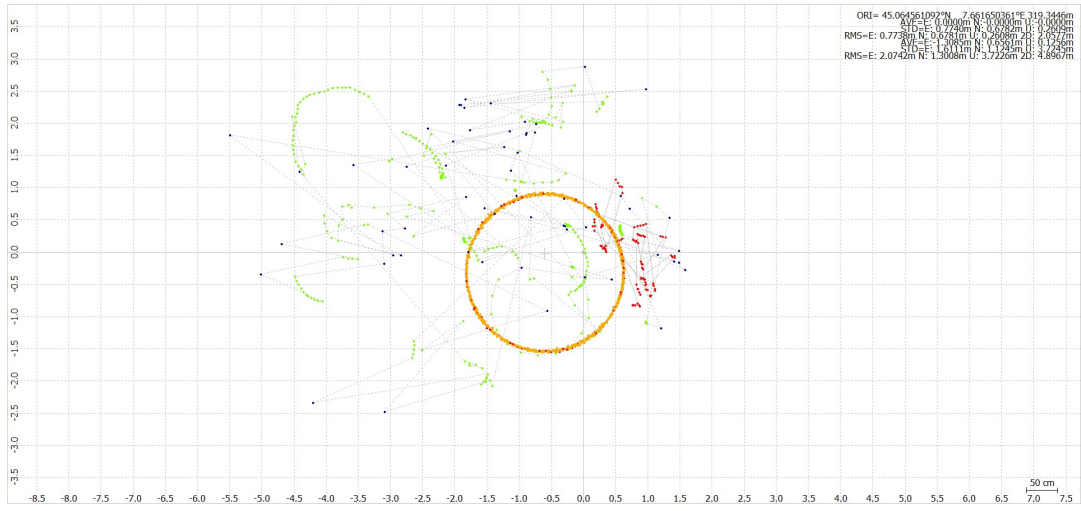


Figure 159: Left side continuous rotation.

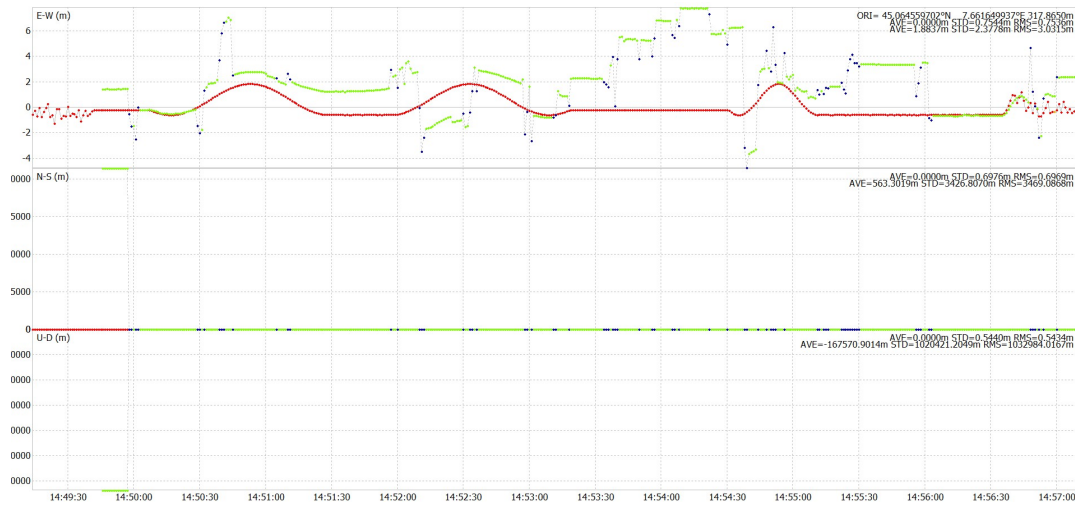


Figure 160: Right side continuous rotation: position variation over coordinates.

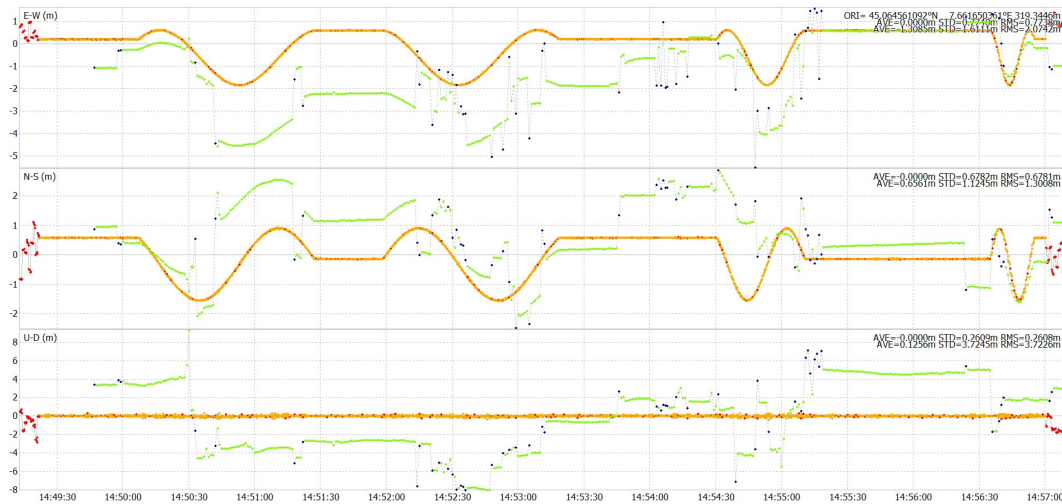


Figure 161: Left side continuous rotation: position variation over coordinates.

Figure 160 and 161 show the position variation over time among the three coordinates. As can be seen, left antennas occupy same positions of right antennas but at different time instants. This is due to the fact that they are moving in opposite directions. In addition, flat trends correspond to static moment, therefore when the rotating platform is set to return to the original position. What can be underlined is that right antennas have an odd behaviour among the N-S and U-D coordinates. In fact, despite the left antennas, which good statistic values are obtained, tremendous values of standard deviation and RMS are observed. This is probably caused by the high level of fixed solution gained by the right omnidirectional antenna.



Figure 162: Right side continuous rotation: velocity variation over coordinates.



Figure 163: Left side continuous rotation: velocity variation over coordinates.

Figure 162 and 163 display the velocity variation through the observation time. As can be seen, speed variations of the right antennas correspond to speed variations of the left antennas, but in opposite directions. The right omnidirectional's odd behaviour showed in the previous graphs are even displayed in the following figures.

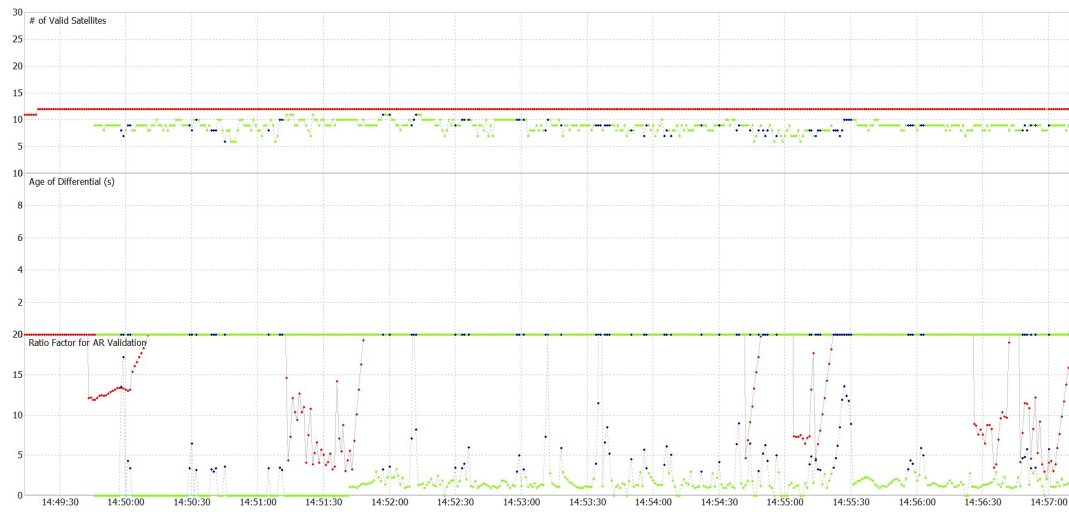


Figure 164: Right side continuous rotation: available satellites over time.



Figure 165: Left side continuous rotation: available satellites over time.

As regard the number of valid satellites (see Figure 164 and 165), a same behaviour is seen for both right and left side. In fact, omnidirectional antennas maintain a constant number of satellites among all the observation window. Conversely, patch antennas vary their trends due to the receiver quality.



Figure 166: Pseudorange and Carrier-Phase residuals of left patch antenna.

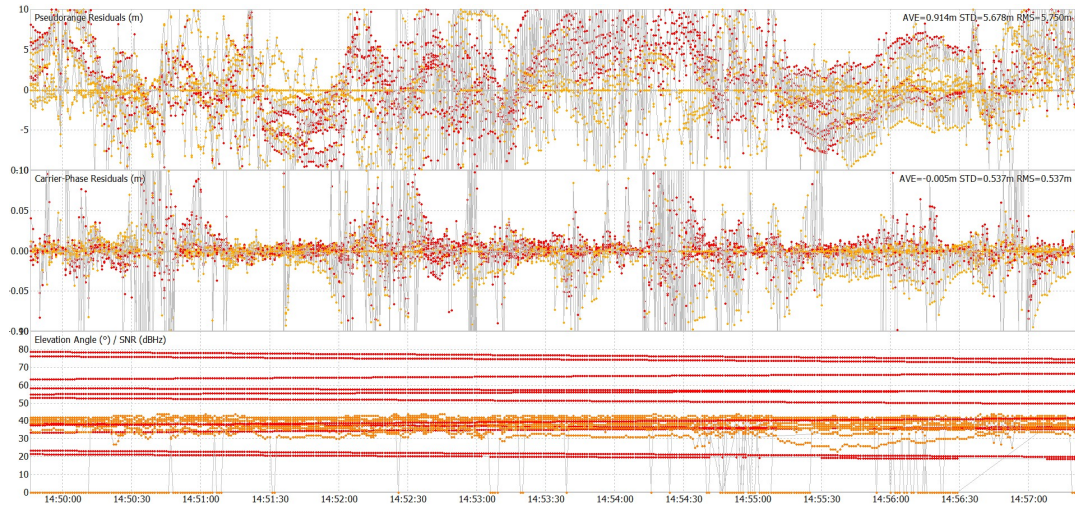


Figure 167: Pseudorange and Carrier-Phase residuals of left patch antenna.

Finally, Figure 166, 167, 168 and 169 show the Pseudorange and Carrier-Phase Residuals for both baseline sides. As can be seen, a more chaotic behaviour is showed by the left omnidirectional antennas. This is even confirmed by the statistic parameters values analysis.

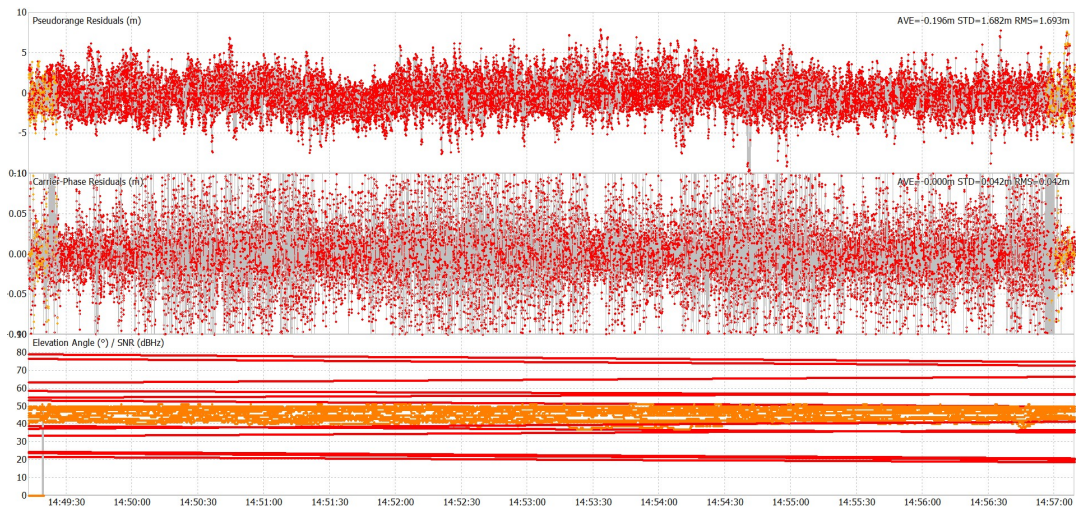


Figure 168: Pseudorange and Carrier-Phase residuals of left patch antenna.

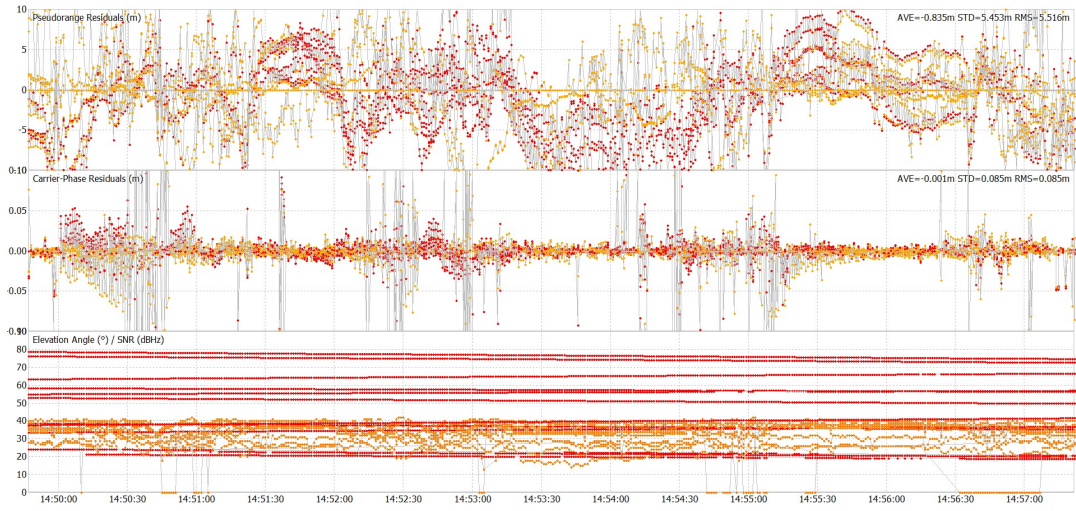


Figure 169: Pseudorange and Carrier-Phase residuals of left patch antenna.

A.5 Dynamic mode - normal configuration: Moving-Base positioning in stepped rotation

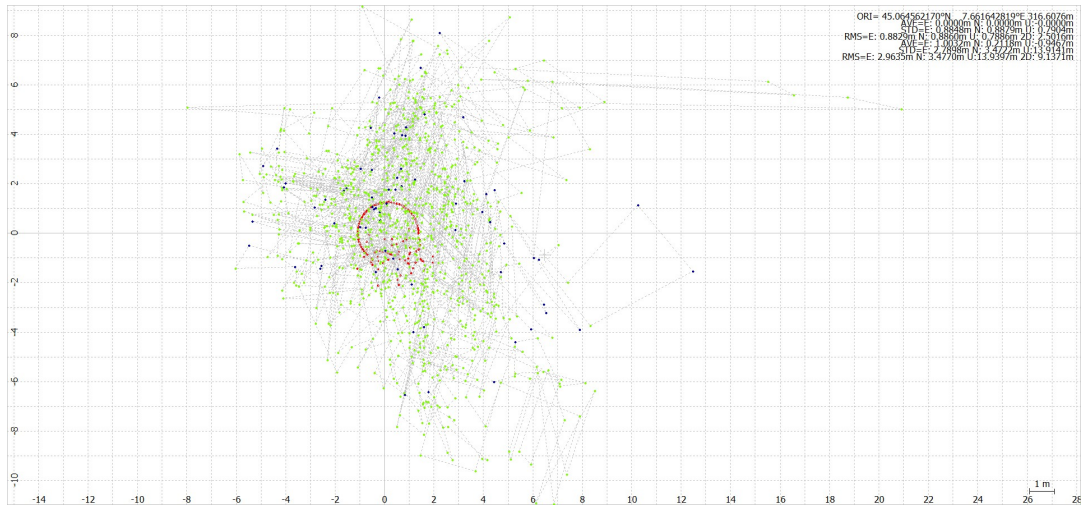


Figure 170: Right side stepped rotation: Ground Tracking.

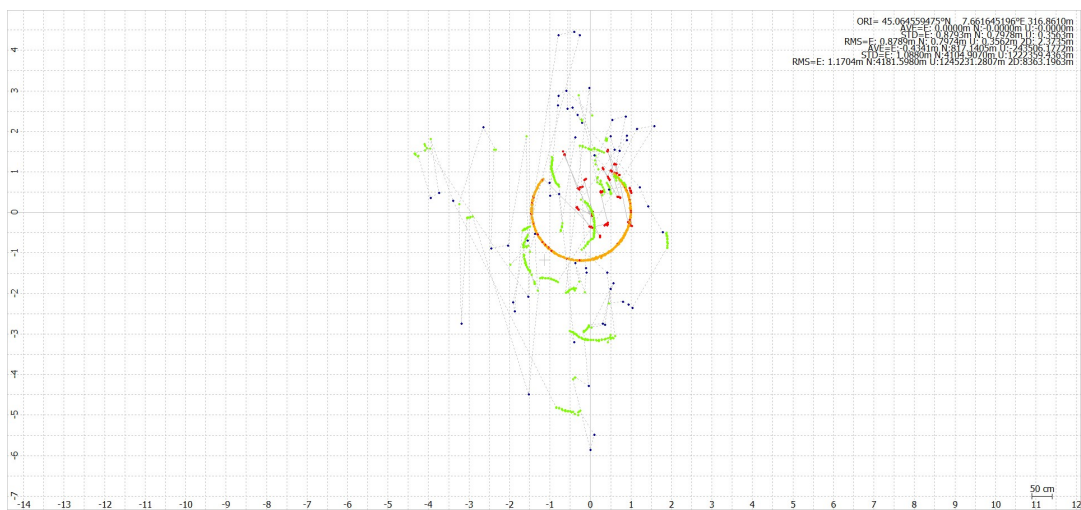


Figure 171: Left side stepped rotation: Ground Tracking.

Finally, here is presented the stepped rotation for the Moving-Base positioning technique. Figure 182 and 183 show the Ground Track of constellation satellites. Even in this case, the left omnidirectional antenna has most its solution float. Conversely, the right one displays a 100% of $Q = 1$ solution. Patch antennas maintain a consistent behaviour with the used technique. In particular, right patch antenna shows a huge scattered ground tracking compared to the left one. According to what has been said before, the omnidirectional antennas do not make a complete circle but rather of 200° , making the flat angle acquisition possible.

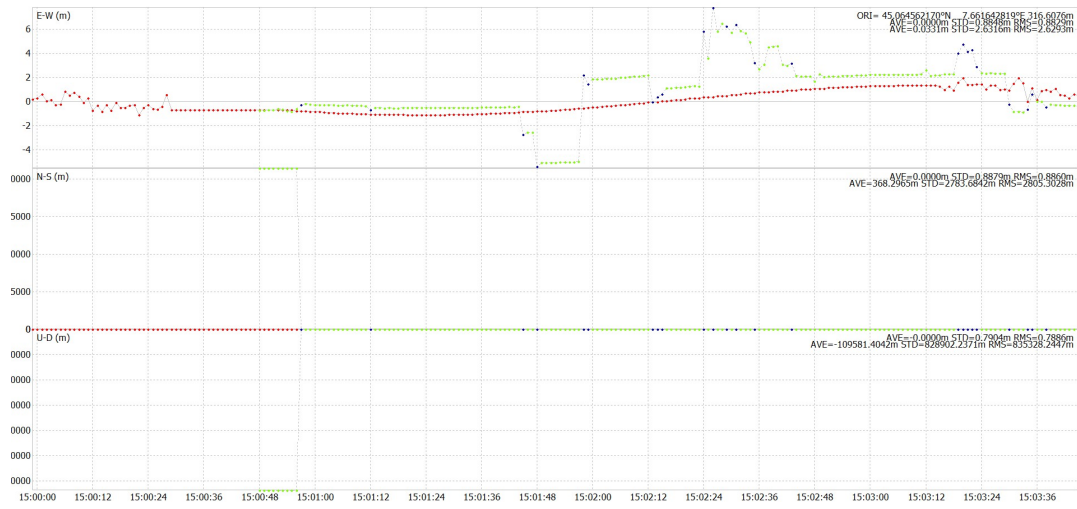


Figure 172: Right side continuous rotation: position variation over coordinates.

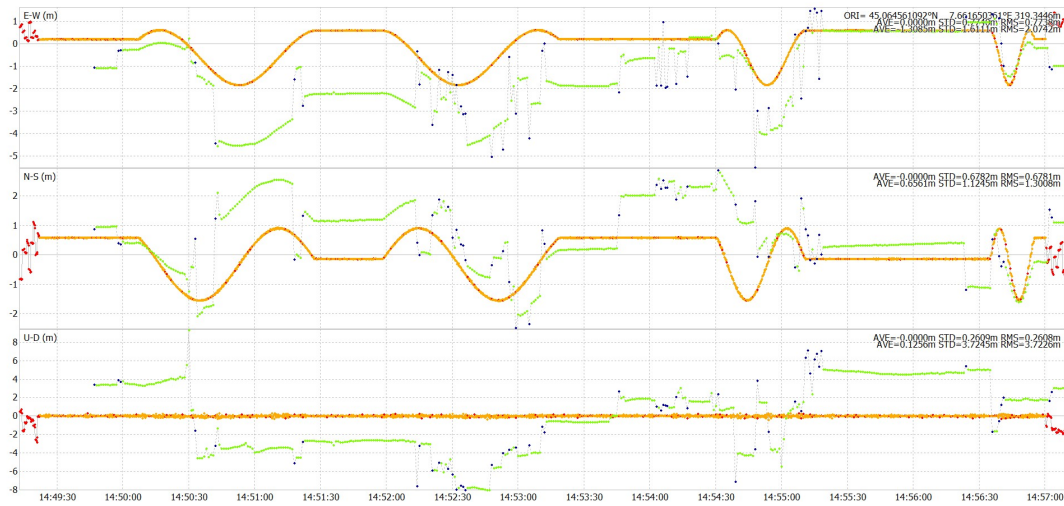


Figure 173: Right side continuous rotation: position variation over coordinates.

Figure 184 and 185 show the position variation among the three coordinates.



Figure 174: Right side continuous rotation: omnidirectional antenna's velocity variation over coordinates.



Figure 175: Right side continuous rotation: patch antenna's velocity variation over coordinates.



Figure 176: Right side continuous rotation: available satellites over time.



Figure 177: Left side continuous rotation: available satellites over time.



Figure 178: Pseudorange and Carrier-Phase residuals of right omnidirectional antenna.

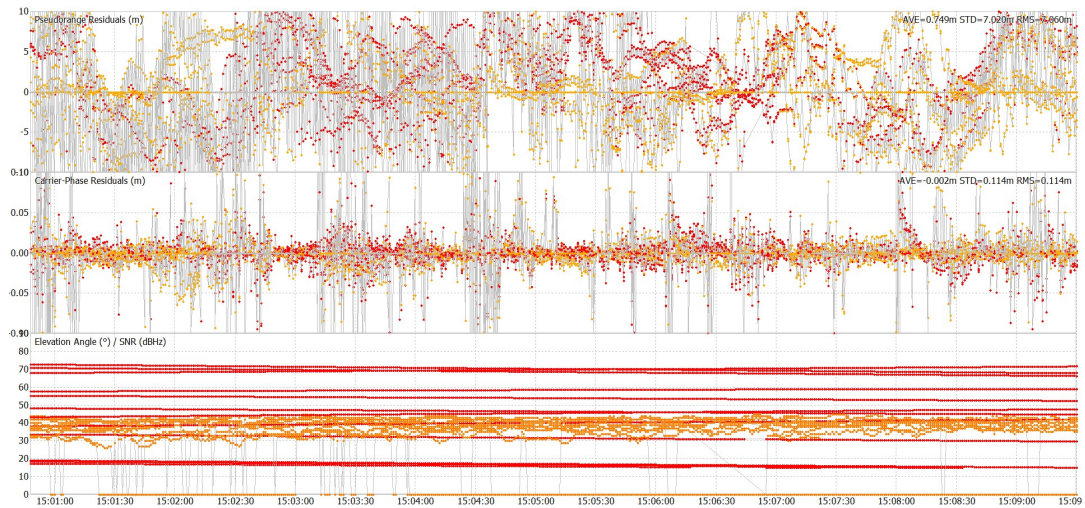


Figure 179: Pseudorange and Carrier-Phase residuals of right patch antenna.

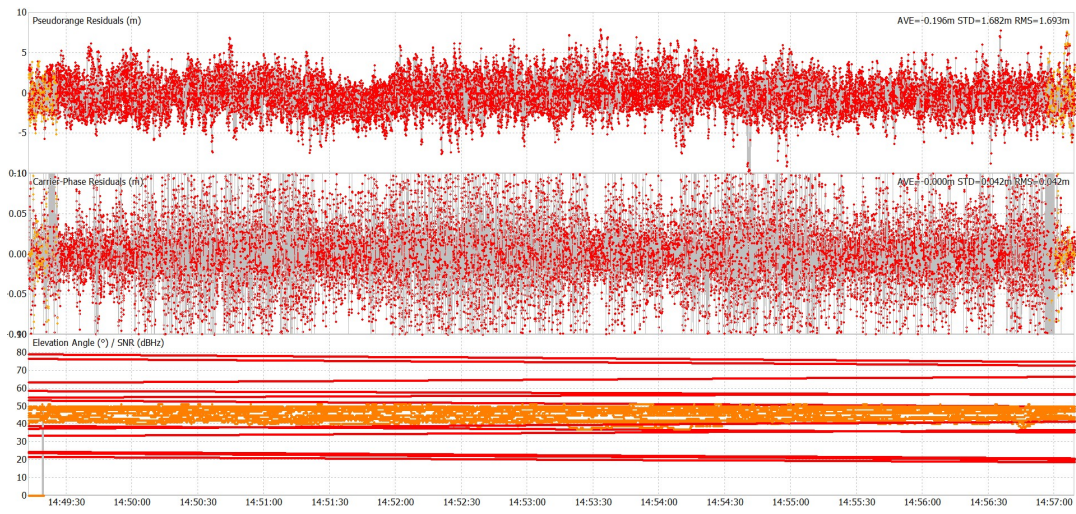


Figure 180: Pseudorange and Carrier-Phase residuals of left omnidirectional antenna.

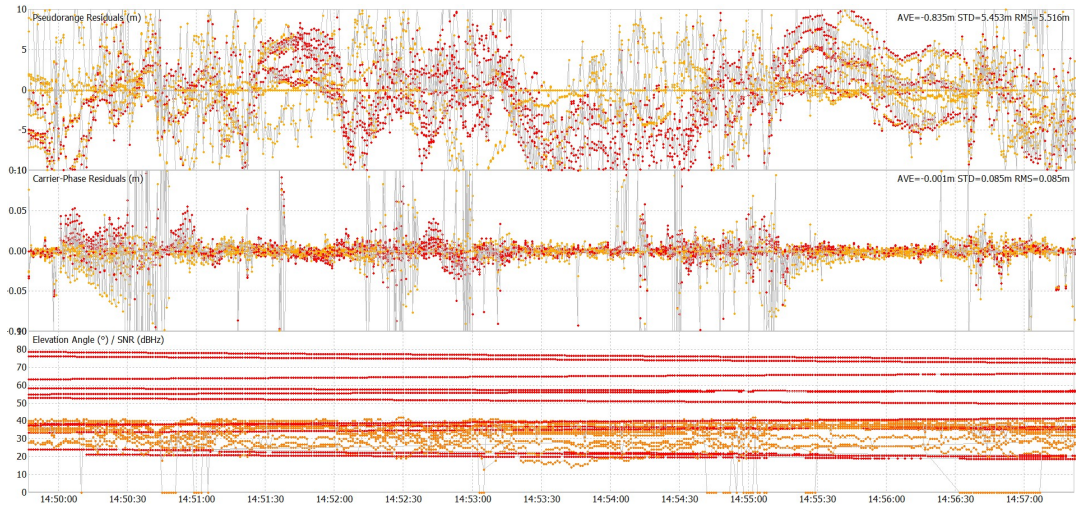


Figure 181: Pseudorange and Carrier-Phase residuals of left patch antenna.

A.5.1 Dynamic mode - reversed configuration: Moving-Base positioning in continuous rotation

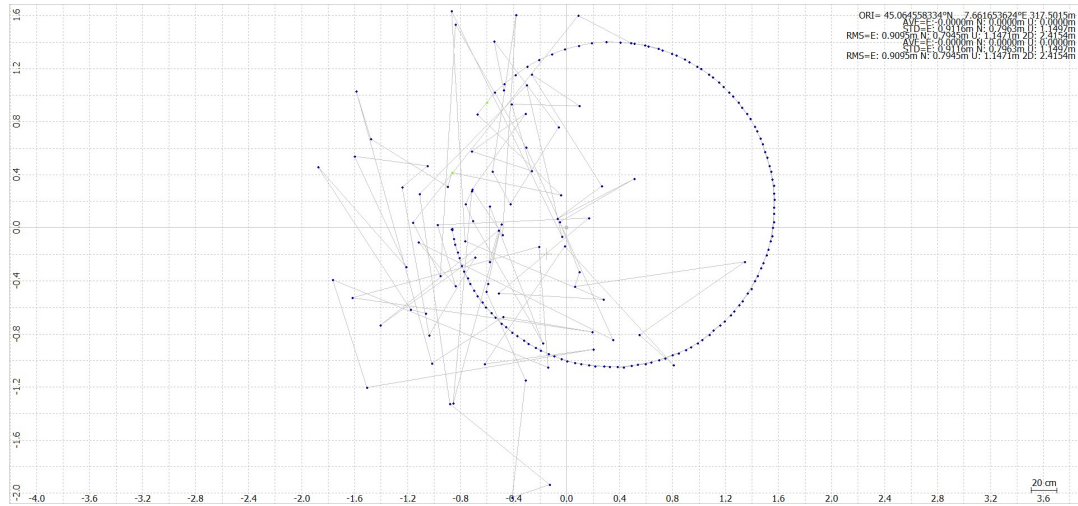


Figure 182: Right side continuous rotation.

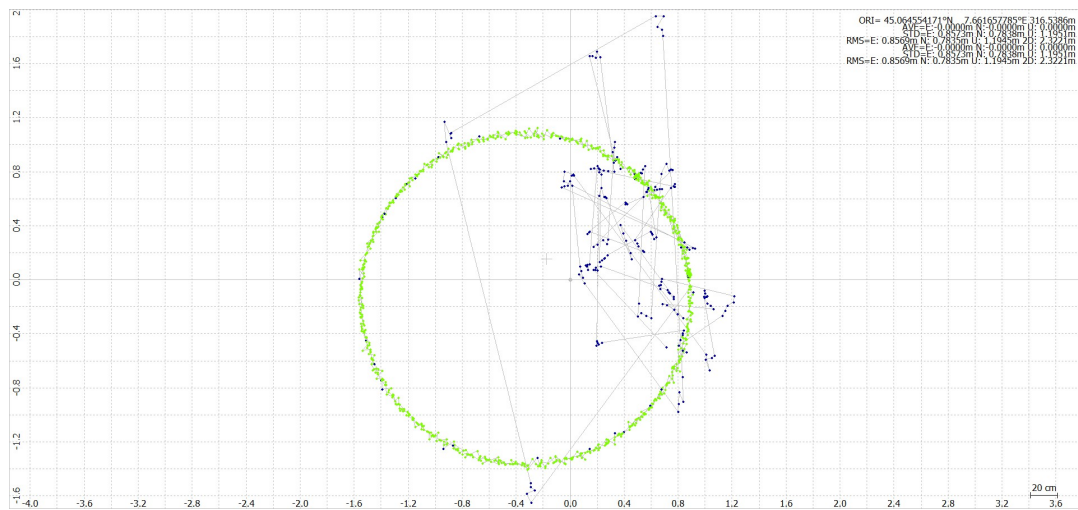


Figure 183: Left side continuous rotation.

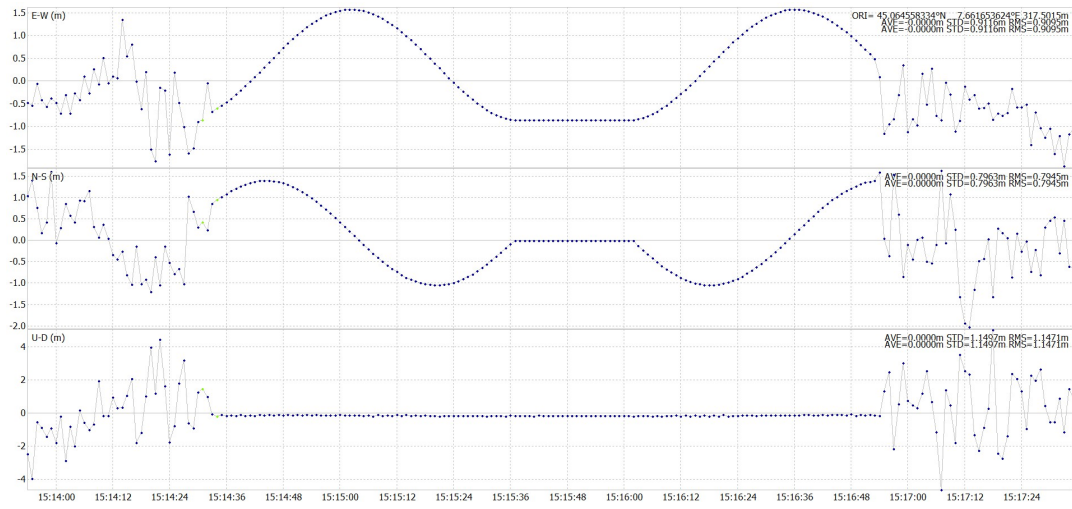


Figure 184: Right side continuous rotation: position variation over coordinates.

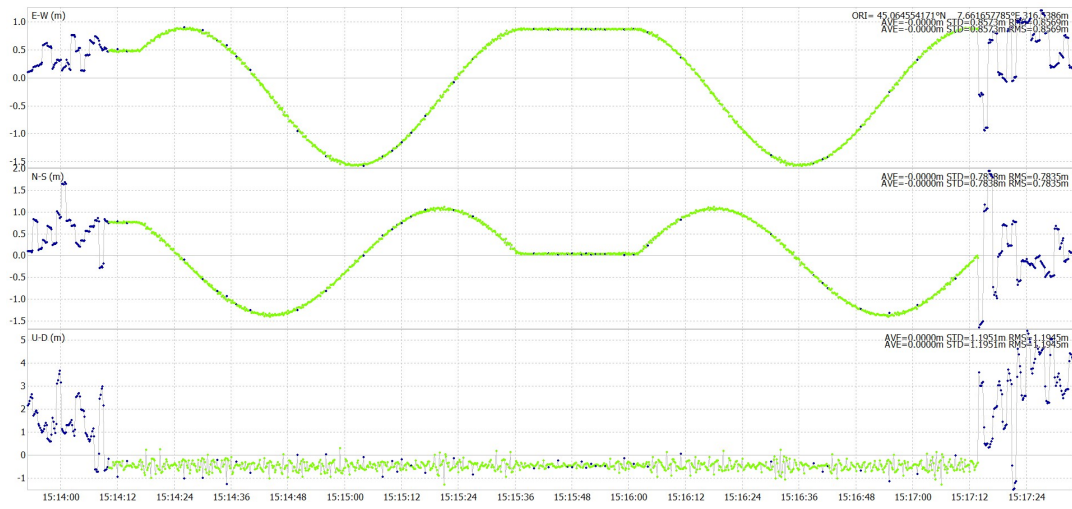


Figure 185: Left side continuous rotation: position variation over coordinates.

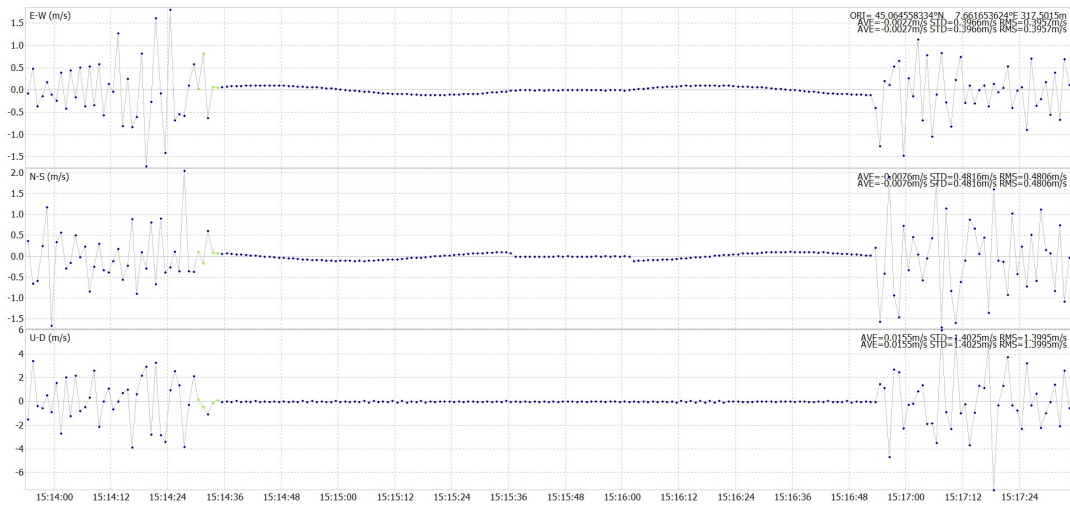


Figure 186: Right side continuous rotation: velocity variation over coordinates.



Figure 187: Right side continuous rotation: available satellites over time.



Figure 188: Right side continuous rotation: available satellites over time.



Figure 189: Left side continuous rotation: available satellites over time.

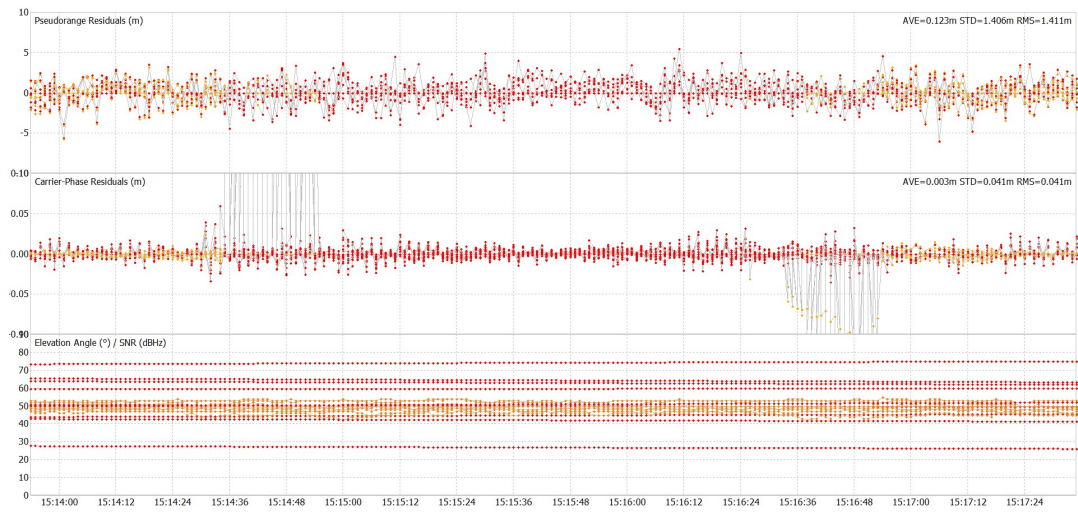


Figure 190: Pseudorange and Carrier-Phase residuals of right antennas.

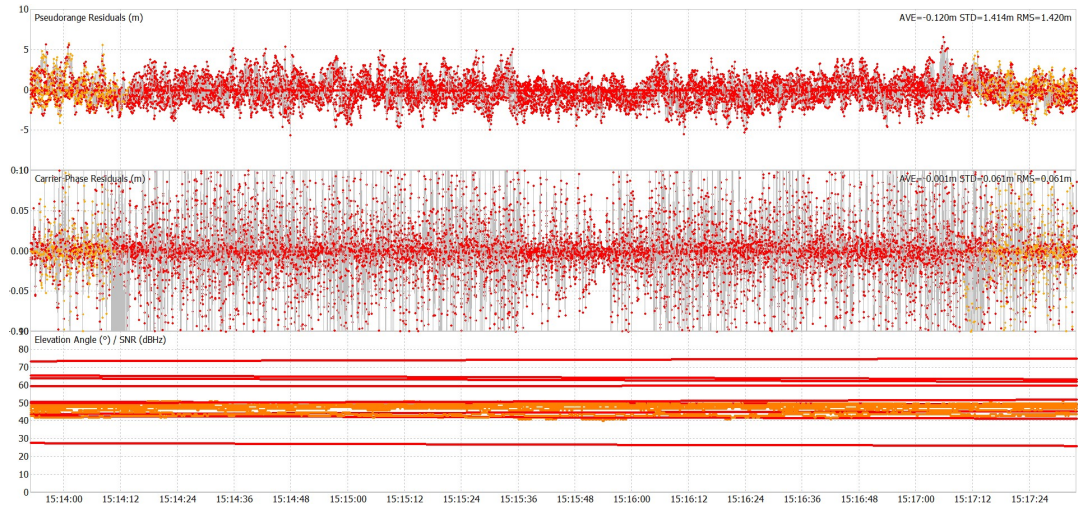


Figure 191: Pseudorange and Carrier-Phase residuals of left antennas.

A.6 Dynamic mode - reversed configuration: Moving-Base positioning in stepped rotation

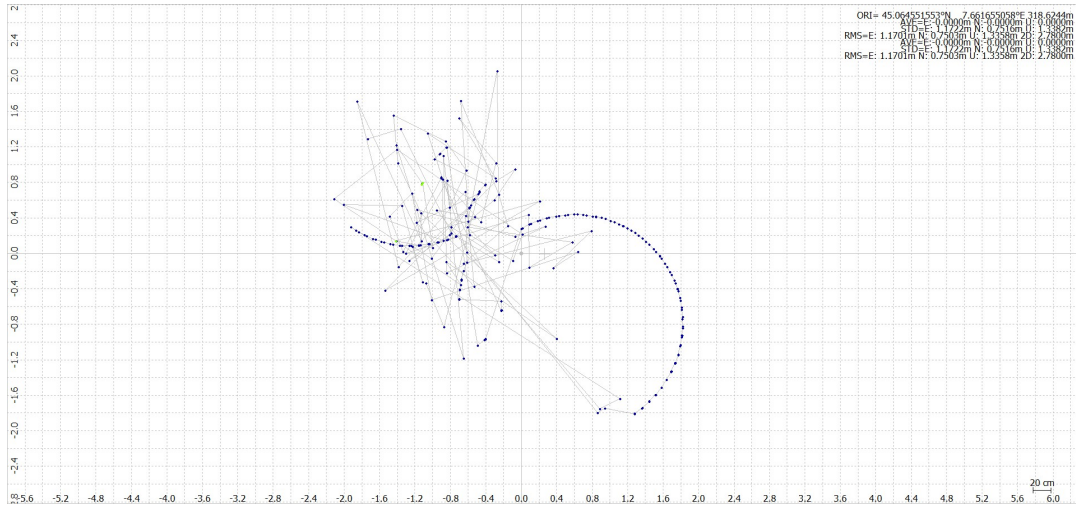


Figure 192: Right side continuous rotation.

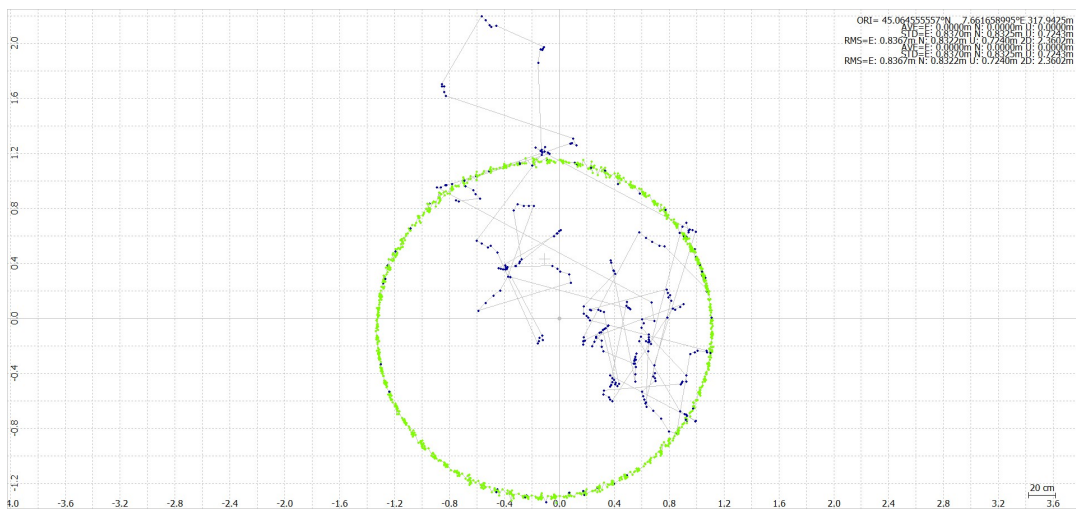


Figure 193: Left side continuous rotation.

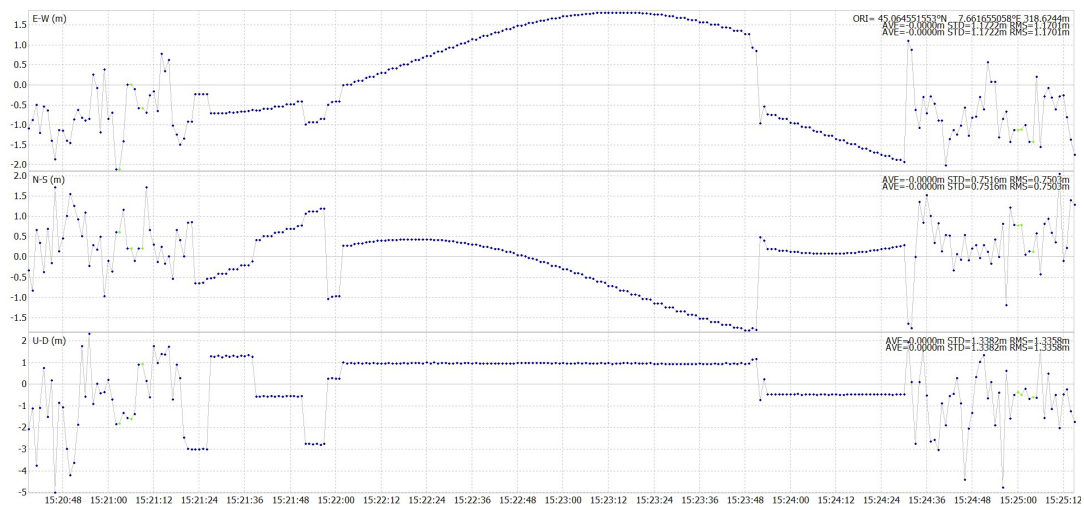


Figure 194: Right side continuous rotation: position variation over coordinates.

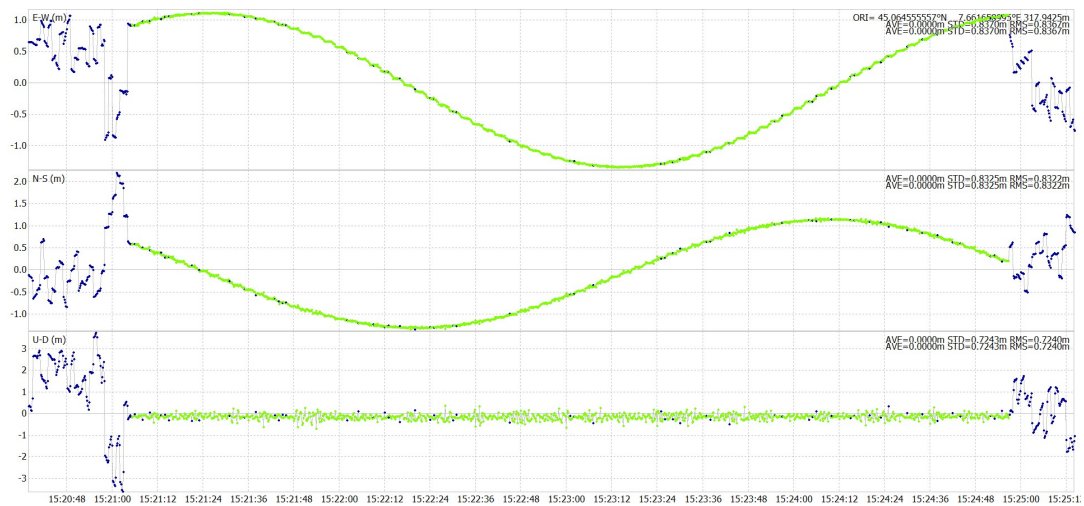


Figure 195: Left side continuous rotation: position variation over coordinates.

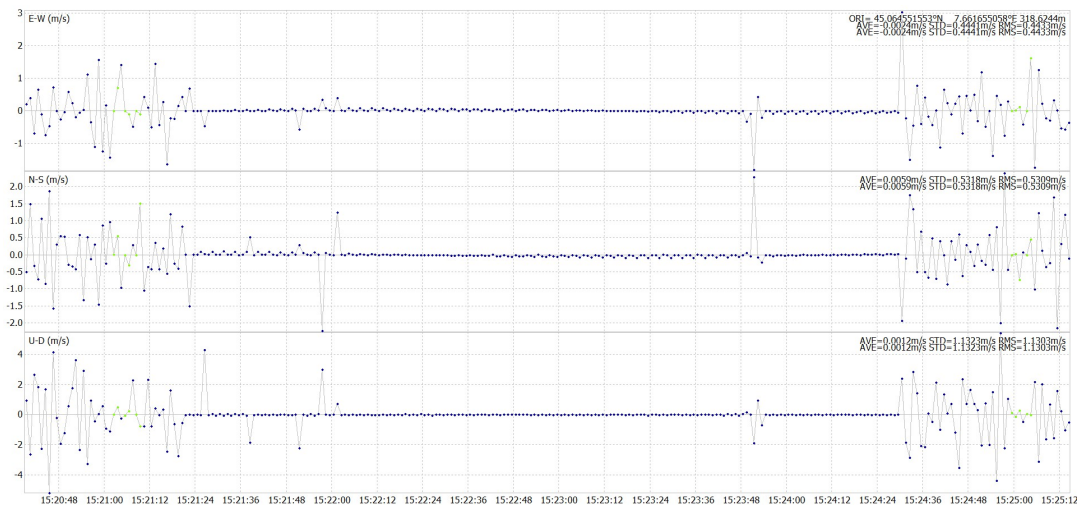


Figure 196: Right side continuous rotation: velocity variation over coordinates.

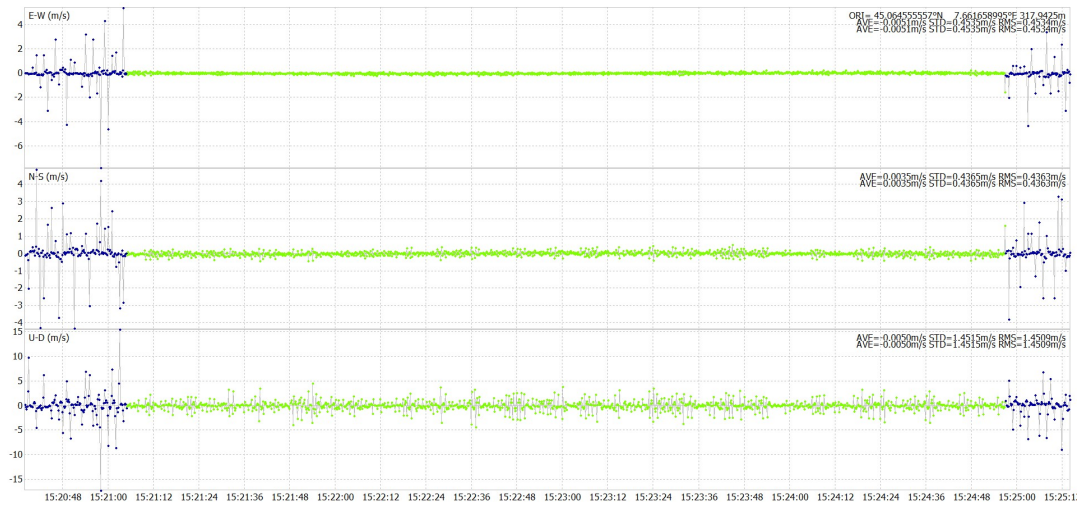


Figure 197: Right side continuous rotation: available satellites over time.

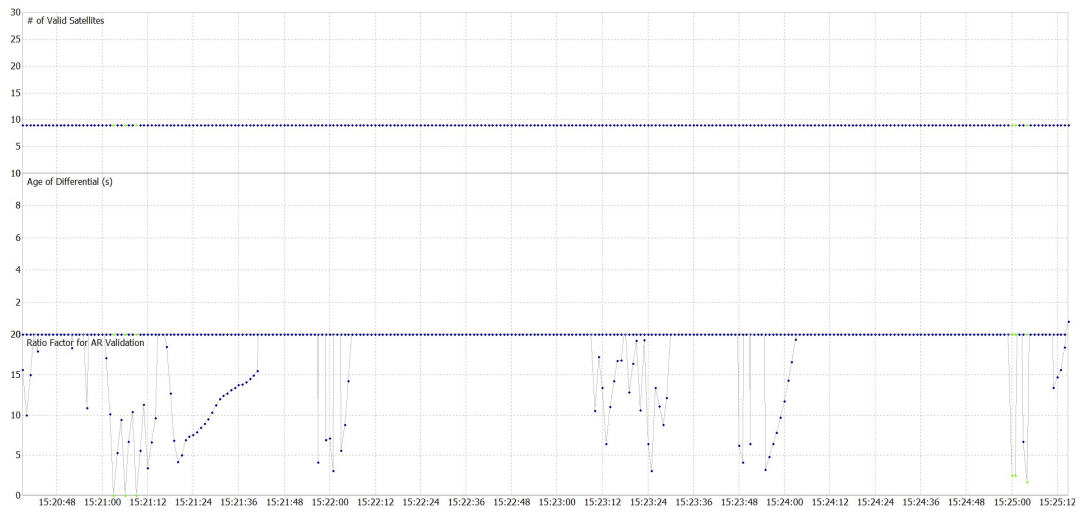


Figure 198: Right side continuous rotation: available satellites over time.



Figure 199: Left side continuous rotation: available satellites over time.



Figure 200: Pseudorange and Carrier-Phase residuals of right antennas.

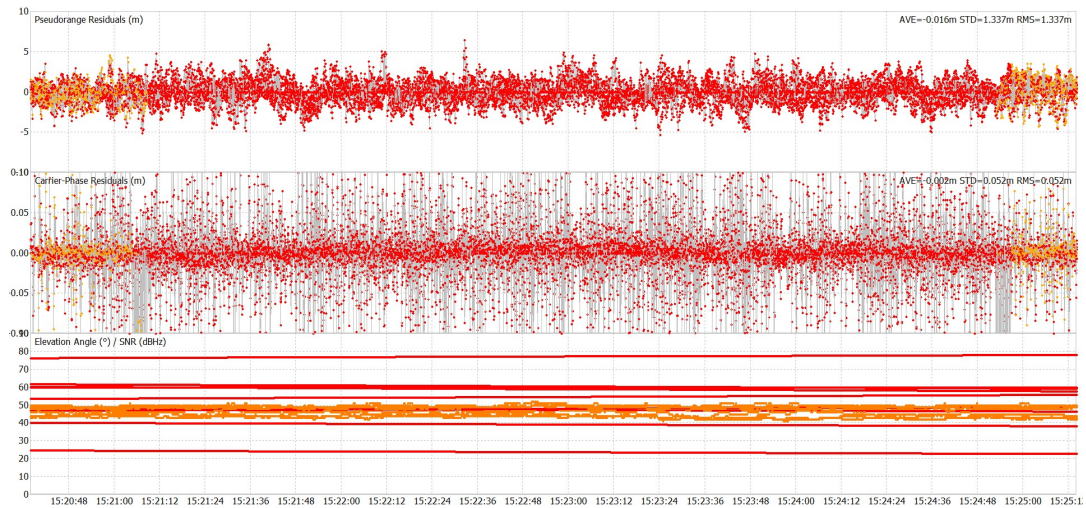


Figure 201: Pseudorange and Carrier-Phase residuals of left antennas.

B Code

```

1 import pandas as pd
2 import matplotlib.pyplot as plt
3 import numpy as np
4 import math
5 from matplotlib.pyplot import figure
6
7
8 #Omnidirectional heading computation in static mode with Kinematic positioning
9
10 dataset1 = pd.read_excel(r'/Users/alessio/Downloads/
11     Heading_estimation_static_kinematic/Omni_dataset.xlsx')
12 dataset_omni = dataset1[0:2325]
13 print(dataset_omni)

```

```

14 baseline1 =[]
15 V_n1 = []
16 theta1 = []
17 for i in range(len(dataset_omni)):
18     baseline1.append(math.sqrt((dataset_omni['E1'][i] - dataset_omni['E2'][i])
19     **2 + (dataset_omni['N1'][i] - dataset_omni['N2'][i])**2))
20     V_n1.append(dataset_omni['N1'][i] - dataset_omni['N2'][i])
21     theta1.append(math.acos(V_n1[i]/baseline1[i]))
22
23 Heading_angle_omni = np.mean(theta1)
24
25 # setting the x - coordinates
26 x = np.arange(0, 2325)
27 # setting the corresponding y - coordinates
28 y = baseline1
29 y1 = 1.3
30 figure(figsize=(12, 6))
31 # plotting the points
32 plt.plot(x, y, color='green', linewidth = 2.0, label = 'Estimated baseline')
33 plt.axhline(np.mean(baseline1), color = 'blue', label = 'Mean')
34 # plt.axhline(np.std(baseline1))
35 plt.axhline(y1, color = 'orange', label = 'Real baseline')
36 plt.xlabel('Time epochs')
37 plt.ylabel('Baseline values (m)')
38 plt.title('Omnidirectional baseline trend among observation window')
39 plt.legend()
40 plt.show()
41
42
43 # setting the x - coordinates
44 x = np.arange(0, 2325)
45 # setting the corresponding y - coordinates
46 y = theta1
47 figure(figsize=(12, 8))
48 # plotting the points
49 plt.plot(x, y, color='yellowgreen', linewidth = 0.7, label = 'Baseline')
50 plt.axhline(np.mean(theta1), color = 'blue', label = 'Mean')
51 # plt.axhline(np.std(theta1), color = 'orange', label = 'Std Deviation')
52 plt.xlabel('Time epochs')
53 plt.ylabel('Angle values (rad)')
54 plt.title('Heading variation for omnidirectional antennas')
55 plt.legend()
56 plt.show()
57
58 #Patch heading computation in static mode with Kinematic positioning and
59     reversed configuration
60 dataset2 = pd.read_excel(r'/Users/alessio/Downloads/
61     Heading_estimation_static_kinematic/Patch_dataset.xlsx')
62 dataset_patch = dataset2[0:2607]
63 print(dataset_patch)
64
65 baseline2 =[]
66 V_n2 = []
67 theta2 = []
68 for i in range(len(dataset_patch)):
69     baseline2.append(math.sqrt((dataset_patch['E1'][i] - dataset_patch['E2'][i])

```

```

69     **2 + (dataset_patch['N1'][i] - dataset_patch['N2'][i])**2))
70     V_n2.append(dataset_patch['N2'][i] - dataset_patch['N1'][i])
71     theta2.append(math.acos(V_n2[i]/baseline2[i]))
72
73 Heading_angle_patch = np.mean(theta2)
74
75 # setting the x - coordinates
76 x = np.arange(0, 2607)
77 # setting the corresponding y - coordinates
78 y = baseline2
79 figure(figsize=(12, 8))
80 # plotting the points
81 plt.plot(x, y, color='green', linewidth = 0.7, label = 'Baseline')
82 plt.axhline(np.mean(baseline2), color = 'blue', label = 'Mean')
83 plt.axhline(np.std(baseline2), color = 'orange', label = 'Std Deviation')
84 plt.xlabel('Time epochs')
85 plt.ylabel('Baseline values (m)')
86 plt.title('Patch baseline trend among observation window')
87 plt.legend()
88 plt.show()
89
90
91 # setting the x - coordinates
92 x = np.arange(0, 2607)
93 # setting the corresponding y - coordinates
94 y = theta2
95 figure(figsize=(12, 8))
96 # plotting the points
97 plt.plot(x, y, color='yellowgreen', linewidth = 0.7, label = 'Heading')
98 plt.axhline(np.mean(theta2), color = 'blue', label = 'Mean')
99 plt.axhline(np.std(theta2), color = 'orange', label = 'Std Deviation')
100 plt.xlabel('Time epochs')
101 plt.ylabel('Angle values (rad)')
102 plt.title('Heading variation among observation window for patch antennas')
103 plt.legend()
104 plt.show()
105
106 #Omnidirectional heading computation in static mode with Kinematic positioning
    and reversed configuration
107
108 dataset3 = pd.read_excel(r'/Users/alessio/Downloads/
    Heading_estimation_static_kinematic_reversed/Omni_dataset2.xlsx')
109 dataset_omni2 = dataset3[0:1302]
110 print(dataset_omni2)
111
112 baseline3 = []
113 V_n3 = []
114 theta3 = []
115 for i in range(len(dataset_omni2)):
116     baseline3.append(math.sqrt((dataset_omni2['E1'][i] - dataset_omni2['E2'][i])
    **2 + (dataset_omni2['N1'][i] - dataset_omni2['N2'][i])**2))
117     V_n3.append(dataset_omni2['N1'][i] - dataset_omni2['N2'][i])
118     theta3.append(math.acos(V_n3[i]/baseline3[i]))
119
120 Heading_angle_omni2 = np.mean(theta3)
121
122 # setting the x - coordinates

```

```

123 x = np.arange(0, 1302)
124 # setting the corresponding y - coordinates
125 y = baseline3
126 figure(figsize=(12, 8))
127 # plotting the points
128 plt.plot(x, y, color='green', linewidth = 1, label = 'Baseline')
129 plt.axhline(np.mean(baseline3), color='blue', label = 'Mean')
130 # plt.axhline(np.std(baseline3), color = 'orange', label = 'Std Deviation')
131 plt.xlabel('Time epochs')
132 plt.ylabel('Baseline values (m)')
133 plt.title('Omnidirectional baseline trend among observation window')
134 plt.legend()
135 plt.show()
136
137
138 # setting the x - coordinates
139 x = np.arange(0, 1302)
140 # setting the corresponding y - coordinates
141 y = theta3
142 figure(figsize=(12, 8))
143 # plotting the points
144 plt.plot(x, y, color='yellowgreen', linewidth = 0.7, label = 'Heading')
145 plt.axhline(np.mean(theta3), color = 'blue', label = 'Mean')
146 plt.axhline(np.mean(theta3), color = 'orange', label = 'Std Deviation')
147 plt.xlabel('Time epochs')
148 plt.ylabel('Angle values (rad)')
149 plt.title('Heading variation among observation window for omnidirectional
150         antennas')
150 plt.legend()
151 plt.show()
152
153 #Patch heading computation in static mode with Kinematic poaitioning and
154     reversed configuration
155 dataset4 = pd.read_excel(r'/Users/alessio/Downloads/
156     Heading_estimation_static_kinematic_reversed/Patch_dataset2.xlsx')
157 dataset_patch2 = dataset4[0:1363]
158 print(dataset_patch2)
159
160 baseline4 = []
161 V_n4 = []
162 theta4 = []
163 for i in range(len(dataset_patch2)):
164     baseline4.append(math.sqrt((dataset_patch2['E1'][i] - dataset_patch2['E2'][i]
165     ])**2 + (dataset_patch2['N1'][i] - dataset_patch2['N2'][i])**2))
166     V_n4.append(dataset_patch2['N2'][i] - dataset_patch2['N1'][i])
167     theta4.append(math.acos(V_n4[i]/baseline4[i]))
168
169 meanb4=np.mean(baseline4)
170 std4=np.std(baseline4)
171 Heading_angle_patch2 = np.mean(theta4)
172
173 # setting the x - coordinates
174 x = np.arange(0, 1363)
175 # setting the corresponding y - coordinates
176 y = baseline4
177 figure(figsize=(12, 8))
178 # plotting the points

```

```

177 plt.plot(x, y, color='green', linewidth = 0.7)
178 plt.axhline(meanb4, color='blue', label = 'Mean')
179 plt.axhline(std4, color = 'orange', label = 'Std Deviation')
180 plt.xlabel('Time epochs')
181 plt.ylabel('Baseline values (m)')
182 plt.title('Patch baseline trend among observation window')
183 plt.legend()
184 plt.show()
185
186
187 # setting the x - coordinates
188 x = np.arange(0, 1363)
189 # setting the corresponding y - coordinates
190 y = theta4
191 figure(figsize=(12, 8))
192 # plotting the points
193 plt.plot(x, y, color='yellowgreen', linewidth = 0.7)
194 plt.axhline(np.mean(theta4), color='blue', label = 'Mean')
195 plt.axhline(np.std(theta4), color = 'orange', label = 'Std Deviation')
196 plt.xlabel('Time epochs')
197 plt.ylabel('Angle values (rad)')
198 plt.title('Heading variation among observation window for patch antennas')
199 plt.legend()
200 plt.show()
201
202
203
204 #ERROR ESTIMATION BETWEEN OMNIDIRECTIONAL AND PATCH ANTENNAS IN NORMAL
    CONFIGURATION
205
206 Head1 = []
207 for i in range(len(dataset_omni)):
208     Head1.append(theta1[i]-theta2[i]) #Differenza tra stime di heading per
        onnidirezionali e patches
209 Mean_Head1 = np.mean(Head1) #valore medio stime heading
210 Std_Head1 = np.std(Head1) #standard deviation heading
211 x1 = np.arange(0, 2325)
212 y1 = Head1
213 figure(figsize=(12, 8))
214 # plotting the points
215 plt.plot(x1, y1, color='red', linewidth = 0.7, label = 'Heading')
216 plt.axhline(Mean_Head1, color='orange', label = 'Mean')
217 plt.axhline(Std_Head1, label = 'Std Deviation')
218 plt.xlabel('Time epochs')
219 plt.ylabel('Angle values (rad)')
220 plt.title('Error estimation between omnidirectional and patch antennas: normal
        configuration')
221 plt.legend()
222 plt.show()
223
224 #ERROR ESTIMATION BETWEEN OMNIDIRECTIONAL AND PATCH ANTENNAS IN REVERSED
    CONFIGURATION
225
226 Head2 = []
227 for i in range(len(dataset_omni2)):
228     Head2.append(theta3[i]-theta4[i]) #Differenza tra stime di heading per
        onnidirezionali e patches
229 Mean_Head2 = np.mean(Head2) #valore medio stime heading

```

```

230 Std_Head2 = np.std(Head2) #standard deviation heading
231 x2 = np.arange(0, 1302)
232 y2 = Head2
233 figure(figsize=(12, 8))
234 # plotting the points
235 plt.plot(x2, y2, color='red', linewidth = 0.7, label = 'Heading')
236 plt.axhline(Mean_Head2, color='blue', linewidth = 0.7, label = 'Mean')
237 plt.axhline(Std_Head2, color='orange', linewidth = 0.7, label = 'Std Deviation')
238 plt.xlabel('Time epochs')
239 plt.ylabel('Angle values (rad)')
240 plt.title('Error estimation between omnidirectional and patches antennas:
           reversed configuration')
241 plt.legend()
242 plt.show()
243
244 #ERROR PARAMETERS ESTIMATION
245
246 print('Mean and Standard deviation for normal configuration:', 'mean:',
       Mean_Head1, 'standard deviation:', Std_Head1)
247 print('Mean and Standard deviation for reversed configuration:', 'mean:',
       Mean_Head2, 'standard deviation:', Std_Head2)

```

Listing 1: Baseline and heading angle estimation from E/N/S coordinates.

```

1 import pandas as pd
2 import matplotlib.pyplot as plt
3 import numpy as np
4 import math
5 from matplotlib.pyplot import figure
6
7
8 #Omnidirectional heading computation in static mode with Kinematic positioning
9
10 dataset1 = pd.read_excel(r'/Users/alessio/Downloads/Continuous_rotation_dx.xlsx'
11 )
12 dataset_omni = dataset1[0:461]
13 print(dataset_omni)
14
15 dL=[]
16 X=[]
17 Y=[]
18 Rad=[]
19 Bearing=[]
20
21 for i in range(len(dataset_omni)):
22     dL.append(dataset_omni['Long2'][i]-dataset_omni['Long1'][i])
23     X.append(np.cos(dataset_omni['Lat2'][i])*np.sin(dL)[i])
24     Y.append(np.cos(dataset_omni['Lat1'][i])*np.sin(dataset_omni['Lat2'][i])-np.
25             sin(dataset_omni['Lat1'][i])*np.cos(dataset_omni['Lat2'][i])*np.cos(dL)[i])
26     Rad.append(np.arctan2(X[i],Y[i]))
27     Bearing.append(Rad[i]*(180/math.pi))
28
29 print(dL)
30 print(X)
31 print(Y)
32 print(Bearing)
33
34 # setting the x - coordinates
35 x = np.arange(0, 461)
36 # setting the corresponding y - coordinates

```

```

34 y = Bearing
35 figure(figsize=(12, 8))
36 # plotting the points
37 plt.plot(x, y, color='green', linewidth = 0.7, label = 'Bearing angle')
38 plt.axhline(np.mean(Bearing), color = 'blue', label = 'Mean')
39 # plt.axhline(np.std(Bearing), color = 'orange', label = 'Std Deviation')
40 plt.xlabel('Time epochs')
41 plt.ylabel('Angle values (Deg)')
42 plt.title('Bearing variation for omnidirectional antennas (normal configuration)')
43 plt.legend()
44 plt.show()
45
46 dataset2 = pd.read_excel(r'/Users/alessio/Downloads/
    Continuous_rotation_dx_reversed.xlsx')
47 dataset_omni2 = dataset2[0:477]
48 print(dataset_omni2)
49
50 dL2=[]
51 X2=[]
52 Y2=[]
53 Rad2=[]
54 Bearing2 = []
55 for i in range(len(dataset_omni2)):
56     dL2.append(dataset_omni2['Long2'][i]-dataset_omni2['Long1'][i])
57     X2.append(np.cos(dataset_omni2['Lat2'][i])*np.sin(dL2)[i])
58     Y2.append(np.cos(dataset_omni2['Lat1'][i])*np.sin(dataset_omni2['Lat2'][i])-
        np.sin(dataset_omni2['Lat1'][i])*np.cos(dataset_omni2['Lat2'][i])*np.cos(dL2)
        [i])
59     Rad2.append(np.arctan2(X2[i],Y2[i]))
60     Bearing2.append(Rad2[i]*(180/math.pi))
61 print(dL2)
62 print(X2)
63 print(Y2)
64 print(Bearing2)
65
66 # setting the x - coordinates
67 x = np.arange(0, 477)
68 # setting the corresponding y - coordinates
69 y = Bearing2
70 figure(figsize=(12, 8))
71 # plotting the points
72 plt.plot(x, y, color='orange', linewidth = 0.7, label = 'Bearing angle')
73 plt.axhline(np.mean(Bearing2), color = 'blue', label = 'Mean')
74 # plt.axhline(np.std(Bearing2), color = 'orange', label = 'Std Deviation')
75 plt.xlabel('Time epochs')
76 plt.ylabel('Angle values (Deg)')
77 plt.title('Bearing variation for omnidirectional antennas')
78 plt.legend(prop={"size":10})
79 plt.show()

```

Listing 2: Bearing estimation from Latitude and Longitude

```

1 import matplotlib.pyplot as plt
2 import numpy as np
3 import math
4 from matplotlib.pyplot import figure
5 from scipy.interpolate import interp1d
6

```

```

7 x = np.linspace(0, 80, num=17, endpoint=True)
8 y = [0.0,-0.63,-0.91,-0.94,-0.94,-0.73,-0.58,-0.41,-0.30,-0.04,0.02,-0.02,-0.16,
9      -0.58,-1.11,-1.64,-2.07]
10 f2 = interp1d(x, y, kind='cubic')
11
12 xnew = np.linspace(0, 80, num=17, endpoint=True)
13 figure(figsize=(12, 8))
14 plt.plot(x, y, 'o', xnew, f2(xnew), '--')
15 plt.ylabel('Phase Center Variation (mm)')
16 plt.xlabel('Elevation (Deg)')
17 plt.title('GPS500 Phase center variation vs Azimuth elevation form 0 to 80 (non-
18 azimuth-dependent pattern)')
19 plt.legend(['PCV data in G01 frequency'], loc='best')
20 plt.show()
21
22 x2 = np.linspace(80, 0, num=17, endpoint=True)
23 y2 =
24     [0.0,0.47,0.69,0.82,0.71,0.52,0.30,-0.07,-0.42,-0.62,-0.66,-0.46,-0.13,0.37,
25      0.77,1.27,1.82]
26 f3 = interp1d(x2, y2, kind='cubic')
27
28 xnew2 = np.linspace(0, 80, num=17, endpoint=True)
29 figure(figsize=(12, 8))
30 plt.plot(x2, y2, 'o', xnew2, f3(xnew2), '--')
31 plt.ylabel('Phase Center Variation (mm)')
32 plt.xlabel('Elevation (Deg)')
33 plt.title('GPS500 Phase center variation vs Azimuth elevation form 0 to 80 (non-
34 azimuth-dependent pattern)')
35 plt.legend(['PCV data in G02 frequency'], loc='best')
36 plt.show()

```

Listing 3: Phase Center Variation (mm) of GPS500 antenna considering the G01 and G02 frequency

References

- [1] S. G. Gupta, M. M. Ghonge, and P. Jawandhiya, "Review of unmanned aircraft system (UAS)," *International Journal of Advanced Research in Computer Engineering & Technology (IJARCET)*, vol. 2, pp. pp: 1646-1658, 2013.
- [2] I.s.c. AN/190. unmanned Aircraft system [Online]. Available: www.icao.int/Meetings/UAS/Documents/Circular%20328_en.pdf
- [3] B.P.Tice, "Unmanned aerial vehicles: The force multiplier of the 1990s," *Airpower Journal*, vol. 5, pp. 41-54, 1991.
- [4] "Unmanned Aerial Vehicle Classification, Applications and Challenges: A Review". Available from: <https://www.researchgate.net/publication/329422590> Unmanned Aerial Vehicle Classification Applications and Challenges: A Review.
- [5] U. E. Franke, "Civilian drones: Fixing an image problem?" *ISN Blog. International Relations and Security Network*. Retrieved, vol. 5, 2015.
- [6] M. A. Fenelon and T. Furukawa, "Design of an active flapping wing mechanism and a micro aerial vehicle using a rotary actuator," *Mechanism and Machine Theory*, vol. 45, pp. 137-146, 2010.

- [7] W. Shyy, Y. Lian, J. Tang, D. Viieru, and H. Liu, *Aerodynamics of low Reynolds number flyers* vol. 22: Cambridge University Press, 2007.
- [8] W. Shyy, H. Aono, C.-k. Kang, and H. Liu, *An introduction to flapping wing aerodynamics* vol. 37: Cambridge University Press, 2013.
- [9] K. Jones, C. Bradshaw, J. Papadopoulos, and M. Platzer, "Bio-inspired design of flapping-wing micro air vehicles," *The Aeronautical Journal*, vol. 109, pp. 385-393, 2005.
- [10] P. M. Joshi, "wing analysis of a flapping wing Unmanned aerial vehicle using CFD," *Development*, vol. 2, 2015.
- [11] B. K. Chung and H. T. Chuah, "Modeling of rf absorber for application in the design of anechoic chamber technologies for future precision strike missile systems," *Progress In Electro- magnetics Research*, vol. 43, pp. 273–285, 2003.
- [12] K. Schauwecker, N. R. Ke, S. A. Scherer, and A. Zell, "Markerless visual control of a quadrotor micro aerial vehicle by means of on-board stereo processing," in *Autonomous Mobile Systems 2012*, ed: Springer, 2012, pp. 11-20.
- [13] R. Austin, *Unmanned aircraft systems: UAVS design, development and deployment* vol. 54: John Wiley & Sons, 2011.
- [14] M. Hassanalian and A. Abdelkefi, "Classifications, applications, and design challenges of drones: a review," *Progress in Aerospace Sciences*, vol. 91, pp. 99-131, 2017.
- [15] E. Torun, "UAV Requirements and design consideration," *Turkish Land Forces Command Ankara (Turkey)2000*.
- [16] C. Soutis, "Fibre-reinforced composites in aircraft construction," *Progress in Aerospace Sciences*, vol. 41, pp. 143-151, 2005.
- [17] H. Eisenbeiss, "A mini unmanned aerial vehicle (UAV): system overview and image acquisition," *International Archives of Photogrammetry. Remote Sensing and Spatial Information Sciences*, vol. 36, pp. 1-7, 2004.
- [18] H. Xiang and L. Tian, "Development of a low-cost agricultural remote sensing system based on an autonomous unmanned aerial vehicle (UAV)," *Biosystems Engineering*, vol. 108, pp. 174-190, 2011.
- [19] E. D. Kaplan and C. J. Hegarty, "Understanding GPS/GNSS Principles and Applications", Third Edition, Artech House, pp. 1-2/10-11, 2017.
- [20] *Global Navigation Satellite Systems Performance Analysis and Augmentation Strategies in Aviation*. Available from: <https://www.researchgate.net/publication/321022891> *Global Navigation Satellite Systems Performance Analysis and Augmentation Strategies in Aviation*.
- [21] Braun J., Rocken C., Meertens C.M., Johanson J. (1993). GPS antenna mixing and phase center corrections. *Eos Trans. AGU, Fall Meeting Supplement*, p. 197.
- [22] Rothacher M, Schaer S, Mervart L, Beutler G (1995). Determination of antenna phase center variations using GPS data. Gendt G. and Dick G. (eds) *Proc 1995 IGS Workshop, GeoForschungs Zentrum Potsdam, Potsdam*, pp 205–220.

- [23] Rothacher M (2001). Comparison of absolute and relative antenna phase center variations. *GPS Solution* 4(4):55–60.
- [24] Zhu SY, Massmann F-H, Yu Y, Reigber Ch (2003). Satellite antenna phase center offsets and scale errors in GPS solutions. *J Geod* 76(11–12): 668–672.
- [25] Dawidowicz, K., (2010), Antenna phase center variations corrections in processing of GPS observations with use of commercial software, *Techn. Sc.*, 13, 120-132.
- [26] EL-Hattab, A., (2013), Influence of GPS antenna phase center variation on precise positioning. 28 November, *NRIAG Journal* (2): 272-277.
- [27] Hofmann-Wellenhof, B., H. Lichtenegger, E. Wasle, (2008), *GNSS–Global Navigation Satellite Systems*. Springer-Verlag Wien, Austria.
- [28] Borre K, Akos DM, Bertelsen N, Rinder P, Jensen SH. *A Software-Deined GPS and Galileo Receiver a Single-Frequency Approach*. Boston: Birkha user Boston; 2007
- [29] Misra P, Enge P. *Global Positioning System: Signals, Measurements and Performance*. Massachusets: Ganga-Jamuna; 2010
- [30] IS-GPS-200H. Interface specification. Navstar GPS Space Segment/Navigation User Interfaces. 2013 Sept:24
- [31] Misra P, Enge P. *Global Positioning System: Signals, Measurements and Performance*. Massachusets: Ganga-Jamuna; 2010.
- [32] Farrell J. *Aided Navigation GPS with High Rate Sensors*. New York: McGraw-Hill; 2008.
- [33] Aboelmagd N, Karmat T, Georgy J. *Fundamentals of Inertial Navigation, Satellite-Based Positioning and their Integration*. 1st ed. New York: Springer-Verlag Berlin Heidelber; 2013.
- [34] Malek Karaim, Mohamed Elsheik, Aboelmagd Noureldin. "GNSS Error Sources"; *IntechOpen*, Ch. 4, pp. 7, Ed. 2018.
- [35] Klobuchar J. Ionospheric time-delay algorithm for single-frequency GPS users. *IEEE Transactions on aerospace and electronic systems*. 1987;(3):325-331
- [36] Juan J, Hernández-Pajares M, Sanz J, Ramos-Bosch P, Aragón-Àngel A, Orús R, et al. Enhanced precise point positioning for GNSS users. *IEEE transactions on geoscience and remote sensing*. 2012;50(10):4213-4222
- [37] Nava B, Coisson P, Radicella S. A new version of the NeQuick ionosphere electron density model. *Journal of Atmospheric and Solar-Terrestrial Physics*;70(15):1856-1862
- [38] Hobiger T, Norbert J. Atmospheric signal propagation. In: Teunissen P, Montenbruck O, editors. *Springer Handbook of Global Navigation Satellite Systems*. Cham: Springer; 2017. pp. 165-193
- [39] Jin S. *Global Navigation Satellite Systems Signal*. InTech: Theory and Applications Croatia; 2012.
- [40] Schuler T. *On Ground-Based GPS Tropospheric Delay Estimation*: Univ. der Bundeswehr Munchen; 2001.

- [41] Meguro J, Murata T, Takiguchi J, Amano Y, Hashizume T. GPS multipath mitigation for urban area using omnidirectional infrared camera. *IEEE transactions on intelligent transportation systems*. 2009;10(1):22-30
- [42] Hofmann-Wellenhof B, Lichtenegger H, Herbert W, Wasle E. *GNSS—Global Navigation Satellite Systems: GPS, GLONASS, Galileo, and More*. Springer Science & Business Media; 2007
- [43] Kunysz W. High performance GPS pinwheel antenna. In: *Proceedings of the ION GPS*. 2000. pp. 19-22
- [44] Daneshmand S, Broumandan A, Sokhandan N, Lachapelle G. GNSS multipath mitigation with a moving antenna array. *IEEE Transactions on Aerospace and Electronic Systems*. 2013;49(1):693-698
- [45] Braasch M. Multipath. In: Teunissen P, Montenbruck O, editors. *Springer Handbook of Global Navigation Satellite Systems*. Cham: Springer; 2017. pp. 443-468
- [46] Xu G, Xu Y. *GPS: Theory, Algorithms and Applications*. Springer; 2016
- [47] Tsui J. *Fundamentals of Global Positioning System Receivers: A Software Approach*. New York: John Wiley & Sons, Inc; 2000
- [48] Wu H. *On-The-Fly GPS Ambiguity Resolution with Inertial Aiding*. Calgary, Canada: Department of Geomatics Engineering, University of Calgary; 2003. [M.S. Thesis]
- [49] IGS products. [Online]. [cited 2017 December 3. Available from: <http://www.igs.org/products>
- [50] Selective Availability. [Online]. Available from: <https://www.gps.gov/systems/gps/modernization/sa/>
- [51] Kaplan E, Hegarty C. *Understanding GPS Principles and Applications*. Norwood, MA, USA: ARTECH HOUSE, Inc; 2006
- [52] Curran J, Bavard M, Closas P, Navarro M. A look at the threat of systematic jamming of GNSS. *InsideGNSS*. 2017;12(5):46-53
- [53] National PNT Advisory Board comments on Jamming the Global Positioning System. *A National Security Threat: Recent Events and Potential Cures*; 2010
- [54] Humphreys T. Interference. In: Teunissen P, Montenbruck O, editors. *Springer Handbook of Global Navigation Satellite Systems*. Cham: Springer; 2017. pp. 469-503
- [55] Jeffrey C. *An Introduction to GNSS. GPS, GLONASS, Galileo and Other Global Navigation Satellite Systems*. Calgary: NovAtel Inc.; 2010
- [56] Spinney, V. (1976), Application of the Global Positioning System as an attitude reference for near-earth users, *New frontiers in aerospace navigation*, pp. 132–136.
- [57] James T. Pinchin. "GNSS Based Attitude Determination for Small Unmanned Aerial Vehicles"; 2011
- [58] "Differential GPS". Available from: https://en.wikipedia.org/wiki/Differential_GPS#Post_processing

- [59] Editorial for Special Issue “UAV Photogrammetry and Remote Sensing”, Fernando Carvajal-Ramírez 1, Francisco Agüera-Vega and Patricio Martínez-Carricondo. Available at: <https://doi.org/10.3390/rs13122327>
- [60] ”The Kalman Filter”, available at: ”<https://thekalmanfilter.com/kalmanfilterexplained-simply/>”